博士学位論文
Doctoral Thesis

論文題目
Thesis Title

Understanding and Modeling the Reaction Mechanism of Carbonate and Phosphate Esters

東北大学大学院工学研究科
Graduate School of Engineering,
TOHOKU UNIVERSITY

専攻/Department: Mechanical Systems Engineering

学籍番号/ ID No: C0TD1004

氏名/Name: Keisuke KANAYAMA

TOHOKU UNIVERSITY
Graduate School of Engineering

Understanding and Modeling the Reaction Mechanism of Carbonate and Phosphate Esters

（炭酸エステルおよびリン酸エステルの反応機構の理解およびモデリング）

A dissertation submitted for the degree of Doctor of Philosophy (Engineering)

Department of Mechanical Systems Engineering

by

Keisuke KANAYAMA

January 9, 2024

Understanding and Modeling the Reaction Mechanism of Carbonate and Phosphate Esters

Keisuke KANAYAMA

Abstract

This dissertation aimed to understand and model the pyrolysis and oxidation mechanisms of carbonate and phosphate esters. With the increasing demand for lithium-ion batteries (LIBs), especially large-scale LIB applications in energy and transport sectors due to environmental and energy problems, LIB fires urgently needed to be dealt with. In such LIB fires, one of the major fire hazards involved in LIB components is the electrolytes, which consist of lithium salts with most commonly, carbonate esters. Cyclic and linear carbonate esters, such as ethylene carbonate (EC), dimethyl carbonate (DMC), diethyl carbonate (DEC) and ethyl methyl carbonate (EMC), are commercially used as LIB electrolyte solvents. Understanding and predicting their combustion characteristic as well as the role of fire-retardant additives, such as trimethyl phosphate (TMP), are important to mitigate LIB fires. In this regard, pyrolysis and oxidation characteristics of linear carbonate esters, i.e., DMC, DEC and EMC, cyclic carbonate ester, i.e., EC, and phosphate ester, i.e., TMP, were investigated experimentally, computationally and theoretically. In this dissertation, a variety of experimental approaches were employed, namely a micro flow reactor with a controlled temperature profile (MFR), shock tube, spherically propagating flame and photoelectron photoion coincidence (PEPICO) spectroscopy as well as conventional gas analyzers, gas chromatography (GC) and time-of-flight mass spectrometry (TOF-MS). The goal of this project is to construct a comprehensive LIB surrogate chemical kinetic model that includes carbonate ester solvents and fire-retardant additives. In Chapter 1 and Chapter 2, the introduction and the experimental approaches (MFR and PEPICO) were given, respectively.

In Chapter 3, pyrolysis and oxidation of DMC, DEC and EMC were investigated using MFR with GC. Species measurements were conducted for 1.5% linear carbonate ester(/O_2)/N_2 mixtures and weak flame observations were conducted for linear carbonate ester/air mixtures. Based on the species measurements, the pyrolysis and oxidation characteristics of DEC and EMC were found to be similar to each other, while differ from DMC. DMC was mainly consumed by H-atom abstraction reactions and a unimolecular decomposition reaction that produces CO_2 and dimethyl ether (DME) under oxidation and pyrolysis conditions, respectively. Meanwhile, DEC and EMC were consumed by analogue unimolecular decomposition reactions that produce C_2H_4 and the rest moiety under both oxidation and pyrolysis conditions. From weak flame observations, gas-phase reactivities were found to be DMC $<$ DEC $\approx$ EMC. Thus, the pyrolysis and oxidation characteristics of the linear carbonate esters can be classified by whether the molecule structure includes an ethyl (ester) group.

In Chapter 4, pyrolysis and oxidation of EC were investigated using MFR with GC and TOF-MS and a shock tube with laser diagnostics, respectively. The unimolecular decomposition of EC was investigated theoretically, which indicates that the most energetically favored decomposition channel is the production of CO_2 and acetaldehyde (CH_3CHO). The first chemical kinetic model that covers pyrolysis and oxidation of EC, DMC, DEC and EMC — LIB electrolyte surrogate model — was constructed through the modeling of EC. The

EC/DMC pyrolysis experiment at the maximum wall temperature ($T_{w,max}$) of 700–1200 K using MFR showed that the EC mole fraction decreased at a lower temperature range as compared to DMC. The shock-tube experiments for the EC oxidation, ignition delay time and CO laser absorption measurements, were conducted at a wide range of equivalence ratios (0.5, 1.0 and 2.0) and temperatures (around 1200–1700 K), and small and large equivalence ratio dependence was observed in the former and latter, respectively. Although a discrepancy in the CO time-history profiles became larger as temperature lowered and/or equivalence ratio increased, the newly constructed model well-captured the experimental results overall for both pyrolysis and oxidation. From reaction flux analyses, the EC decomposition reaction producing CO_2 and CH_3CHO was the dominant EC consumption pathways at both pyrolysis and oxidation conditions. Laminar flame speeds of H_2/air mixtures doped with 0.5% EC were measured. A significant drop in the simulated laminar flame speed was observed with the EC addition compared to neat H_2/air mixtures over the equivalence ratio range of 0.8 to 3.0.

In Chapter 5, global combustion properties, i.e., laminar flame speeds and ignition delay times, of multi-component (EC/DMC, EC/DEC and EC/EMC) as well as single-component LIB electrolyte solvents (EC, DMC, DEC and EMC) were simulated using the LIB electrolyte surrogate model. By blending EC with the linear carbonate esters, the simulated laminar flame speeds decreased. The simulated laminar flame speed of EC/DMC was slower than that of EC/DEC and EC/EMC at 500 K, atmospheric pressure and near stoichiometric conditions. This is the opposite trend to the liquid-based flammability classification, suggesting that the gas-phase combustion properties of carbonate esters need to be considered in certain LIB fire scenarios.

In Chapter 6, photoelectron characterization of the most fundamental CO_3-moiety, carbonic acid (H_2CO_3), was investigated using synchrotron vacuum ultraviolet (VUV) radiation and PEPICO spectroscopy, aiming to understand the synchrotron-based technique, which is applied to explore the TMP pyrolysis mechanism in the following chapter. H_2CO_3 was produced from di-*tert*-butyl carbonate flash pyrolysis and detected with PEPICO spectroscopy. Photoelectron spectrum of gaseous H_2CO_3 was obtained for the first time and moreover, its two of three conformers, namely *cis-cis* and *cis-trans* H_2CO_3, were identified conformer-selectively with the aid of Franck–Condon simulations.

In Chapter 7, pyrolysis of TMP, an organophosphorus compound, was investigated using synchrotron VUV radiation and PEPICO spectroscopy combined with a pyrolysis reactor. Hydrocarbon, oxygenated and phosphorus-containing reactive intermediates including radicals were isomer-selectively detected in the experiment by obtaining photoion mass-selected threshold photoelectron spectra (ms-TPES). TMP unimolecular decomposition was also investigated theoretically, and H-transfer and CH_3-transfer isomerization were found to be energetically favored channels, followed by methanol/methyl loss and DME loss, respectively. Based on the experimental results with the support of quantum chemical calculations, thermal decomposition reaction pathways of TMP were proposed. The newly reported reactions, such as the DME production channel, have been eluded discussions and are not included in a currently available TMP chemical kinetic model in the literature. In addition, analogue DME production channel was also found in dimethyl methylphosphonate (DMMP) unimolecular decomposition in the present work, which has neither been reported nor included in a literature DMMP model. These unimolecular decomposition reactions potentially impact model predictions and thus may need to be considered for future modeling.

Table of Contents

List of Figures

List of Tables

Chapter 1

Introduction

This dissertation tackles to reveal the gas-phase combustion chemistry of carbonate and phosphate esters behind lithium-ion battery fires.

1.1 General backgrounds

Our planet is threatened by our activities. Human activities have significantly driven environmental changes since the Industrial Revolution [1], marking an era called the Anthropocene [2]. According to the planetary boundaries proposed by Rockström et al. [3,4] as shown in Figure 1.1, six out of nine boundaries have already been crossed in 2023 [5,6]. For instance, the lower boundary and upper boundary, which means increasing risk and may lead to irreversible change if exceeded, for the CO_2 concentration in the atmosphere in the climate change are set to 350 and 450 ppm, respectively. However, the latest researches reported the current CO_2 concentration to be 417 ppm in 2022 [6,7], approaching the upper boundary. Thus, addressing these environmental problems is an immediate priority. Meanwhile, the worlds energy demand is also escalating not only because of the industrialization and economic growth but also the population growth. As for today, we still largely rely on fossil fuels such as oil, coals and natural gas as energy sources, which account for around 80% of world primary energy consumption in 2022 [8]. Based on a roadmap for the net-zero greenhouse gas (GHG) emissions by 2050 aiming to achieve the global temperature increase within 1.5 °C reported by the International Energy Agency (IEA) [9], the transition of those fossil fuels to low/zero-carbon technologies is pivotal. They also referred to the importance of the stability, availability and accessibility of the energy supplies as well as the robust economic growth during the transition. To contribute to the Sustainable Development Goals (SDGs) [10] from aspects such as affordable and clean energy (Goal 7) and climate action (Goal 13), strategies to mitigate GHG emissions are introduced in the next section.

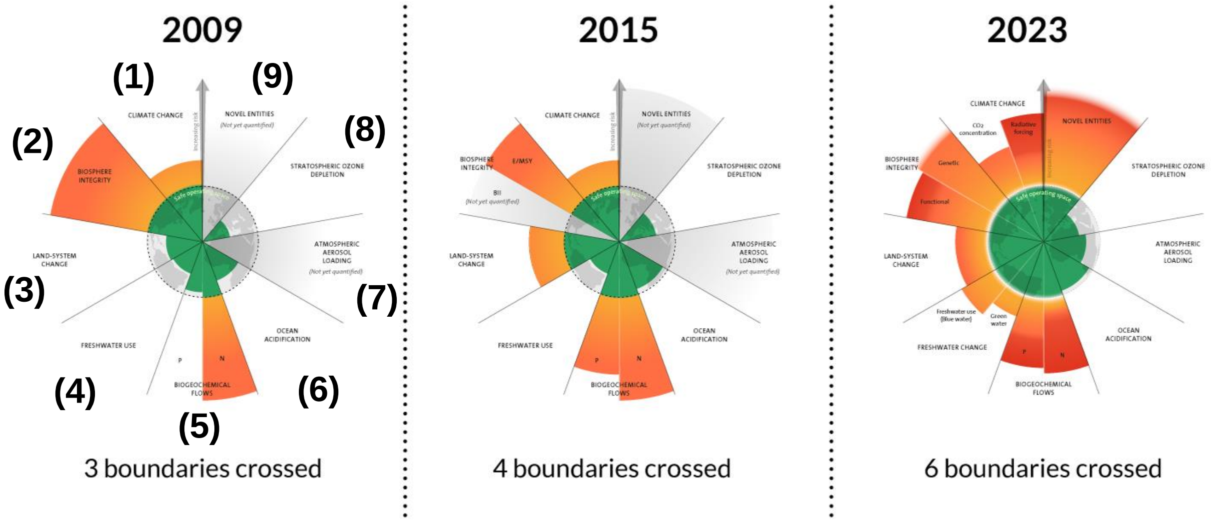

Figure 1.1 Change in planetary boundaries over years [3–6]. Image taken from Stockholm Resilience Centre, Stockholm University [11], with modification. (1) Climate change, (2) biosphere integrity, (3) land-system change, (4) freshwater change, (5) biogeochemical flows, (6) ocean acidification, (7) atmospheric aerosol loading, (8) stratospheric ozone depletion and (9) novel entities.

1.1.1 Mitigation of GHG emissions from energy and transport sectors

As world's GHG emission by sector shown in Figure 1.2 [12], the total amount of emission generally tends to increase, reaching to about 53.8 Gt CO_{2eq} in 2022. Here, CO_2, CH_4, N_2O and fluorinated species are considered as GHG, and they are converted to CO_2-equivalent amount (CO_{2eq}) based on their Global Warming Potential (GWP) values. Note that the drop in 2020 is due to COVID-19 pandemic [12]. The GHG emissions from the power industry are dominant over the years, accounting for roughly 30% in 2022, and those from transport show the third largest amount. In order to reduce emissions from those sectors, there are various technologies challenging the mitigation of GHG emissions from energy/transport.

In terms of the transformation of fossil fuels, alternative fuels such as biofuels and hydrogen/ammonia are gaining attentions. The former are typically oxygenated fuels such as alcohols, ethers and esters. As they are produced from renewable biomass that absorbs CO_2

from the atmosphere by photosynthesis while they grow up, the net-CO_2 cycle is generally regarded to be superior to conventional hydrocarbon fuels. The latter are carbon-free fuels that do not emit CO_2 from combustion. Hydrogen and fuel ammonia have been recently adopted as a specific sector that is expected for the growth to realize the carbon neutralization by 2050 by the Japanese government [13]. Another technology is, of course, the use of renewable energy such as solar and wind power instead of combustion energies. Both powers can generate electricity without GHG emissions during their operation, thus considered as representatives of clean energy sources. A challenge of solar and wind power is, however, their intermittency as frequently discussed (e.g., [14]). To compensate for their inconsistent power generation and supply, power needs to be stored and distributed depending on the demand.

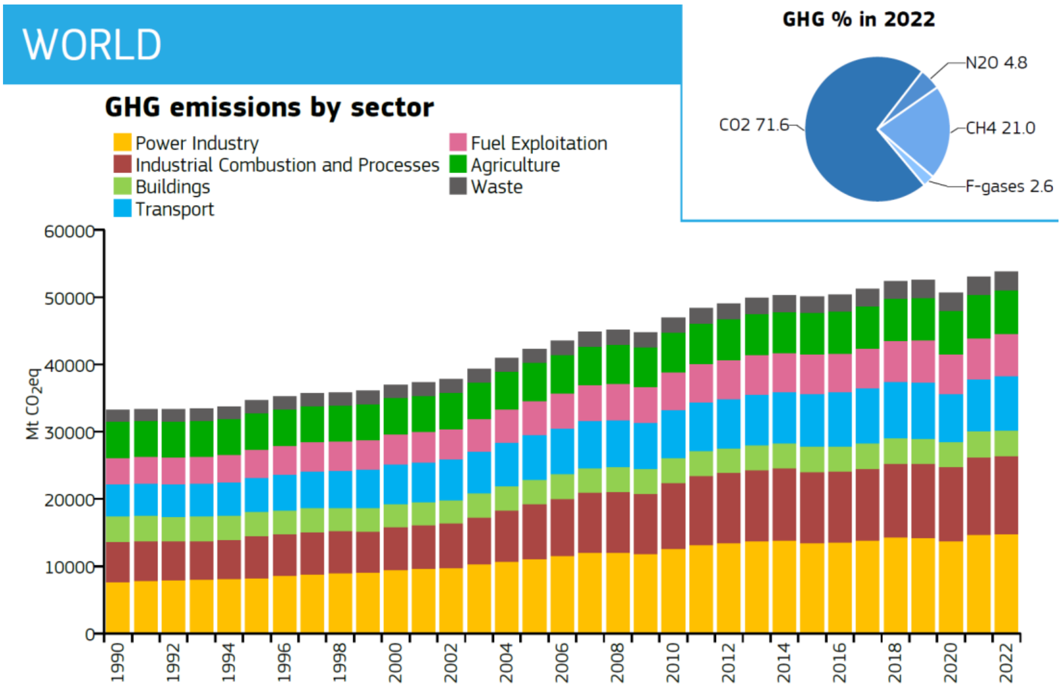

Year	GHG emissions Mt CO_2eq/yr	GHG emissions per capita t CO_2eq/cap/yr	GHG emissions per unit of GDP PPP t CO_2eq/kUSD/yr	Population
2022	53786.039	6.762	0.386	7.954G
2015	50134.384	6.792	0.436	7.381G
2005	42318.428	6.470	0.515	6.540G
1990	33268.121	6.242	0.641	5.330G

Figure 1.2 World greenhouse gas (GHG) emissions by sector reported in 2023 [12].

In addition to the utilization of low/zero-carbon fuels and renewable energies, lithium-ion batteries (LIBs) also aid the energy and transport sectors in stepping away from GHG emissions. According to Jeevarajan et al. [15], electrochemical battery energy storage systems have made a big leap in adoption among other storage systems such as mechanical (e.g., flywheel), thermal (e.g., latent phase change material), chemical (e.g., fuel cells) and electrical (e.g., supercapacitor), and moreover, LIB has become preferred for grid-level installations among rechargeable batteries. The number of electric vehicles (EV), including both battery and plug-in hybrid, has also been rapidly increasing, e.g., 26 million in 2022 from 5 million in 2018 [16]. Thus, large-scale LIB technology is expandingly being applied in the energy and transport sectors [17].

1.1.2 Lithium-ion battery (LIB)

Since LIB was invented in 1985 by Yoshino et al. [18,19] and commercialized by Sony corporation in 1991, LIB has been used in many applications thanks to its high energy density compared to other secondary batteries, portable size and weight, lack of memory effect and charge-discharge cycle durability. For instance, small electronic devices, such as smartphones and laptops, and even large-scall products, such as electric vehicles and energy storage systems. The main components of LIB are cathode, anode, separators and electrolytes, as shown in Figure 1.3. The cathode provides Li^+ for the anode during the charging process, while Li^+ moves in the opposite direction during the discharge process. The cathode material consists of transition metal oxides that contain Li^+, such as $LiCoO_2$, $LiMn_2O_4$, $Li(Ni_xCo_yAl_z)O_2$ and $Li(Ni_xCo_yMn_z)O_2$, which are called as LCO, LMO, NCA and NCM, respectively. The conventional anode is, as defined by Yoshino et al. [18], made from carbonaceous materials such as graphite or $Li_4Ti_5O_{12}$. These electrodes are isolated from each other by the separator to prevent an internal short circuit without hindering the transfer of free Li^+ [20]. As a conventional separator, a polyolefin membrane, which is made from polyethylene or polypropylene, is used [21]. Some of the requirements for the separator, apart from the high electrical insulation, are such that good interaction with electrolytes, e.g., wettability and permeability, as the liquid electrolytes infill the pore space of both electrodes and separators [22]. The electrolytes, which is regarded as the “blood” of the LIB [22], enable Li^+ to circulate through the LIB cell. The widely used electrolytes consist of Li salts, most commonly lithium hexafluorophosphate ($LiPF_6$), and organic solvents, such as ethylene carbonate (EC), dimethyl carbonate (DMC), diethyl carbonate (DEC), ethyl methyl carbonate (EMC) and propylene carbonate (PC), i.e., carbonate esters [23]. Typical compositions of commercially available $LiPF_6$-based LIB electrolytes are listed in Table 1.1. The electrochemical and physical reasons for the use of the mixture of those carbonate esters as electrolyte solvents are their high dielectric constant that facilitates the dissociation of Li salts and low viscosity that facilitates Li^+ to float around, respectively.

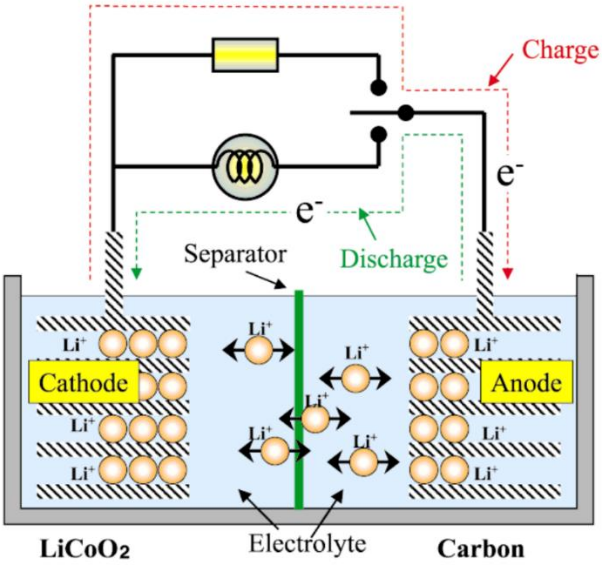

Figure 1.3 Schematic of the LIB electrochemical mechanism [24].

Table 1.1 Commercially available $LiPF_6$-based LIB electrolytes (1 M $LiPF_6$).

Electrolyte solvents	Mixture weight ratio	Designation
EC/DMC	1/1	LP30
EC/DEC	1/1	LP40
EC/EMC	1/1	LP50
EC/DEC/DMC	1/1/1	LP71
EC/PC/DMC	1/1/3	LP100

1.2 LIB fires

Although the LIB performance is attractive for many products, a main concern is fire safety, in which flammable electrolytes are regarded as one of the main fire causes involved. Here, LIB fire incidents and the fire mechanisms is presented first. Then, how we contribute to mitigation of the LIB fires by understanding and modeling the reaction mechanisms of carbonate/phosphate esters will be proposed.

1.2.1 LIB fire incidents

As the number and size of LIB applications increase, the LIB fires have become more serious and urgent problems to be dealt with. Many LIB-related fire incidents have been reported for such as smartphones [25], electric vehicles [26] and energy storage systems [27]. A general process of the LIB fire accidents can be given as follows. An internal short circuit triggers a thermal runaway event, which is a self-enhanced temperature increase, leading to fire and/or explosion. For instance, a large-scale LIB energy storage system in Australia caught a fire in 2021. According to the investigation report [27], a leakage within the liquid cooling system of one of the battery packs causing arcing in the power electronics of the battery modules, leading to heating of the battery cells, eventually followed by a thermal runaway event and fire.

A LIB fire process for the typical scenario, i.e., thermal runaway caused by an internal short circuit, and its interpretation are given in Figure 1.4. Initial causes of the LIB fires are mechanical (e.g., crash and penetration), electrical (e.g., overcharge and overdischarge) and thermal (e.g., overheat) abuse as well as manufacturing defect (e.g., contamination). These initial abuse may directly trigger thermal runaway or damage the separator by tearing mechanically, piercing with grown dendrite [28] or high temperatures, which leads to an internal short circuit [29]. Whether the event after an internal short circuit proceeds to thermal runaway or ends up without thermal runaway depends on battery materials and generated heat.

During the thermal runaway event, as temperature is high enough to vaporize liquid electrolytes (e.g., boiling point of DMC and DEC is 90.5°C and 126°C, respectively [30]), the flammable, gas-phase carbonate esters are produced, and the thermal runaway eventually leads to fire or even explosion.

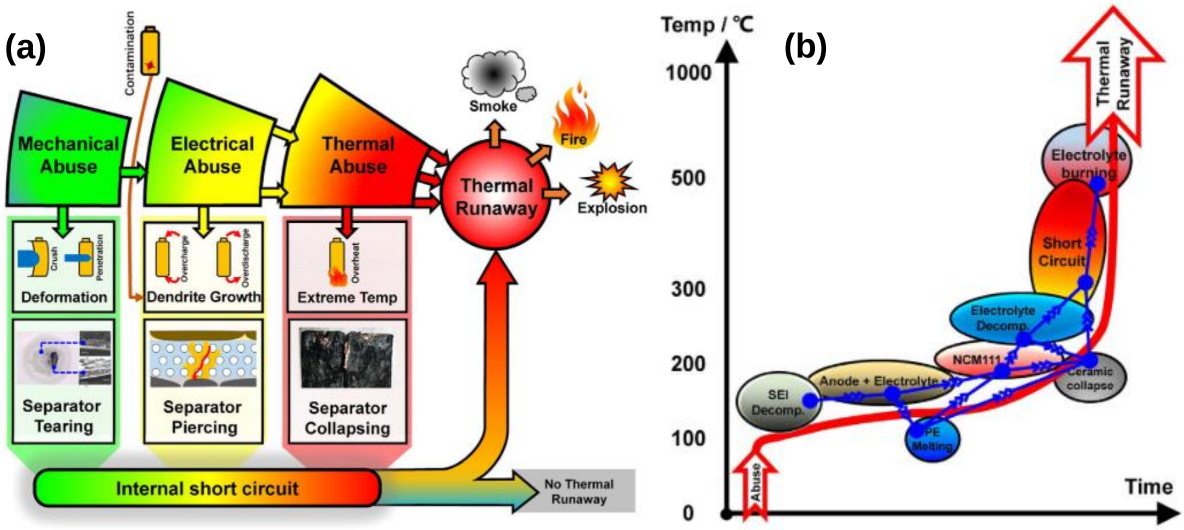

Figure 1.4 (a) LIB fire process for the most common scenario with thermal runaway, and (b) a qualitative interpretation during a thermal runaway event [29].

Among the LIB components, electrolytes are one of the most probable fire hazards because a large part of combustion enthalpy is delivered from electrolytes [31], especially electrolyte solvents [32] when LIB fire occurs. As mentioned above, the vaporized electrolytes can be produced during a thermal runaway event and ejected outside the LIB cell through safety vents, if fail-safe mechanism works [33]. This venting system release the generated gases inside the cell to reduces the cell inner pressure, aiming to avoid a rupture of the cell and explosion. Figure 1.5 shows battery cell surface temperature and mass changes as well as images of the cells during the thermal runaway event, which is triggered by heating with an external electric heater. As temperature increases, the safety vent opens to reduce pressure at around 150 °C where mass decreases and smokes becomes visible (Figure 1.5b–c). The vent gas composition deviates depending on such factors as electrolyte composition, electrode material, battery state-of-charge and aging [34], but likely to be electrolyte gases as well as aerosols and partially reacted gaseous species involved [35,36]. Thus, the gas-phase electrolyte solvents, i.e., carbonate esters, are potentially vented under elevated temperature situations regardless of whether the thermal runaway is accomplished or not.

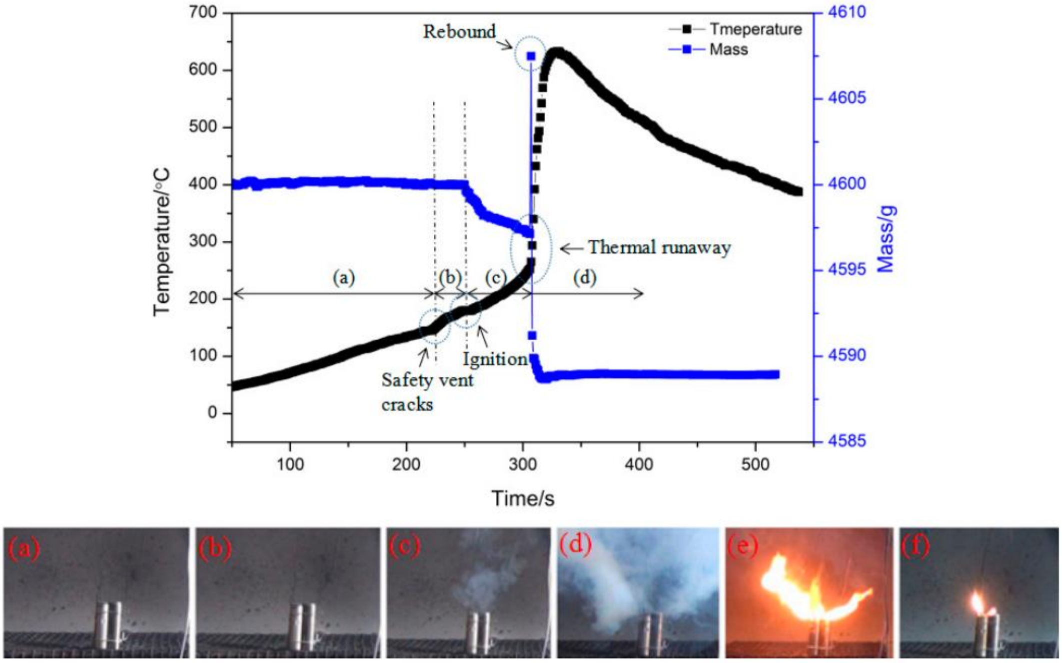

Figure 1.5 Change in battery surface temperature and mass (top) and a series of fire process images (bottom) during thermal runaway experiment of a battery [25].

Taking a fire risk of the vented gases that consists of vaporized electrolytes and partially reacted products into account, we need to investigate their gas-phase flammability. Especially, inferring a LIB fire situation where the vent gases are already present and react by an ignition source, such as a spark caused by an electrical defect, gas-phase chemistry is of importance. The LIB fire mechanism considering such a scenario accompanying with the vent gas release is illustrated in Figure 1.6.

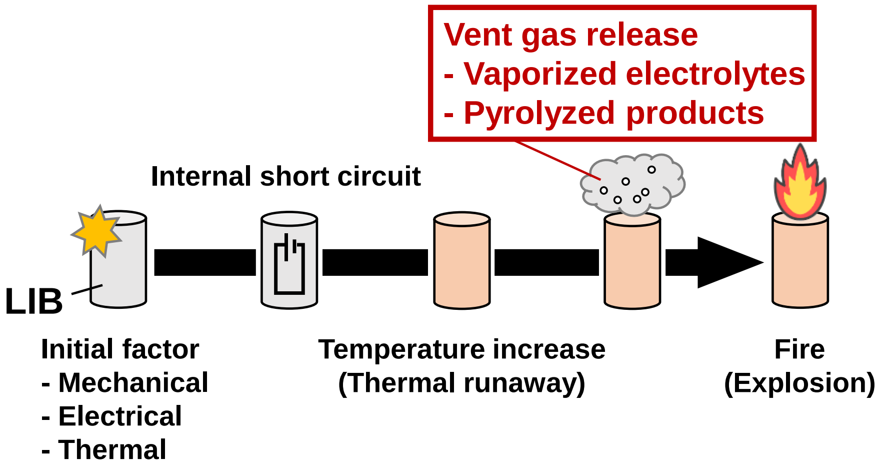

Figure 1.6 Schematic of the LIB fire mechanism in a vent gas release scenario.

1.2.2 How to prevent and/or mitigate fires?

To prevent LIB fires, not only electrochemical performance but also thermal performance of LIB as well as each component and function are tested before being commercialized. Generally, a safety of LIB is examined by nail penetration, overcharge, externally heating and external short circuit tests [37]. These conventional methods could be useful for a comprehensive evaluation of LIB's safety, but precise evaluations and understanding of potential fire dangers involving each component, especially electrolytes, is difficult. The thermal stability of electrode and separator materials are examined in terms of oxygen release and shutdown function, respectively. The flammability of electrolytes is currently evaluated and classified based on liquid state properties such as boiling point, flash point and auto-ignition temperature, which largely rely on phase changes, as listed in Table 1.2. For instance, DMC is classified to be a higher fire hazard category (Class I-B) than DEC (Class I-C) according to the NFPA 30 classification scheme [38] whose flammability definition is based on flash point and boiling point. However, as pointed out in the previous section, gas-phase flammability also needs to be taken into account in a scenario when gaseous electrolytes are exhausted during the thermal runaway event or the venting event.

Table 1.2 Current liquid-base flammability classification of LIB electrolytes.

Electrolyte solvents	Boing point (°C) [39]	Flash point (°C) [23]	Classification by NFPA 30 [38] [a]
DMC	91	16	Class I-B
DEC	126	25	Class I-C
EMC	107	24	Class I-C
EC	248	143	Class III-B
EC/DMC (1/1 wt/wt)		23	Class I-B
EC/DEC (1/1 wt/wt)		37	Class I-C
EC/EMC (1/1 wt/wt)		29	Class I-C

[a] Class I-B and I-C are categorized to flammable and III-B is combustible.

Motivated by these factors, this thesis tries to aid LIB fire prevention and/or mitigation through understanding and modeling the gas-phase reaction mechanisms of carbonate esters. As demonstrated by Harris et al. [36], simulating flame properties is helpful to evaluate a relative suitability of the carbonate esters for the use of LIB electrolyte solvents. Chemical kinetic models are necessary for those combustion simulations, which also include pyrolysis and ignition, and desirably being in high-prediction power. Towards model predictions for gas-phase combustion properties of the LIB electrolyte solvents, a comprehensive chemical kinetic model that includes major carbonate esters is required. Another strategy to mitigate LIB fires is to add fire suppressants to electrolytes. Organophosphorus compounds (OPCs) are known as commonly used fire-retardant additive candidates to LIB electrolytes, such as trimethyl phosphate (TMP) and dimethyl methylphosphonate (DMMP) [40,41], thanks to their good solubility of lithium salts and liquid properties. However, the roles of OPC as a fire-retardant are different between liquid- and gas-phase because phase-change properties are dominant in the former while radical chain reactions are important in the latter as detailed in Chapter 7. This also leads to the importance of understanding of gas-phase chemistry of phosphonate esters, which are expected to mitigate LIB fires, depending on the scenario considered.

1.3 Chemical kinetic models of carbonate/phosphate esters

In order to predict and evaluate gas-phase combustion characteristics (including ignition, flame, pyrolysis and emission) of carbonate and phosphate esters, chemical kinetic models are essential. Currently available models of dimethyl carbonate (DMC), diethyl carbonate (DEC), ethyl methyl carbonate (EMC) and ethylene carbonate (EC) as well as trimethyl phosphate (TMP), which are the subjected esters in this thesis, are listed in Table 1.3. Although a model that covers those carbonate esters is required to carry out the model predictions of combustion properties of LIB electrolyte mixtures, no comprehensive chemical kinetic model for the carbonate esters was available at the time. Thus, the first chemical kinetic model that includes the main LIB electrolyte solvents, i.e., EC, DMC, DEC and EMC, called as LIB electrolyte surrogate model, has been constructed in this thesis. To model complex combustion reactions, we believe that a step-by-step study starting from pyrolysis is important. Thermal decomposition of TMP is investigated to first understand the reaction mechanism including the formation of phosphorus intermediates, key gas-phase fire-suppression carriers, towards an implementation of a TMP model to the LIB electrolyte surrogate model in the future, as the idea shown in Figure 1.7.

Table 1.3 List of chemical kinetic models of carbonate and phosphorus esters focused on this thesis and available in the literature. Asterisks (*) denote our work discussed in this thesis.

Target ester	Author(s)	Group(s) [a]	Year	Ref.
DMC	Glaude et al.	LLNL	2005	[42]
DMC	Hu et al.	Xi’an Jiaotong	2015	[43]
DMC	Sun et al.	Tsinghua	2016	[44]
DEC	Nakamura et al.	TU/NUIG	2015	[45]
DEC	Sun et al.	Tsinghua	2017	[46]
DMC, DEC, EMC *	Takahashi et al.	TU	2022	[47]
EC, DMC, DEC, EMC *	Kanayama et al.	TU/TAMU	2024	[48]
TMP [b]	Jayaweera et al.	LLNL	2005	[49]

[a] Representative(s) taken from corresponding author(s)’s affiliation. LLNL: Lawrence Livermore National Laboratory, TU: Tohoku University, NUIG: National University of Ireland, Galway, TAMU: Texas A&M University. [b] Also includes other OPCs, such as DMMP.

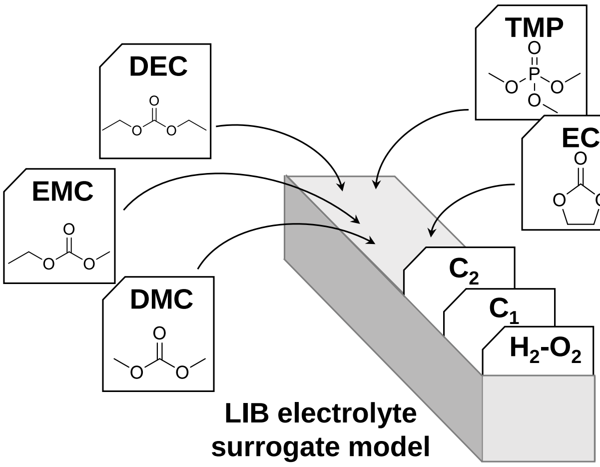

Figure 1.7 Idea of LIB electrolyte surrogate model and future extension to fire-retardant additives. Schematic inspired from [50].

1.4 *Objectives and outline of the dissertation*

Motivated by the backgrounds mentioned in the earlier sections, this dissertation investigates the pyrolysis and oxidation characteristics of carbonate and phosphate esters that are widely used as LIB electrolyte solvents and their fire-retardant additive. The principal objectives are as follows:

1. Understand pyrolysis and oxidation mechanisms of gas-phase carbonate and phosphate esters by conducting species measurements using various experimental techniques,
2. Construct a comprehensive chemical kinetic model that includes linear and cyclic carbonate esters to promote further investigation of the combustion characteristics of LIB electrolytes including phosphorus esters.

This dissertation comprises eight chapters. Chapter 1 presents the background, motivation and objectives of this dissertation. Chapter 2 describes experimental techniques employed in this dissertation, namely, a micro flow reactor with a controlled temperature profile (MFR) and photoelectron photoion coincidence (PEPICO) spectroscopy. Chapter 3 investigates the pyrolysis and oxidation characteristics of linear carbonate esters, dimethyl carbonate (DMC), diethyl carbonate (DEC) and ethyl methyl carbonate (EMC), using MFR. A reactivity evaluation and reaction analyses of the linear carbonate esters as well as chemical kinetic modeling of EMC are also carried out. Chapter 4 focuses on pyrolysis and oxidation of a cyclic carbonate ester, ethylene carbonate (EC), examined by MFR and shock tube. In this chapter, the first comprehensive chemical kinetic model of linear and cyclic carbonate esters called as “LIB electrolyte surrogate model” are proposed. Laminar flame speed measurements of EC-doped mixtures were also performed. Chapter 5 demonstrates numerical simulations of global combustion properties, i.e., laminar flame speed and ignition delay time, of the single- and multi-component carbonate esters using the LIB electrolyte surrogate model to obtain an outlook for their gas-phase flammability. Chapter 6 introduces PEPICO spectroscopy by investigating photoelectron characteristics of carbonic acid (H_2CO_3), the most fundamental CO_3 moiety. Chapter 7 works on the pyrolysis of trimethyl phosphate (TMP), an organophosphorus compound, utilizing the PEPICO technique. Quantum chemical calculations are also conducted to obtain further mechanistic insights into TMP pyrolysis. Finally, Chapter 8 gives the conclusions of this dissertation.

Chapter 2

Experimental approaches

This chapter provides principles and features of the two unique experimental techniques employed in this thesis, namely a micro flow reactor with a controlled temperature profile (MFR) and photoelectron photoion coincidence (PEPICO) spectroscopy.

2.1 Micro flow reactor with a controlled temperature profile (MFR)

A micro flow reactor with a controlled temperature profile (MFR) [51,52] is a simple but unique, high-fidelity tool to investigate pyrolysis and oxidation characteristics of test gaseous mixtures and to validate chemical kinetic models. A major difference from the conventional laminar flow reactor systems widely used in the combustion field, such as a jet-stirred reactor (JSR) and plug-flow reactor (PFR), is that MFR takes a temperature gradient into account for a phenomenon observed. This raises the problem type to one-dimension from zero-dimension assumed in JSR and PFR, resulting in avoiding the well-known inlet boundary problems of zero-dimensional systems, e.g., pre-reactions, non-ideal mixing and finite-rate thermalization [53], by considering the whole region of the temperature ramping stage in MFR. This feature of MFR not only facilitates us to conduct experiments but also may realize high-fidelity validation of chemical kinetic models. In the following parts, a general description of MFR is given first, then more details of a specific phenomenon, namely weak flame, which this dissertation handles, are explained.

MFR consists of a quartz tube and an external heat source as depicted in Figure 2.1. The inner diameter of the quartz tube is smaller than the ordinary quenching diameter of test mixtures [54,55]. A stationary temperature profile is formed on the tube inner wall surface along the flow direction, given by the external heat source, for which a hydrogen/air flat-flame burner or an electronic heater are often used. When a test mixture that includes oxidizer is introduced into MFR, the mixture is heated according to the given wall temperature profile, and various types of flames are observed at a certain temperature range depending on conditions.

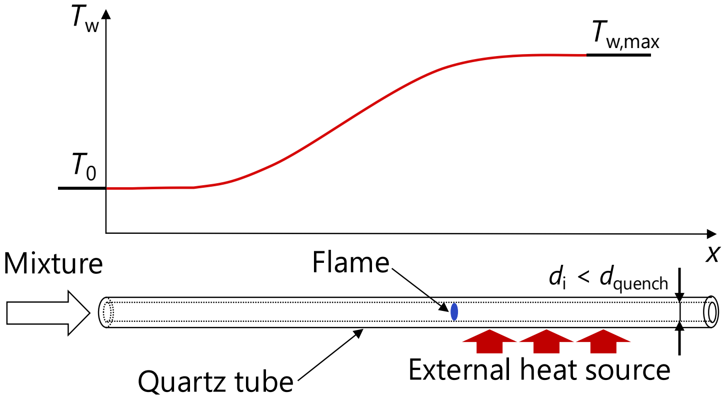

Figure 2.1 Schematic of a micro flow reactor with a controlled temperature profile (MFR).

2.1.1 *Flame responses in MFR*

Depending on the inlet flow velocity of a test mixture, three types of flame dynamics were experimentally observed in MFR by Maruta et al. [51,56], a normal flame, flames with repetitive extinction and ignition (FREI) and a weak flame. These flame dynamics were also proven with a theoretical analysis by Minaev et al. [57], as schematic of the modified Fendell curve shown in Figure 2.2a [58]. At high inlet flow velocity conditions (typically, higher than a few tens cm/s at standard temperature and pressure), a stable normal flame is observed (Figure 2.2b). At intermediate inlet flow velocity conditions (about several cm/s to a few tens cm/s), an unsteady behavior that autoignition occurs at the higher-temperature side and a flame propagates upstream (the lower-temperature side) followed by extinction, called as FREI, is observed (Figure 2.2c). This corresponds to an unstable solution depicted as black dashed line in Figure 2.2a. At low inlet flow velocity conditions (a few cm/s), a stable flame, namely weak flame, whose stabilizing location corresponds to the ignition branch, is observed (Figure 2.2d). This means that a weak flame position represents an ignition-related characteristic of a test mixture. The characteristics of this weak flame are introduced in more detail in Section 2.1.3 as we focus on this phenomenon in this dissertation.

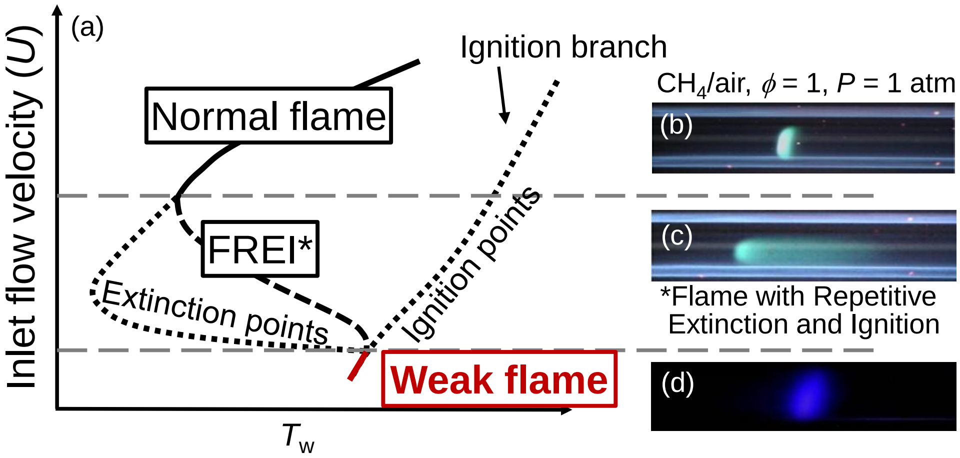

Figure 2.2 Flame responses in MFR. (a) Theoretically obtained flame trajectory as a function of location [57,58]. Experimentally obtained images of (b) normal flame [56], (c) FREI [56] and (d) weak flame [59] of stoichiometric methane/air mixtures at atmospheric pressure.

2.1.2 Flame and soot responses in MFR

Soot formation behavior depending on inlet flow velocity in MFR was also investigated in our previous studies [60–62]. As a test mixture is heated by the external heat source, not only a self-sustaining flame condition but also combustion outside the flammability limit [63,64] can be handled. Figure 2.3 shows the flame and soot responses in MFR at fuel-rich conditions. Four types of response were observed depending on inlet flow velocity and equivalence ratio: (a) only soot formation, (b) normal flame and soot formation at upstream and downstream sides, respectively, (c) normal flame and (d) none of them. As the equivalence ratio increases, i.e., more fuel and less oxidizer, soot formation appears below the inlet flow velocity of 25 cm/s due to lowered O/C ratio. Meanwhile, as inlet flow velocity increases, soot formation disappears above the equivalence ratio of 2.5 due to shortened residence time. The soot formation characteristics are also affected by the temperature profile (maximum temperature and the length of its region), pressure and fuel. By controlling these parameters, we are able to investigate gas-phase chemistry at (ultra) fuel-rich and moreover, pyrolysis conditions by avoiding soot formation, as further introduced in Section 2.1.3.2.

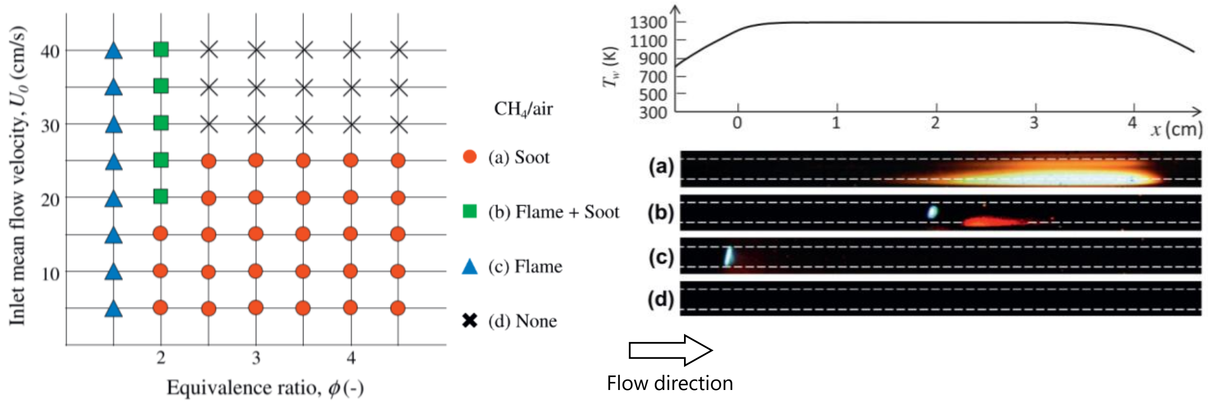

Figure 2.3 Flame and soot responses in MFR. (a) Only soot, (b) flame with soot, (c) flame without soot and (d) none of them were observed depending on equivalence ratio and inlet flow velocity for fuel-rich methane/air mixtures at atmospheric pressure [60].

2.1.3 Weak flames

The reactor channel is smaller than the ordinary quenching diameter, showing strong heat transfer between the gas and the tube wall surface. Thanks to the small amount of input enthalpy and small Peclet number at the weak flame conditions, the difference between the gas temperature and the reactor wall surface is very small even at a reaction zone, e.g., less than 10–20 K for a stoichiometric CH_4/air weak flame [56]. The gas temperature in MFR is, thus, strongly governed by T_w at the weak flame conditions, enabling one to investigate gas-phase oxidation and pyrolysis characteristics without an excess dilution. By utilizing weak flame, mainly two ways of gas-phase characterization of test mixtures can be conducted as follows.

2.1.3.1 Reactivity evaluation of test mixtures

As a weak flame position presents ignition-related properties as introduced in Section 2.1.1, relative gas-phase reactivity of test mixtures can be evaluated by comparing their weak flame positions. Figure 2.4 shows weak flame images of various hydrocarbon fuels in air [65,66] where the (main) weak flame positions generally follow the order of research octane number (RON). There are also additional chemiluminescence zones (depicted as white boxes) observed at a lower temperature side for RON < 100, which indicates multi-stage reactions as detailed in the next section. These weak flame positions are known to be less sensitive to inlet flow velocity [56,67,68]. The higher the gas-phase reactivity is, the lower the temperature weak flame stabilizes, enabling to evaluation of the relative reactivity of test mixtures. This reactivity evaluation technique has been applied to hydrocarbons (e.g., *n*-alkanes/alkenes [59,69], primary reference fuels (PRF) [70] and diesel surrogates [71]), syngas [72,73], oxygenates (e.g., dimethyl ether (DME) [68] and ethanol [70]) as well as low-reactive fuels such as hydrofluorocarbon [74] and ammonia [75]. The latter two are especially profited from the feature of MFR, i.e., preheating zone, as their ignition delay times are much longer than the conventional hydrocarbon fuels.

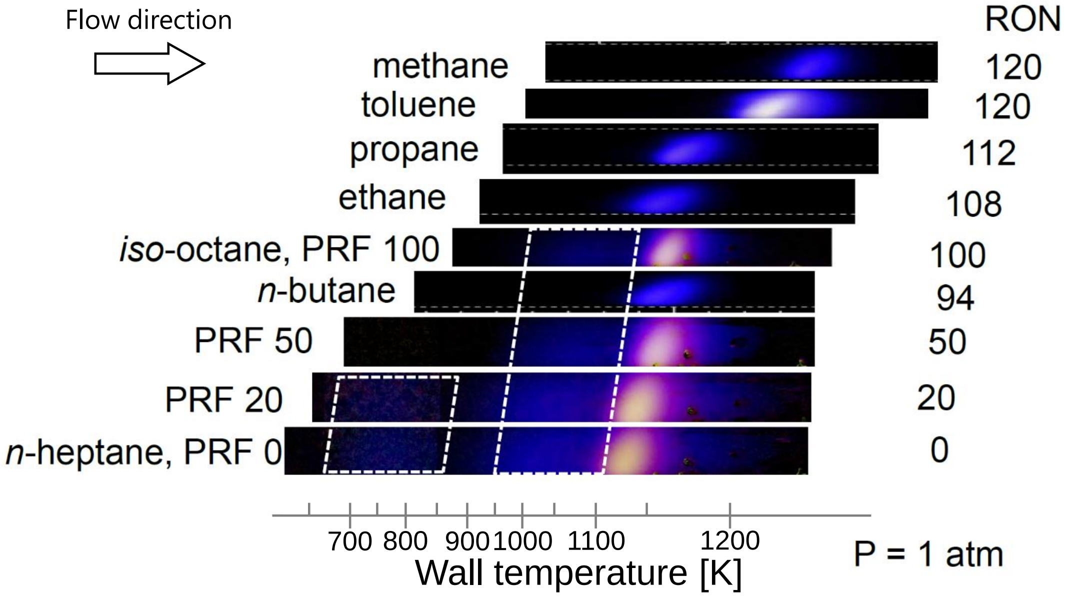

Figure 2.4 Weak flame images stabilizing at different position depending on the research octane number (RON) (from [65,66] with modification). Note that experimental conditions (e.g., inlet flow velocity, temperature profile, exposure time) are not exactly the same to each other [59,76–78].

2.1.3.2 Spatial separation of multi-stage reactions

Another feature of weak flame is that a series of reactions can be spatially separated at certain temperature regions. As shown in Figure 2.5, an *n*-heptane/air mixture exhibits three chemiluminescence zones in its weak flame image [67]. By carrying out species measurements, these were identified as cool, blue and hot flames from the low-temperature side. Thus, multi-stage oxidation initiated with low-temperature oxidation (LTO), which produces formaldehyde (CH_2O) typically at around 700 K, followed by the CO production at the intermediate-temperature range (around 900 K), and then CO to CO_2 oxidation at the higher-temperature range (around 1100 K) was successfully separated in MFR. Similarly, multi-stage oxidation in such as *n*-heptane/toluene mixtures [77], DME [68,79], DME/CH_4 mixtures [80] and DEE [81] were observed and confirmed by chemiluminescence and species measurements with gas chromatography (GC) or laser-induced fluorescence (LIF) diagnostics. Apart from these LTO induced multi-stage oxidation, a difluoromethane/air mixture exhibited multi-stage oxidation that was initiated by the production of intermediates (CO, H_2O and CF_2O) and hydrogen fluoride (HF) followed by CO to CO_2 oxidation [82], in which species measurements using Fourier Transform Infrared spectroscopy (FTIR) were conducted.

Owing to the broadened reaction zone and strongly governed temperature profile at a weak flame condition in MFR, species measurements at a temperature-region of interest in a series of phenomenon can be performed by varying a maximum temperature or shifting a sampling position. This is applicable not only to the multi-stage oxidation but also to such as low-reactivity fuels [83–85] and sooting conditions [64,86]. Figure 2.6 presents a schematic image of species measurements under near sooting conditions using MFR [64,86]. To focus on the formation and growth of polycyclic aromatic hydrocarbons (PAHs) and their precursors, we lowered the maximum wall temperature ($T_{w,max}$) and shortened the $T_{w,max}$-region in the species measurements, as compared to those in the flame and soot observation experiments. Consequently, the gas-phase species were successfully investigated by avoiding the subsequent soot formation process. Since soot formation will also be expected at pyrolysis conditions, which this dissertation works on, this technique will be advantageous. More importantly, as a gas temperature is strongly controlled by the wall temperature at a weak flame condition, high dilution is not necessary even at pyrolysis conditions where endothermic reactions take place, which also facilitates species measurements [87]. Speciation data obtained using MFR helps understanding of gas-phase chemistry as well as detailed validation and construction of chemical kinetic models [88].

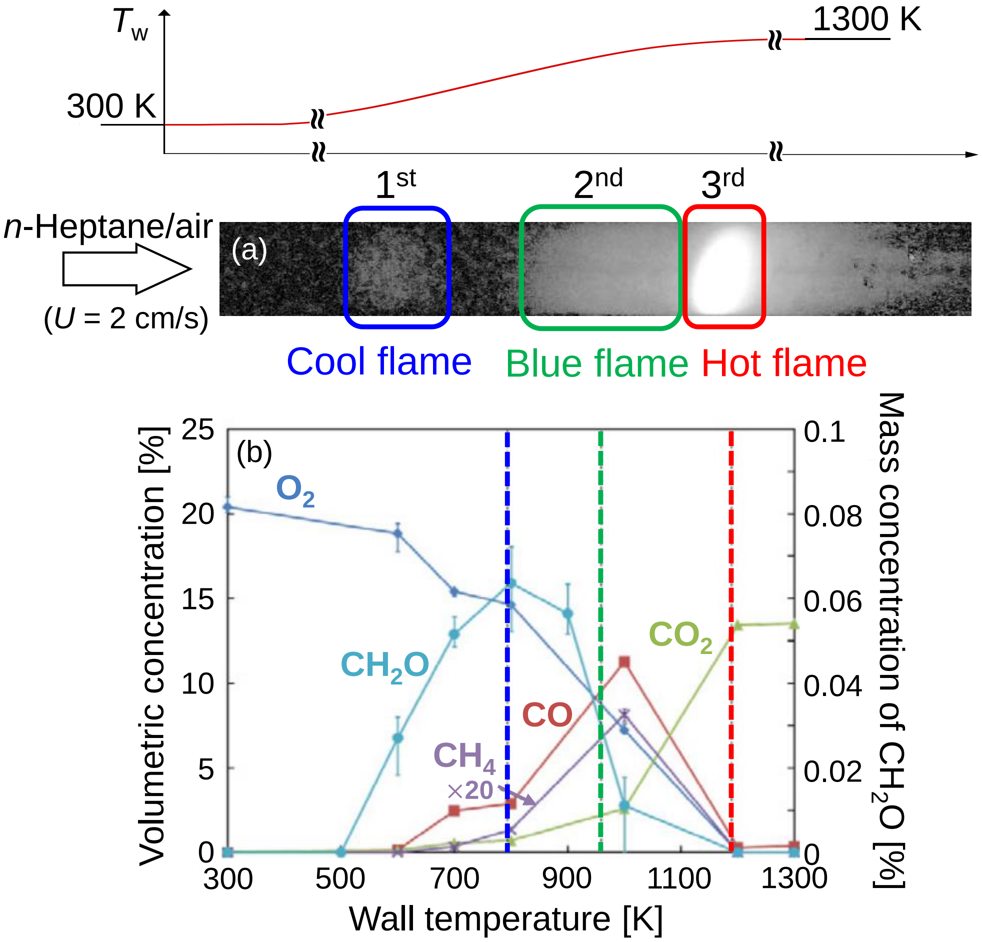

Figure 2.5 Weak flame image and measured species profiles of multi-stage oxidation of an *n*-heptane/air mixture in MFR at atmospheric pressure (from [67] with modification).

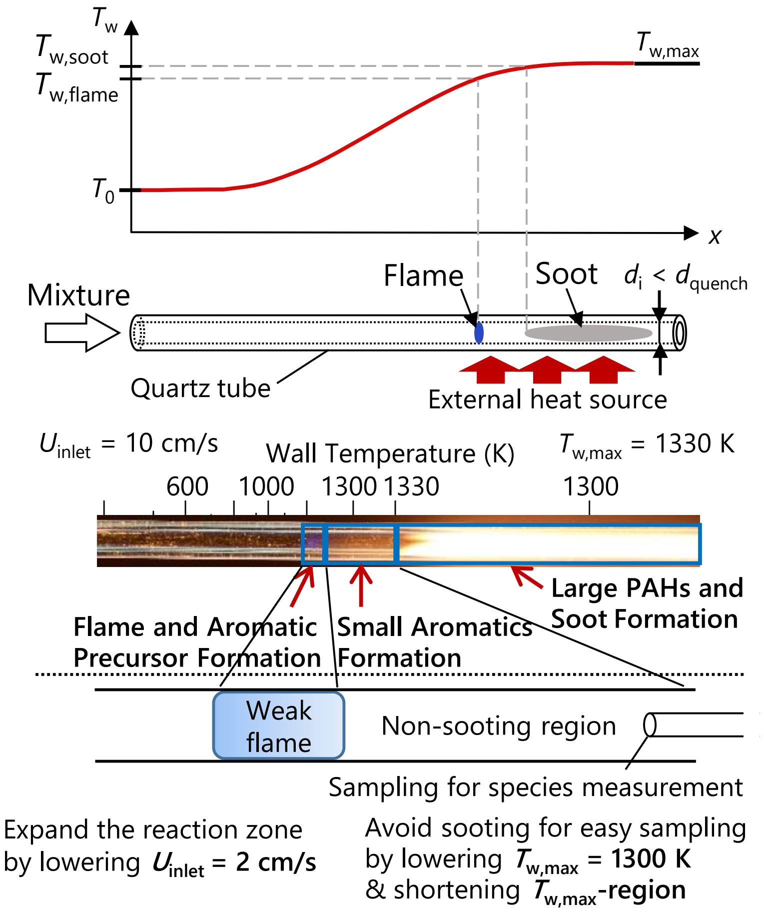

Figure 2.6 An idea to investigate gas-phase chemistry by avoiding soot formation at fuel-rich conditions in MFR. Flame and soot image is for a C_2H_6/air mixture. Modified based on figures from [64,86].

2.2 Synchrotron vacuum ultraviolet (VUV) radiation and photoelectron photoion coincidence (PEPICO) spectroscopy

Experiments in Chapter 6, Chapter 7 and Appendix A are conducted at Swiss Light Source (SLS), Paul Scherrer Insitut (PSI), Switzerland, using synchrotron vacuum ultraviolet (VUV) radiation and photoelectron photoion coincidence (PEPICO) spectroscopy. Synchrotron facilities provide a wide range of radiation, which is tunable and depends on their usage. SLS is a third-generation synchrotron facility with the 2.4 GeV storage ring of 288 m circumference. The beamline layout of SLS is shown in Figure 2.7. Electrons are generated by an electron gun, pre-accelerated in a linear accelerator (LINAC) to 100 MeV and further accelerated in a booster ring to 2.4 GeV. The accelerated electrons are then accumulated in the storage ring. The electrons in the storge ring are held on the orbit by magnets. The storage ring current is kept at 400 mA during operation in top-up mode, which frequently injects electrons into the storage ring to maintain synchrotron radiation constant. In the following parts, VUV beamline and PEPICO technique are introduced, which enable us to investigate gaseous molecules in complex conditions, especially in pyrolysis and combustion conditions focused on in this thesis.

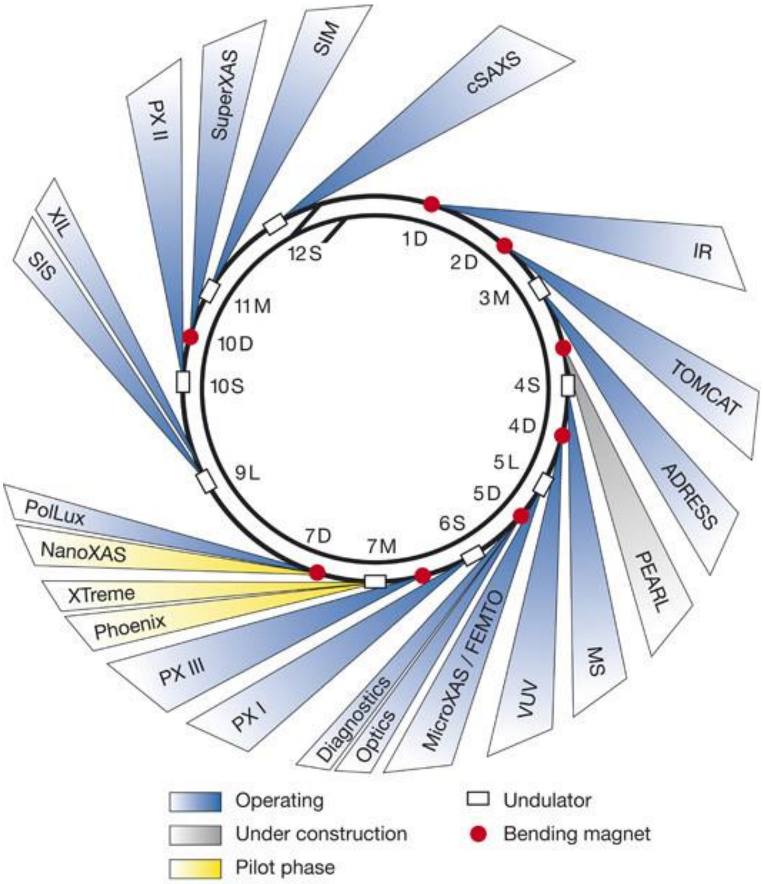

Figure 2.7 Beamline layout of the SLS. Image taken from [89].

2.2.1 *VUV beamline (X04DB) at SLS*

Vacuum ultraviolet (VUV) beamline at SLS provides synchrotron radiation in the photon energy range of 5–30 eV (approximately 40–250 nm wavelength) with a photon flux of 10^{11} photons/s at 10 eV [90]. This photon energy range is sufficient to remove electrons from the valence shell for photoionization [91]. Advantages of using synchrotron VUV radiation as a light source are its tunability and flux as well as resolution as compared to lasers and discharge lamps, respectively [90]. Figure 2.8 shows a layout of the VUV beamline. The radiation is provided by a bending magnet where the radiation spreads over a horizontal angle of 8 mrad, passing through the vertical and horizontal slits and X-ray blocker. Light is then monochromatized by being collimated onto a plane blazed grating, and focused on the exit slit. The photon energy can be scanned by moving the grating to keep the deviation angle (2θ) constant according to the equation:

$$m\lambda = 2d\cos\theta\sin\varphi$$

where m is the diffraction order, λ is the wavelength, d is the line spacing and φ is the scan angle. The monochromatic VUV light goes through the differentially pumped rare gas filter (such as Ne, Ar and Kr) and/or a MgF_2 window to suppress higher order radiation before reaching the PEPICO endstation.

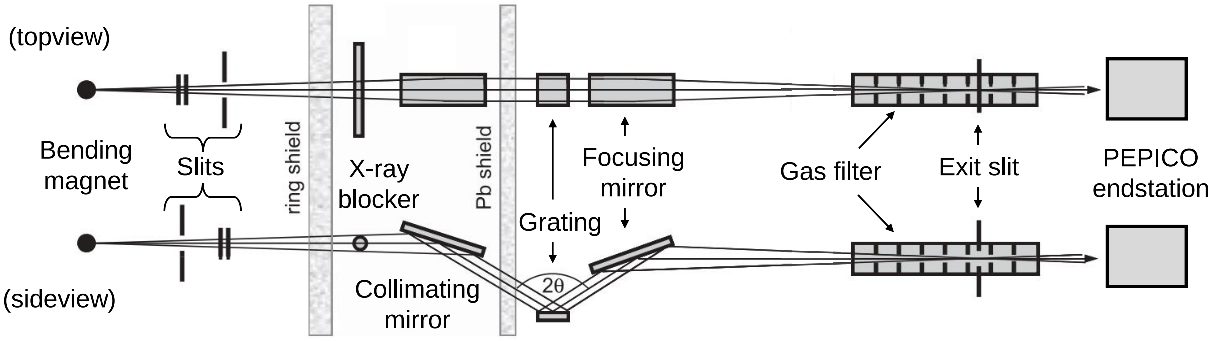

Figure 2.8 Configuration of the X04DB beamline (from [90] with modification).

2.2.2 *Photoionization and photoelectron spectroscopy*

Photoionization process of a molecule AB can be described as:

$$AB + h\nu \rightarrow AB^+ + e^- .$$

This process takes place when the given photon energy is greater than binding energy, I_j, of the electron attached to a molecular orbital, j. The minimum energy to eject the electron is defined as ionization energy (*IE*). According to Koopmans' theorem [92], this ionization energy is equal in magnitude (but negative) to orbital energy of the highest occupied molecular orbital (HOMO), i.e., an electron is removed from the HOMO upon ionization. When photon energy is larger than ionization energy, ejected electrons possess excess kinetic energy, E_{kin}. Figure 2.9 shows idealized photoionization process and the resulting photoelectron spectrum of an atom. By detecting and recording the ejected photoelectrons at a known photon energy, photoelectron (PE) spectrum as a function of kinetic energy of photoelectron can be obtained. From these photon and kinetic energies, the binding energy of an electron in the atom can be derived. If the species is a molecule, an excess energy remains as internal energy, i.e., vibrational and rotational energy, $E^*_{vib,rot}$, in the ion upon ionization. Thus, the PE spectrum of a molecule contains additional lines at:

$$E_{kin} = h\nu - IE - E^*_{vib,rot} \cdot$$

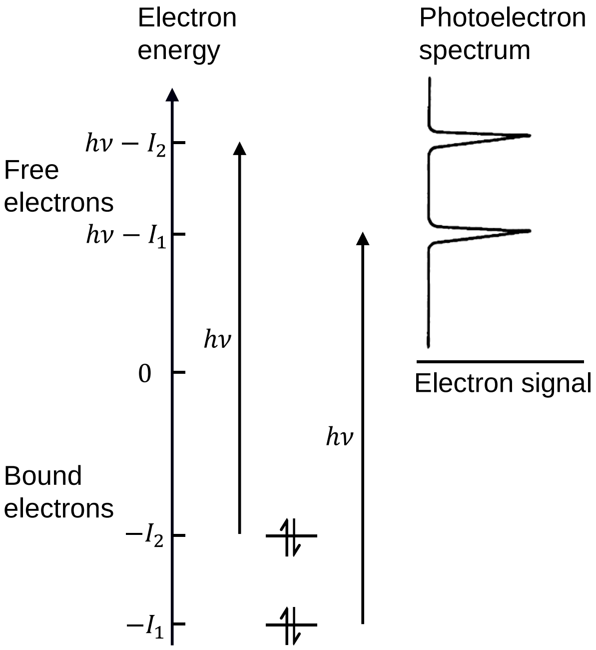

Figure 2.9 Photoionization process and photoelectron spectrum of an atom [93].

Figure 2.10 shows a schematic of vibronic transitions and the resulting vibrational progression of diatomic molecule upon photoionization [94]. As the mass of a nucleus is much larger than that of an electron, the coordinates of nuclei in the system are assumed to be fixed when the electronic transition occurs, and the resulting overlaps of vibrational wave functions of the initial and final states determine the vibrational structure in the PE spectrum. This is called the Franck–Condon principle, and the square of the vibrational wave function overlap integral, $q_{v',v''} = |\int \Psi_{v'}\Psi_{v''}\mathrm{d}r|^2$, is called the Franck–Condon factor (FCF). As its fundamental assumption lies on the Born–Oppenheimer approximation, the transition probability, P, can be given as [95]:

$$P \propto {\mu_{trs}}^2 = \left|\iint \Psi_{E'}^{*}\mu_E\Psi_{E''}\mathrm{d}\tau_E\right|^2 \left|\int \Psi_{v'}\Psi_{v''}\mathrm{d}r\right|^2$$

where μ_{trs} is the transition dipole moment, the first term on the right side is square of the electronic transition dipole moment and the second term is the vibrational wave function overlap integral (FCF), $q_{v',v''}$. The initial state and final state are denoted as $''$ and $'$, respectively. Ψ is the electronic (E) and vibrational (v) wave functions. τ_E and r is the electronic and nuclear coordinates, respectively. The electronic transition dipole moment has non-zero value in the electronic transition (if the transition is allowed). Thus, the FCF indicates a relative transition intensity among transitions of identical electronic states. When the geometry change (ΔQ) is small upon ionization (Figure 2.10a), the FCF is largest for the 0-0 transition (the transition from the vibrational ground state of neutral to cation), at which photon energy corresponds to the adiabatic ionization energy (AIE), showing a strong peak in the PE signal. When ΔQ is large upon ionization (Figure 2.10b), on the other hand, the overlap of the vibrational wave functions at the 0-0 transition is small, resulting in a small FCF. This may cause a lack of the transition information in PE spectrum in some cases [96]. The FCF is largest at the <0|3> transition in Figure 2.10b, which corresponds to vertical ionization. Thus, we can obtain vibrational information upon ionization as well as ionization energies from photoelectron spectrum. These vibrational progression can be simulated using quantum chemical calculation software such as Gaussian 16 [97] and ezFCF [98].

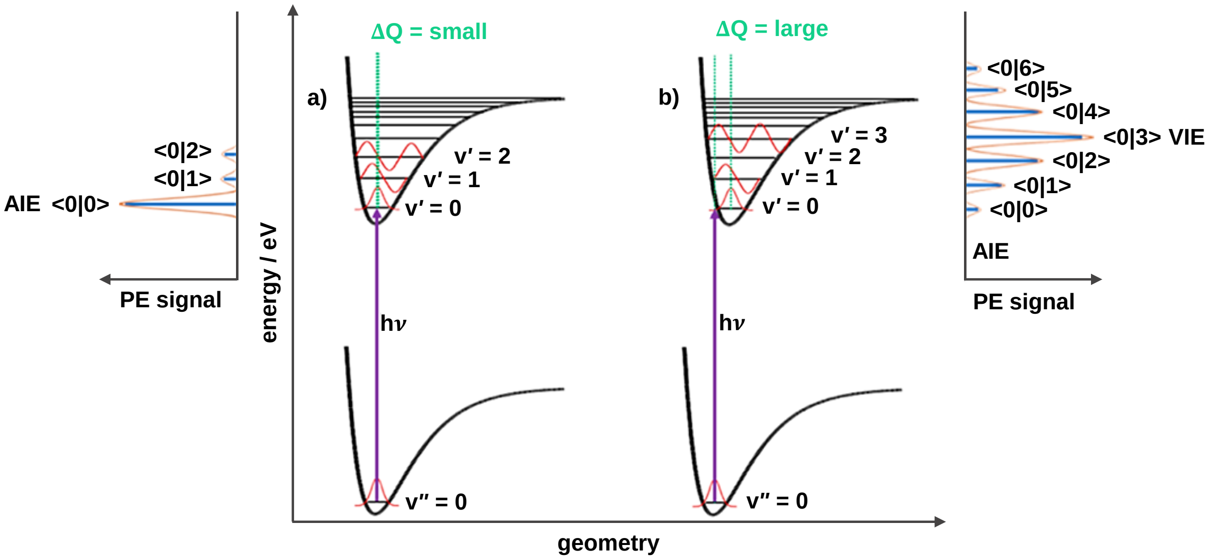

Figure 2.10 Electronic transitions and photoelectron spectrum of a diatomic molecule (from [94] with modification).

2.2.3 *Double imaging i²PEPICO spectroscopy*

In the field of combustion chemistry, mainly four synchrotron facilities equipping VUV beamline are utilized to investigate gas-phase chemistry under complex conditions, e.g., pyrolysis [99,100], combustion [101,102] and catalysis [103,104]. Namely, SLS (Switzerland), SOLEIL (France), ALS (USA) and NSRL (China). Since many elusive and reactive species contribute to chemical reactions in those harsh conditions, capturing and identifying them is crucial to reveal the reaction mechanisms as well as to construct chemical kinetic models. In this regard, so-called molecular-beam mass spectrometry (MBMS) is one of the powerful techniques that enable us to sample and detect reactive intermediates such as radicals. There are two methods for ionization employed in mass spectrometry, i.e., electron (impact) ionization (EI) and photoionization (PI) methods. In general, an advantage of the PI method over the EI method are such as the suppression of fragmentation upon ionization, and thus they are called as soft and hard ionization, respectively. Meanwhile, a lab-scale PIMS offers limited access to photon energy and flux. Thus, by using a synchrotron VUV radiation as a light source for the PIMS, species capture with flexible and sensitive single-photon ionization is possible.

In this thesis, the synchrotron-based VUV photoionization technique at SLS, double imaging photoelectron photoion coincidence (i^2PEPICO) spectroscopy [105–107], which is a combined technique of PIMS and PE spectroscopy, is used. A schematic of the i^2PEPICO setup is shown in Figure 2.11. The i^2PEPICO setup mainly consists of two high-vacuum chambers, (a) molecular beam source (sampling) chamber (ca. $< 10^{-4}$ mbar) and (b) ionization chamber (ca. $< 10^{-6}$ mbar). A SiC microtubular reactor (1 mm inner diameter and 2 mm outer diameter) is installed in the source chamber (there are other types of reactors, e.g., catalytic reactor, available as well). Gaseous samples leaving the reactor expand into high vacuum, forming a MB. The MB is then skimmed and introduced to the ionization chamber where the skimmed MB and the monochromatic VUV radiation intersect perpendicularly. Upon photoionization, photoions and photoelectrons are accelerated towards opposite directions under a constant electric field and detected by position-sensitive delay line anode detectors (DLD40, Roentdek) in delayed coincidence [108]. This provides time-of-flight (TOF) information, which can be converted to a mass spectrum, and velocity map images (VMI) of both photoions and photoelectrons (Figure 2.11c and d, respectively). The VMI give us visual information about kinetic energy of detected photoions and photoelectrons. For the former, signals from the MB and rethermalized room-temperature background (RT-BG) are spatially separated and plotted in ion VMI, as shown in Figure 2.11c. Moreover, Figure 2.11c on the left shows a narrow velocity distribution along the MB axis, while Figure 2.11c on the right shows a lateral broadening of the MB component, which indicates that kinetic energy is released due to dissociative photoionization (DPI). Thus, direct photoionization signals of products and DPI signals can be distinguished by utilizing the ion VMI. The latter, electron VMI as shown in Figure 2.11d, provides kinetic energy information of photoelectron (E_{kin}), which enable us to plot a photoelectron spectrum with restricted signals to photoelectrons within threshold kinetic energy, i.e., threshold photoelectron spectrum (TPES). By scanning photon energy and combining obtained TOF data and VMI, photoion mass-selected threshold photoelectron spectrum (ms-TPES) can be recorded. Thanks to restricting the signals to the threshold photoelectrons at each mass, transitions and vibrational progression upon photoionization can be observed in the ms-TPES, which is a fingerprint of a molecule.

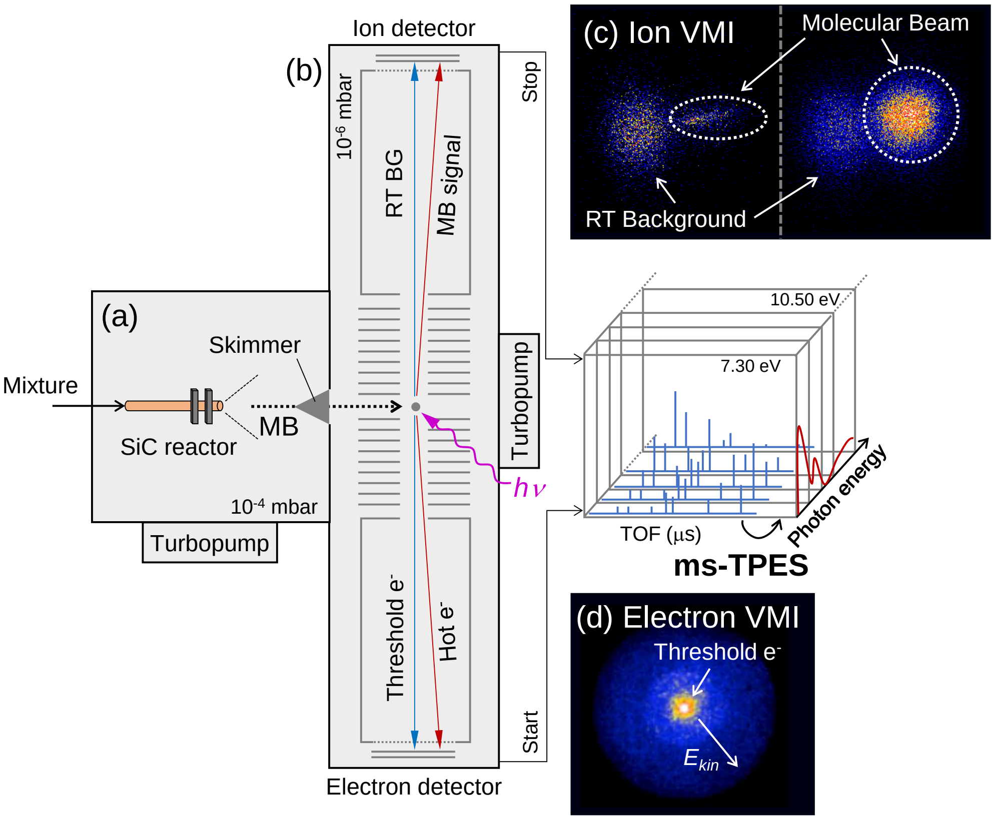

Figure 2.11 Schematic of i^2PEPICO setup. (a) Molecular beam (MB) source chamber, (b) ionization chamber, (c) ion velocity map image (VMI) and (d) electron VMI.

Figure 2.12 shows an example of ms-TPES and photoionization (PI) spectrum. The PI spectrum, also called as photoionization efficiency (PIE) curve, is plotted by taking all electrons into account. In the PI spectrum (top), the onset of the signal increase is clearly observed, at which indene can be identified according to its ionization energy and PI spectrum, while the following tends to monotonically increase as photon energy increases. Thus, the identification of other isomers, if exist, is difficult without changes in the slope. When taking a look at the ms-TPES (bottom), in addition to the peaks corresponding to the transition and vibrational progress of indene, additional peaks appeared at higher photon energies, which are identified to be two other isomers. As mentioned above, ms-TPES is a vibrational fingerprint spectrum of a molecule that reflects threshold photoionization and thus is powerful information to identify species isomer-selectively in isomer-diversity conditions such as pyrolysis, combustion and catalysis. For the species identification, photoionization data and photoelectron spectra are available at such as Photoelectron Photoion Spectral Compendium (PEPISCO) [94], Photoionization Cross Section database [109] and NIST chemistry Webbook [110].

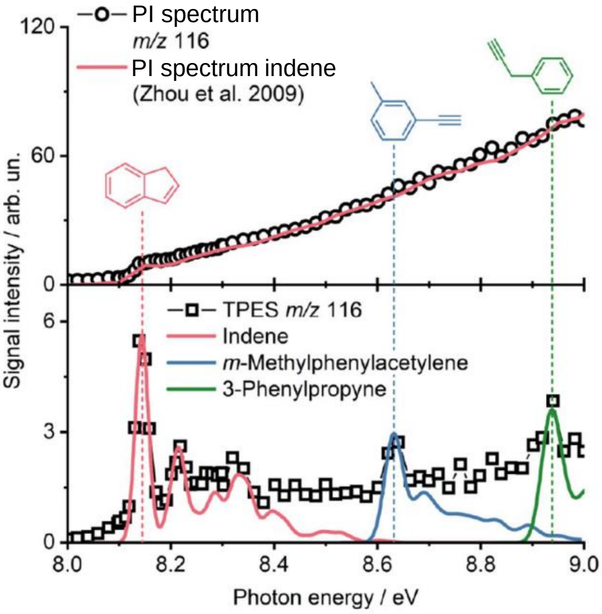

Figure 2.12 Example of photoionization (PI) spectrum (top) and mass-selected threshold photoelectron (ms-TPE) spectrum (bottom) [99]. Original data is from [111].

Ion VMI is another advantage of i^2PEPICO for obtaining ms-TPES. Three types of ms-TPES can be constructed based on ion VMI region-of-interest (ROI) signals, that is RT-BG, MB and all. Figure 2.13 shows the ion VMI and ms-TPES with the corresponding ROI marked in blue, gray and green for RT-BG, MB and all, respectively. At lower reactor temperatures, ms-TPES constructed using MB signals (MB ms-TPES) possesses structural features that is well reproduced by FC simulations. However, at higher temperatures, a discrepancy between MB ms-TPES and FC simulations becomes apparent where MB ms-TPES shows red shift and broadening due to hot and sequence bands, as compared to e.g., MB ms-TPES recorded at room temperature. Restricting signals to either RT-BG or whole ROI gives rise to well-resolved ms-TPES even at the high reactor temperatures without offset from that recorded at room temperature. This indicates that constructing ms-TPES using rethermalized RT-BG or whole ROI signals would be, in general, better for the use of species identification at such as pyrolysis and combustion conditions by suppressing extra bands. Note that this does not hold in some cases, such as OH radicals, which were reported to be primarily present in the MB but disappear in the RT-BG upon the rethermalization process due to wall collision as compared to H_2O [112], and also some species investigated in this thesis (Chapter 7).

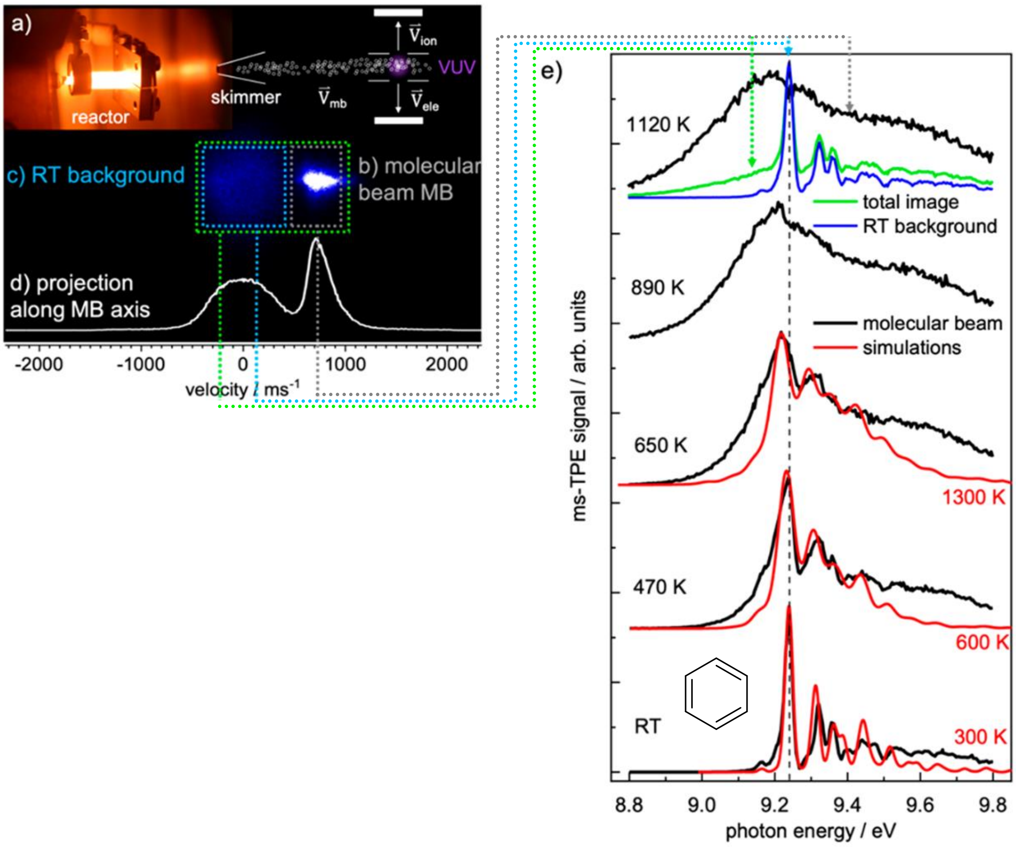

Figure 2.13 Temperature and ion VMI region-of-interest dependence on ms-TPES [94,113]. (a) Pyrolysis reactor, (b and c) molecular beam (MB) and room-temperature (RT) background signal components, (d) velocity distribution and (e) temperature-dependent ms-TPE spectra.

Chapter 3

Pyrolysis and oxidation of dimethyl carbonate, diethyl carbonate and ethyl methyl carbonate

This chapter works on the systematic understanding of pyrolysis and oxidation characteristics of linear carbonate esters, dimethyl carbonate (DMC), diethyl carbonate (DEC) and ethyl methyl carbonate (EMC), using MFR. Chemical kinetic models of DMC and DEC from literatures were validated with the MFR speciation data, and a comprehensive model for the linear carbonate ester was proposed by constructing an EMC model. Gas-phase reactivities of the linear carbonate esters were also investigated through the weak flame observations.

3.1 Introduction

On the one hand, linear carbonate esters have gained a great attention as a fuel additive and alternative fuel to fossil fuels to mitigate smoke and CO_2 emissions from combustion. Generally, linear carbonate esters, such as dimethyl carbonate (DMC), possess high O/C ratio in their molecular structure and miscibility to the engine fuels without a phase change [114,115]. These features motivated researchers to study emissions and performances of engines utilizing linear carbonate esters with conventional diesel/gasoline fuels, especially aiming to reduce particulate and smoke emissions [116–119], to realize clean combustion technologies. Although combustion of carbonate esters produces CO_2, they can be synthesized from CO_2 and alcohols, e.g., methanol and ethanol for DMC and diethyl carbonate (DEC), respectively, with catalysis [120,121], potentially being able to achieve the carbon neutralization. Thus, these bio-derived fuels may play an important role in low carbon combustion techniques.

On the other hand, as being described in Chapter 1, the linear carbonate esters, such as DMC, DEC and ethyl methyl carbonate (EMC) shown in Figure 3.1, are widely-used electrolyte solvents of a lithium-ion battery (LIB) and are regarded as a potential LIB fire cause [22,23]. As the combustion enthalpy of electrolytes, which mostly comes from the electrolyte solvents but less influence of salts [32], accounts for a large part of the combustion heat when LIB fires occur [31], combustion characteristics of the linear carbonate esters are crucial factors that determines the magnitude of the LIB-fire incidents. Most well-known properties that are considered as a flammability of these electrolyte solvents would be a flash point, auto-ignition temperature and self-extinguishing time [122]. These liquid-base properties, however, are strongly governed by the phase change, i.e., evaporation process of the liquid electrolyte solvents [39,123], which would differ from the gas-phase flammability. In some scenarios as introduced in Chapter 1, LIB fires occur regardless of whether the thermal runaway event is accomplished or not, such as the vent gases release through a mechanical safety vent system to reduce the inner pressure of LIB. Thus, investigating the gas-phase combustion properties with the chemistry behind them is an urgent task.

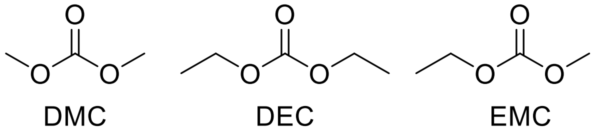

Figure 3.1 Molecular structures of DMC, DEC and EMC.

Ignition delay times and laminar flame speeds are the global gas-phase combustion properties, and those of DMC [43,124–129], DEC [45,130,131] and, only recently, EMC [129,132] have been studied by several groups as listed in Table 3.1. In addition to these global combustion parameters, experimental data of chemical speciation under combustion as well as pyrolysis are also important to understand the chemistry and to validate and construct accurate chemical kinetic models. Accordingly, the speciation data of DMC [44,126,133–135], DEC [45,46,131,134–136] and EMC [47,135] pyrolysis and oxidation have been obtained as well (Table 3.1). There were, however, only a limited number of experiments conducted at the same conditions among these three linear carbonate esters, and moreover, very few data of EMC. For example, studies on DMC oxidation mostly focused on high temperatures but not on low-to-intermediate temperatures.

Table 3.1 Experimental studies on pyrolysis and combustion characteristics of DMC, DEC and EMC. Laminar flame speed (LFS), ignition delay time (IDT) and speciation (SP). Initial temperature (T_0), reflected-shock temperature and pressure (T_5, P_5), compression temperature and pressure (T_c, P_c), flame temperature (T_f) and maximum wall temperature ($T_{w,max}$).

Mixture	ϕ (-)	T (K)	P (atm)	Property / Method	Year / Ref.
DMC/air	0.65–1.6	T_0 = 298–358	1.0	LFS / Heat flux burner	2013 / [124]
DMC/air	0.84–1.32	T_0 = 300	1.0	LFS / Spherically propagating flame	2020 / [125]
DMC/air	0.7–1.5	T_0 = 318–423	1.0	LFS / Spherically propagating flame	2021 / [126]
DMC/O_2/(N_2 or He)	0.7–1.5	T_0 = 358, 423	1.0–8.0	LFS / Spherically propagating flame	2021 / [128]
DMC/air	0.81–1.42	T_0 = 403	1.0	LFS / Spherically propagating flame	2024 / [129]
DMC/O_2/Ar	0.5–2.0	T_5 = 1100–1600	P_5 = 1.2–10	IDT / Shock tube	2015 / [43]
DMC/O_2/(N_2 or Ar)	0.5–2.0	T_c (T_5) = 795–1585	P_c (P_5) = 2.0–40	IDT / Rapid compression machine, Shock tube	2018 / [127]
DMC/O_2/79.25% Ar/20%He	0.5–2.0	T_5 = 1307–1642	P_5 = 1.25–1.33	IDT / Shock tube	2021/ [126]
DMC/air	1.0	T_5 = 1203–1342	P_5 = 0.97–1.18	IDT / Shock tube	2024 / [129]
8%DMC/N_2, 39%O_2/N_2	Non-premixed	T_f = 1626	1.0	SP / Opposed flow diffusion flame	2004 / [133]
DMC/O_2/Ar	1.0, 1.5	T_f = 2242, 2319	0.027, 0.033	SP / Burner stabilized premixed flame	2016 / [44]
2%DMC/Ar	∞	842–1490	0.04, 0.20, 1.0	SP / Plug-flow reactor	2016/ [44]
DMC/O_2/99.25% Ar+He	0.5–2.0, ∞	T_5 = 1232–2499	P_5 = 1.09–1.57	SP / Shock tube	2021 / [126]
1.5%DMC/O_2/N_2	1.0	$T_{w,max}$ = 700–1300	1.0	SP / MFR	2022 / [134] [a]
1.5%DMC/N_2	∞	$T_{w,max}$ = 700–1200	1.0	SP / MFR	2022 / [134] [a]

DMC/79.75%Ar/ 20%He	∞	T_5 = 1309–1664	1.22–1.37	SP / Shock tube	2023 / [135]
DEC/air	0.7–1.3	T_0 = 393	1.0–3.0	LFS / Spherically propagating flame	2017 / [130]
DEC/air	0.79–1.38	T_0 = 403	1.0	LFS / Spherically propagating flame	2023 / [131]
DEC/air	0.5–2.0	T_c (T_5) = 660–1300	P_c (P_5) = 30	IDT / Rapid compression machine, Shock tube	2015 / [45]
DEC/air	0.5–2.0	T_5 = 1182–1406	P_5 = 1.08–1.15	IDT / Shock tube	2023 / [131]
0.1%DEC/O_2/N_2	0.5–2.0	500–1200	10	SP / Jet-stirred reactor	2015 / [45]
0.1%DEC/O_2/N_2	0.5–2.0	560–1220	1.0	SP / Jet-stirred reactor	2017 / [130]
DEC/O_2/50%Ar	1.5	T_f = 2436	0.033	SP / Burner stabilized premixed flame	2017 / [46]
2%DEC/Ar	∞	692–1137	0.04, 0.20, 1.0	SP / Plug-flow reactor	2017 / [46]
0.0225/0.052% DEC/Ar, 0.55% DEC/0.55%Kr/Ne	∞	T_5 = 830–1024, 1012–1203	1.7–2.0, 1.0	SP / Shock tube	2021 / [136]
0.048%DEC/Ar	∞	T_5 = 663–770	1.0–2.0	SP / Plug-flow reactor	2021 / [136]
1.5%DEC/O_2/N_2	1.0	$T_{w,max}$ = 700–1300	1.0	SP / MFR	2022 / [134] [a]
1.5%DEC/N_2	∞	$T_{w,max}$ = 700–1000	1.0	SP / MFR	2022 / [134] [a]
DEC/79.75%Ar/ 20%He	∞	T_5 = 1233–1701	1.17–1.36	SP / Shock tube	2023 / [135]
DEC/O_2/79.25% Ar/20%He	0.5–2.0	T_5 = 1236–1669	P_5 = 1.26–1.28	SP / Shock tube	2023 / [131]
EMC/air	0.7–1.5	T_0 = 423	1.0–8.0	LFS / Spherically propagating flame	2023 / [132]
EMC/air	0.79–1.4	T_0 = 403	1.0	LFS / Spherically propagating flame	2024 / [129]
EMC/air	0.5–2.0	T_5 = 1175–1481	P_5 = 0.99–1.30	IDT / Shock tube	2024 / [129]
1.5%EMC/O_2/N_2	0.5–1.5	$T_{w,max}$ = 700–1300	1.0	SP / MFR	2022 / [47] [a]
1.5%EMC/N_2	∞	$T_{w,max}$ = 700–1000	1.0	SP / MFR	2022 / [47] [a]
EMC/79.75%Ar/ 20%He	∞	T_5 = 1300–2374	0.92–1.34	SP / Shock tube	2023 / [135]

[a] Present study.

There were several chemical kinetic models available from the literature for DMC [42–44,127] and DEC [45,46], while there was none available for EMC. The first detailed chemical kinetic model of DMC was developed by Glaude et al. [42] based on a model of dimethoxy methyl (DMM) and dimethyl ether (DME) in 2005. This model was validated with speciation for DMC opposed-flow diffusion flames [133]. Hu et al. modified some of the DMC reactions in the Glaude (2005) model by analogy to methyl butanoate based on their ignition delay time experiments [43]. Sun et al. performed theoretical calculations for the DMC unimolecular decomposition reactions and the updated model was validated with speciation under pyrolysis (plug-flow reactor) and flame conditions [44] as well as the aforementioned data [43,133]. A few modifications for the Sun (2016) model were then proposed by Alexandrino et al. based on their ignition delay time data [127]. The major differences in the four DMC models are summarized in Table 3.2. As for the chemical kinetic model of DEC, the first one was developed by Nakamura et al. [45] in 2015 upon AramcoMech 1.3 [137] with rate constants of DEC related reactions taken from literature, analogically determined to ethyl esters and alkanes and theoretically calculated. The model was validated with speciation in a jet-stirred reactor and ignition delay times obtained in their study. Sun et al. conducted theoretical calculations for the DEC unimolecular decomposition reactions, updated the Nakamura (2015) model and validated it with speciation under pyrolysis (plug-flow reactor) and flame conditions [46].

The aims of the present study were (1) to systematically understand the pyrolysis and oxidation mechanisms of DMC, DEC and EMC by focusing on the molecular structure, and (2) to construct the first chemical kinetic model that includes the three linear carbonate esters, DMC, DEC and EMC. To this end, pyrolysis and oxidation characteristics of DMC, DEC and EMC were experimentally investigated using MFR by conducting species measurements and weak flame observations. Computations were also performed using detailed chemical kinetic models to validate the models as well as to perform further chemical kinetics analyses. A chemical kinetic model of the linear carbonate esters (DMC, DEC and EMC) was constructed by modeling EMC based on analogy.

Table 3.2 Major differences in the four detailed chemical kinetic models of DMC.

Reaction/Model		Glaude (2005) [42]	Hu (2015) [43]	Sun (2016) [44]	Alexandrino (2018) [127]
Base model		DMM and DME [138]	AramcoMech 1.3 [137]	AramcoMech 1.3 [137]	AramcoMech 2.0 [139]
Unimole. decompn. reactions of DMC	DMC = CH_3OCH_3 + CO_2	Theoretical and analogy	Glaude (2005)	Theoretical	Sun (2016)
	DMC = COC*OOj + CH_3	Analogy (DME [138])	Analogy (methyl butanoate [140])	Theoretical calculation	Sun (2016)
	DMC = CH_3OCO + CH_3O				Hu (2015)
H-atom abstraction reactions of DMC		Analogy (alkanes)	Analogy (methyl butanoate [140]) DMC+OH/+H: Glaude (2005)	Analogy (methyl formate [141]) DMC+O/+H: Theoretical [142,143]	Sun (2016)

3.2 Experimental and computational methods

3.2.1 MFR experiments

To investigate pyrolysis and combustion characteristics of DMC, DEC and EMC, two types of experiments were carried out using MFR, i.e., species measurements and weak flame observations. Speciation data can be obtained with the species measurement, and gas-phase ignition-related property can be evaluated with the weak flame observation. See Section 2.1 for more detail as well as general description on MFR. Figure 3.2 shows schematics of the experimental setups. A major difference between the two experiments is the external heat source used, either an electric heater (Figure 3.2a) or a hydrogen/air flat-flame burner (Figure 3.2b), which forms different temperature profiles. The experiments were conducted at Tohoku University.

(a) Species measurements

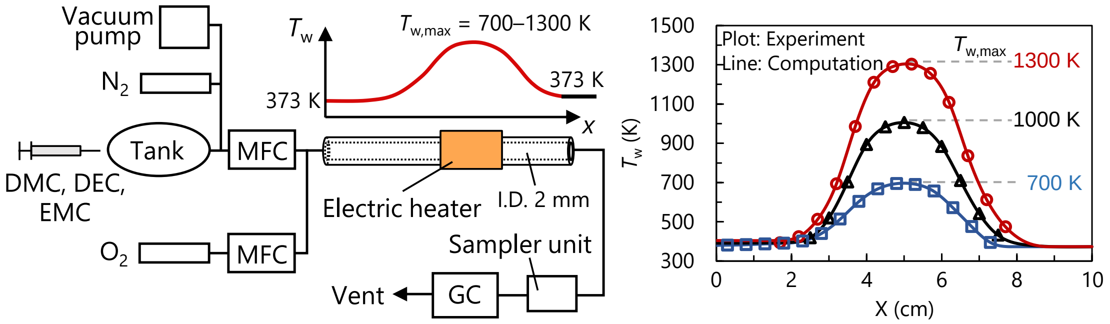

(b) Weak flame observations

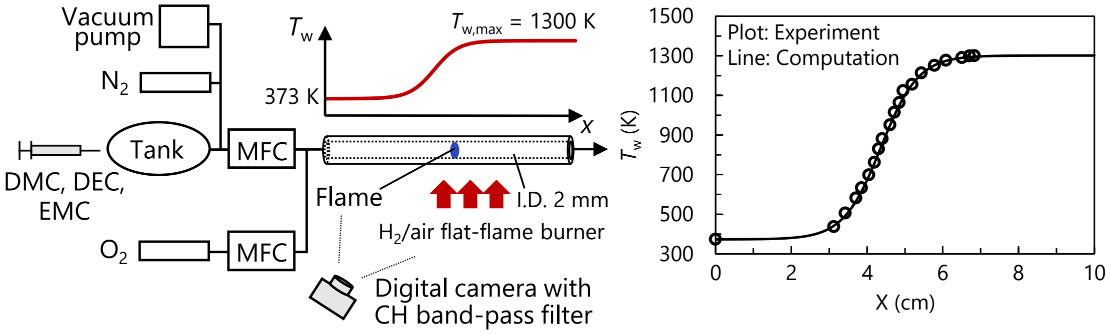

Figure 3.2 Schematics of experimental setup of (a) species measurements and (b) weak flame observations using MFR. Some of the measured wall temperature profiles (T_w) and those used in the computations are shown on the right.

3.2.1.1 *Species measurements*

Species measurements for DMC, DEC and EMC pyrolysis and oxidation were conducted using MFR combined with a gas chromatograph (GC), as shown in Figure 3.2a. A quartz tube (80 mm length, 2 mm inner diameter, 4 mm outer diameter) was employed as a reactor channel. An electric heater was used as an external heat source to provide stationary wall temperature profiles (T_w). The maximum wall temperatures ($T_{w,max}$) were varied between 700–1300 K with 50 or 100 K steps, as some representative cases are shown in Figure 3.2a. Temperature profiles were preliminarily measured with a K-type thermocouple by inserting it from the downstream of the reactor and putting a nitrogen flow of 3.77 sccm on, which corresponds to the conditions at the measurements. A correlation between the applied voltage and $T_{w,max}$ was also measured simultaneously. Table 3.3 summarizes the experimental conditions for species measurements.

Table 3.3 Experimental conditions of species measurements.

Mixture composition (in mol)	ϕ (-)	$T_{w.max}$ (K)	P (atm)	U_{in} at 373 K (cm/s)
1.5%DMC/N_2	∞	700–1200	1.0	2.7
1.5%DEC/N_2	∞	700–1000	1.0	2.7
1.5%EMC/N_2	∞	700–1000	1.0	2.7
1.5%DMC/4.5%O_2/N_2	1.0	700–1300	1.0	2.7
1.5%DEC/9.0%O_2/N_2	1.0	700–1300	1.0	2.7
1.5%EMC/6.75%O_2/N_2	0.5, 1.0, 1.5	700–1300	1.0	2.7

As for the mixture preparation, liquid DMC (> 99.5% purity, Kishida Chemical Co., Ltd.), DEC (> 98.0% purity, FUJIFILM Wako Pure Chemical Corporation) and EMC (> 99.5% purity, Kishida Chemical Co., Ltd.) were vaporized and mixed with N_2 (> 99.999% purity) in a heated stainless tank (1 litter) by the partial pressure method. The tank was heated at 373 K to avoid the condensation of DMC, DEC and EMC. Baratron (628F, MKS Instruments) was used as a manometer. A high-temperature mass flow controller (MFC, HORIBA SEC-8440F) kept at 373 K was used to control the flow rate of carbonate ester/N_2 mixtures. Conversion factors of DMC/N_2, DEC/N_2 and EMC/N_2 mixtures were determined based on calculated mixture density and heat capacity at 373 K using Cantera 2.5.1 [144] with thermodynamics data from Sun model [44], Nakamura model [45] and Takahashi model [47], respectively. For pyrolysis experiments, carbonate ester/N_2 mixtures were supplied to the reactor at inlet flow velocity of (U_{in}) 2.7 cm/s at 373 K and atmospheric pressure. Because a soot formation was observed at higher temperature conditions during pyrolysis, $T_{w,max}$ was limited up to 1200 K for DMC and 1000 K for DEC and EMC. For oxidation experiments, carbonate ester/N_2 mixtures were premixed in the transfer line with O_2 (> 99.99995% purity) whose flow rate was controlled by a room-temperature MFC and introduced into the reactor at inlet flow velocity of 2.7 cm/s at 373 K and atmospheric pressure. Equivalence ratio (ϕ) was targeted to 1.0 for DMC and DEC oxidation and 0.5, 1.0 and 1.5 for EMC oxidation (only $\phi = 1.0$ will be discussed in this thesis), and $T_{w,max}$ was varied up to 1300 K. In both pyrolysis and oxidation cases, the initial mole fraction of the carbonate esters in mixtures was fixed to 0.015 and balanced with N_2. Exhaust gases from the downstream exit of the reactor were directly transferred to a sampler unit and introduced into GC (Shimadzu Tracera). All transfer lines from the tank to the reactor as well as the reactor to GC were heated up at 373 K to avoid the condensation of reactants, unburnt carbonate esters and water.

Stable, major species, O_2, H_2, CO, CO_2, CH_4, C_2H_4 and C_2H_6, were measured using GC equipped with a MICROPACKED-ST column (30 m length, 0.25 mm inner diameter, 10 μm film thickness, Shinwa Chemical Industries Ltd.) and a barrier ionization detector (BID, Shimadzu BID-2010 Plus). The sampler unit was kept at 373 K and sampling volume was set to 50 μl. Helium (> 99.99995% purity) was used as a carrier gas. Split ratio was set to 20 and the carrier gas was controlled with the linear velocity control method at 30.8 cm/s. BID temperature was set to 483 K. Standard gases were used for the identification and quantification of the measured species.

Experiments were repeated for more than three times for each condition, and an error in the measured mole fractions due to the repetition of species measurements are shown as error bars in each figure. The experimental uncertainty in the inlet mixture composition including partial pressure-based mixture preparation in the tank and the flow rate determined based on the calculated conversion factors is estimated to be approximately ± 5%. The uncertainty in T_w is ± 5 K and that in the species measurement is approximately ± 3%.

3.2.1.2 Weak flame observations

An experimental setup for weak flame observations of DMC, DEC and EMC are shown in Figure 3.2b. A longer quartz tube (200 mm length, 2 mm inner diameter, 4 mm outer diameter) than the one used in the species measurements was employed as a reactor channel. For the weak flame observations, a hydrogen/air flat-flame burner was used as an external heat source instead of an electric heater. A stationary temperature profile with $T_{w,max}$ = 1300 K was given to the reactor inner wall surface as shown in Figure 3.2b. Methods for the T_w

profile measurement and mixture preparations were the same as the species measurement experiments described in the previous section. The uncertainty in T_w is approximately ± 10 K. Stoichiometric carbonate ester/O_2/N_2 mixtures ($N_2 : O_2 = 79 : 21$) were supplied to the reactor at U_{in} = 2.7 cm/s at 373 K and atmospheric pressure. As the N_2-to-O_2 ratio is fixed to the air composition, the mixtures for the weak flame observations are hereafter called as DMC/air, DEC/air and EMC/air.

A digital still camera (Nikon D800) with a CH band-pass filter (Edmund Optics Ltd., transparent wavelength of 431.2 nm, half bandwidth of 6.4 nm) was used to observe a weak flame. As chemiluminescence from a weak flame is very faint, exposure time was set to 30 s. Weak flame positions in the experiment were defined as a maximum peak location in the luminosity profile along with the tube-axis direction, which was averaged in the tube-radial direction in the pre-processing.

3.2.2 MFR computations

Computations modeling the MFR system were also performed to validate literature chemical kinetic models of DMC and DEC as well as a newly constructed EMC model and to analyze gas-phase pyrolysis and combustion reactions of the linear carbonate esters. At low inlet flow velocity conditions (a few cm/s) in MFR, i.e., weak flame conditions, the flow field in the reactor can be assumed to be a reactive flow without a boundary layer. One- and two-dimensional computations of the MFR system at a weak flame condition showed little multi-dimensional effect on computational heat release and species profiles [65]. Thus, the one-dimensional steady-state computation using the PREMIX code implemented in Chemkin-Pro v19.0 [145] with an additional term in the gas-phase energy equation [51] (see below) is feasible to model the MFR system at weak flame conditions and was used in the present study. The additional term in the gas-phase energy equation is convective heat transfer between the gas and the reactor inner wall where the modified gas-phase energy equation [51] is give as:

$$\dot{M}\frac{\mathrm{d}T}{\mathrm{d}x} - \frac{1}{c_\mathrm{p}}\frac{\mathrm{d}}{\mathrm{d}x}\left(\lambda A\frac{\mathrm{d}T}{\mathrm{d}x}\right) + \frac{A}{c_p}\sum_{k=1}^{K}\rho Y_k V_k c_{\mathrm{p}k}\frac{\mathrm{d}T}{\mathrm{d}x} + \frac{A}{c_p}\sum_{k=1}^{K}\dot{\omega}_k h_k W_k - \frac{A}{c_p}\frac{4\lambda Nu}{d^2}(T_\mathrm{w} - T) = 0\,.$$

The fifth term corresponds to the convective heat transfer term. T_w, T, d and Nu are the wall temperature, gas-phase temperature, channel inner diameter and Nusselt number, respectively (see Nomenclature for the others). The Nusselt number was set to the constant value, $Nu = 4$, considering the cases of isothermal wall ($Nu = 3.66$) and constant heat flux ($Nu = 4.36$). This computational model has been successfully applied to various fuels, such as hydrocarbons [44–47] and oxygenates [50–52].

The same conditions to the experiments (mixture composition, inlet flow velocity, pressure and T_w profile) were given to the computations. The T_w-profiles applied in the computations with the measured ones in the experiments are shown in Figure 3.3. The computational domain was set to x = 0–10 cm. Species mole fractions at x = 10 cm were compared with the species measurement results. Computational weak flame positions were defined as a maximum peak location in the heat release rate (HRR) profile as a HRR peak position is found to be in agreement with an experimental weak flame position defined by the chemiluminescence from CH* (e.g., [67]). Surface reactions are not considered in the present study because the radical quenching effect on a heated quartz surface was reported to be negligibly small under atmospheric pressure [146,147].

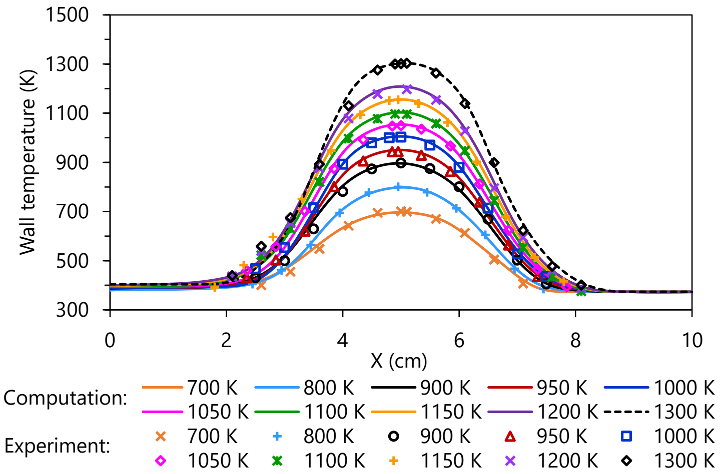

Figure 3.3 Measured wall temperatures (T_w) and the profiles used in computation.

As for the detailed chemical kinetic models of DMC, those proposed by Glaude et al. (102 species, 442 reactions) [42], Hu et al. (275 species, 1586 reactions) [43], Sun et al. (257 species, 1563 reactions) [44] and Alexandrino et al. (257 species, 1563 reactions; based on AramcoMech 1.3 [137] instead of originally used AramcoMech 2.0 [139]) [127] were used. Hereafter these models are called as Glaude (2005), Hu (2015), Sun (2016) and Alexandrino (2018) model. As for DEC, models from Nakamura et al. (355 species, 1959 reactions) [45] and Sun et al. (341 species, 1980 reactions) [46] (hereafter called as Nakamura (2015) and Sun (2017) model, respectively) were used. An EMC model (371 species, 2076 reactions) was constructed in the present study [47] of which brief description will be given in the following Section 3.3.

3.3 Chemical kinetic modeling of EMC

Through the modeling of EMC, we constructed a chemical kinetic model that covers the three linear carbonate esters, i.e., DMC, DEC and EMC, as a first step towards a LIB electrolyte surrogate model, which also includes a cyclic carbonate ester, i.e., EC, as described in Chapter 4. Herein, a brief description on the EMC modeling is given. Detailed information on each reaction can be found in our paper [47].

The first EMC model was constructed based on a DEC model from the literature, according to our experimental results that showed similar reactivities between EMC and DEC rather than DMC, as discussed later in the following Section 3.4. Although a detailed comparison of the DEC literature models will be carried out in the following section as well, in brief, a model by Nakamura et al. [45] was found to better predict our experimental results than that by Sun et al. [46], thus the Nakamura (2015) model was adopted as a base model in this study.

We adopted unimolecular decomposition reactions of EMC with their theoretically obtained rate constants proposed by Notario et al. [148]. Rate constants of H-atom abstraction reactions from the methyl and ethyl groups of EMC were analogically taken from DMC and DEC, respectively, considering their similarities in molecular structure (see Figure 3.1). A rate constant for an important intermediate from EMC decomposition, methyl formic acid (MFA, COC*OOH), which rapidly decomposes to CH_3OH and CO_2 via a four-center transition state, was also taken from the work by Notario et al. [148]. Thermochemical parameters of MFA were calculated using a THERM [149] software, which is based on Benson's group additive method [150]. The THERM group data was taken from a KUCRS [151] software. Transport parameters of MFA were taken from those used for CJOC*OOH in the Nakamura (2015) model. For the other EMC-related species, their thermochemical and transport parameters were taken from the Nakamura (2015) model as well. To make our model applicable for DMC calculations as well, a DMC sub-model by Alexandrino et al. [127] was implemented in the present linear carbonate ester model, which hereafter called as Takahashi (2022) model [47]. This Takahashi (2022) model includes 371 species and 2076 reactions.

3.4 Results and discussion

To systematically understand pyrolysis and oxidation characteristics of DMC, DEC and EMC, the experiments were conducted at comparative conditions. Speciation data for species measurements at pyrolysis (Section 3.4.1) and oxidation (Section 3.4.2) are presented first with model validation. Then, gas-phase reactivities of the linear carbonate esters are evaluated based on weak flame observations (Section 3.4.3). Finally, the reaction mechanisms of DMC, DEC and EMC are summarized (Section 3.4.4).

3.4.1 Species measurements at pyrolysis conditions

Species measurements were conducted at 700–1200 K for DMC pyrolysis and 700–1000 K for DEC and EMC pyrolysis to avoid soot formation. Preliminary to the species measurement experiments, soot observations were conducted for 1.5%DMC/N_2 and

1.5%DEC/N_2 mixtures using the same setup as the weak flame observation experiment. Soot formation was not observed even at $T_{w,max}$ = 1200 K during the DMC pyrolysis, whereas soot formation was observed at $T_{w,max}$ = 1100 K during the DEC pyrolysis. As residence time at $T_{w,max}$ region for the flame observation setup is longer than that for the species measurement setup due to the different external heat source applied (see Section 3.2.1), soot formation would be suppressed with the latter setup [64,86]. Thus, non-formation of soot would be guaranteed with the present species measurement setup at $T_{w,max}$ = 1200 K for the DMC pyrolysis. DMC was reported to have greater synergistic effect as additive to propane on reducing acetylene level, which is a key soot/PAH precursor, compared with two other different C_3 oxygenates (*iso*-propanol and dimethoxy methane) [133] because of its high oxygen content as well as the absence of C–C bond in DMC. On contrary, DEC includes C–C bonds and its O/C ratio is lower than DMC. Consequently, soot tended to yield at lower temperatures for the DEC pyrolysis than the DMC pyrolysis. This would be similar in EMC as it also involves C–C bond in the molecular structure although O/C ratio is higher than in DEC. To prevent soot formation during pyrolysis, therefore, species measurements were conducted at $T_{w,max} \leq$ 1000 K for the DEC and EMC cases. Computations were extended to $T_{w,max}$ = 1300 K to observe the general trend in the species growth at higher temperatures.

3.4.1.1 DMC pyrolysis

Experimental and computational mole fractions of DMC, H_2, CO, CO_2, CH_4, C_2H_4, C_2H_6 for a 1.5%DMC/N_2 mixture are shown in Figure 3.4. Experimental results are discussed first, followed by a comparison of experimental and computational results.

H_2, CO, CO_2, CH_4, C_2H_4, C_2H_6 as well as C_2H_2 (not shown in the figure) were measured in the DMC pyrolysis case. The measured CO_2 and CH_4 mole fractions start increasing at around $T_{w,max}$ = 1000 K followed by H_2, CO and C_2H_6 production at $T_{w,max}$ = 1050 K. The measured C_2H_4 mole fraction increases at around $T_{w,max}$ = 1100 K where that of C_2H_6 shows a peak. C_2H_2 was detected at $T_{w,max}$ = 1150 K and 1200 K, showing measured mole fraction of approximately 240 and 540 ppm, respectively. Thus, the soot formation can be expected at higher temperature than $T_{w,max}$ = 1200 K from species measurements as well because of the soot/PAH precursor C_2H_2 yield. The measured CO_2 and CO mole fractions at $T_{w,max}$ = 1200 K were ca. 0.015 and 0.012, respectively, accounting for 94% of O-atom in the fuel, i.e., the oxygen balance. The carbon balance at $T_{w,max}$ = 1200 K was ca. 91%, ensuring that most parts of the pyrolysis products were measured in the experiment.

By comparing the experimental and computational results, the predictions using the Sun (2016) and Alexandrino (2018) models are in good agreement with most of the measured species mole fractions. The computational results using the Hu (2015) model fairly predicts the onset of the measured species mole fractions as similar to the Sun (2016) and Alexandrino (2018) models, whereas it overpredicts H_2 and CO mole fractions and underpredicts CO_2 and C_2H_4 mole fractions at higher temperatures, especially at $T_{w,max}$ = 1200 K. The computational result using the Glaude (2005) model shows higher onset temperatures of the measured species than the experimental results by around 100 K. The higher initiation temperature with the Glaude (2005) model is also observed in computed DMC mole fractions when compared to the other three models. One of the major differences between the Glaude (2005) model and the other three models is the rate constant of an unimolecular decomposition reaction of DMC, DMC = COC*OOj + CH_3, where * and j denote a double bond and radical site, respectively. The rate constant used in the Glaude (2005) model is much higher than that used in the Hu (2015), Sun (2016) and Alexandrino (2018) models. Based on the comparison, Sun (2016) and Alexandrino (2018) models show the best prediction among the four models for the DMC pyrolysis.

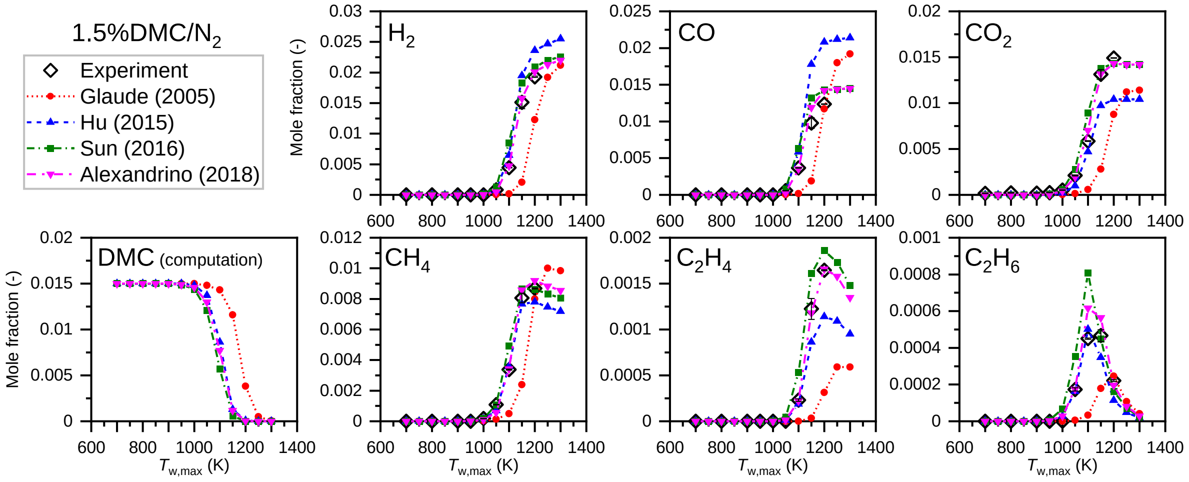

Figure 3.4 Measured and computed mole fractions of H_2, CO, CO_2, CH_4, C_2H_4 and C_2H_6 for a 1.5%DMC/N_2 mixture under atmospheric pressure. The experiment was carried out at $T_{w,max}$ = 700–1200 K. Computed mole fractions of DMC are also shown.

3.4.1.2 DEC pyrolysis

Experimental and computational mole fractions of DEC, H_2, CO, CO_2, CH_4, C_2H_4, C_2H_6 for a 1.5%DEC/N_2 mixture are shown in Figure 3.5. Experimental results are discussed first, followed by a comparison of the experimental and computational results.

H_2, CO, CO_2, CH_4 and C_2H_4 were measured in the DEC pyrolysis case, while C_2H_6 and C_2H_2 were not quantitatively measured at the temperature studied (the lower detection limits in this experiment were around 100 ppm for both). The measured CO_2 and C_2H_4 mole fractions start increasing at around $T_{w,max}$ = 750 K, and stay almost constant of 0.015 at $T_{w,max}$ = 850–1000 K. The measured H_2, CO and CH_4 mole fractions increase from around $T_{w,max}$ = 950 K. C_2H_6 signals were detected at $T_{w,max}$ = 950 K and 1000 K but they were too small to be quantified (near or less than 100 ppm). The carbon-balance and oxygen-balance at $T_{w,max}$ = 900 K were about 60% and 67%, respectively. The reason for the missing carbon and oxygen will be given in the following part but note that these are not due to the experimental failure.

Compared with the experimental results, both computational results using the Nakamura (2015) and Sun (2017) models reproduce the onset of the measured H_2, CO and CH_4 mole fractions well, for which the computational results are almost equivalent to each other up to

$T_{w,max}$ = 1300 K. There is a large discrepancy between the two models for the CO_2 and C_2H_4 mole fractions where the Nakamura (2015) model better reproduces the experimental results. The computational result using the Sun (2017) model shows the production of CO_2 and C_2H_4 at higher temperature region than the experimental results by more than 50 K. A similar tendency also appears in the computed DEC mole fraction as well as computed C_2H_5OH mole fraction (Figure 3.6) where the computational results using the Nakamura (2015) model shows faster consumption and production, respectively, than that using the Sun (2017) model. These CO_2, C_2H_4 and C_2H_5OH are major decomposition products from DEC [46,136,152]. Taking the computed C_2H_5OH mole fractions into account, the carbon- and oxygen-balance are calculated to be almost 100% at $T_{w,max}$ = 900 K, which explains the missing carbon and oxygen in the experiment. By performing sensitivity analyses for the CO_2 and C_2H_4 mole fractions, a thermal decomposition reaction of DEC that produces ethoxy formic acid (EFA) and ethylene, DEC = CCOC*OOH + C_2H_4 (R3-1), are found to be highly sensitive in both model cases as shown in Figure 3.7 (oxidation case is also shown). According to Notario et al. [148], the subsequent reaction of EFA rapidly proceeds to produce ethanol and carbon dioxide, CCOC*OOH => C_2H_5OH + CO_2 (R3-2), compared to R1. This results in the much less sensitivity of R3-2 to CO_2 and C_2H_4 mole fractions. It is also worth mentioning that there is another decomposition reaction of EFA considered in the Sun (2017) model that produces ethylene and carbonic acid, CCOC*OOH => C_2H_4 + HOC*OOH (R3-3), which is also less sensitive to the C_2H_4 mole fraction. Thus, the DEC unimolecular decomposition R3-1 is the rate determine reaction, and is a key to predict the decomposition products at low temperatures of around $T_{w,max}$ = 800 K. A rate constant of R3-1 obtained from shock tube experiments by Herzler et al. [152] is adopted in the Nakamura (2015) model, while that obtained from theoretical calculations by Sun et al. [46] is used in their model. The latter one is lower than the former one, for instance, approximately 4.3 times lower at 800 K and 1 atm. To further look into the rate constant of R3-1, literature data are compared with those used in the two models as shown in Figure 3.8. An experimentally and theoretically obtained rate constant of R3-1 by AlAbbad et al. [153] shows similar values as the one used in the Nakamura (2015) model at near atmospheric pressure. Sela et al. [136] conducted shock tube experiments and theoretical calculations for the unimolecular thermal decomposition of DEC, and they also reported that the rate constant of R3-1 from Sun et al. [46] was lower than their experimentally and theoretically obtained rate constants in particular at low temperatures. The rate constants reported by Sela et al. [136] are close to the one used in the Nakamura (2015) model and moreover, their theoretically obtained rate constant is even higher than the latter up to around 1400 K. Considering the slight underprediction of the measured CO_2 and C_2H_4 mole fractions using the Nakamura (2015) model observed in the present experiment, there would be a room for the model to be further improved by adopting the rate constant from Sela et al. [136] (see Section 3.4.2.2). The computed C_2H_4 mole fraction in Figure 3.5 show a second increase at $T_{\mathrm{w,max}}$ = 1000–1100 K for both Nakamura (2015) and Sun (2017) model cases. Based on the rate of production analysis of C_2H_4, the second increase was driven by the decomposition of C_2H_5OH, $C_2H_5OH = C_2H_4 + H_2O$ (R3-4). From the comparison of the experiments and computations, the Nakamura (2015) model provides better predictions on the measured species during the DEC pyrolysis.

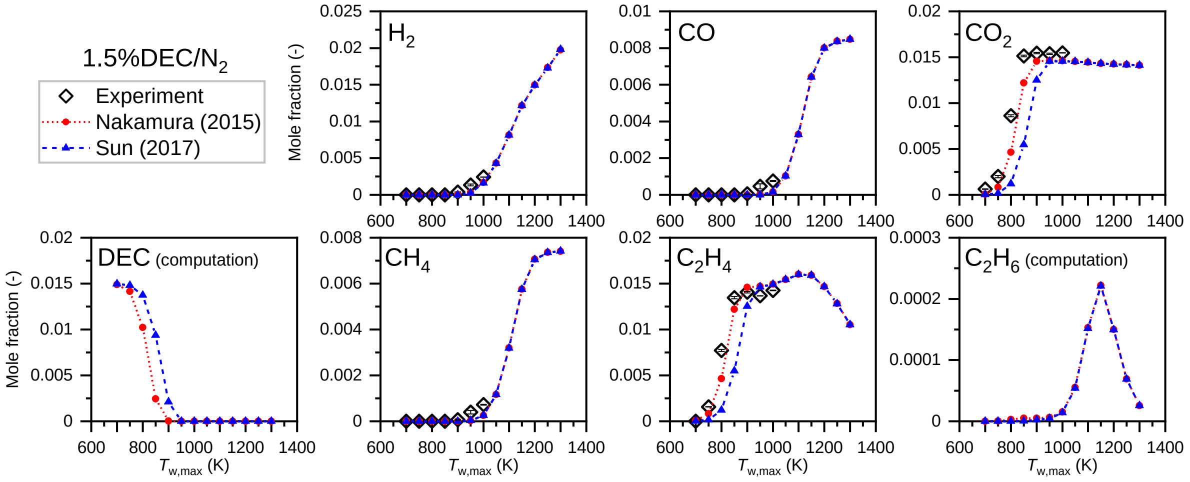

Figure 3.5 Measured and computed mole fractions of H_2, CO, CO_2, CH_4, C_2H_4 and C_2H_6 for a 1.5%DEC/N_2 mixture under atmospheric pressure. The experiment was carried out at $T_{\mathrm{w,max}}$ = 700–1000 K. Computed mole fractions of DEC and C_2H_6 are also shown.

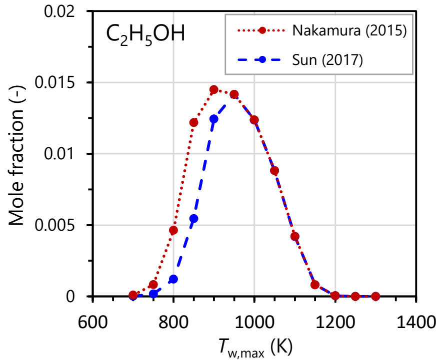

Figure 3.6 Computed mole fractions of C_2H_5OH for a 1.5%DEC/N_2 mixture at pyrolysis condition under atmospheric pressure.

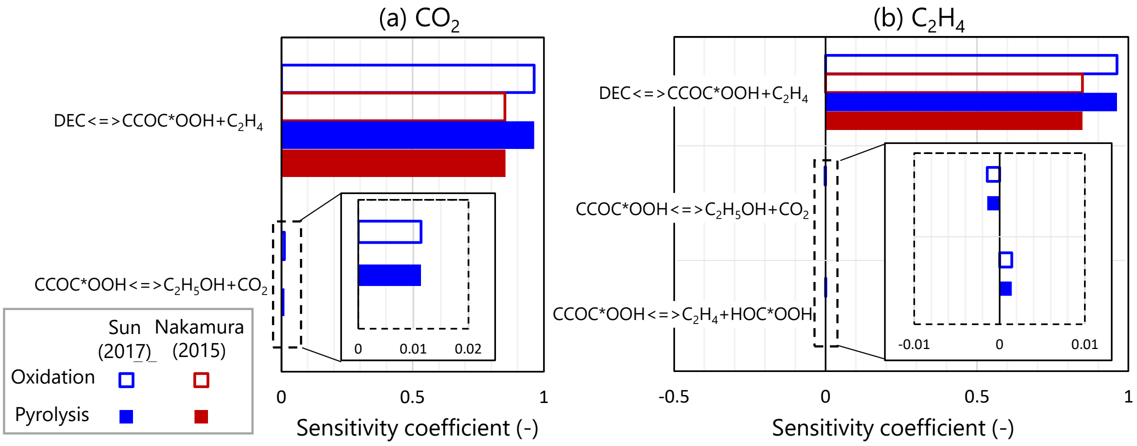

Figure 3.7 Sensitivities to (a) CO_2 and (b) C_2H_4 mole fractions performed for DEC pyrolysis (filled box) and oxidation (open box) at 800 K of the $T_{\mathrm{w,max}}$ = 800 K case.

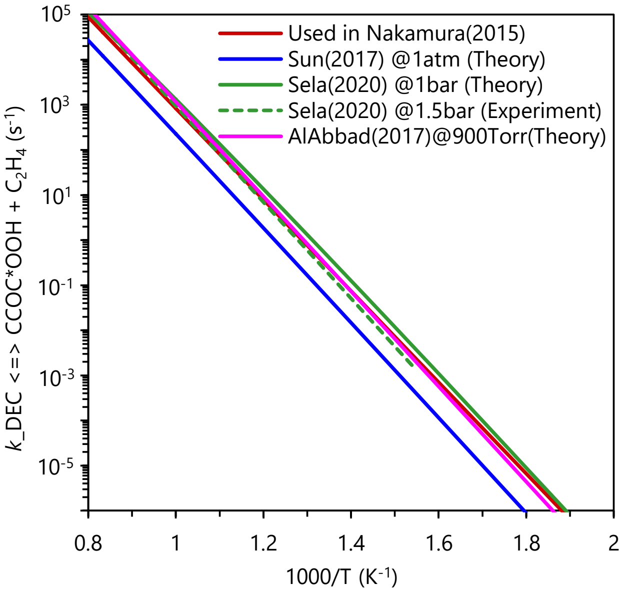

Figure 3.8 Rate constants of R3-1 (DEC = CCOC*OOH + C_2H_4) used in the Nakamura (2015) and Sun (2017) models as well as reported by AlAbbad et al. [153] and Sela et al. [136].

3.4.1.3 EMC pyrolysis

Experimental and computational mole fractions of EMC, H_2, CO, CO_2, CH_4, C_2H_4, C_2H_6 for a 1.5%EMC/N_2 mixture are shown in Figure 3.9. Experimental results are discussed first, followed by a comparison of the experimental and computational results.

H_2, CO, CO_2 and C_2H_4 were measured in the EMC pyrolysis case, while CH_4 and C_2H_6 were not detected in the present experiment. The measured CO_2 and C_2H_4 mole fractions start increasing at $T_{w,max}$ = 800 K, and reach to around 0.012. The measured H_2 and CO mole fractions slightly increase at $T_{w,max}$ = 1000 K. The carbon-balance and oxygen-balance at $T_{w,max}$ = 900 K are calculated to be around 60% and 55%, respectively.

Computational results using the Takahashi (2022) model quantitatively reproduce the measured species mole fractions although the computational results show slightly higher CO_2 and C_2H_4 mole fractions at the intermediate temperatures around $T_{w,max}$ = 900–1000 K than the experimental results. The computed H_2, CO, CH_4 and C_2H_6 mole fractions increase above $T_{w,max}$ = 1100 K, i.e., above the temperature studied in the experiment. Computed CH_3OH mole fraction at $T_{w,max}$ = 900 K was around 0.015, being similar to those of CO_2 and C_2H_4, which implies that the unimolecular decomposition of EMC producing equivalent CO_2, C_2H_4 and CH_3OH (COC*OOCC = COC*OOH + C_2H_4 (R3-5) and then COC*OOH => CH_3OH + CO_2 (R3-6)) [148] is dominant during EMC pyrolysis. This could explain the missing carbon and oxygen in the experiment.

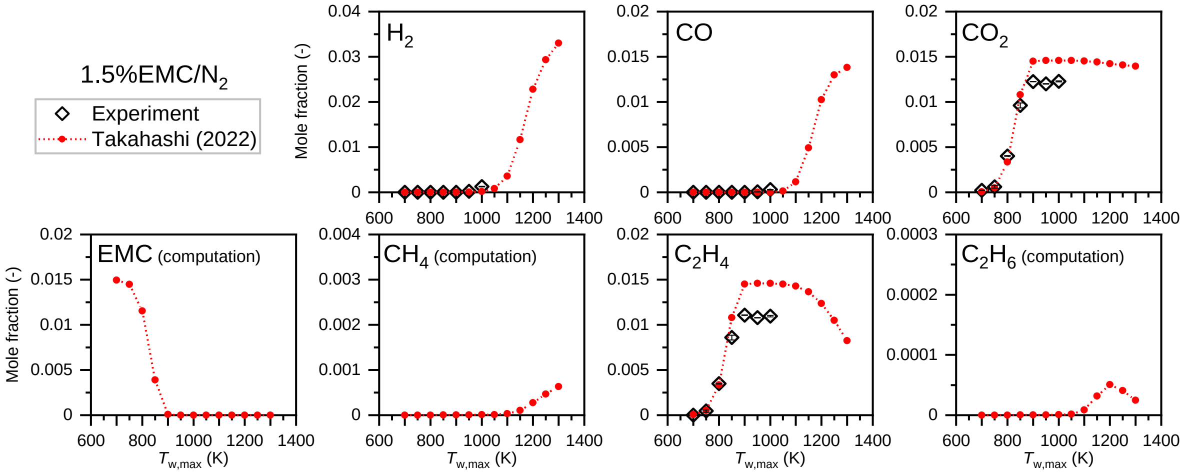

Figure 3.9 Measured and computed mole fractions of H_2, CO, CO_2, CH_4, C_2H_4 and C_2H_6 for a 1.5%EMC/N_2 mixture under atmospheric pressure. The experiment was carried out at $T_{w,max}$ = 700–1000 K. Computed mole fractions of EMC, CH_4 and C_2H_6 are also shown.

3.4.1.4 Comparison between DMC, DEC and EMC pyrolysis

Figure 3.10 shows a comparison of the species profiles of DMC, DEC and EMC pyrolysis in MFR. Based on the computed mole fractions of DMC, DEC and EMC, the onsets of both DEC and EMC consumption locate at a lower temperature region (around $T_{w,max}$ = 750–800 K) than that of DMC locating at an intermediate-temperature region (around $T_{w,max}$ = 1000–1050 K). In the DMC case, the measured species mole fractions rapidly increase once DMC decreases. Meanwhile, there is a gap of approximately 250 K between the onset temperatures of the initial products (CO_2 and C_2H_4) and the other measured species in DEC and EMC cases. According to theoretical calculations, a four-center CO_2 elimination reaction producing dimethyl ether (DME), DMC = DME + CO_2 (R3-7), is an energetically preferable DMC decomposition channel (barrier height of 71.1 kcal/mol) [44,143]. Although the four-center CO_2 elimination reaction producing diethyl ether (DEE), DEC = DEE + CO_2 (R3-8), lies in the DEC case as well (barrier height of ca. 64.5–67.4 kcal/mol), the most energetically favorable channel is that producing C_2H_4 and EFA (CCOC*OOH) via a six-center transition state (44.9–47.3 kcal/mol), that is, DEC = EFA + C_2H_4 (R3-1) [46,136]. The same is also reported for EMC unimolecular decomposition [148], which more likely to produce C_2H_4 and MFA (COC*OOH) by EMC = MFA + C_2H_4 (R3-5) than CO_2 and ethyl methyl ether (EME) by EMC = EME + CO_2 (R3-9). EFA and MFA subsequently decompose via a four-center CO_2 elimination reaction producing C_2H_5OH and CH_3OH, respectively. Thus, although DEC and EMC decompose at the low-temperature region, the pooled products, i.e., CO_2, C_2H_4 and alcohols, are relatively stable at those temperatures. This leads to a gap between the onset of the initial products and secondary products, e.g., H_2 and CO, where the latter is likely to be determined by temperature. Consequently, there is less difference in the onset temperatures of the production of reforming gas compounds between DMC and DEC/EMC pyrolysis (around $T_{\mathrm{w,max}}$ = 1000 K). When comparing the DEC and EMC pyrolysis, the computed C_2H_4 mole fraction decreases after reaching the plateau in the EMC case, unlikely to the case of DEC where the second increase is appeared due to the decomposition of C_2H_5OH (R3-4). As EMC produces CH_3OH, which further decomposes to such as CH_2O to produce CO, the CH_4 and C_2H_6 production seemed to be suppressed compared to DEC.

(a) 1.5%DMC/N_2

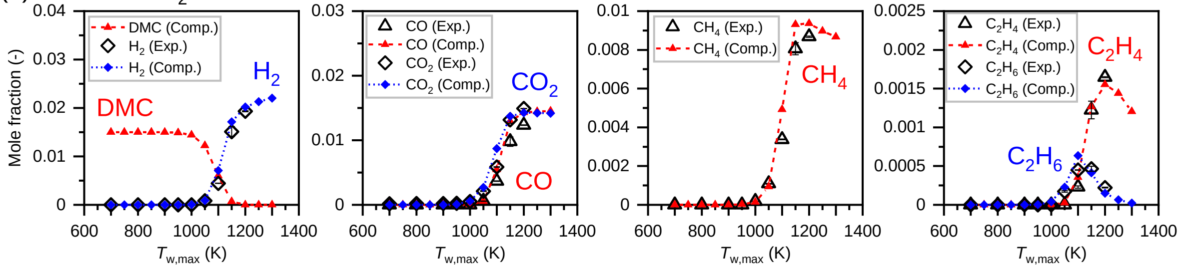

(b) 1.5%DEC/N_2

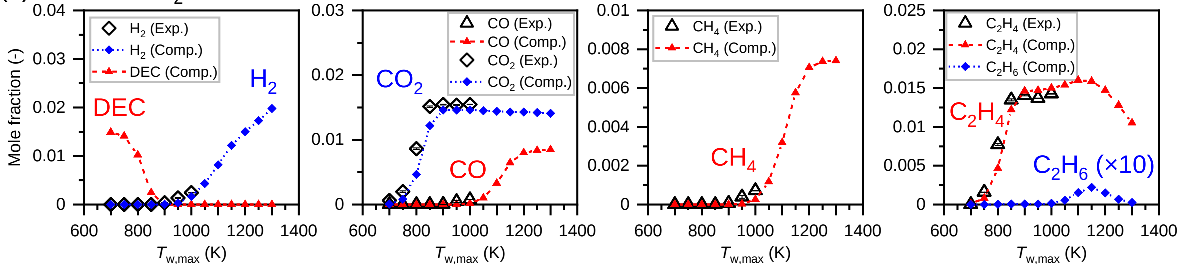

(c) 1.5%EMC/N_2

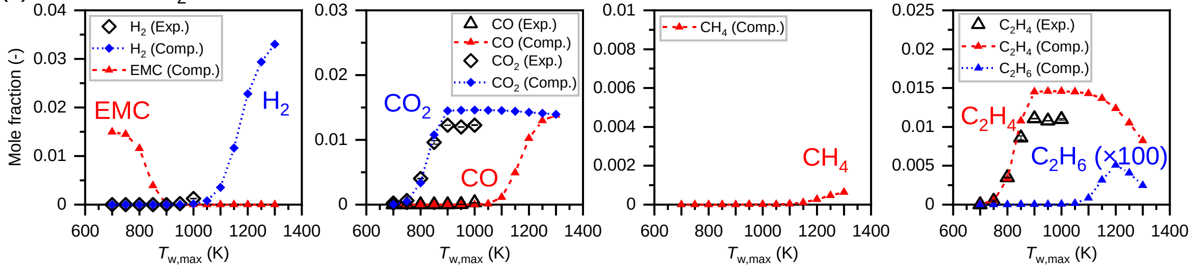

Figure 3.10 Measured and computed mole fractions of H_2, CO, CO_2, CH_4, C_2H_4 and C_2H_6 for (a) 1.5%DMC/N_2, (b) 1.5%DEC/N_2 and (c) 1.5%EMC/N_2 mixtures under atmospheric pressure. Computational results are those using Takahashi model [47].

3.4.2 Species measurements at oxidation conditions

3.4.2.1 DMC oxidation

Experimental and computational mole fractions of O_2, H_2, CO, CO_2, CH_4, C_2H_4, C_2H_6 for a stoichiometric 1.5%DMC/4.5%O_2/N_2 mixture are shown in Figure 3.11. Experimental results are discussed first, followed by a comparison of the experimental and computational results.

In DMC oxidation, O_2, H_2, CO, CO_2, CH_4, C_2H_4 and C_2H_6 were measured. The measured O_2 mole fraction rapidly decreases between $T_{w,max}$ = 1000 and 1150 K where the production of the other measured species is observed. The measured H_2, CO, CH_4, C_2H_4 and C_2H_6 mole fractions peak at around $T_{w,max}$ = 1050–1100 K, and they were not able to be detected above $T_{w,max}$ = 1150 K. The measured CO_2 mole fraction continues to increase until $T_{w,max}$ = 1150 K where it reaches approximately 0.047. At the high temperature region above $T_{w,max}$ = 1150 K, the carbon balance in the experiments corresponds to around 104%, which indicates that DMC has been fully converted to CO_2.

By comparing computational results with the experimental results, the computed O_2 mole fractions using Glaude (2005) and Hu (2015) models are depleted at slightly lower temperatures ($T_{w,max}$ = 1100 K) than the experiment, while those using Sun (2016) and Alexandrino (2018) models reproduce the experimental result well. The slight overprediction of seemingly DMC oxidation by the Glaude (2005) and Hu (2015) models is also confirmed for other species, especially for H_2, CO, CO_2 and CH_4 mole fractions. The computed H_2, CO and CH_4 mole fractions rapidly decrease and that of CO_2 reaches almost 0.045, i.e., the completion of CO to CO_2 oxidation, at $T_{w,max}$ = 1100 K. Meanwhile, the computational results for the other species than O_2 using the Sun (2016) and Alexandrino (2018) models are also in good agreement with the experimental results. A difference in the Sun (2016) and Alexandrino (2018) models is the rate constant of a DMC unimolecular decomposition reaction, DMC = CH_3OCO + CH_3O (R3-10). The rate constant of R3-10 used in the Sun (2016) model was replaced with that of Hu (2015) model by Alexandrino et al. [127]. Although H-atom abstraction reactions from DMC by radicals are known to be primary DMC consumption reactions at oxidation conditions [42–44], the H-atom abstraction reactions in the each model were determined differently. Glaude et al. [42] determined based on analogy to alkanes, Hu et al. [43] determined based on analogy to methyl butanoate [140] and Sun et al. [44] determined based on analogy to methyl formate [141] and took theoretically proposed ones for O and H radicals by Peukert et al. [142,143], as major differences in the DMC models are summarized in Table 3.2 in Section 3.1. A reason for the difference in the computational results with the Glaude (2005) and Hu (2015) models and the Sun (2016) and Alexandrino

(2018) models could be due to these H-atom abstraction reactions. Another reason could be a difference in the CO_2 elimination reaction from DMC, i.e., DMC = DME + CO_2 (R3-7). The rate constant of R3-7 used in the Glaude (2005) and Hu (2015) models are the same, being varied from that usen in the Sun (2016) and Alexandrino (2018) models. Overall, Sun (2016) and Alexandrino (2018) models seem to provide better prediction of DMC oxidation.

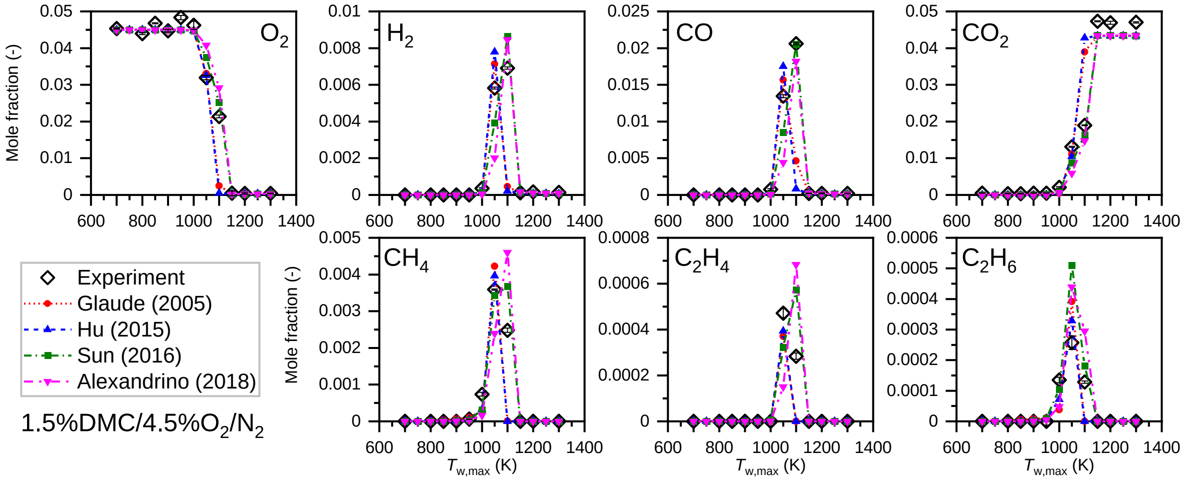

Figure 3.11 Measured and computed mole fractions of O_2, H_2, CO, CO_2, CH_4, C_2H_4 and C_2H_6 for a stoichiometric 1.5%DMC/4.5%O_2/N_2 mixture at $T_{w,max}$ = 700–1300 K under atmospheric pressure.

3.4.2.2 DEC oxidation

Experimental and computational mole fractions of O_2, H_2, CO, CO_2, CH_4, C_2H_4, C_2H_6 for a stoichiometric 1.5%DEC/9.0%O_2/N_2 mixture are shown in Figure 3.12. Experimental results are discussed first, followed by a comparison of the experimental and computational results.

O_2, H_2, CO, CO_2, CH_4, C_2H_4 and C_2H_6 were also quantified in the DEC oxidation. The measured O_2 mole fraction decreases above $T_{w,max}$ = 900 K and is almost depleted at around $T_{w,max}$ = 1050–1100 K. At the corresponding temperature range, the measured H_2, CO, CH_4 and C_2H_6 mole fractions increase and hit a peak at around $T_{w,max}$ = 950–1000 K. Whereas, the measured CO_2 and C_2H_4 mole fractions increase at much lower temperatures (around $T_{w,max}$ =

750 K) than the other measured products and moreover, than the O_2 consumption temperature range. The measured CO_2 mole fraction shows a plateau at around $T_{w,max}$ = 850–1000K followed by a second rapid increase, reaching approximately 0.074 at the higher temperatures. The conversion of DEC to CO_2 at this high-temperature region is almost 99% based on carbon balance in the experiment. The measured C_2H_4 mole fraction peaks at around $T_{w,max}$ = 850 K where the value is nearly equal to the inlet mole fraction of DEC, i.e., 0.015. Considering the molecular structure of DEC, the first increase in the measured CO_2 mole fraction and the increase in the measured C_2H_4 mole fraction at the low-temperature region (around $T_{w,max}$ = 750–850 K) likely to be caused by the DEC thermal decomposition. Meanwhile, the second increase in the measured O_2 mole fraction observed at $T_{w,max}$ = 1000–1100 K corresponds to CO to CO_2 oxidation as the measured CO mole fraction is simultaneously depleted.

From a comparison between the experimental and computational results, both Nakamura (2015) and Sun (2017) models are in good agreement with the measured O_2, H_2, CO, CH_4 and C_2H_6 mole fractions. There are, however, discrepancies between the measured and computed CO_2 and C_2H_4 mole fractions at the low-temperature region for the case of the Sun (2017) model. The model prediction using the Nakamura (2015) model captures the increases in CO_2 and C_2H_4 mole fractions well, while the Sun (2017) model underpredicts the initial increases, as the same tendency was observed in the pyrolysis case in Section 3.4.1.2. As discussed therein, a reason could be the difference in the rate constant of the C_2H_4 elimination reaction, DEC = EFA + C_2H_4 (R3-1), where the one used in the Nakamura (2015) model is faster than that used in the Sun (2017) model. We attempted trial computations by adopting the theoretical rate constant of R3-1 reported by Sela et al. [136], which is even faster than the one used in the Nakamura (2015) model, to the two models. Consequently, both model predictions show almost identical results with each other as well as better agreements with the experimental results in both oxidation and pyrolysis cases., as shown in Figure 3.13 Thus, the principal factor of the discrepancy observed in the computed mole fractions of DEC, CO_2, C_2H_4 and C_2H_5OH at lower temperature region ($T_{w,max}$ = 700–900 K) between Nakamura (2015) model and Sun (2017) model attributed mainly to the difference in the rate constant of R3-1. The model prediction with the Nakamura (2015) model is better than the other one also in the oxidation conditions.

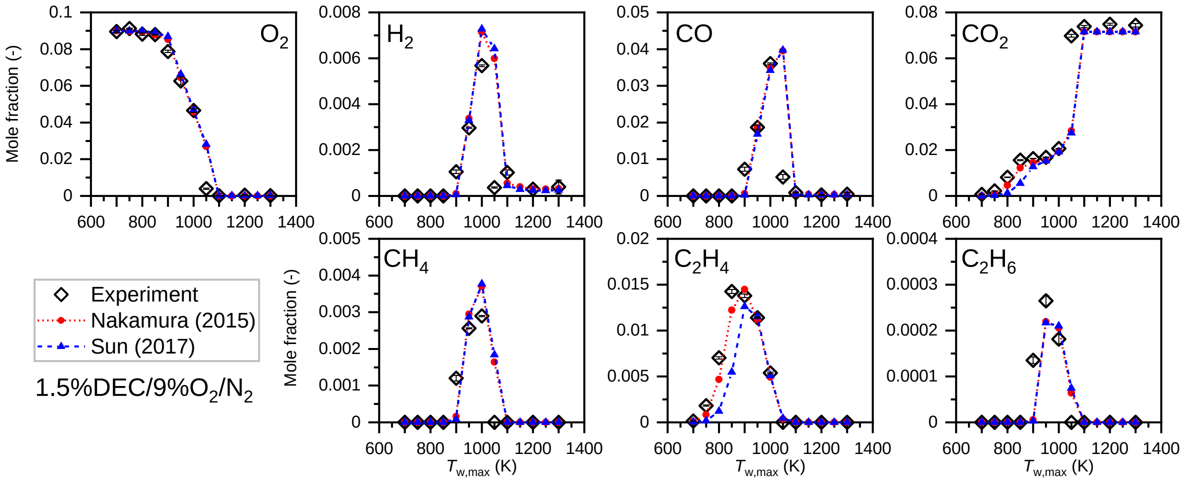

Figure 3.12 Measured and computed mole fractions of O_2, H_2, CO, CO_2, CH_4, C_2H_4 and C_2H_6 for a stoichiometric 1.5%DEC/9.0%O_2/N_2 mixture at $T_{w,max}$ = 700–1300 K under atmospheric pressure.

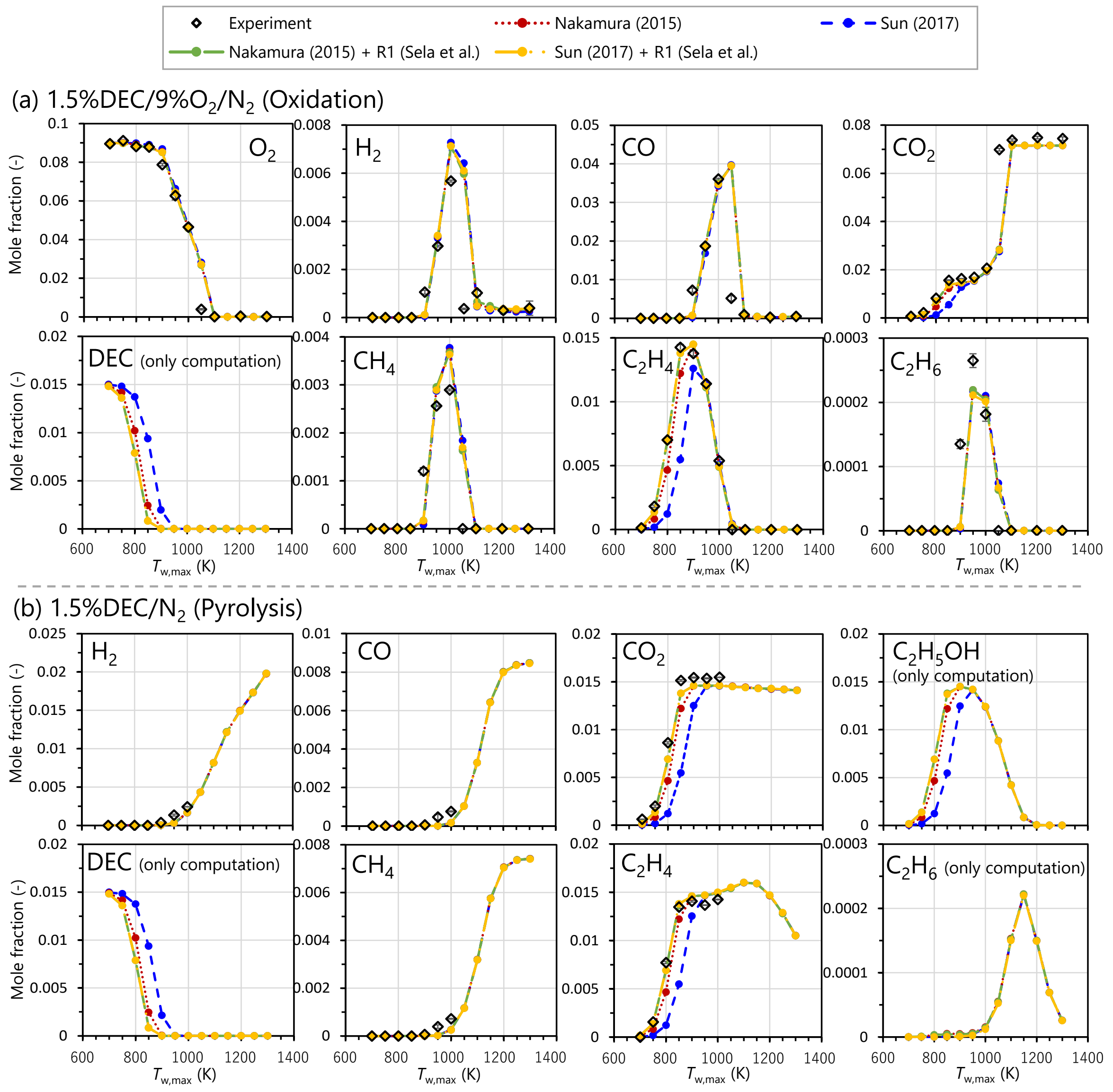

Figure 3.13 Trial computations for (a) 1.5%DEC/9%O_2/N_2 oxidation and (b) 1.5%DEC/N_2 pyrolysis adopting the theoretical rate constant of R3-1 reported by Sela et al. [136] to Nakamura (2015) model and Sun (2017) model. Computational results: original Nakamura (2015) model (red), original Sun (2017) model (blue), modified Nakamura (2015) model (green), and modified Sun (2017) model (yellow).

3.4.2.3 EMC oxidation

Experimental and computational mole fractions of O_2, H_2, CO, CO_2, CH_4, C_2H_4, C_2H_6 for a stoichiometric 1.5%EMC/6.8%O_2/N_2 mixture are shown in Figure 3.14. Experimental results are discussed first, followed by a comparison of the experimental and computational results.

O_2, H_2, CO, CO_2, CH_4, and C_2H_4 were quantitatively detected, while C_2H_6 was not detected (below 100 ppm) in the EMC oxidation. The measured O_2 mole fraction hardly decreases at the low-temperature region (below $T_{\mathrm{w,max}}$ = 850 K), starts decreasing at around $T_{\mathrm{w,max}}$ = 900–950 K and is fully consumed at around $T_{\mathrm{w,max}}$ = 1050–1000 K. The measured H_2, CO and CH_4 mole fractions starts increasing at $T_{\mathrm{w,max}}$ = 900–950 K, having a peak at around $T_{\mathrm{w,max}}$ = 1000 K. The measured CO_2 and C_2H_4 mole fractions, on the other hand, increase at the low-temperature region ($T_{\mathrm{w,max}}$ = 750–850 K) where the measured O_2 mole fraction remains constant of 0.068. The increase in the measured CO_2 mole fraction gets gradual at $T_{\mathrm{w,max}}$ = 850–1000 K, followed by a second rapid increase at $T_{\mathrm{w,max}}$ = 1000–1050 K. The conversion of EMC to CO_2 at the high-temperature region ($T_{\mathrm{w,max}}$ = 1050–1300 K) was about 100%. The measured C_2H_4 mole fraction has a peak at around $T_{\mathrm{w,max}}$ = 850–900 K where the values are approximately 0.013, roughly the same to the input EMC mole fraction.

The computational results using the Takahashi (2022) model reproduce the measured species mole fractions well. Based on reaction analysis, a dominant reaction for the consumption of EMC in the oxidation conditions was found to be unimolecular decomposition of EMC producing C_2H_4 and MFA, EMC = MFA + C_2H_4 (R3-5), being the same to that in the pyrolysis conditions. As MFA rapidly decomposes to CH_3OH and CO_2 by MFA => CH_3OH + CO_2 (R3-6) [148], the EMC thermal decomposition is responsible for the increase in C_2H_4 mole fraction accompanied by the first increase in CO_2 mole fraction at the low-temperature region ($T_{\mathrm{w,max}}$ = 750–850 K). The second increase in CO_2 mole fraction is caused by the completion of CO to CO_2 oxidation. The computed C_2H_6 mole fraction shows a peak at around $T_{\mathrm{w,max}}$ = 1000 K but the peak value is less than 100 ppm, reasonably explaining the experimental observation.

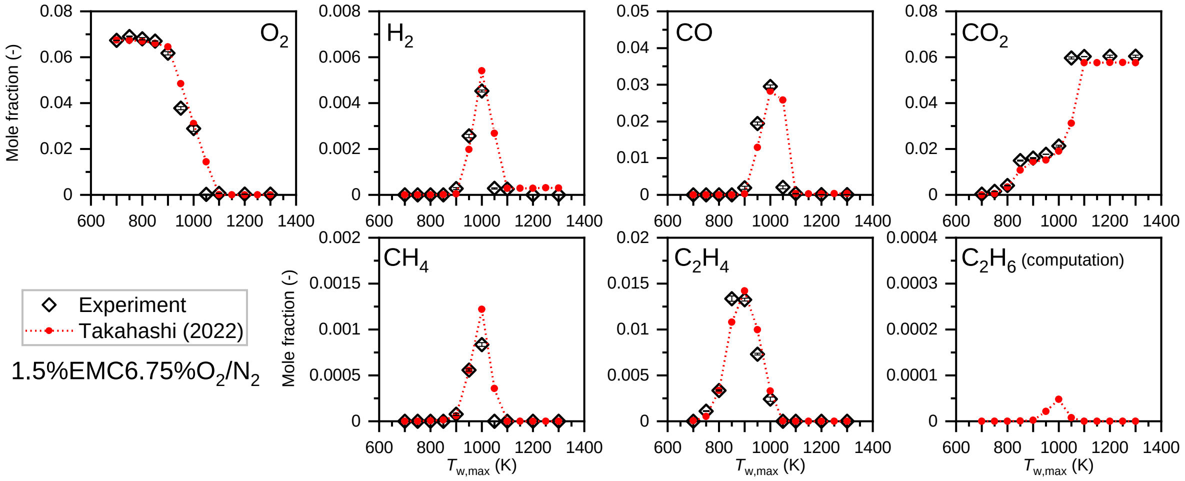

Figure 3.14 Measured and computed mole fractions of O_2, H_2, CO, CO_2, CH_4, C_2H_4 and C_2H_6 for a stoichiometric 1.5%EMC/6.75%O_2/N_2 mixture at $T_{w,max}$ = 700–1300 K under atmospheric pressure. Computed mole fractions of C_2H_6 are also shown.

3.4.2.4 Comparison between DMC, DEC and EMC oxidation

Figure 3.15 presents the comparison among oxidation of DMC, DEC and EMC. Similar to the pyrolysis case in MFR (Section 3.4.1.4), the oxidation characteristics can be classified to DMC and DEC/EMC. DMC oxidation reactions become significant above $T_{w,max}$ = 1000 K where the decrease in O_2 mole fraction and increases in the measured intermediates and products initiate. The DMC oxidation completes at around $T_{w,max}$ = 1150 K by accounting for the CO_2 mole fraction profile. DEC and EMC oxidation is initiated by the two-step unimolecular decomposition reactions producing C_2H_4, CO_2 and alcohols, i.e., C_2H_5OH and CH_3OH, respectively, at the lower-temperature region ($T_{w,max}$ = 750–850 K) as compared to DMC oxidation. The subsequent reactions, however, seem to be dominant above $T_{w,max}$ = 900 K where the measured intermediates increase and peak in their mole fractions, followed by the completion of CO to CO_2 oxidation at around $T_{w,max}$ = 1050 K in both DEC and EMC cases. A plateau, thus, appears in the CO_2 mole fraction at the temperature range in between, i.e., $T_{w,max}$ = 850–1000 K, resulting in the two-step CO_2 increase and a less difference in the temperature where oxidation completes compared with DMC. The two-step increase in the measured CO_2 mole fraction also appears in the DMC case at around $T_{w,max}$ = 1050 K, before

CO to CO_2 oxidation completes, although the plateau is much shorter than that observed in DEC and EMC. Based on the rate of CO_2 production analysis performed for the DMC oxidation at $T_{w,max}$ = 1050 K case, CO_2 was found to be produced by the DMC thermal decomposition, DMC = DME + CO_2 (R3-7), at this temperature range.

(a) 1.5%DMC/4.5%O_2/N_2

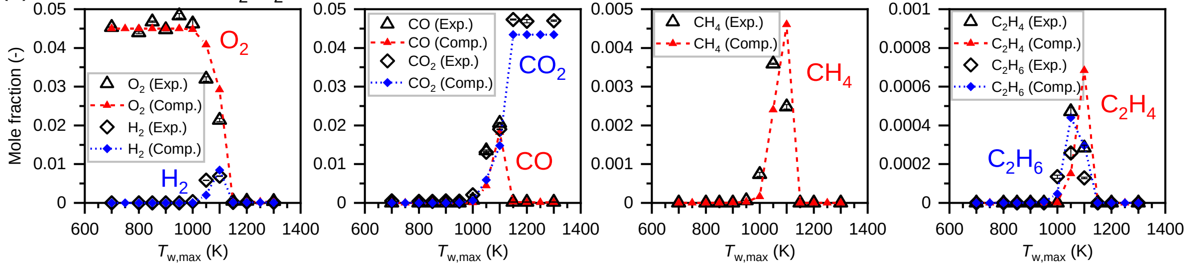

(b) 1.5%DEC/9%O_2/N_2

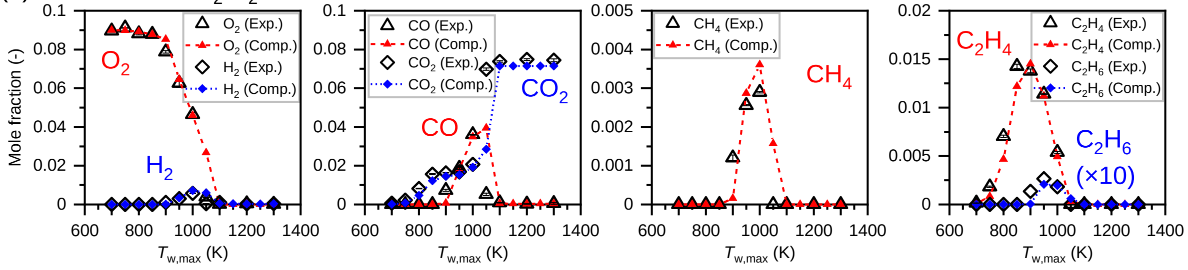

(c) 1.5%EMC/6.75%O_2/N_2

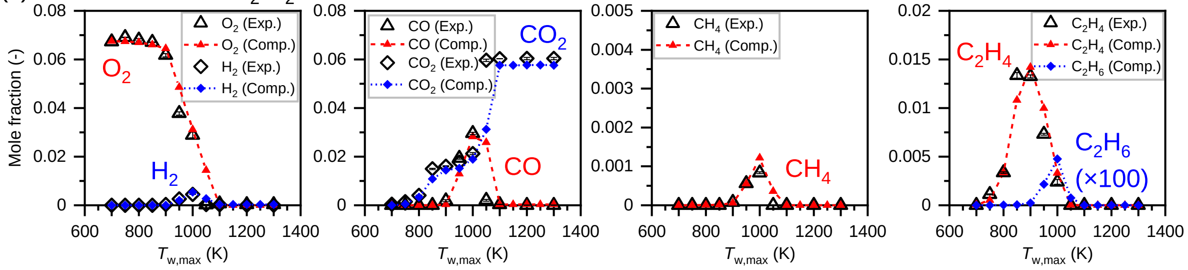

Figure 3.15 Measured and computed mole fractions of O_2, H_2, CO, CO_2, CH_4, C_2H_4 and C_2H_6 for stoichiometric (a) 1.5%DMC/4.5%O_2/N_2, (b) 1.5%DEC/9.0%O_2/N_2 and (c) 1.5%EMC/6.75%O_2/N_2 mixtures at $T_{w,max}$ = 700–1300 K under atmospheric pressure. Computational results are those using Takahashi model [47].

3.4.3 Weak flame observations of DMC, DEC and EMC

3.4.3.1 Gas-phase reactivities of DMC, DEC and EMC

To evaluate gas-phase reactivities of DMC, DEC and EMC, weak flames of the three carbonate esters were observed. The experimentally observed weak flame images and their normalized luminosity profiles are shown in Figure 3.16. The weak flame position of DMC locates downstream (higher-temperature) side and those of EMC and DEC locate upstream (lower-temperature) side at 1187 K, 1128 K and 1123 K, respectively. The comparison of the weak flame positions, therefore, indicates that gas-phase reactivities of EMC and DEC are equally higher than that of DMC. From a viewpoint of the molecular structure, their reactivity can be classified by whether it consists of an ethyl (or ethyl ester) group.

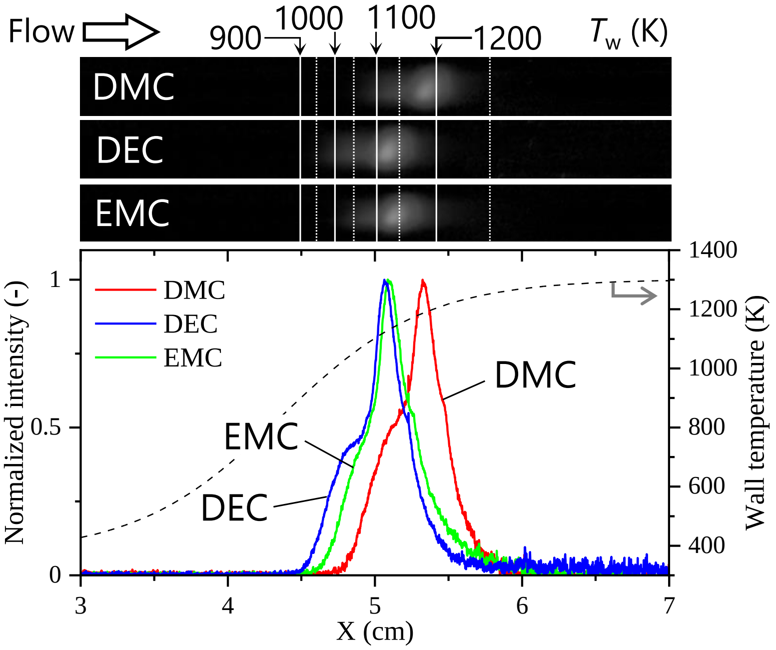

Figure 3.16 Experimental weak flame images and normalized luminosity profiles of stoichiometric DMC/air, DEC/air and EMC/air mixtures at U_{in} = 2 cm/s, $T_{w,max}$ = 1300 K and atmospheric pressure.

The experimental weak flames of DMC and DEC are compared with computational results using models from the literature. The computational result of EMC is shown in the next part, and only the results of DMC and DEC are discussed here. Figure 3.17 shows the experimental luminosity profiles and the computational HRR profiles for stoichiometric DMC/air and DEC/air mixtures. Computational weak flame positions of DMC performed with Sun (2016) and Alexandrino (2018) models agree with the experimental results well, while those performed with Glaude (2005) and Hu (2015) models locate at lower temperatures than the experimental weak flame position, i.e., overpredicting the DMC reactivity. Computational weak flame positions of DEC performed with both Nakamura (2015) and Sun (2017) models predict the experimental weak flame position well. Both computational results of DEC show a negative HRR region at around T_w = 800–950 K (x = 4.3–4.6 cm). At this region, the endothermic reaction is caused by thermal decomposition reactions of the fuel. The relative weak flame positions of the computational results of DMC (Sun (2016) and Alexandrino (2018) models) and DEC (Nakamura (2015) and Sun (2017) models) qualitatively reproduce the experimental tendency, i.e., higher reactivity of DEC than DMC. Based on the results of species measurements as well as weak flame observations, Alexandrino (2018) model and Nakamura (2015) model predict the experimental results of respectively DMC and DEC well among the models. The difference in the reactivity of DMC and DEC is further examined using these two chemical kinetic models.

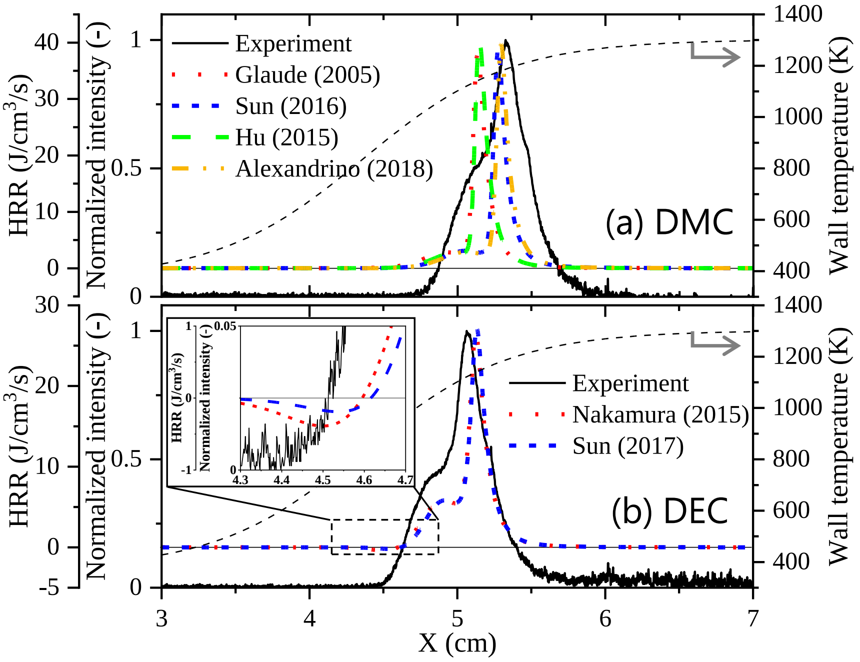

Figure 3.17 Normalized experimental luminosity and computational HRR profiles of stoichiometric (a) DMC/air and (b) DEC/air mixtures at U_{in} = 2 cm/s, $T_{w,max}$ = 1300 K and atmospheric pressure. Computations were performed with: (a) Glaude (2005) [42] (red), Hu (2015) [43] (green), Sun (2016) [44] (blue) and Alexandrino (2018) [127] (yellow) models; (b) Nakamura (2015) [45] (red) and Sun (2017) [46] (blue) models.

3.4.3.2 Multi-stage reactions of DMC, DEC and EMC

Figure 3.18 shows a comparison of the weak flame luminosity and HRR profiles among the three linear carbonate esters. The computational results of Alexandrino (2018), Nakamura (2015) and Takahashi (2022) models are shown. EMC also shows the negative HRR at the similar temperature region to DEC. The computational weak flame position of EMC is in agreement with the experimental result. As the DEC and EMC weak flame structures and their dominant reactions were analogues to each other, discussion hereafter will be given mainly focusing on DMC and DEC.

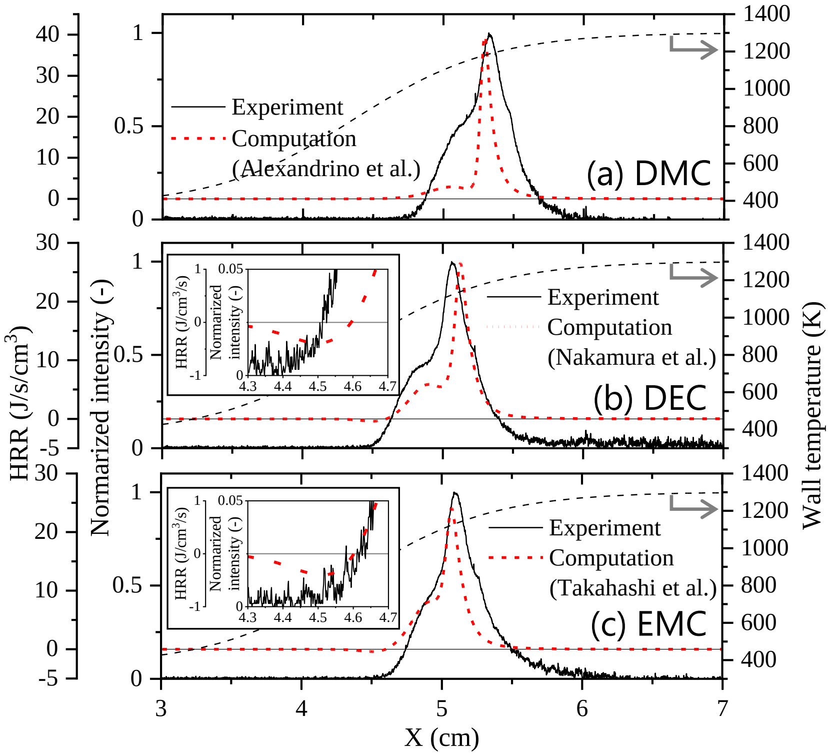

Figure 3.18 Normalized experimental luminosity and computational HRR profiles of stoichiometric (a) DMC/air, (b) DEC/air and (c) EMC/air mixtures at U_{in} = 2 cm/s, $T_{\mathrm{w,max}}$ = 1300 K and atmospheric pressure. Computations were performed with (a) Alexandrino (2018) [127], (b) Nakamura (2015) [45] and (c) Takahashi (2022) [47] models.

Flame structures of the DMC, DEC and EMC weak flames are analyzed to compare species profiles between the two carbonate esters. Figure 3.19 shows the computational profiles of the major species and HRR for stoichiometric DMC/air mixture (Alexandrino

(2018) model), DEC/air mixture (Nakamura (2015) model) and EMC/air mixture (Takahashi (2022) model) at $T_{\mathrm{w,max}}$ = 1300 K. HRR profile of DMC shows a two-stage reaction that involves a small hill followed by the large peak, while that of DEC shows a three-stage reaction that additionally involves the negative HRR region at low temperatures (T_{w} = 800–950 K, x = 4.3–4.6 cm). According to the species profile, consumption of DEC initiates at lower temperature than that of DMC, e.g., the T_{w} where 30% of fuel are consumed is approximately at 1030 K in the DMC case and 830 K in the DEC case. In the DMC case, the DMC mole fraction hardly decreases at low temperatures (below T_{w} = 950 K, x = 4.6 cm), and the consumption becomes significant at intermediate temperatures (T_{w} = 950–1100 K, x = 4.6–5.0 cm). Peaks of CO and CH_4 mole fractions appear in a region between intermediate to high temperatures (approximately x = 5.0 cm) followed by the HRR peak and completion of the oxidation at high temperatures (above T_{w} = 1100 K, x = 5.0 cm). In the DEC case, the consumption of DEC proceeds at x = 4.3–4.6 (T_{w} = 800–950 K), which corresponds to the negative HRR region. The C_2H_4 mole fraction peaks and CO_2 mole fraction shows a first increase in this low-temperature region (below T_{w} = 950 K, x = 4.6 cm). Thus, the DEC thermal decomposition reactions, which are endothermic reactions, are likely to occur in the low-temperature region. In the following intermediate temperature region (T_{w} = 950–1100 K, x = 4.6–5.0 cm), HRR turns to positive and CO mole fraction shows a peak. With the further increase in the temperature (above T_{w} = 1100 K, x = 5.0 cm), HRR shows the peak, and the CO_2 mole fraction shows a second increase with a simultaneous decrease in the CO mole fraction. Based on the computational weak flame structure, the three-stage reaction initiated by the thermal decomposition, followed by oxidation of decomposition products to CO and CO oxidation to CO_2, is observed in the DEC oxidation. This three-stage reaction is distinct from the three-stage oxidation driven by LTO observed in earlier studies with such as *n*-heptane and DME [67,68]. There is a remarkable difference in fuel consumption of DMC and DEC/EMC, which is driven by the differences in primary fuel consumption reactions depending on the molecular structures. The weak flame structural characteristics of DMC, DEC and EMC also can be differentiated between DMC and DEC/EMC, according to their molecular structures.

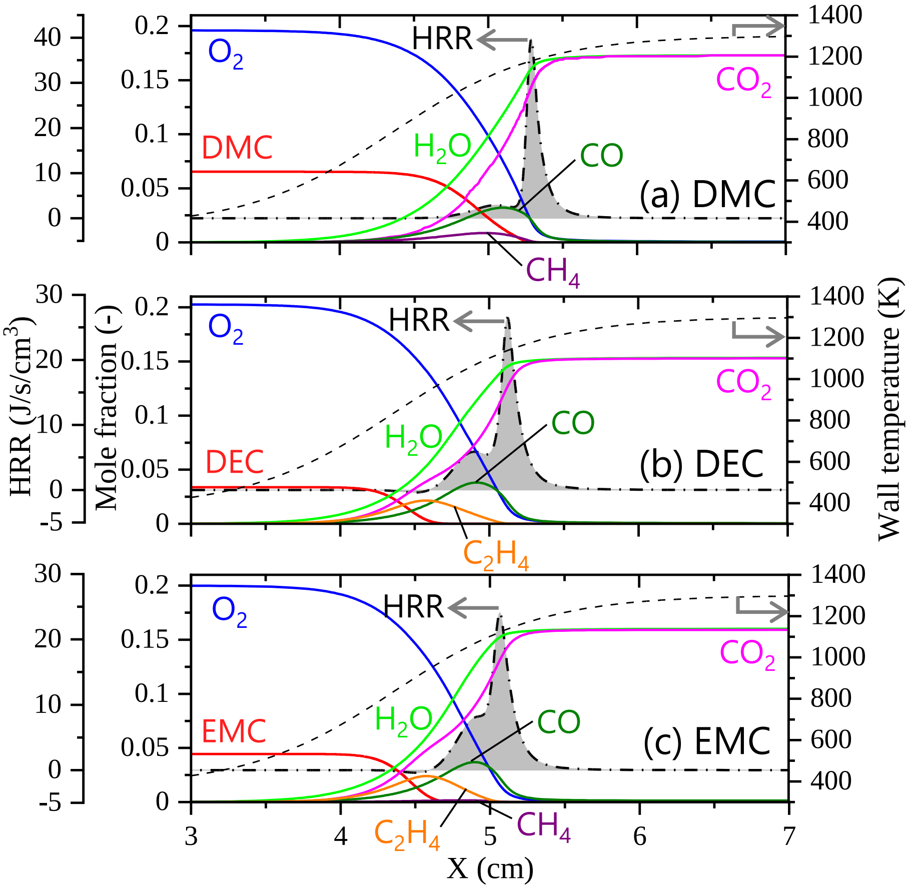

Figure 3.19 Flame structures of stoichiometric (a) DMC/air, (b) DEC/air and (c) EMC/air weak flames at U_{in} = 2 cm/s, $T_{w,max}$ = 1300 K and atmospheric pressure. Computations were performed with (a) Alexandrino (2018) [127], (b) Nakamura (2015) [45] and (c) Takahashi (2022) [47] models.

Rate of production analysis is conducted for DMC and DEC consumption aiming to identify their dominant reactions at the initial stage of oxidation. Figure 3.20 shows top 3 reactions in the rate of fuel consumption reactions of a DMC/air mixture (Alexandrino (2018) model) and a DEC/air mixture (Nakamura (2015) model). In both DMC and DEC cases, major fuel consumption reactions are found to be H-atom abstraction reactions with H and OH radicals and unimolecular decomposition reactions. In the DMC case, the H-atom abstraction reactions are preferred, while a thermal decomposition reaction, CO_2 elimination reaction (R3-7), shows less contribution to DMC consumption. On contrary, in the DEC case, the thermal decomposition reaction (R3-1) that produces EFA and C_2H_4 is dominant, while the H-atom abstraction reactions show little contribution to DEC consumption. The unimolecular CO_2 elimination reactions from fuel is a characteristic reaction pathway for esters [42,141] due to the presence of an ester [—C(=O)O—] group. The CO_2 elimination reaction is more significant than other unimolecular decomposition reactions in the DMC case. Fuels that involve ethyl esters, however, are known to be preferably decomposed into C_2H_4 and the rest moiety of the fuel [154,155], and this reaction also plays an important role in the DEC as well as EMC oxidation cases. The difference in the fuel consumption reactions governing the initial stage of oxidation is a primary factor that leads to the difference in the gas-phase reactivity between DMC and DEC/EMC.

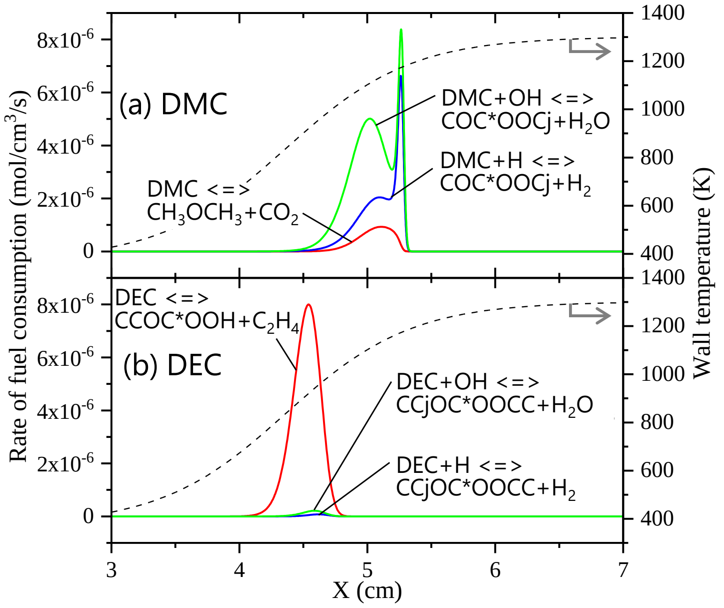

Figure 3.20 Top 3 reactions from rate of fuel consumption reactions for stoichiometric (a) DMC/air computed with Alexandrino (2018) model [127] and (b) DEC/air computed with Nakamura (2015) model [45] at U_{in} = 2 cm/s, $T_{w,max}$ = 1300 K and atmospheric pressure. Fuel decomposition reactions (red lines) and H-atom abstraction reactions (blue lines: fuel + H reactions; green lines: fuel + OH reactions). "*": double bond; "j": radical site on the preceding carbon atom.

3.4.4 Reaction pathways of DMC, DEC and EMC oxidation

Reaction path analyses for DMC, DEC and EMC oxidation were performed to obtain an overview of their oxidation mechanisms. Figure 3.21 shows major reaction pathways of DMC/air, DEC/air and EMC/air mixtures at low- and intermediate-temperature conditions (T_w = 830 K and 1030 K, respectively). In the DMC case, although fuel consumption reactions hardly proceed at the low-temperature condition (T_w = 830 K), reactions to CO production via C_1 pathway rapidly proceed once DMC is consumed at T_w = 1030 K. In the DEC case, the major intermediates and final product, C_2H_5OH, C_2H_4 and CO_2, are produced by the thermal decomposition of DEC at low temperature (T_w = 830 K), but the decomposition products are relatively stable and few active radicals are produced. Even though there is a radical loop that consumes O_2 and produces H_2O_2 via HO_2 by two-step reactions from C_2H_5OH to CH_3CHO, its enhancement in the oxidation is still very weak at low temperatures. A previous study on the comparison of reactivity of *n*-alkene fuels using MFR [69] indicated a higher reactivity of C_2H_4 than the other *n*-alkene fuels due to its radical loop enhancement on reactivity at around 1000 K, which consumes H radicals and produces HO_2 radicals between C_2H_4 and C_2H_5, leading to a large amount of OH radical production via H_2O_2. This radical loop appears at the intermediate-temperature condition (T_w = 1030 K) in the DEC case as well. Nevertheless, little radical production at low temperatures results in a temperature gap between the fuel consumption and the subsequent reaction regions. The same explanation can be applied to EMC oxidation although a major intermediate differs from DEC, i.e., CH_3OH instead of C_2H_5OH. From the comparison of gas-phase reactivity of three carbonate esters, the reactivity of DEC and EMC are found to be higher than that of DMC, being classified by whether the fuel molecular structure consists of an ethyl (ester) group. The primary difference in their reactivity is driven by the fuel consumption reactions resulting from the difference in the fuel molecular structure, i.e., the H-atom abstraction reactions for DMC and the thermal decomposition reaction that produces C_2H_4 and the rest moiety for DEC and EMC.

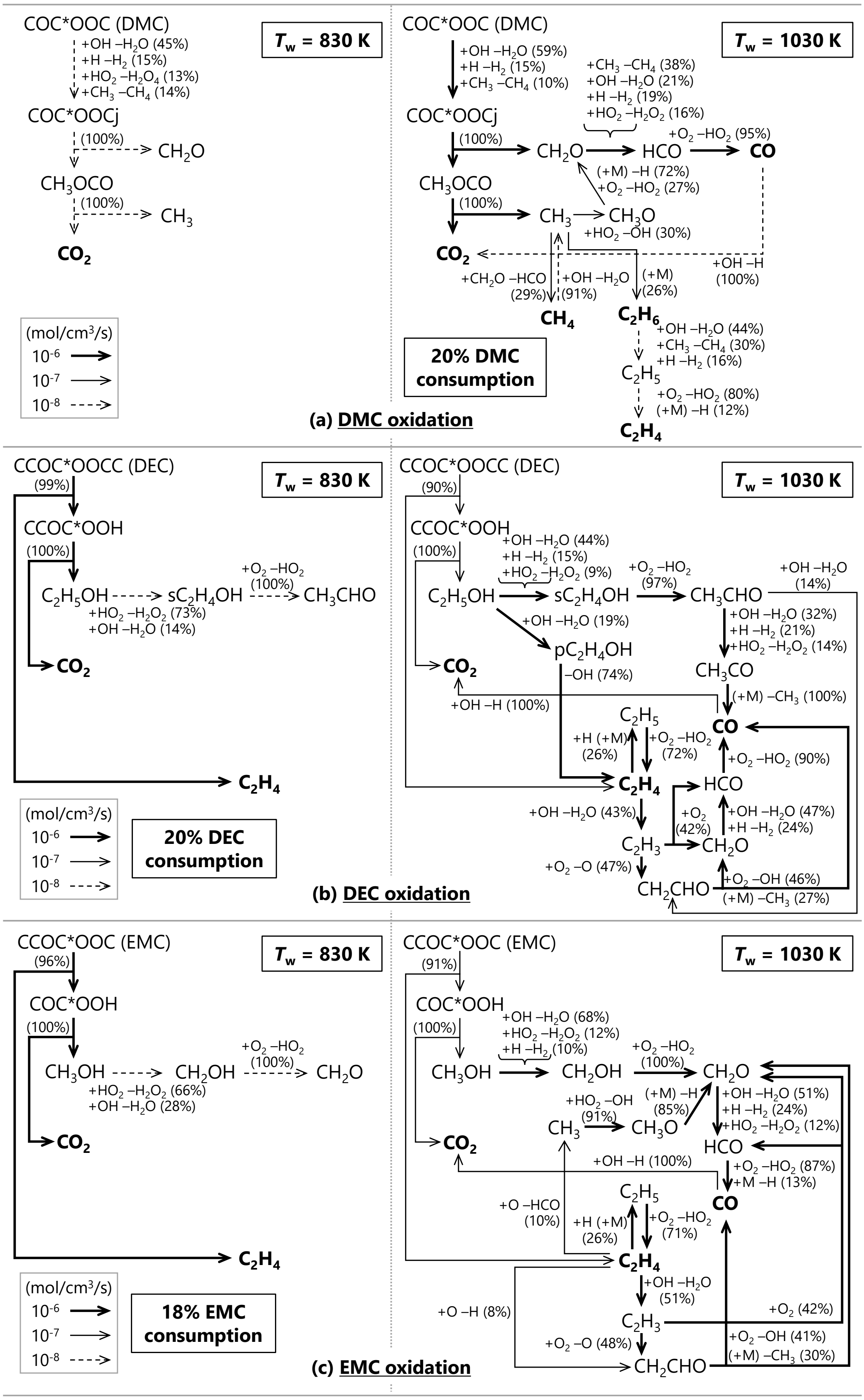

Figure 3.21 Reaction pathways of (a) DMC, (b) DEC and (c) EMC oxidation in air at ϕ = 1.0, T_w = 830 and 1030 K in the case of $T_{w,max}$ = 1300 K. Measured species are shown in bold. Flux analyses were performed with (a) Alexandrino (2018) [127], (b) Nakamura (2015) [45] and (c) Takahashi (2022) [47] models.

3.5 Conclusions

Pyrolysis and oxidation characteristics of dimethyl carbonate (DMC), diethyl carbonate (DEC) and ethyl methyl carbonate (EMC) were investigated using a micro flow reactor with a controlled temperature profile (MFR). Species measurements for oxidation and pyrolysis of DMC, DEC and EMC were performed by gas chromatography at various maximum wall temperature conditions ($T_{\mathrm{w,max}}$ = 700–1300 K) and atmospheric pressure. Gas-phase reactivities of the three liner carbonate esters were examined by weak flame observations. Major differences in the reaction mechanisms of DMC, DEC and EMC are illustrated in Figure 3.22.

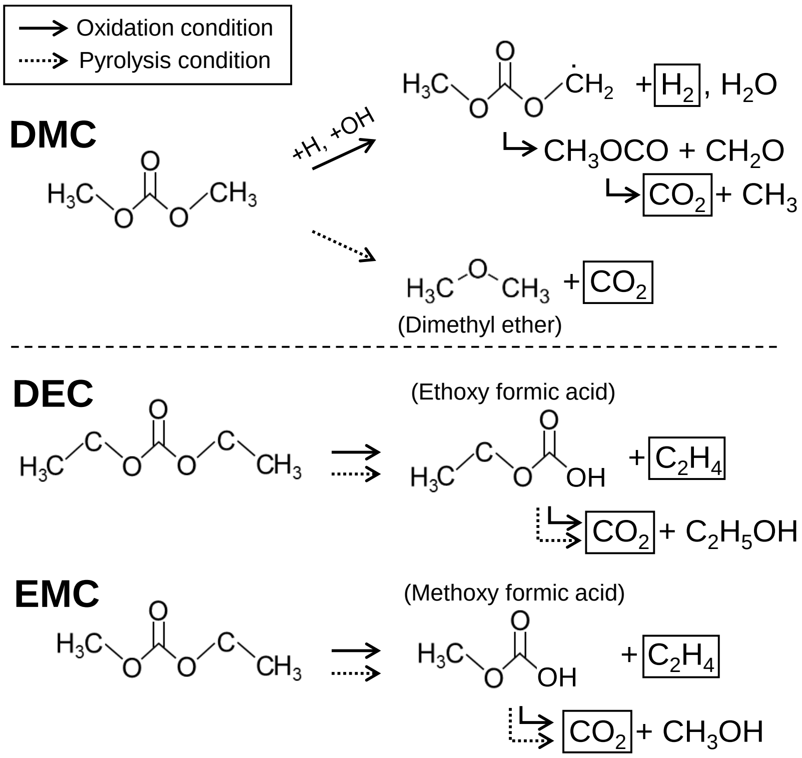

Figure 3.22 Schematic of dominant initial reaction pathways for DMC, DEC and EMC pyrolysis and oxidation. Species shown in the box are measured in the experiment.

From the results of species measurements for DMC oxidation case, production of H_2 and CH_4 became significant at $T_{\mathrm{w,max}}$ = 1000 K, followed by a relatively rapid CO production and the subsequent decrease, which corresponds to the completion of CO to CO_2 oxidation. In the

DEC case, production of CO_2, directly derived from the DEC decomposition due to the existence of ester/carbonate group in its molecular structure, is initiated at low-temperature region (around $T_{w,max}$ = 750 K) in both oxidation and pyrolysis conditions. In addition to the CO_2 production, C_2H_4 was produced at the low-temperature region, indicating that the thermal decomposition reaction of DEC producing CO_2, C_2H_4 and C_2H_5OH is favorably occurred even at the oxidation condition. The measured CO_2 mole fraction in DEC case, once showed a plateau between $T_{w,max}$ = 850–1000 K followed by the second dramatic increase. The second increase in CO_2 mole fraction that corresponded to the completion of oxidation through CO to CO_2 occurred at an intermediate-temperature region (around $T_{w,max}$ = 1000 K). Although fuel consumption of DEC seemed to proceed from lower temperature than DMC, the difference in temperature of the completion of oxidation was much less than that of the initiation of fuel consumption. The similar explanation to DEC can be applied to the EMC cases.

Weak flames of DEC and EMC located at almost same T_w, which was lower than that of DMC, indicating that the gas-phase reactivities of the three carbonate esters are DMC $<$ DEC $\approx$ EMC. The reactivity can be thus classified by whether the molecular structure involves the ethyl (or ethyl ester) group. Computational HRR profile of DMC showed a two-stage reaction, whereas that of DEC and EMC showed a three-stage reaction that was initiated with a negative HRR at low temperatures (T_w = 800–950 K). The three-stage reaction is driven by thermal decomposition and is distinct from the one driven by low-temperature oxidation (LTO) observed for *n*-heptane and dimethyl ether in the earlier studies. Based on rate of production analysis, dominant fuel consumption reactions were H-atom abstraction reactions with H and OH radicals in DMC oxidation, while the thermal decomposition reactions producing C_2H_4 and the rest moiety were dominant in DEC and EMC oxidation (ethoxy formic acid (EFA) and methoxy formic acid (MFA), respectively). The difference in the fuel consumption reactions resulted in faster DEC and EMC consumption at low temperatures than DMC. Major reaction pathways in DEC as well as EMC oxidation, however, have little advantage in promoting oxidation at the low-temperature region because the subsequent unimolecular decomposition reactions produce relatively stable species (CO_2, C_2H_4 and C_2H_5OH/CH_3OH) and few reactive radicals. The difference in reactivity of DMC and DEC/EMC largely relies on the initial fuel consumption reactions, which reflect the difference in the molecular structure.

Chapter 3 based on:

K. Kanayama, S. Takahashi, S. Morikura, H. Nakamura, T. Tezuka and K. Maruta, Study on oxidation and pyrolysis of carbonate esters using a micro flow reactor with a controlled temperature profile. Part I: Reactivities of dimethyl carbonate, ethyl methyl carbonate and diethyl carbonate, *Combust. Flame* 237 (2022) 111810.

S. Takahashi, **K. Kanayama**, S. Morikura, H. Nakamura, T. Tezuka and K. Maruta, Study on oxidation and pyrolysis of carbonate esters using a micro flow reactor with a controlled temperature profile. Part II: Chemical kinetic modeling of ethyl methyl carbonate, *Combust. Flame* 238 (2022) 111878.

Chapter 4

Pyrolysis and oxidation of ethylene carbonate

This chapter is dedicated to the understanding of pyrolysis and oxidation characteristics of the cyclic carbonate ester, ethylene carbonate (EC), as well as the development of the first chemical kinetic model of EC using a MFR and shock tube. A model involving both the linear and cyclic carbonate esters, i.e., DMC, DEC, EMC and EC, named “LIB electrolyte surrogate model” is constructed. In addition to speciation data of EC pyrolysis and oxidation, global combustion properties (ignition delay times and laminar flame speeds) of EC mixtures are also obtained.

4.1 Introduction

Understanding and modeling a series of LIB fire mechanisms is crucial from the fire safety aspect, especially for implementation of the larger-scale applications. Zhang et al. [156] demonstrated a thermal runaway simulation of a LIB to identify its safe-limit by varying heat source temperature and duration assumed as internal short circuit induction parameters, but without considering chemical reactions. Cellier et al. [157] performed a large eddy simulation for a forced ignition of vented gases from a LIB cell using a reduced chemical kinetic model, assuming that the electrolyte components are not in the vent gases in vapor phase but are already decomposed into smaller flammable molecules (H_2, CO, CO_2, and C_1–C_3 hydrocarbons). Motivated by the LIB fire risk under the situation where the vaporized electrolytes and partially reacted gases exist (Figure 1.6), the present study focuses on gas-phase chemistry of electrolyte solvents. A comprehensive gas-phase chemical kinetic model of LIB electrolytes is necessary not only to enhance the abovementioned simulations but also to understand the role of the vaporized electrolytes during LIB fires.

Ethylene carbonate (EC), a cyclic carbonate ester, is an important chemical component of the electrolytes used in LIBs, as shown in Figure 4.1. EC has a large dielectric constant, which facilitates the dissociation of lithium salts [23,158]. EC also helps to create an effective solid electrolyte interphase that prevents solvents from decomposing on the graphite anode [159]. Meanwhile, due to the high viscosity of EC (1.9 mPa s at 313 K [158]), linear carbonate esters, such as dimethyl carbonate (DMC), ethyl methyl carbonate (EMC) and diethyl carbonate (DEC), are blended as electrolyte solvents for practical use. Typical compositions of commercially available lithium hexafluorophosphate ($LiPF_6$)-based LIB electrolytes are listed Table 1.1. Since carbonate esters are flammable and are considered as a potential fire cause of LIB fires [22], their pyrolysis and combustion data is important to understand the reaction mechanisms and to construct the comprehensive LIB electrolyte model.

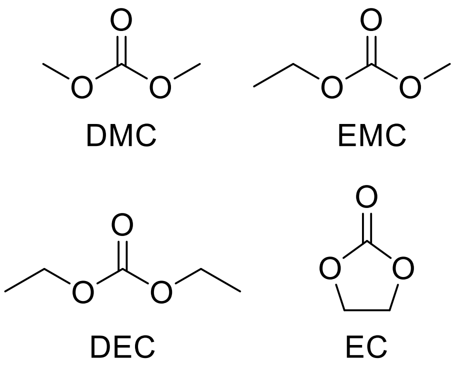

Figure 4.1 Molecular structures of linear and cyclic carbonate esters widely used in LIB electrolytes. Dimethyl carbonate (DMC), ethyl methyl carbonate (EMC), diethyl carbonate (DEC), and ethylene carbonate (EC).

Pyrolysis and combustion characteristics as well as chemical kinetic models for the linear carbonate esters (DMC, DEC and EMC) have been studied (see Chapter 3). However, there have been few reported studies on the cyclic carbonate ester, EC, up to date. A density functional theory (DFT) calculation for the decomposition of the EC radical cation performed at the B3LYP/6-311++G(d,p) level by Xing et al. [160] suggested that the most probable reaction would be CO_2 formation pathways. The CO_2 formation is a typical decomposition channel for carbonate esters, e.g., dialkyl carbonate esters produce ether and CO_2, although its mechanism might differ for linear and cyclic carbonate esters. Only recently, CO laser absorption measurements for neat EC pyrolysis were successfully performed using a shock tube at near-atmospheric pressure by Grégoire et al. [161].

The goal of this chapter is to obtain the experimental data of EC pyrolysis and oxidation using a micro flow reactor with a controlled temperature profile (MFR), a shock tube and a closed combustion vessel, and to propose a detailed chemical kinetic model of EC that also includes the linear carbonate esters (DMC, EMC and DEC), named as "LIB electrolyte surrogate model". First, for EC pyrolysis, unimolecular decomposition of EC is theoretically investigated by quantum chemical calculations. Then, pyrolysis characteristics of an EC/DMC mixture are experimentally investigated by species measurements using a time-of-flight mass spectrometer (TOF-MS) and a gas chromatograph (GC) connected to MFR. For EC oxidation, the ignition delay time and CO laser absorption measurements are conducted using a shock tube. Laminar flame speed measurements are performed for H_2/air mixtures seeded with EC. The first LIB electrolyte surrogate model is constructed and validated with the experimental data. Further numerical analyses are performed, especially to reveal the reaction mechanisms of EC pyrolysis and oxidation.

4.2 Experimental and computational methods

The MFR experiments were conducted at Tohoku University (TU) and the shock tube and flame speed experiments were performed at Texas A&M University (TAMU) in collaboration with the Turbo Machinery Laboratory.

4.2.1 MFR experiments and computations for EC/DMC pyrolysis

A MFR was employed to perform the species measurements and one-dimensional computations for the pyrolysis of an EC/DMC mixture. DMC was used as a solvent for EC because of the difficulty in the mixture preparation of neat EC due to its very low vapor pressure, which is in a solid state at room temperature and atmospheric pressure. And also, because the DMC pyrolysis was found to be initiated at relatively high temperatures as compared to the DEC and EMC pyrolysis [47,134] (Chapter 3). This DMC pyrolysis characteristic is expected to suppress the chemical and analytical interference to the EC pyrolysis caused by decomposition products from the solvents. In this regard, although the experiment is not for a neat EC pyrolysis, EC chemistry could be investigated and more importantly, the newly constructed EC pyrolysis sub-model (see Section 4.3.2) could be validated. The MFR system has been successfully employed to examine the pyrolysis and oxidation characteristics of the linear carbonate esters, DMC, DEC and EMC, and for the model construction and validation in the previous chapter [47,134]. Details of the experimental advantages and computational validity of MFR as well as the methods have already been described (Section 2.1 and Section 3.2), thus brief descriptions are given here.

Species measurements were conducted using TOF-MS and GC connected to a MFR. A schematic of the experimental setup is presented in Figure 4.2. A quartz tube (2 mm inner diameter, 4 mm outer diameter, 80 mm length) whose inner diameter is smaller than the ordinary quenching diameter was used as the reactor channel. An electric heater was used as an external heat source to form a stationary temperature profile on the inner wall surface of the reactor. Owing to the nature of the MFR, the small Peclet number, the gas temperature in the reactor is strongly governed by the wall temperature (T_w). The maximum wall temperature ($T_{w,max}$) was varied between 700–1200 K. The T_w profiles were measured by a K-type thermocouple inserted from the downstream side of the reactor. The measured T_w profiles are presented in Figure 3.3. The uncertainty in T_w was estimated to be $\pm$ 5 K. EC/DMC liquid (1:1 in liquid volume ratio, i.e., 0.56:0.44 in molar ratio, lithium battery grade, contamination of water $<$ 6.2 ppm, Kishida Chemical Co., Ltd.) was vaporized and mixed with N_2 ($>$ 99.999% pure) in a vacuumed, heated tank (373 K). The mixture ratio of EC/DMC and N_2

was controlled based on the partial pressure method and was set to EC/DMC of 0.2% and N_2 of 99.8% (i.e., 0.112%EC/0.088%DMC/99.8%N_2) in molar ratio. Baratron (628F, MKS Instruments) was used as the manometer. The mixture was supplied to the reactor at the inlet flow velocity of 2.7 cm/s at 373 K, controlled by a high-temperature mass flow controller (HORIBA SEC-8440F). The experimental uncertainty largely relies on the low fuel concentration due to the very low vapor pressure of EC, which is approximately 0.39 kPa at 362 K [162]. The uncertainties in the fuel fraction in the tank were estimated to be ± 5% based on the uncertainty of the pressure measurement. The experiments were conducted at atmospheric pressure. For the TOF-MS measurements, exhaust gases from the downstream exit of the reactor were diverged at the six-way valve and introduced into the TOF-MS. For the GC measurements, the exhaust gases were sampled online and introduced into the GC. To prevent the condensation of the fuels and water vapor, all the lines from the heated tank to the reactor and the sampling line were kept at 373 K.

The carbonate esters (EC and DMC) were measured using TOF-MS. The ionization voltage was set to 70 eV, and the time resolution was 0.5 sec. The signals at *m/z* 88 and 90, molecular ions, were traced for EC and DMC, respectively. EC and DMC were quantified by the absolute calibration method. The uncertainty in the species measurement of EC and DMC was approximately ± 20% and ± 15%, respectively, due to the relatively low signal intensities. Inorganic species (H_2, CO and CO_2) and C_1–C_2 hydrocarbons (CH_4, C_2H_2, C_2H_4 and C_2H_6) were measured using GC equipped with a MICROPACKED-ST column (1.0 mm inner diameter, 3.0 m length, 10 mm film thickness). A TC-BOND U capillary column (0.25 mm inner diameter, 30 m length, 8.0 mm film thickness) was used to measure oxygenates (formaldehyde (CH_2O), acetaldehyde (CH_3CHO) and dimethyl ether (DME)). The sampling volume was set to 500 μl. A dielectric-barrier discharge ionization detector was used, and its temperature was set to 483 K. Helium ($>$ 99.99995% pure) was used as the carrier gas. Standard gases were used for the quantification of the inorganic species, C_1–C_2 hydrocarbons and DME. The measured signal intensities of the aldehydes were normalized by each peak value. The uncertainty in the species measurement with the GC was approximately ± 3%. Experiments were repeated more than three times for each condition, and the errors in the measured mole fractions due to the repetition of species measurements with the TOF-MS or GC are shown in Figure 4.10.

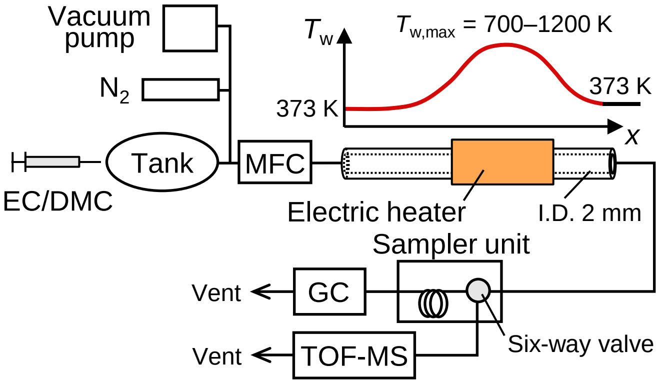

Figure 4.2 Experimental setup of species measurements for EC/DMC pyrolysis using MFR.

The flow field in the MFR at low inlet flow velocity conditions (approximately a few cm/s) can be assumed to be a reactive flow without a boundary layer. The PREMIX code with an additional term in the gas-phase energy equation [51], i.e., a convective heat transfer term between the gas and the reactor inner wall, was used to perform the one-dimensional steady-state computation of MFR. The same conditions in the experiments (mixture composition, inlet flow velocity, T_w profiles and pressure) were applied to the computations. A comparison between the measured T_w profiles and those used in the computations is shown in Figure 3.3 in Chapter 3 (the same T_w-profile as the previous works [47,134]). The computational domain was set to 0–10 cm, and the computational species mole fractions at x = 10 cm were compared with the experimental results. As for the chemical kinetic model, an EC pyrolysis model constructed in the present study, as described in Section 4.3.2 (the EC pyrolysis sub-model + the model for the linear carbonate esters (DMC, DEC and EMC) [47,134]), was used.

4.2.2 Shock-tube experiments and computations for EC oxidation

The oxidation of EC in diluted mixtures was carried out for three equivalence ratios (ϕ = 0.5, 1.0 and 2.0) in a shock-tube at TAMU. Ignition delay time (IDT), a global combustion parameter, and CO time-history profiles were measured. The CO time-history measurement has great advantages to validate a model and to gain kinetics insight into the CO formation, especially for oxygenated fuels as there would be two different CO formation channels, i.e., pyrolysis-derived CO formation and oxidation-derived CO formation. The importance of oxygenate chemistry during the pyrolysis of linear carbonate esters (DMC, EMC and DEC) was discussed in a shock-tube CO laser absorption measurement study by Grégoire et al. [135].

To allow the gas-phase study of a neat EC, a custom-made heating jacket was used to maintain the shock tube at a uniform temperature of between 100°C (CO measurements in 99.7% He/Ar) and 120°C (ignition delay time (IDT) measurements in 95% Ar), avoiding condensation of EC during the experiments. A custom-made heating jacket is also used for the mixing tank, and its temperature was set to 120°C (CO measurements) or 140°C (IDT measurements). In addition, heating elements and fiberglass insulation set at 120°C (CO measurements) or 140°C (IDT measurements) were also applied to the critical experimental components, such as the manifold and the vial containing the solid EC.

To prevent any possible condensation, especially during the mixture preparation, as much as 0.19 kPa of EC was used in the mixture preparation for CO measurements and 0.96 kPa for the IDT measurements, to obtain the fuel-rich mixture (ϕ = 2.0). The heating system ensures that the pressure of EC remained constant and well-below the recorded maximum of 1.5 kPa at 140°C (note that this does not constitute an accurate measurement of the saturating vapor pressure of EC). The mixtures were prepared as follows: the coarsely powdered EC was introduced in a heated vial and degassed multiple times to ensure no unwanted air remained in the mixture. The vaporized EC was then transferred and isolated into the mixture tank via the heated manifold, in which the absence of condensation was verified by vacuuming it to a high vacuum enough and confirming no pressure increase when the vacuum system was turned off. The pressure of EC introduced in the tank was validated by re-opening the tank to the manifold after the vacuuming phase, before continuing with the next gases, namely O_2, (He,) and Ar. Note that due to the difficulty in vaporizing EC, the final mixtures were large enough for a couple of experiments only for IDT measurements. The results presented herein are thus the results of many mixture preparations. The solid EC was purchased from Sigma Aldrich with a purity of 98%, and the gases, O_2, He, Ar, and air (21% O_2 in N_2) were provided by Praxair, all with 99.999% purity.

The study of the chemical kinetics for EC with ignition delay time and CO laser absorption measurements at high temperatures and near atmospheric pressure was performed using a shock tube located at Texas A&M University. This facility consists of a driver section (7.62 cm inner diameter and 3.25 m long) and a driven section (16.2 cm inner diameter and 7.88 m long) separated by a single polycarbonate (0.25 mm thickness) diaphragm. Helium is filled in the driver section until the diaphragm breakage and relaxes towards the low-pressure section, forming a shock wave propagating into the test gas. At the end of the tube, the reflected shock generates an ideal experiment with constant temperature and pressure for about 2 ms. Five PCB P113A22 piezoelectric pressure transducers are placed on the sidewall along the end of the driven section, which allow the measurement of the incident shock wave velocity by detecting the passage of the shock wave. As the last pressure transducer is located very close to the endwall (1.6 cm), the incident velocity can be inferred at the endwall by extrapolation [163]. The post-reflected-shock conditions were calculated using the 1-D normal shock equations (T_5 and P_5) obtained with the initial temperature and pressure conditions, T_1, P_1, the speed of the shock wave, v_s, and the initial mole fractions of the mixtures. The final T_5 and P_5 can be determined within ± 0.8% and ± 1.0%, respectively [164].

A vacuum system, including a vane pump and a turbomolecular pump, enables a pressure of 10^{-5} kPa prior to each experiment to maintain high purity for these experiments. More details on the shock tube can be found in Mathieu et al. [165]. The IDT and CO laser absorption measurements were conducted for temperatures ranging from 1228 to 1717 K and pressures ranging from 0.98 to 1.69 atm for three equivalence ratios ϕ = 0.5, 1.0, and 2.0. Table 4.1 lists the experimental conditions covered during this study. See following parts for more information of the IDT and CO laser absorption measurements.

Table 4.1 Experimental conditions covered during the course of this study for the oxidation of EC in 0.95 Ar for the IDT measurements in 0.997 He/Ar for CO measurements (helium was used to expedite the vibrational relaxation of CO, see [166] for more details).

ϕ	X_{EC}	X_{O2}	X_{He}	X_{Ar}	T_5 (K)	P_5 (atm)
Shock-tube ignition delay time						
0.5	0.0083	0.0417	-	0.9500	1304–1546	1.17–1.52
1.0	0.0143	0.0357	-	0.9500	1228–1587	1.10–1.69
2.0	0.0222	0.0278	-	0.9500	1262–1507	1.04–1.44
Shock-tube CO absorption						
0.5	0.0005	0.0025	0.2000	0.7970	1284–1695	0.98–1.11
1.0	0.0009	0.0021	0.1995	0.7975	1345–1717	1.02–1.06
2.0	0.0013	0.0017	0.2015	0.7955	1303–1704	1.01–1.10

Computations for a shock tube (ignition delay times and CO time-history profiles) were performed using a zero-dimensional homogeneous reactor model in the AURORA package implemented in ANSYS Chemkin-Pro v19 [145]. The initial conditions (mixture composition, temperature and pressure) as well as the definition of ignition delay times (see next part) were the same as the experiments. A LIB electrolyte surrogate model constructed in this study (Section 4.3.3) was used as a chemical kinetic model.

4.2.2.1 *Ignition delay time measurements*

Ignition delay times were measured both at the sidewall location (same location as the CO diagnostic below) and at the endwall of the shock tube. In both cases, pressure and OH* chemiluminescence were measured. At both locations, the OH* chemiluminescence was measured using 307 nm filters with a 10 nm full width at half maximum. At the sidewall location, a 1 mm slit was used along with a concave focusing mirror redirecting the OH* beam path to a Hamamatsu photomultiplier tube in a custom-made housing. A similar photomultiplier was used at the endwall location. Despite the relatively high dilution level used (95% Ar), the experiments exhibited a noticeable increase in pressure at the ignition event. The IDT was thus measured at the endwall location and is defined as the time interval between the detection of the incident shock wave at the endwall location and the time at which the tangent to the maximum slope of the OH* signal crosses the baseline, as shown in Figure 4.3. The overall uncertainty on these IDT measurements is estimated at around 25%, which includes the uncertainties on T_5 and P_5 discussed above, the uncertainty in the measurements, and the uncertainty in the mixture due to the very low vapor pressure of EC.

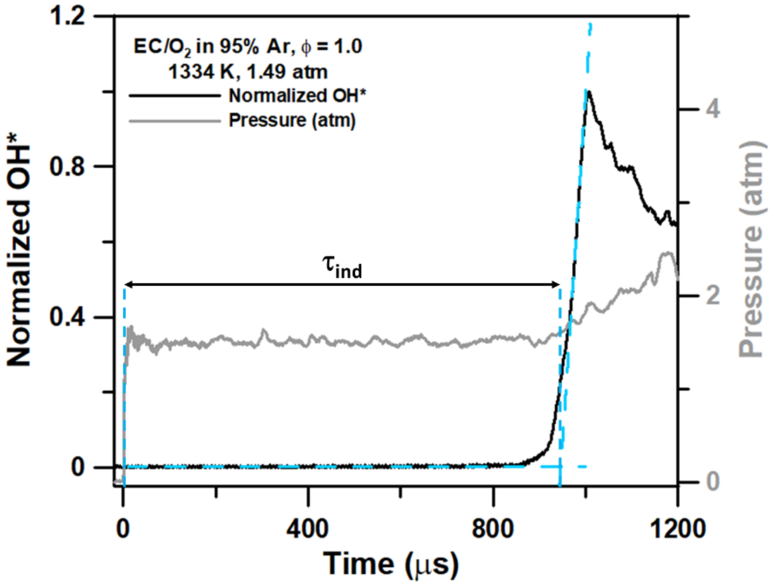

Figure 4.3 Definition method of the ignition delay time.

4.2.2.2 CO laser absorption measurements

The CO laser absorption measurements are performed at the end of the shock tube using the two sapphire optical window ports. A tunable quantum cascade laser produces coherent light near 4.8 μm to monitor the P(20) line of the 1 ← 0 band of CO and is centered at 2059.91 cm^{-1} prior to each test with a removable cell containing a low pressure mixture of CO in 90% Ar. This quantification technique works in relative isolation from H_2O and CO_2 absorption [167] as well other intermediates found during EC oxidation such as CH_4, C_2H_2, C_2H_4, C_2H_6, and CH_3CHO [161]. The laser beam is divided into two intensities, namely the incident and transmitted intensities, I_0 and I_t, where I_0 represents the neat signal without interaction with CO, and I_t is the transmitted signal that goes through the reacting gases in the shock tube and gets absorbed by CO, decreasing its intensity. These two intensities are collected by two InSb detectors after passing optical elements (irises, lenses and bypass filters) and are processed to obtain time histories of CO mole fractions, based on the Beer-Lambert relation:

$$I_t/I_0 = exp(-k_\nu P L X_{CO}) \qquad \text{(Eq. 4-1)}$$

where k_ν is the absorption coefficient, P is the pressure, L is the path length (corresponding to the shock-tube inner diameter), and X_{CO} is the CO mole fraction. Experimentally, the detector's offsets and imbalances were also taken into account, as described in Mulvihill [168]. Note that a light emission experiment was made at the highest temperature for $\phi = 2.0$, to verify that the measurement is exclusively due to CO production. The absorption coefficient, k_ν, was characterized over a large span of temperature and is described with the following temperature-dependent equation:

$$k_\nu = 23.78\, exp^{-0.000646\, T}\ . \qquad \text{(Eq. 4-2)}$$

This calibration was obtained using a mixture of 2,000 ppm CO in 0.2 He/0.798 Ar, replicating similar dilution and collision partners (He and Ar) at atmospheric pressure and a goodness-of-fit R^2 value of 0.9984 was determined.

During the experiments, the exothermicity from the decomposition of the EC induces an increase in the temperature T_5 (ΔT = 25 and 40 K at most for the highest temperatures of ϕ = 0.5 and 2.0, respectively). The absorption coefficient can be computed as a time-varying parameter in Eq. 4-2 by implementing simulated time-varying temperatures with the current kinetics model. Finally, previous studies estimated the uncertainties of the CO measurements at around 5.5% [161] and a representative CO time-history measurement for the oxidation of EC in 0.997 He/Ar at $\phi = 1.0$ is presented in Figure 4.4.

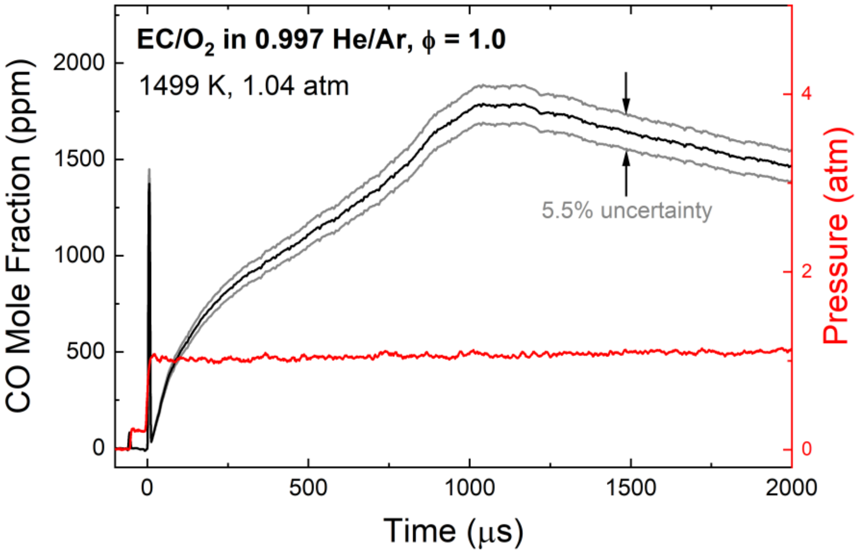

Figure 4.4 CO time-history profiles for the oxidation of EC at $\phi = 1.0$, 1499 K, 1.04 atm.

4.2.3 Laminar flame speed experiments and computations for H_2/air mixtures doped with EC

As preparing the neat EC/air mixture is challenging due to the physical properties of EC, laminar flame speed measurements were carried out for H_2/air mixtures seeded with 0.5% EC at 423 K and 1 atm. The main purpose of this measurement is to validate the (EC sub-)model with laminar flame speeds of EC-containing mixtures for which well-investigated H_2/air mixtures were selected as a base component. The combustion chemistry of hydrogen is well-studied (see Figure 4.5 for a comparison between laminar flame speed data [169,170] and model predictions for H_2/air mixtures at various temperatures), and it is assumed that the combustion chemistry of EC can be tested this way, since a large difference in the laminar flame speeds is expected compared to the neat H_2 mixture, which reflects the combustion chemistry of EC.

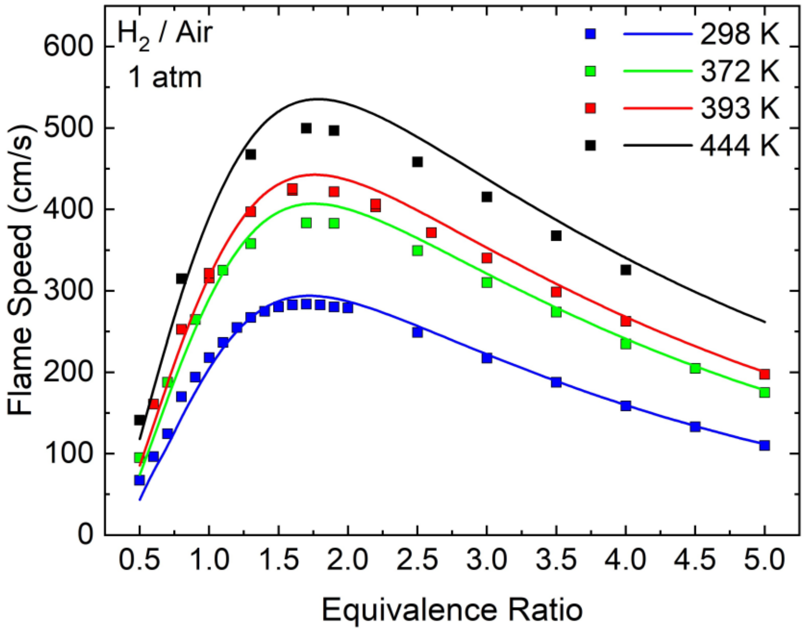

Figure 4.5 Comparison between the NUIGMech 1.1 model and experimental data for the laminar flame speed for H_2/air mixtures at an initial pressure of 1 atm and at initial temperatures of 298, 372, 393, and 444 K. 393 K data from Sikes et al. [169], and 298, 372, and 444 K data from Krejci et al. [170].

All laminar flame speed experiments were conducted using the High-Temperature-High-Pressure (HTHP) constant volume vessel at Texas A&M University. The experimental setup consists of a cylindrical-chamber vessel (total volume of approximately 25.8 L, inner diameter of 31.8 cm, length of 28.0 cm) specifically designed to study flame propagation and combustion processes under controlled conditions. The vessel has a sturdy construction to withstand the high temperatures and pressures involved in the experiments. To maintain the desired experimental conditions, the vessel is equipped with a heating jacket, which has the capability to heat the vessel up to 600 K. Furthermore, the vessel is designed to handle high-initial-pressure tests with pressures up to 10 atm. To facilitate optical diagnostics, the vessel is fitted with two opposed optical accesses. These window ports provide different viewing angles and optical paths to observe and analyze the flame propagation. Each optical access is equipped with a high-quality glass window (6.4 cm thickness). These windows are designed to withstand the high temperatures and pressures within the vessel while providing a clear optical pathway for optical diagnostics. More details about this apparatus can be found elsewhere [169–172]. A modified Z-type schlieren imaging setup was used to capture the spherically propagating flame. The schlieren setup consists of a light source generated by a mercury lamp and sent through the vessel, then captured by a high-speed Photron FastCam SA 1.1 camera. The high-speed camera has the capability of capturing up to 25,000 fps. The captured images are then processed using an in-house Python code for edge detection. The non-linear equation developed by Chen [173] is then used to get the burning velocity. Chemical kinetics modeling is then used to get the burned-to-unburned density ratio needed to obtain the unstretched, unburned flame speed.

In the present study, EC was used as an additive to H_2/air mixtures (ϕ = 0.8–3.0) with a fixed percentage of 0.5% vol. for all conditions due to the difficulty of the preparation of neat EC/air mixtures as mentioned above. The tested mixtures were prepared using the partial pressure method. A vial containing the EC was wrapped with heating tapes and heated up to 100°C. The stainless-steel vial containing the EC was hooked up to a heated-manifold next to the HTHP vessel. The heated manifold was flushed twice with EC vapors to remove any other substance. The EC vapor was introduced to the HTHP vessel to the desired pressure equivalent to the targeted 0.5% vol. Then, H_2 and air were introduced to the vessel through a manifold connected with the gas cylinders. The mixtures were left for 10 minutes to be mixed well before the flame speed measurement started. The usual uncertainty in the laminar flame speed measurements using the current HTHP vessel apparatus is 3% [174]. However, due to the low vapor pressure of EC and the consequence difficulty in the mixture preparation, the uncertainty in the present laminar flame speed measurements is larger than usual, which gives rise to 10–20 %.

Computations for the laminar flame speeds were performed using a one-dimensional freely propagating flame model in ANSYS Chemkin-Pro v19 [145]. The initial conditions (mixture composition, temperature and pressure) were the same as the experiments. A LIB electrolyte surrogate model constructed in this study (Section 4.3.3) was used as a chemical kinetic model.

4.3 Theoretical calculations and chemical kinetic modeling

Towards a LIB electrolyte surrogate model, EC unimolecular decomposition was investigated theoretically first (Section 4.3.1), followed by a construction of the EC pyrolysis model (Section 4.3.2). This EC pyrolysis model was further elaborated to the LIB electrolyte surrogate model with the implementation of EC oxidation reactions as well as updates in base-/sub-models (Section 4.3.3).

4.3.1 Unimolecular decomposition of EC

To investigate the EC unimolecular decomposition reactions, quantum chemical calculations were performed. First, the EC decomposition was explored by utilizing the Global Reaction Route Mapping (GRRM) [175] program. Stationary points (equilibrium and transition states) as well as dissociation channels were found by the anharmonic downward distortion following (ADDF) [176] method implemented in the GRRM20 [175] program combined with Gaussian 16 [97] at the B3LYP/6-31G(2df,p) level of theory. The B3LYP/6-31G(2df,p) method was chosen because the geometry optimization and frequency analysis of 1,3-dioxolane, a five-membered ring involving two oxygen atoms, which is similar to EC molecular structure as shown in Figure 4.6, was reported at this level of theory by Wildenberg et al. [177]. Sela et al. [136] calculated the potential energy surface of DEC unimolecular decomposition by the G4 composite method implemented in Gaussian 09, which showed slightly different energies as compared to that calculated by Sun et al. [46] at the CCSD(T)-F12/cc-pVTZ-F12//B3LYP/cc-pVTZ level of theory (see Chapter 3 for the consequence difference in the rate constants where using the former’s one showed good agreements with the experimental results) but the energetically preferable channels were the same. Starting with the optimized geometries obtained by GRRM20, the stationary points were recalculated by the G4 method implemented in Gaussian 16 in the present study.

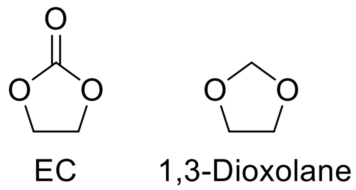

Figure 4.6 Molecular structures of EC and 1,3-dioxolane.

The potential energy surface of the EC unimolecular decomposition calculated at the G4 level of theory is illustrated in Figure 4.7. The calculated G4 energies at 0 K include the zero-point energy (ZPE) correction and are relative to that of EC. The most dominant decomposition channel of EC is:

$$\mathrm{EC} \rightarrow \mathrm{CH_3CHO} + \mathrm{CO_2} \qquad \text{(R4-1)}$$

via TS1 (67.4 kcal/mol), and the second is:

$$\mathrm{EC} \rightarrow \mathrm{C_2H_4O} + \mathrm{CO_2} \qquad \text{(R4-2)}$$

via TS2 (74.1 kcal/mol), both leading to CO_2 and C_2H_4O isomers (acetaldehyde (CH_3CHO) and ethylene oxide (C_2H_4O), respectively). The transition-state structures of TS1 and TS2 are presented in Figure 4.8. There is another decomposition channel producing CO_2 and C_2H_4O isomer, vinyl alcohol (C_2H_3OH), via TS4 (93.8 kcal/mol):

$$\mathrm{EC} \rightarrow \mathrm{C_2H_3OH} + \mathrm{CO_2}\ ; \qquad \text{(R4-3)}$$

however, its barrier is much higher than that of R4-1 and R4-2 by 26.4 kcal/mol and 19.7 kcal/mol, respectively. Although a dissociation channel producing H_2 via TS3 shows the third lowest barrier height, it is still higher than that of TS1 by 19.3 kcal/mol and TS2 by 13.0 kcal/mol, respectively. Thus, R4-1 and R4-2 are found to be clearly the energetically preferred unimolecular decomposition channels for the EC decomposition. It is also worth mentioning that R1 is the entropically preferred channel as well.

By comparing with the unimolecular decomposition of linear carbonate esters, a four-centered CO_2 elimination reaction producing dimethyl ether (DME, CH_3OCH_3) is the dominant channel for DMC decomposition [44,143]:

$$\mathrm{DMC} \rightarrow CH_3OCH_3 + CO_2\,. \qquad \text{(R4-4)}$$

The barrier height for this channel is reported to be 71.1 kcal/mol at CCSD(T)/cc-pV∞Z//M06-2X/cc-pvtz level of theory by Peukert et al. [143] and 71.0 kcal/mol at CCSD(T)-F12/VTZ-F12//QCISD/cc-pVTZ level of theory by Zhang et al. [178]. For the unimolecular decomposition of DEC and EMC, in which both chemical structures involve an ethyl ester group, the dominant decomposition channel is known to be a retro-ene reaction, a six-centered reaction producing C_2H_4 and alkoxy acid (ethoxy formic acid (EFA) and methoxy formic acid (MFA), respectively) [46,136], as discussed in Chapter 3. The alkoxy acid rapidly decomposes into CO_2 and alcohol (ethanol and methanol in DEC and EMC, respectively) through a four-centered elimination reaction [148,179]. The direct four-centered CO_2 elimination reactions producing ether (diethyl ether (DEE) and ethyl methyl ether (EME), respectively) from DEC and EMC are minor channels because their energy barriers are much higher as compared to those of the six-centered C_2H_4 elimination reactions, e.g., approximately 20 kcal/mol higher in the case of the DEC unimolecular decomposition calculated at the CCSD(T)-F12/cc-pVTZ-F12//B3LYP/cc-pVTZ [46] and G4 levels [136].

Decomposition channels of the EC radical (1,3-dioxolan-2-one-4-yl, CY(CJOC*OOC) where “CY”, “*” and “J” denote a cyclic structure, double bond and radical site, respectively) were also explored using the GRRM method at the B3LYP/6-31G(2df,p) level of theory, and energies were recalculated at the G4 level of theory. The dominant decomposition pathway is found to be a dissociation channel producing CO_2 and CH_2CHO:

$$\mathrm{CY(CJOC^*OOC)} \rightarrow CH_2CHO + CO_2 \qquad \text{(R4-5)}$$

with the barrier height of 23.6 kcal/mol. This ring-opening reaction undergoes via a CC–O bond dissociation at the β site of the radical site, followed by a CO–C bond dissociation at the other β site. The second energetically preferred decomposition channel of the EC radical is found to be a ring-opening isomerization occurring at the CO–C bond:

$$\text{CY(CJOC*OOC)} \rightarrow \text{O*CCOCJ*O}\,. \qquad\qquad \text{(R4-6)}$$

The barrier height for R4-6 was much higher than that of R4-5 by 12.9 kcal/mol. Thus, R4-5 is an energetically favored unimolecular decomposition channel for the EC radical.

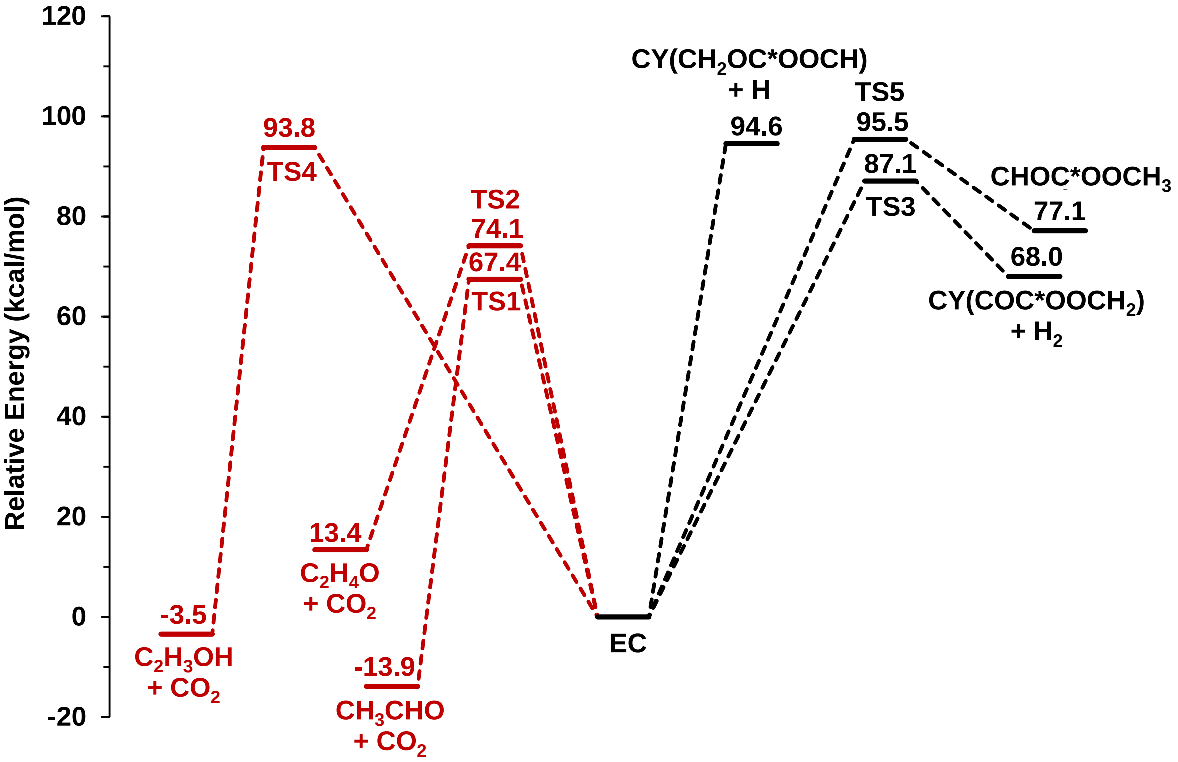

Figure 4.7 Potential energy surface of EC unimolecular decomposition calculated at the G4 level of theory (energies at 0 K including ZPE correction). The decomposition channels leading to CO_2 production are highlighted with red lines. “*”: double bond, “CY”: cyclic structure.

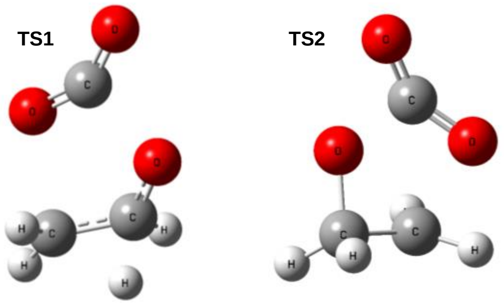

Figure 4.8 Transition-state structures of the EC decomposition (left: TS1, right: TS2).

4.3.2 Chemical kinetic modeling of EC pyrolysis

The EC pyrolysis model [180] was constructed based on the chemical kinetic model for linear carbonate esters (DMC, DEC and EMC) [47] as developed in the previous chapter (see Section 3.3). In brief, the linear carbonate ester model [47] was developed based upon a DEC model by Nakamura et al. [45], which adopts AramcoMech 1.3 [137] as a base model (C_0–C_4 chemistry), and a DMC and EMC sub-models by Alexandrino et al. [127] and Takahashi et al. [47], respectively.

From the calculated EC unimolecular decomposition, the three CO_2 production reactions, of which two of them are the most energetically favored channels among the EC decomposition, were considered in the present EC pyrolysis model. High-pressure-limit (HPL) rate constants of R4-1–R4-3 were calculated over the temperature range of 300–3000 K using GPOP [181] software. The obtained rate parameters are listed in Table 4.2 in the next part. The calculated rate constant of R4-1 for EC is 0.96 s^{-1} at 1000 K, while that of R4-4 reported for DMC is 0.13 s^{-1} at 1000 K [44]. In addition, the calculated rate constants of R4-2 and R4-3 are 0.021 s^{-1} and 1.8×10^{-7} s^{-1} at 1000 K, respectively. This implies that R4-2 and R4-3 would have little contribution to the EC decomposition at intermediate temperatures. These rate constants are shown in Figure 4.9. Although the pressure-dependent rate constants of R4-1–R4-3 were also calculated with the Rice–Ramsperger–Kassel–Marcus (RRKM) theory using SSUMES [182] software, there are little difference in the rate constant of R4-1 between the HPL and 1 atm cases up to 1200 K as shown in Figure 4.9. Thus, we simply applied the HPL rate constants in the present work as our final target, i.e., LIB fires, take place at around atmospheric pressure conditions. Based on the analogy to 1,3-dioxolane, rate constant parameters of the H-atom abstraction reactions from EC by H, O, OH, HO_2, CH_3, CH_3O, CH_3O_2 and C_2H_5 were taken from the work of Wildenberg et al. [177]. Rate constants of the ring-opening reactions of the EC radical (R4-5 and R4-6) were calculated using the GPOP [181] software as well. Subsequent reactions to R4-6 were analogically taken from

Wildenberg et al. [177]. The thermodynamic parameters of EC and related species were calculated using the THERM [149] software, similar to the EMC modeling, as the consistency of the thermodynamic parameters in a whole chemical kinetic model is highly important. The THERM code is based on Benson's group additivity method [150], which is widely applied to many programs to estimate the thermodynamic parameters [50]. The THERM group values were taken from KUCRS [151] software. The transport parameters of EC and related species were calculated using the KUCRS [151] software. The present EC pyrolysis model [180] includes 369 species and 2085 reactions in total.

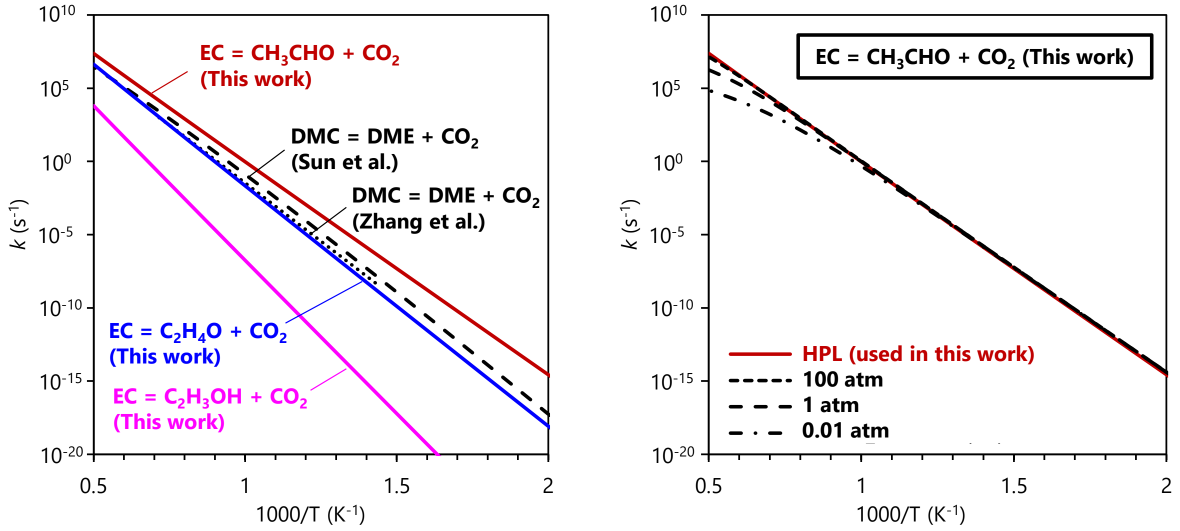

Figure 4.9 Theoretically obtained rate constants of CO_2 formation reactions of EC (this study) and DMC (literature [44,178]).

4.3.3 *LIB electrolyte surrogate model*

A LIB electrolyte surrogate model was constructed through modeling of the EC oxidation based upon the EC pyrolysis model [180]. The newly constructed LIB electrolyte surrogate model is the first comprehensive chemical kinetic model that covers widely-used LIB electrolyte components, both the linear and cyclic carbonate esters, and thus, enables us to predict gas-phase reactions of multi-component LIB electrolytes. In addition to the construction of an EC oxidation sub-model, updates in the base model and the linear carbonate esters sub-models were also made as described in the following paragraphs. Key reactions in the present EC sub-model are summarized in Table 4.2. The present LIB electrolyte surrogate model consists of 160 species and 961 reactions.

In the present EC sub-model, two initiation reactions of EC were added (with the reaction numbers corresponding to that in the model): EC $\leftrightarrows$ CY(CJOC*OOC) + H (−R945) and EC + O_2 $\leftrightarrows$ CY(CJC*OOC) + HO_2 (R946). The reaction rate constants were analogically taken from those of 1,3-dioxolane (see Figure 4.6 for the molecular structure) studied by Wildenberg et al. [177,183]. Based on their recent theoretical calculations for H-atom abstraction reactions from 1,3-dioxolane [183], the H-atom abstraction reactions from EC by OH, H, CH_3, and HO_2 were updated from those used in the EC pyrolysis model, accordingly. Theoretical calculations (Section 4.3.1) for the decomposition of the EC radical, CY(CJOC*OOC), indicated that the major decomposition channel is the dissociation into CH_2CHO and CO_2 (R957), and the ring-opening β-scission reaction producing O*CCOCJ*O (R958) is the second energetically favored channel [180]. The subsequent reactions to O*CCOCJ*O, O*CCOCJ*O $\leftrightarrows$ CH_2CHO + CO_2 (R959) and O*CCOCJ*O $\leftrightarrows$ OCH_2CHO + CO (R960), were determined based on the analogy to one of the ring-opened products from 1,3-dioxolane (O*CJOCC). The rate constants of R957–R960 were taken from [180,183].

The base model was also updated in the present LIB electrolyte surrogate model according to the recent shock-tube studies on the pyrolysis of DMC, EMC, DEC and EC by Grégoire et al. [135,161]. AramcoMech 1.3 [137] was replaced with the C_0–C_2 base model in NUIGMech 1.1 [184,185] in the present model. NUIGMech 1.1 well-reproduced experimentally obtained the global combustion properties, *e.g.*, ignition delay time and laminar flame speed, for H_2/CO/CO_2/C_1–C_3 hydrocarbons mixed gases [186], which are reported to be released during the LIB thermal runaway events [17]. In EMC and DEC pyrolysis, methanol and ethanol chemistry, respectively, were found to have a potential impact on the time-dependent CO prediction [135]. Similarly, acetaldehyde and ethylene oxide (oxirane, $C_2H_4O1\text{-}2$) chemistry showed high sensitivities and rate-of-production contributions to the CO profile during EC pyrolysis [161]. Modifications made for reactions of ethanol, acetaldehyde, $C_2H_4O1\text{-}2$, and $C_2H_3O1\text{-}2$ by Grégoire et al. [135,161] were applied to the present model.

The DMC, EMC, and DEC sub-models were also updated in the LIB electrolyte surrogate model. Some reactions related to DMC, EMC, and DEC were reviewed by Grégoire et al. [135] based on CO time-history measurements during pyrolysis. As suggested in our MFR studies on CO_2 measurements for DMC oxidation/pyolysis [134,180], a theoretically obtained rate constant of DMC $\leftrightarrows$ $CH_3OCH_3 + CO_2$ by Zhang et al. [178] at 1 atm was fitted to the 2-parameter Arrhenius expression and used in the present model.

Table 4.2 Rate constant expressions of EC reactions in the LIB electrolyte surrogate model ($k = AT^n\exp(-E_a/RT)$, units in s^{-1}, cm^3 and kcal/mol). Reaction numbers corresponds to those in the LIB electrolyte surrogate model.

No.	Reaction	A	n	E_a	Ref.
Unimolecular decomposition of EC					
R942	EC = $CH_3CHO + CO_2$	4.69×10^{11}	0.863	65.419	[180]
R943	EC = $C_2H_4O1\text{-}2 + CO_2$	4.10×10^{12}	0.643	74.298	[180]
R944	EC = $C_2H_3OH + CO_2$	4.21×10^{11}	0.759	94.650	[180]
R945	CY(CJOC*OOC) + H = EC	1.00×10^{14}	0.000	0.000	[177] [a]
Bimolecular initiation					
R946	EC + O_2 = CY(CJOC*OOC) + HO_2	2.51×10^{-6}	5.486	43.891	[183] [a]
H-atom abstraction from EC					
R947	EC + OH = CY(CJOC*OOC) + H_2O	1.30×10^{12}	0.220	1.721	[183] [a]
	PLOG/ 0.0100 2.21×10^{11} 0.271 0.471/				
	PLOG/ 0.1000 1.61×10^{13} −0.186 1.699/				
	PLOG/ 1.0000 1.30×10^{12} 0.220 1.721/				
	PLOG/ 10.000 4.06×10^{10} 0.708 1.277/				
	PLOG/ 100.00 1.97×10^{9} 1.122 0.823/				
R948	EC + H = CY(CJOC*OOC) + H_2	5.46×10^{11}	0.699	5.830	[183] [a]
	PLOG/ 0.0100 2.09×10^{11} 0.604 4.476/				
	PLOG/ 0.1000 9.49×10^{12} 0.209 5.633/				
	PLOG/ 1.0000 5.46×10^{11} 0.699 5.830/				
	PLOG/ 10.000 2.14×10^{9} 1.476 5.112/				
	PLOG/ 100.00 2.43×10^{7} 2.096 4.493/				
R949	EC + O = CY(CJOC*OOC) + OH	2.01×10^{1}	3.680	−1.650	[177] [a]
R950	EC + CH_3 = CY(CJOC*OOC) + CH_4	2.08×10^{7}	1.477	9.246	[183] [a]
	PLOG/ 0.0100 4.72×10^{6} 1.304 7.330/				
	PLOG/ 0.1000 5.31×10^{6} 1.439 7.711/				

	PLOG/ 1.0000 2.08×10^{7} 1.477 9.246/				
	PLOG/ 10.000 3.04×10^{4} 2.422 8.559/				
	PLOG/ 100.00 3.36×10^{2} 3.074 8.117/				
R951	EC + HO_2 = CY(CJOC*OOC) + H_2O_2	1.87×10^{8}	1.327	15.815	[183] [a]
	PLOG/ 0.0100 3.94×10^{8} 0.994 14.672/				
	PLOG/ 0.1000 7.10×10^{9} 0.725 15.690/				
	PLOG/ 1.0000 1.87×10^{8} 1.327 15.815/				
	PLOG/ 10.000 2.55×10^{5} 2.246 14.923/				
	PLOG/ 100.00 1.46×10^{3} 2.957 14.191/				
R952	EC + CH_3O_2 = CY(CJOC*OOC) + CH_3O_2H	2.55×10^{-2}	4.230	9.023	[177] [a]
R953	EC + CH_3O = CY(CJOC*OOC) + CH_3OH	3.33×10^{0}	3.710	0.423	[177] [a]
R954	EC + O_2CHO = CY(CJOC*OOC) + HO_2CHO	7.24×10^{-1}	3.980	9.058	[177] [a]
R955	EC + OCHO = CY(CJOC*OOC) + HOCHO	1.00×10^{13}	0.000	17.690	[177] [a]
R956	EC + C_2H_5 = CY(CJOC*OOC) + C_2H_6	2.33×10^{5}	1.840	9.451	[177] [a]
Ring opening and decomposition of product					
R957	CY(CJOC*OOC) = CH_2CHO + CO_2	4.91×10^{12}	0.335	20.903	[180]
R958	CY(CJOC*OOC) = O*CCOCJ*O	1.06×10^{13}	0.279	33.731	[180]
R959	O*CCOCJ*O = CH_2CHO + CO_2	6.63×10^{28}	−5.616	18.216	[183] [b]
	PLOG/ 0.0100 1.76×10^{21} −3.971 13.345/				
	PLOG/ 0.1000 4.04×10^{26} −5.285 16.120/				
	PLOG/ 1.0000 6.63×10^{28} −5.616 18.216/				
	PLOG/ 10.000 6.25×10^{28} −5.295 19.715/				
	PLOG/ 100.00 1.35×10^{24} −3.654 19.078/				
R960	O*CCOCJ*O = OCH_2CHO + CO	1.10×10^{27}	−5.216	23.477	[183] [b]
	PLOG/ 0.0100 4.05×10^{4} 0.755 18.120/				
	PLOG/ 0.1000 4.58×10^{16} −2.580 19.878/				
	PLOG/ 1.0000 1.10×10^{27} −5.216 23.477/				
	PLOG/ 10.000 4.59×10^{33} −6.689 27.601/				
	PLOG/ 100.00 9.53×10^{30} −5.442 28.558/				

[a] Analogy to 1,3-dioxolane. [b] Analogy to O*CJOCC.

4.4 Results and discussion

Two slightly different models are used in EC/DMC pyrolysis (Section 4.4.1) and EC oxidation (Sections 4.4.2–4.4.4) parts, i.e., the EC pyrolysis model (Section 4.3.2) and the latest LIB electrolyte surrogate model (Section 4.3.3), respectively. Thus, to distinguish them, reaction numbers are shown in different ways, for which R4-# (EC pyrolysis model) and R# (LIB electrolyte surrogate model) are used.

4.4.1 EC/DMC pyrolysis in MFR

The experimental characteristics of the pyrolysis of the EC/DMC mixture and the validation of the EC pyrolysis model are discussed based on the species evolution, followed by the reaction analysis.

4.4.1.1 Species speciation and model prediction

EC, DMC, H_2, CO, CO_2 and C_1–C_2 hydrocarbons were measured with TOF-MS and GC at $T_{\mathrm{w,max}}$ = 700–1200 K, while CH_2O, CH_3CHO and DME were measured with GC at $T_{\mathrm{w,max}}$ = 900–1200 K. The experimental carbon balance at $T_{\mathrm{w,max}}$ = 1200 K was approximately 104%, excepting the aldehydes, which almost disappear at the corresponding temperature. The calculated carbon balance was approximately 97.1% without the aldehydes at $T_{\mathrm{w,max}}$ = 1200 K, while that with the aldehydes accounted for more than 98.9% at the all conditions studied. This implies that most products were successfully measured under the present pyrolysis conditions. Further measurements at $T_{\mathrm{w,max}}$ > 1200 K were not conducted in the present experiment because of the depletion of EC and DMC at $T_{\mathrm{w,max}}$ = 1200 K and the possible soot formation. Computations were, however, extensively performed up to $T_{\mathrm{w,max}}$ = 1300 K. Figure 4.10 shows the experimental and computational results for pyrolysis of the 0.112%EC/0.088%DMC/N_2 mixture at atmospheric pressure. In the following parts, the experimental results are discussed first, followed by a comparison with the computational results.

The measured EC mole fraction rapidly decreases at $T_{\mathrm{w,max}}$ = 1000–1050 K and depletes at around $T_{\mathrm{w,max}}$ = 1100 K. Meanwhile, the measured DMC mole fraction decreases at $T_{\mathrm{w,max}}$ = 1050–1100 K and depletes at around $T_{\mathrm{w,max}}$ = 1200 K. The temperature range where DMC pyrolysis occurs in this study well-corresponds to that reported for a flow-reactor experiment by Sun et al. [44]. Although the inlet EC and DMC mole fractions are slightly higher than the target values, which is largely due to the difficulty in the mixture preparation as well as low signal intensities of EC and DMC molecular ions (see below), the present experimental approach using MFR and TOF-MS seems feasible to provide the overall fuel consumption trend. As for their detection using TOF-MS, much better inlet EC and DMC mole fractions were able to be obtained by adopting their fragment ions, *m/z* 43 and *m/z* 59 for EC and DMC, respectively, which showed higher signal intensities as compared to the molecular ions. For instance, calibrated concentrations using fragment ions at 700 K were 0.127% (*m/z* 43) for EC (ideal: 0.112%) and 0.095% (*m/z* 59) for DMC (ideal: 0.088%), both being within ca. 10% error. However, the molecular ion signals (*m/z* 88 and 90 for EC and DMC, respectively) were used in the present study because of the difficulty in distinguishing signals of EC from acetaldehyde (*m/z* 44), which is produced at higher temperatures as discussed later and possesses the same fragment ion (*m/z* 43) as EC. The measured H_2, CH_4 and CO mole fractions start increasing at around $T_{\mathrm{w,max}}$ = 1100 K. The measured CO_2 mole fraction starts increasing at around $T_{\mathrm{w,max}}$ = 1000–1050 K, at which the temperature range is similar to where the measured EC mole fraction starts to decrease while is lower than that of other measured inorganic species and C_1–C_2 hydrocarbons. C_2H_6, C_2H_4 and C_2H_2 are produced in order at $T_{\mathrm{w,max}} \geq 1050$ K. The measured C_2H_6 mole fraction hits a peak at around $T_{\mathrm{w,max}}$ = 1150 K, while the measured C_2H_4 and C_2H_2 mole fractions continue to increase within the temperature range studied. The measured DME mole fraction increases at $T_{\mathrm{w,max}}$ = 1050–1100 K and reaches approximately 110 ppm at $T_{\mathrm{w,max}}$ = 1100–1150 K. The measured CH_2O intensity also rapidly increases at $T_{\mathrm{w,max}}$ = 1050–1100 K and shows a peak at $T_{\mathrm{w,max}}$ = 1150 K. This temperature range ($T_{\mathrm{w,max}}$ = 1050–1100 K) where the measured DME and CH_2O increase overlaps with the temperature range where the measured DMC mole fraction decreases. The measured CH_3CHO intensity rapidly increases at around $T_{\mathrm{w,max}}$ = 1000–1050 K, which corresponds to the onset temperature range of the EC consumption and CO_2 production. Thus, CH_3CHO can be a good marker of EC decomposition. The measured CH_3CHO intensity peaks at around $T_{\mathrm{w,max}}$ = 1100 K, followed by a rapid decrease. From the species measurements, EC is found to decompose at lower temperatures (T_w = 1000–1050 K) than DMC (T_w = 1050–1100 K), which successfully minimized solvent interference on EC pyrolysis as we expected.

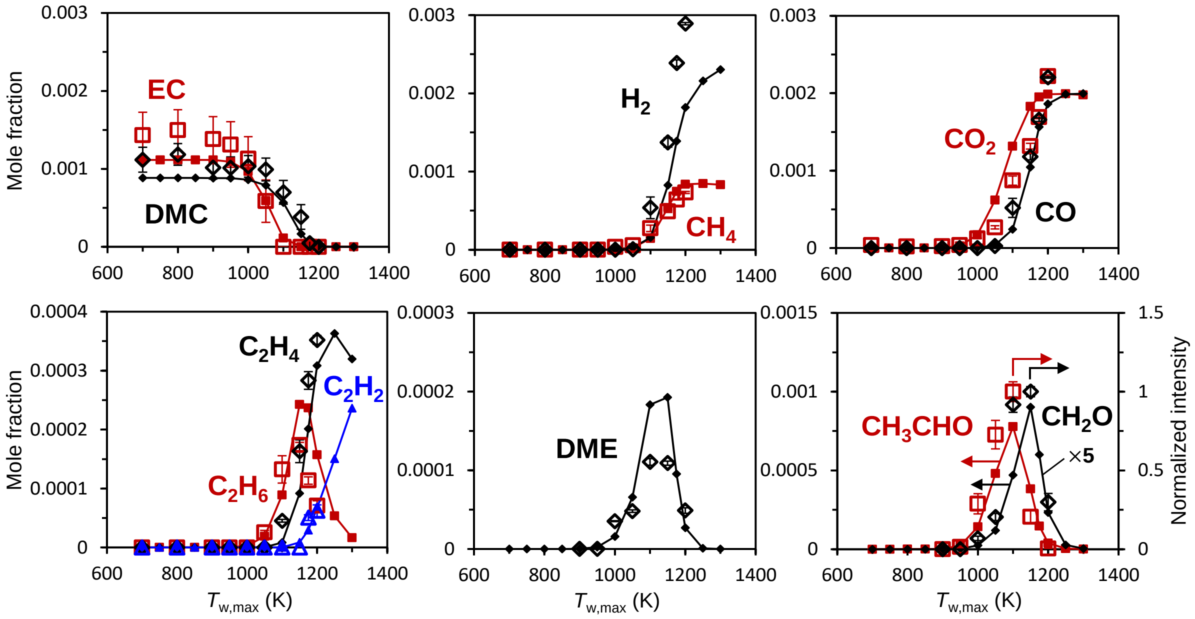

Figure 4.10 Measured (open symbol) and computed (closed symbol with line) mole fractions of EC, DMC, H_2, and C_1–C_2 species for 0.112%EC/0.088%DMC/N_2 mixtures at atmospheric pressure. Signal intensities normalized by a maximum value are shown for the measured aldehydes (CH_2O and CH_3CHO). Computations were conducted using the EC pyrolysis model [180].

Comparing the computational results to the experimental results, the present EC pyrolysis model predicts the overall trend well. The computed EC and DMC mole fractions reproduce the consumption trends of the measured EC and DMC mole fractions well, i.e., the EC consumption occurs at lower temperatures as compared to DMC. The computed H_2, CO and CO_2 mole fractions are slightly lower than the measured values at $T_{w,max}$ = 1200 K, which may be derived by the uncertainty in the inlet mixture composition. In contrast, the model slightly overpredicts the CO_2 mole fraction at around $T_{w,max}$ = 1050–1150 K. A possible reason would be due to the rate constant of the CO_2 elimination reaction of DMC (R4-4). The rate constant of R4-4 used in the present EC pyrolysis model is that theoretically obtained by Sun et al. [44].

This theoretically obtained rate constant by Sun et al. [44] is higher than experimentally and theoretically obtained ones by Zhang et al. [178] (see Figure 4.9 for comparison). The similar slight overprediction of the CO_2 production in DMC pyrolysis can also be observed in our previous DMC pyrolysis study [134] (Section 3.4.1.1) as well as the work by Sun et al. [44] at the similar temperature range. The computed C_2H_6 and C_2H_4 mole fractions show a peak at around $T_{w,max}$ = 1150 K and 1250 K, respectively, while the computed C_2H_2 mole fraction continues to increase up to $T_{w,max}$ = 1300 K. The model slightly overpredicts the DME mole fraction at $T_{w,max}$ = 1050–1150 K, which is consistent with the CO_2 overprediction discussed above. A trial computation adopting the rate constant of R4-4 proposed by Zhang et al. [178] to the EC pyrolysis model was attempted to see the influence of R4-4 rate constant on the DMC, CO_2 and DME mole fractions. As a consequence, the model prediction at $T_{w,max}$ = 1050–1150 K improved for CO_2 and especially, DMC and DME mole fractions with the modification (not shown here). The computed CH_2O mole fraction peaks at around $T_{w,max}$ = 1150 K, which agrees with the experimental peak position. The computed CH_3CHO mole fraction starts increasing at around $T_{w,max}$ = 1000 K and shows a peak value of 0.0008 at $T_{w,max}$ = 1100 K. The peak position of the computed CH_3CHO mole fraction also agrees with that of the experiment. Based on the comparison between the experimental and computational results, the present EC pyrolysis model was ensured to well-reproduce the speciation of the measured species. To investigate EC/DMC pyrolysis mechanisms in more detail, reaction analyses are carried out using the EC pyrolysis model.

4.4.1.2 Reaction pathways of EC/DMC pyrolysis

Figure 4.11 shows the reaction pathways of the EC/DMC pyrolysis at the temperatures corresponding to 30% consumption of EC and DMC (T_w = 1080 K and 1140 K, respectively). The dominant EC consumption reaction is R4-1 producing CO_2 and acetaldehyde (CH_3CHO), which accounts for approximately 95% at both temperature cases. Although the production channel of CO_2 and ethylene oxide (C_2H_4O), R4-2, is the second energetically preferred EC unimolecular decomposition channel based on the theoretical calculation, it shows little contribution to the EC consumption (less than 5%) under the conditions studied. The dominant DMC consumption reaction is the CO_2 elimination reaction producing DME (CH_3OCH_3), R4-4, which accounts for slightly less than 70%. Theoretical calculations for the DMC unimolecular decomposition [44,143] showed that the CH_3–O bond dissociation is the energetically second lowest decomposition channel. This dissociation reaction contributes about 18% to the DMC consumption at T_w = 1140 K. As discussed in the previous part (Section 4.4.1.1), the temperature range of DMC conversion in the EC/DMC pyrolysis is similar to that in the DMC pyrolysis studied by Sun et al. [44]. This can be explained as EC mainly decomposes into the stable species (CO_2 and CH_3CHO) and produces few radicals, leading to little promotion effect on DMC consumption. All the reaction pathways subsequent to the unimolecular decomposition reactions of EC and DMC reach CH_3, CO and CO_2. CH_3 then produces the C_2 species through the recombination reaction, and the evolution of the C_2 species gradually proceeds, as was observed in the experiment.

The H-atom abstraction reactions show a relatively high contribution to DMC consumption (ca. 15%) but little contribution to EC consumption (2%). This would be attributed to the unique unimolecular decomposition reactions of the carbonate esters that directly produce stable intermediates after the fuel decomposition, and to the lower temperature range of the EC decomposition as compared to DMC, as well as to the preference of the H-atom abstraction depending on the molecular structure. The EC radical decomposition reaction, which follows to the H-atom abstraction reaction by H radical, shows that the ring-opening reaction initiated by the CC–O bond dissociation (R4-5) is dominant in the EC case. Interestingly, in contrast, CO–C bond dissociation that is similar to R4-6 was the primary ring-opening reaction for 1,3-dioxolane oxidation at low-temperature and high-pressure conditions [177]. Although the molecular structures of EC and 1,3-dioxolane are similar (only the difference is the presence of a C=O bond), the preferred ring-opening reactions are contrary.

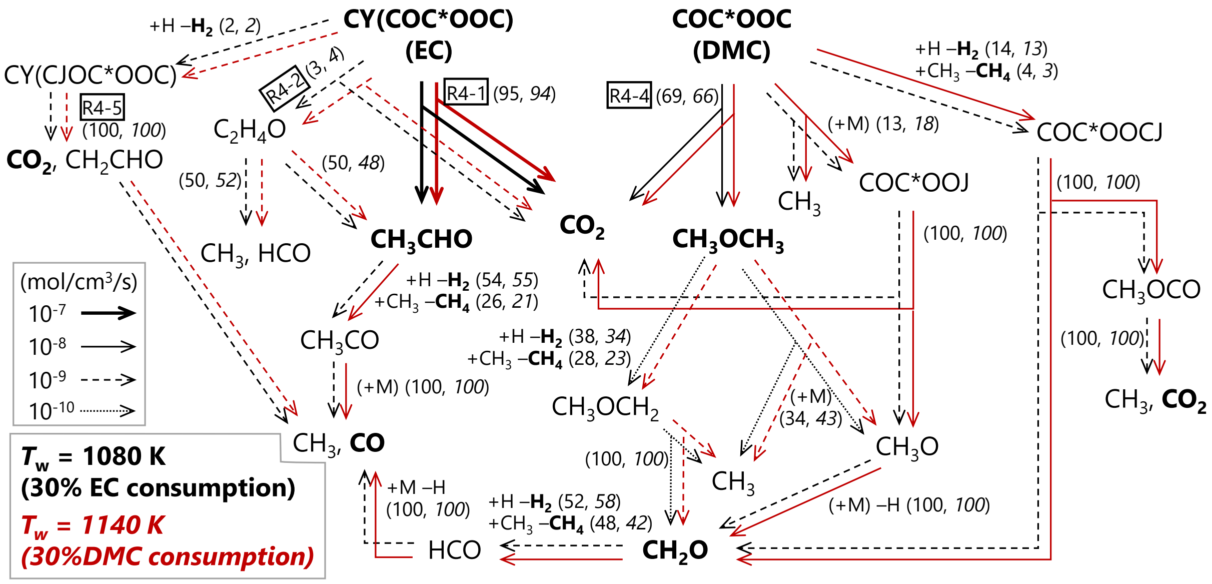

Figure 4.11 Reaction pathways of EC/DMC pyrolysis. Black and red arrows are the major reaction pathways analyzed at 30% consumption of EC (T_w = 1080 K) and DMC (T_w = 1140 K) for the case of $T_{w,max}$ = 1200 K. Numbers in the parenthesis are percent contributions of each reaction to the consumption of reactants at (1080 K, *1140 K*). Measured species in the present study are shown in bold. "*": double bond, "J": radical site. The analyses were done using the EC pyrolysis model [180].

4.4.2 *Ignition delay times of EC*

Experimental and computational ignition delay times (IDTs) of EC at ϕ = 0.5, 1.0 and 2.0 in 95% Ar and at near-atmospheric pressure in the shock tube are shown in Figure 4.12. Experimental results show only a minor effect of equivalence ratio on IDT. By comparing ϕ = 0.5 and ϕ = 2.0, the ignition delay time of the fuel-lean case tend to be longer than the fuel-rich case. The effective activation energies of IDT in both fuel-lean and fuel-rich cases appear to be quite similar, and they are greater than the activation energy observed for the stoichiometric case. Consequently, this leads to shorter IDT values on the low-temperature side and longer IDT values on the high-temperature side when compared to the cases with ϕ = 0.5 and 2.0, respectively. Computational results using the LIB electrolyte surrogate model are in reasonable agreement with the measured IDTs considering the relatively larger uncertainty in the experiments than usual due to the difficulty in the preparation of EC mixtures. The present model slightly overpredicts the IDT at ϕ = 0.5, especially for the high-temperature side. On the other hand, it underpredicts the IDT at ϕ = 2.0 for the low-temperature side. The effective activation energy of IDT in the computational result at ϕ = 1.0 is larger than that in the experimental result, leading to the underprediction and overprediction at the low- and high-temperature sides, respectively.

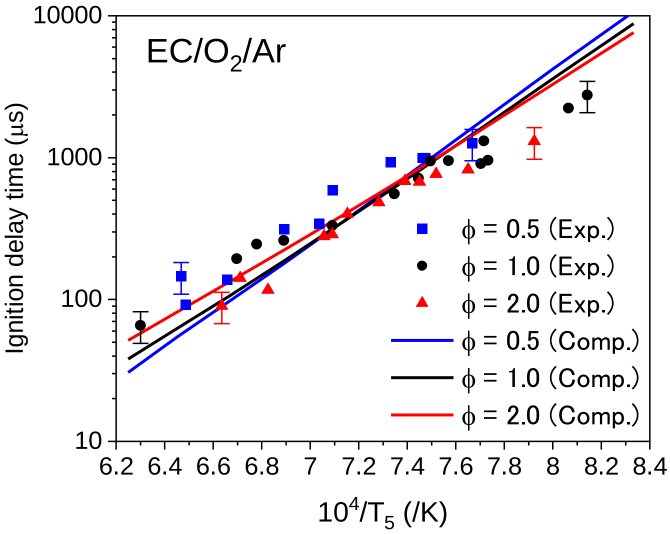

Figure 4.12 Ignition delay times of EC at ϕ = 0.5, 1.0 and 2.0 and near-atmospheric pressure in 95%Ar dilution. Error bars are shown only for the extreme conditions.

4.4.3 Time-history CO profiles of EC oxidation in ST

Measured CO mole fractions as a function of time during EC oxidation at ϕ = 0.5, 1.0 and 2.0, near-atmospheric pressure, and varied temperatures under 99.7% He/Ar dilution in the shock tube are shown in Figure 4.13. Note that the two spikes that appear in the CO profile at around 0 μs are due to the rapid density change in the mixture caused by the passage of incident and reflected shock waves across the laser beam path, which results in the temporary beam steering, so they are not due to CO formation. At the fuel-lean (ϕ = 0.5, Figure 4.13a) and stoichiometric (ϕ = 1.0, Figure 4.13b) conditions, the time-dependent CO mole fractions display a two-stage CO formation. First the CO mole fraction gradually increases, and this first formation stage is fully visible at low-temperature conditions, e.g., 1284 K for $\phi = 0.5$, within the measured time frame. The second increase in the CO mole fraction appears at intermediate-temperature conditions, e.g., 1384 K for $\phi = 0.5$, reaching a peak CO mole fraction of approximately 1000 ppm and 1800 ppm at $\phi = 0.5$ and 1.0, respectively. The position of the peak shifts to shorter delay-times as temperature increases, and at high-temperature conditions, e.g., 1695 K for $\phi = 0.5$, the CO profile shows one continuous rapid increase followed by a monotonically decrease (the decrease being due to the CO-to-CO_2 oxidation). The CO mole fractions reach their peak both at around 250 μs for the highest temperature cases at $\phi = 0.5$ (1695 K) and 1.0 (1717 K), while the peak values are different, around 1000 ppm and 1600 ppm, respectively. Similarly, at the fuel-rich conditions ($\phi = 2.0$, Figure 4.13c), the CO profile shows the gradual increase at low-temperature conditions (1303 K); the two-stage increase at intermediate-temperature conditions (1499 K); and the rapid, continuous increase at the high-temperature condition (1704 K). The shape after reaching a maximum value of CO mole fraction, however, differs from the fuel-lean and stoichiometric cases, showing almost a plateau, which is similar to the pyrolysis cases [161]. Moreover, CO mole fraction for the highest temperature case at $\phi = 2.0$ (1704 K) becomes a maximum of approximately 3500 ppm at around 500 μs, which is two times slower than those at $\phi = 0.5$ and 1.0 for a similar temperature of 1706 ± 11 K. The conversions of EC to CO at the maximum-CO time are 67%, 62%, 90%, and 125% at $\phi = 0.5$, 1.0, 2.0 and pyrolysis, respectively, with the pyrolysis results from Grégoire et al. [161].

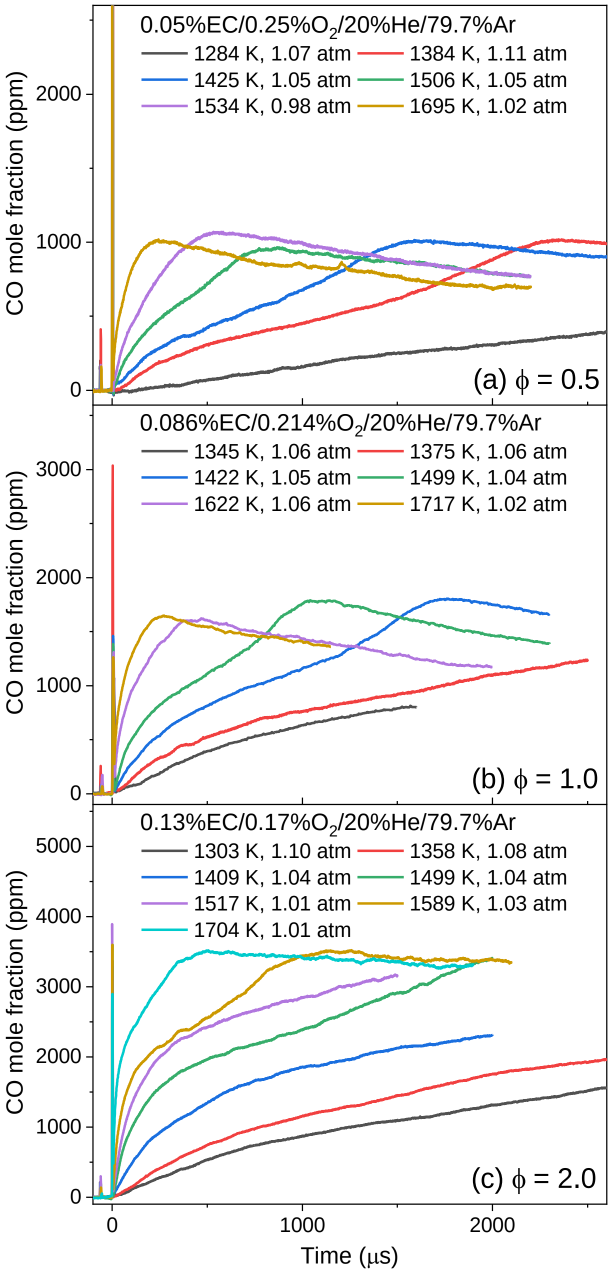

Figure 4.13 Experimental CO time-history profiles for EC oxidation at (a) ϕ = 0.5, (b) ϕ = 1.0 and (c) ϕ = 2.0 under dilution conditions and at near-atmospheric pressure and varied temperatures (1284–1717 K).

Figure 4.14 shows the comparison between the measured and computed CO time-history profiles for EC oxidation at representative low-, intermediate- and high-temperature conditions. See Figure 4.15 for all temperature cases, in which computational results using the present LIB electrolyte surrogate model for the EC pyrolysis conditions [161] are also shown. The present LIB electrolyte surrogate model satisfactorily reproduces the measured CO mole fractions. The model shows excellent agreement with the intermediate- and high-temperature results at the fuel-lean and stoichiometric conditions, while it underpredicts CO yields at low-temperature and/or fuel-rich conditions. The similar trend to the latter was also reported by Grégoire et al. [161] for EC pyrolysis in the shock tube using our previous EC pyrolysis model. They made an update on reactions mainly related to $C_2H_4O1\text{-}2$, and their tentative model showed improvements in the prediction of CO time-history profiles, especially in the timing of the CO peaks at intermediate temperatures. Their tentative model, however, also continued to underpredict the CO mole fraction, which led to the conclusion that a deeper look into acetaldehyde chemistry by validating models with such CO laser-absorption measurements would be necessary as acetaldehyde was a main pyrolysis product from EC. In this context, they conducted CO time-history measurements for acetaldehyde pyrolysis and found that their model as well as literature models overestimated CO mole fraction, which was the opposite trend to the EC pyrolysis [161]. Although the trend was different, reviewing the acetaldehyde chemistry would be the first step to filling the experimental and computational discrepancy. This conclusion would be similar to the low-temperature and/or fuel-rich conditions in oxidation as well if the dominant products were the stable acetaldehyde and CO_2 from EC thermal decomposition. The conversion of EC to CO at the peak-CO value is 64% for the computational result at $\phi = 2.0$ and 1704 K, being almost the same as those at $\phi = 0.5$ and 1.0. This outcome would also suggest that insights into the detailed kinetics for C_2 species at fuel-rich conditions is important, a conclusion that was also reached in a recent study with DEC oxidation under similar conditions [131].

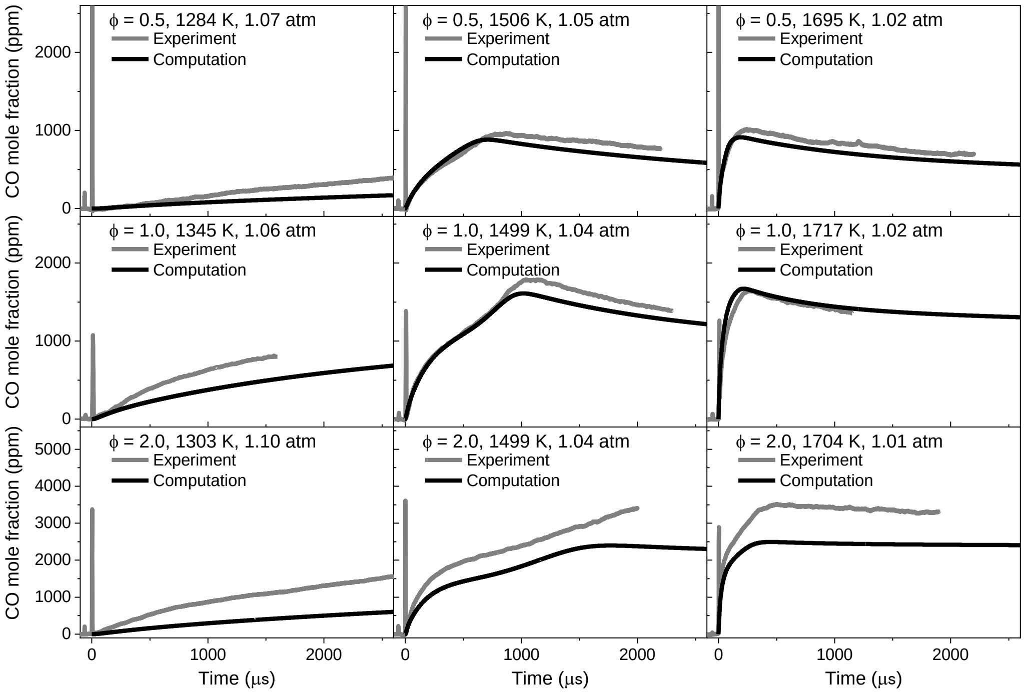

Figure 4.14 Experimental (grey) and computational (black) CO time-history profiles for EC oxidation at ϕ = 0.5 (top), 1.0 (middle) and 2.0 (bottom) at near-atmospheric pressures and representative temperatures: low (left), intermediate (middle) and high (right) at around 1300 K, 1500 K and 1700 K, respectively.

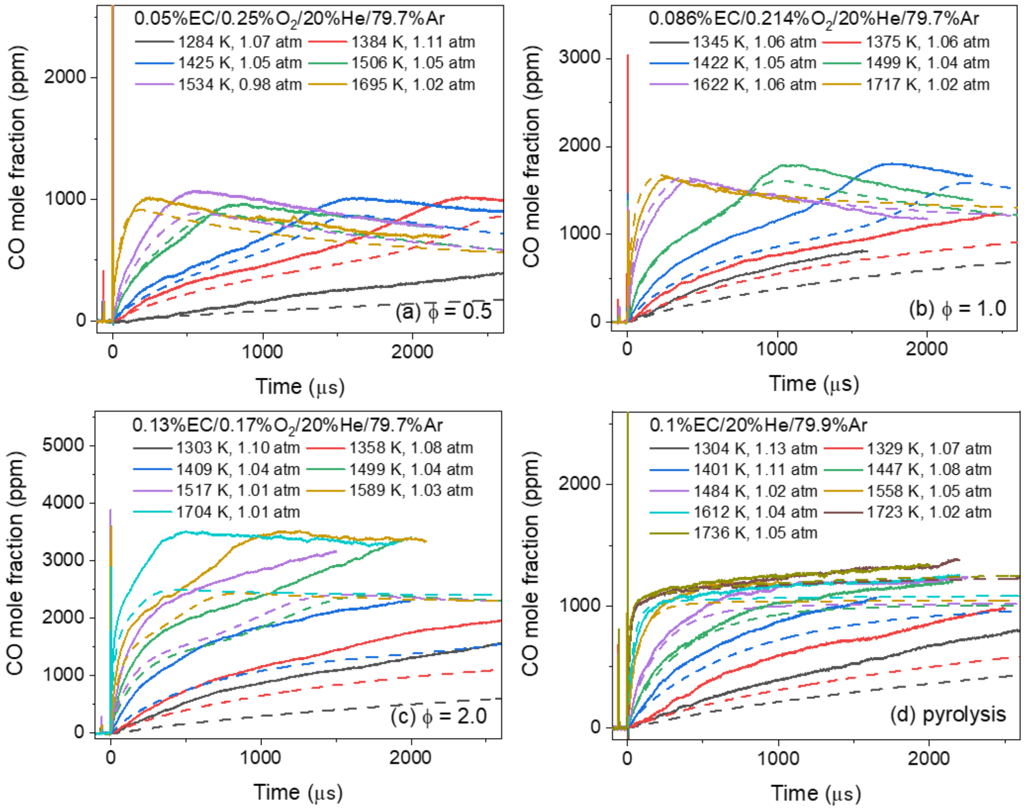

Figure 4.15 Experimental and computational CO time-history profiles for oxidation and pyrolysis of EC. The pyrolysis experimental data (d) is from Grégoire et al. [161].

Reaction pathways for EC oxidation at $\phi = 1.0$, near-atmospheric pressure, 1500 K and where 30% of EC is consumed (4–5 μs) are depicted in Figure 4.16, together with a pyrolysis case as a comparison. The major pathways of EC oxidation and pyrolysis are similar under the conditions considered, i.e., the onset of CO formation. The dominant EC consumption pathway is the unimolecular decomposition reaction producing acetaldehyde and CO_2, EC $\leftrightarrows$ $CH_3CHO + CO_2$ (R942), which accounts for 90% of EC consumption, and the second dominant pathway produces ethylene oxide and CO_2, EC $\leftrightarrows$ $C_2H_4O1\text{-}2 + CO_2$ (R943), contributing 8% to the EC consumption. Since $C_2H_4O1\text{-}2$ is unstable as compared to CH_3CHO [187], the subsequent reactions for $C_2H_4O1\text{-}2$ rapidly produces HCO (via $C_2H_4O1\text{-}2 \leftrightarrows CH_3 + HCO$ (R264)) and then CO (via HCO + M $\leftrightarrows$ H + CO + M (R187)). Consequently, this reaction pathway (EC → $C_2H_4O1\text{-}2$ → HCO → CO) drives the CO formation at the beginning until subsequent reactions for CH_3CHO become significant at around 30 μs. It should be noted that an isomerization of $C_2H_4O1\text{-}2$ to CH_3CHO has accounted for about half of the $C_2H_4O1\text{-}2$ consumption under EC/DMC pyrolysis at $T_{w,max}$ = 1200 K in MFR using the previous EC pyrolysis model [180], but this isomerization has a minor contribution to $C_2H_4O1\text{-}2$ consumption with the present LIB electrolyte surrogate model. This difference results from the updates in the $C_2H_4O1\text{-}2$ decomposition reactions. The rate constants of $C_2H_4O1\text{-}2 \leftrightarrows CH_3 + HCO$ (R264) and $C_2H_4O1\text{-}2 \leftrightarrows CH_3CHO$ (R265) are similar in AramcoMech 1.3 and NUIGMech 1.1, whereas those theoretically obtained by Joshi et al. [187] indicate a difference of two orders of magnitude at 1200 K where R264 is dominant. The rate constants and branching ratio of R264 and R265 are shown in Figure 4.17 (although there are seven decomposition pathways reported in the literature [187], only two of them that are included in AramcoMech 1.3 and NUIGMech 1.1). The H-atom abstraction reactions from EC show a small contribution (ca. 2%) mostly by EC + H $\leftrightarrows$ CY(CJOC*OOC) + H_2 (R948). Both two subsequent reactions to the EC radical produce CH_2CHO, followed by the decomposition into CO directly or via CH_2CO. The latter pathway competes with HCCO formation where a slight difference is observed between the oxidation and pyrolysis conditions as it produces CO and CO_2 at oxidation but produces solely CO at pyrolysis.

The second increase in the CO time-history profile is driven by mainly two pathways, $CH_2O \rightarrow HCO \rightarrow CO$ and $HCCO \rightarrow CO$ (see Figure 4.18 for the CO rate-of-production (ROP) analysis at the representative temperatures for the oxidations). Based on the ROP analysis, $CH_3 + O \leftrightarrows CH_2O + H$ (R115), $CH_2 + O_2 \leftrightarrows CH_2O + O$ (R83) and $C_2H_4 + O \leftrightarrows CH_2 + CH_2O$ (R300) and $C_2H_2 + O \leftrightarrows HCCO + H$ (R378) were the major CH_2O and HCCO production reactions at around 700–800 μs, respectively. CO oxidation to CO_2 is enhanced at the later stage (around 1000 μs) where the net CO rate of production turns negative, and the experimental and computational CO mole fractions start decreasing. The change in the major CO formation pathways at $\phi = 1.0$ as time proceeds is illustrated in Figure 4.19.

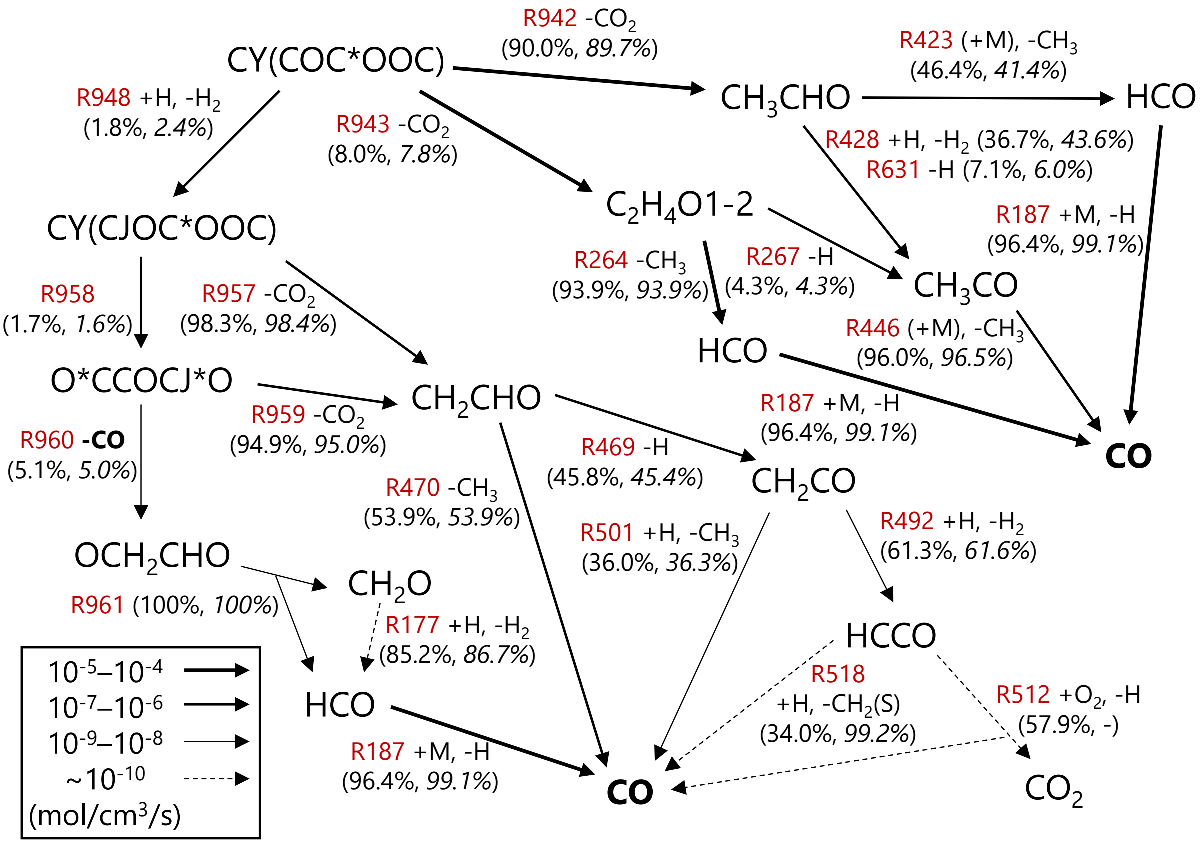

Figure 4.16 Reaction pathways analysis for EC oxidation (0.086%EC/0.214%O_2/20%He/79.7%Ar, ϕ = 1.0, 1499 K and 1.04 atm) and pyrolysis (0.1%EC/20%He/79.9%Ar, 1484 K and 1.02 atm) at 30% EC consumption (4–5 μs). The pyrolysis condition is from the experiment by Grégoire et al. [161]. Numbers in the parenthesis are the percent contributions of each reaction to the consumption of the parent species at oxidation and *pyrolysis* conditions. Arrows show the order of magnitude of the total rate-of-consumption for each reaction pathway (mol/cm^3/sec).

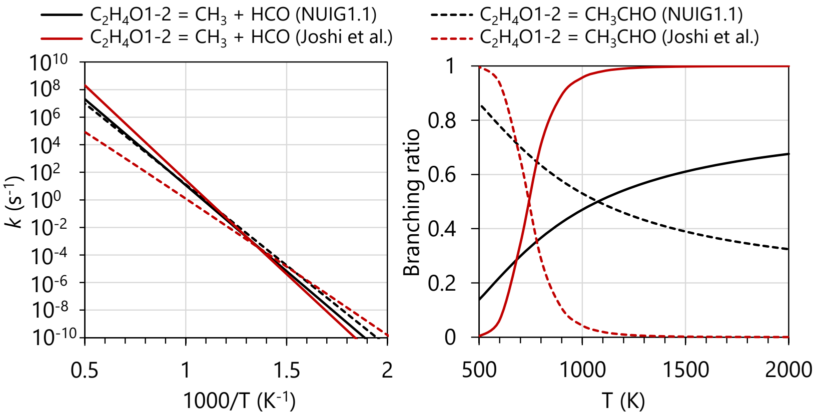

Figure 4.17 Rate constants of unimolecular decomposition reactions of ethylene oxide (C_2H_4O1-2) adopted in NUIGMech 1.1 [43,44] (black) and theoretically calculated by Joshi et al. [41] (red). Five other reactions for the latter are not included in this figure, which account for up to 8% in total in the branching ratio at 2000 K.

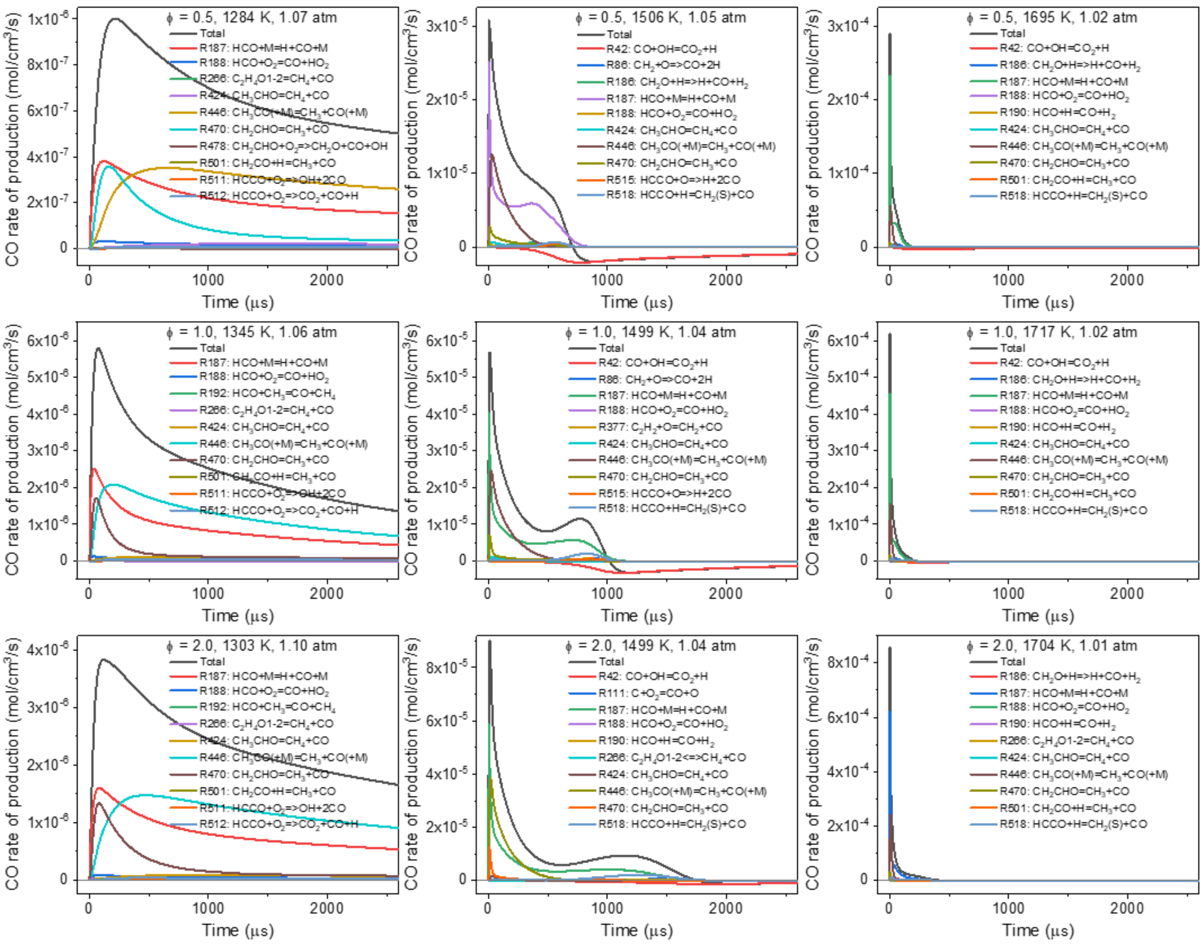

Figure 4.18 CO rate-of-production analysis at ϕ = 0.5 (top), 1.0 (middle) and 2.0 (bottom) and at around 1300 K (left), 1500 K (middle) and 1700 K (right). Top 10 reactions in each case are shown.

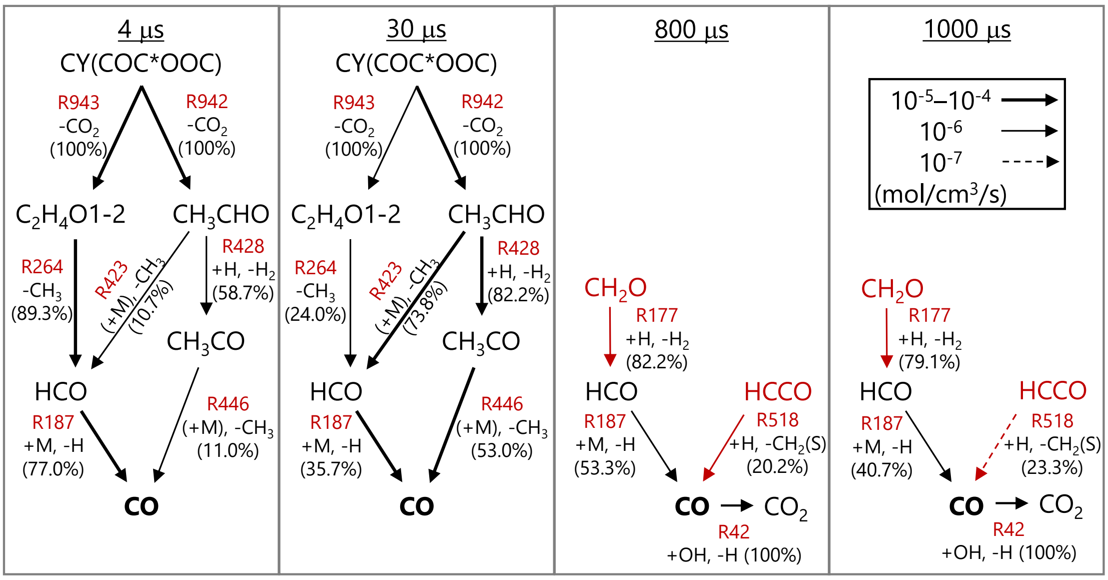

Figure 4.19 Change in the major CO formation pathways at ϕ = 1.0, 1499 K and 1.04 atm. Numbers in the parenthesis are the percent contributions of each reaction to the products, except for those CO to CO_2 that account for the CO consumption.

Together with the ROP analysis, the CO sensitivity analysis was performed to investigate the equivalence ratio and temperature effects on the CO formation. The top 10 sensitive reactions at ϕ = 0.5, 1.0 and 2.0 and at around 1300, 1500 and 1700 K are shown in Figure 4.20. A general trend is discussed first, followed by temperature/equivalence ratio dependence trends. R943 (EC $\leftrightarrows$ $C_2H_4O1\text{-}2 + CO_2$) is the most sensitive reaction for CO formation at all conditions. The onset of the CO formation is especially sensitive to this reaction (see Figure 4.21 for the sensitivity coefficient as a function of time) as the reaction pathway via $C_2H_4O1\text{-}2$ (EC → $C_2H_4O1\text{-}2$ → HCO → CO) proceeds faster than that via CH_3CHO. In contrast, R942 (EC $\leftrightarrows$ $CH_3CHO + CO_2$) shows a negative sensitivity coefficient at all conditions as it competes with R943. $C_2H_4O1\text{-}2$ mostly produces HCO (R264: $C_2H_4O1\text{-}2 \leftrightarrows CH_3 + HCO$), followed by the HCO decomposition to CO (R187: HCO + M $\leftrightarrows$ H + CO + M), producing H-radical in the net reaction system. Although CH_3CHO also proceeds toward CO via HCO (R423: CH_3CHO (+M) $\leftrightarrows$ CH_3 + HCO (+M)) or CH_3CO (R428: $CH_3CHO + H \leftrightarrows CH_3CO + H_2$), the latter consumes H-radical. Thus, R264 and R423 exhibit a positive sensitivity coefficient while R428 shows a negative sensitivity coefficient to the CO formation in general. Note that although R428 possesses the positive sensitivity coefficient at its peak sensitive value at high-temperature/fuel-rich conditions in Figure 4.20, it seems to have a negative sensitivity overall to the CO formation over the test time as apparent in Figure 4.21. Finally, as HCO is one of the major sources of CO, its decomposition reaction R187 shows a positive sensitivity at all conditions considered. In contrast, the CO formation is less sensitive to the decomposition reaction of CH_3CO, CH_3CO (+M) $\leftrightarrows$ CH_3 + CO (+M) (R446).

Comparing the low versus intermediate and high temperatures, the CO formation is relatively sensitive to R948 (EC + H $\leftrightarrows$ CY(CJOC*OOC) + H_2), −R945 (EC $\leftrightarrows$ CY(CJOC*OOC) + H), R470 ($CH_2CHO \leftrightarrows CH_3 + CO$), and R267 ($C_2H_4O1\text{-}2 \leftrightarrows CH_3CO + H$) at low temperatures for at least two equivalence ratio cases. At fuel-rich condition, R948 shows a positive sensitivity at the intermediate temperature as well, and R434 (CH_3CHO +

$CH_3 \leftrightarrows CH_3CO + CH_4$) is listed only at $\phi = 2.0$. To understand the influence of H-atom abstraction reactions from EC on the CO formation, we attempted a trial computation using the rate constants of the H-atom abstraction reactions with the analogy to tetrahydrofuran [188] (e.g., the rate constant theoretically obtained for the H-atom abstraction with OH-radical from tetrahydrofuran (THF) at C-atom adjacent to O- and another C-atom [189] is approximately four times higher than that of 1,3-dioxalane at the similar configuration [183] at 1000 K and 1 atm), but this change in the rates coefficients did not modify the computed CO mole fractions. It is also worth mentioning that the rate constants of the H-atom abstraction with H-radical from 1,3-dioxalane and tetrahydrofuran at the aforementioned position hardly differ, the latter one [190] is 1.4 times faster than the former one [183]. As for R945, the same rate constant as 1,3-dioxalane is used in THF [188,190] based on the analogy to alkane [191]. Although a careful attention is needed for how far we can apply the analogy to oxygenates, these comparisons between the two similar molecular structures that involve O-atom(s) in their five-member ring suggest that the H-atom abstractions from EC seem not be a primary factor for the CO underprediction. Meanwhile, reactions involving oxygenated intermediates such as aldehydes and alcohols play important roles in the CO time-history profile in particular for carbonate esters [131,135,161] and need to be further investigated at fuel-rich/pyrolysis conditions and low-to-intermediate temperatures. Under these conditions, model predictions for the time-history profiles of CO and H_2O vary among well-known mechanisms and show a relatively large discrepancy from experiments even for C_0–C_3 blended gaseous or ethanol/CO_2 mixtures [186,192]. Modification in the C_0–C_2 chemistry essentially affects not only the CO profile but also whole combustion and pyrolysis properties, which is a huge project and beyond the scope of the present work.

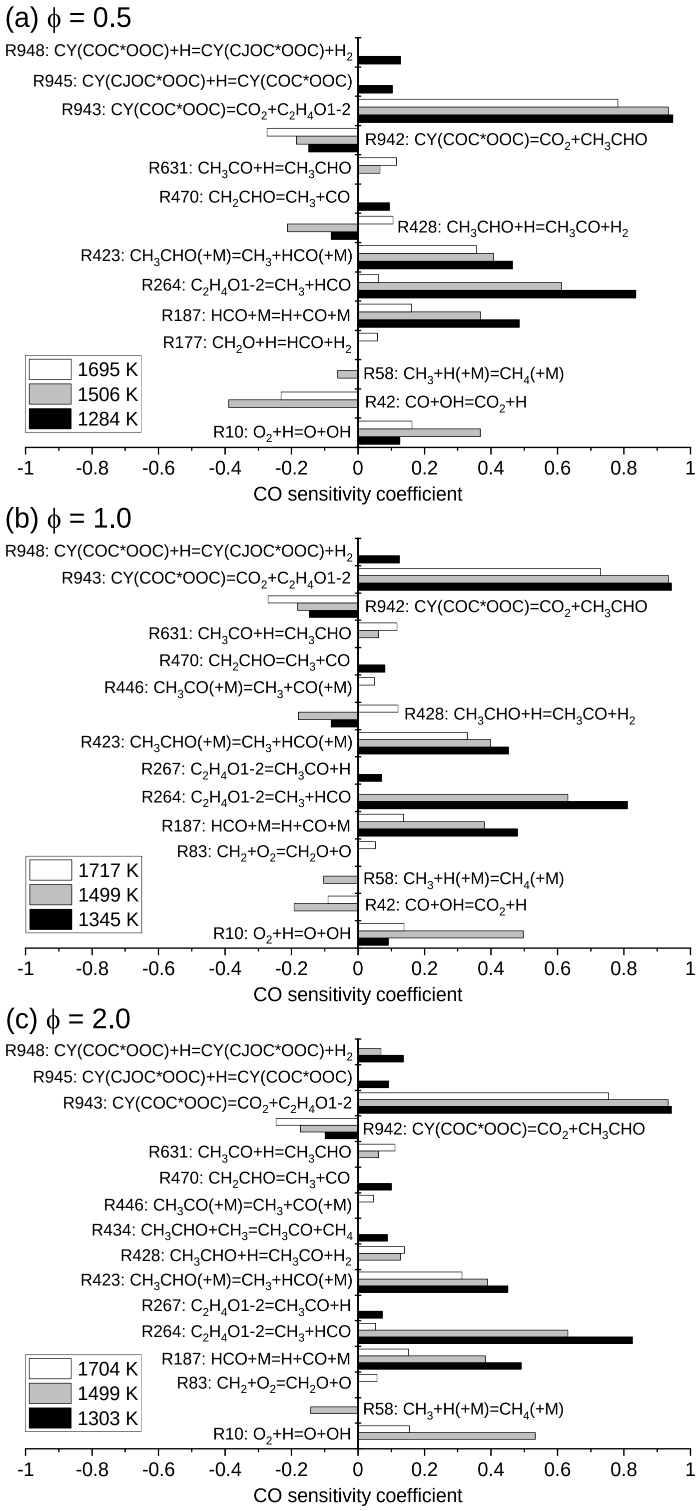

Figure 4.20 CO sensitivity coefficients for (a) ϕ = 0.5, (b) ϕ = 1.0 and (c) ϕ = 2.0 at low, intermediate and high temperatures. The coefficients were taken from the peak sensitivity value.

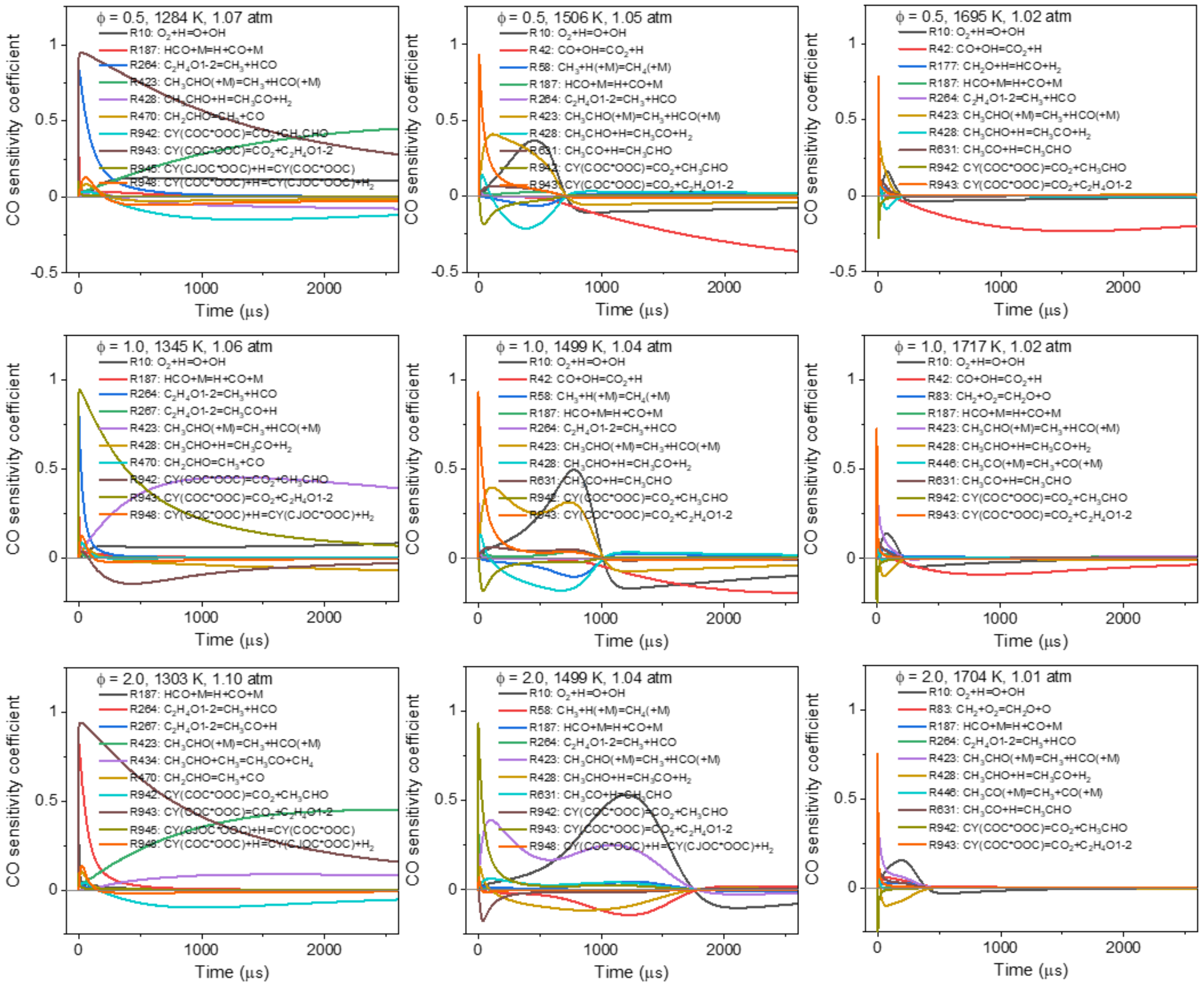

Figure 4.21 CO sensitivity coefficients at ϕ = 0.5 (top), 1.0 (middle) and 2.0 (bottom) and at around 1300 K (left), 1500 K (middle) and 1700 K (right). Top 10 reactions in each case are shown.

4.4.4 *Laminar flame speed of H_2/air mixtures doped with EC*

As explained in Section 4.2.3, due to the difficulty in the preparation of a neat EC/air mixture, laminar flame speed measurements were conducted for H_2/air mixtures doped with EC. The reasons why we chose a H_2/air mixture are its combustion chemistry is well-studied (see Figure 4.5) and thus, the EC model can be validated. Practically, the flame speeds of H_2 and EC mixtures are also important for LIB fires since the thermal runaway gases potentially involve both components. Despite a small addition of EC, 0.5% mol., a large effect can be seen on the laminar flame speed in Figure 4.22, which reflects EC chemistry. According to the model predictions, the maximum flame speed is reduced by about 13%, and the equivalence ratio at which this maximum flame speed is reached is shifted: ϕ = 1.7 for the neat H_2/air mixture, and ϕ = 1.55 for the mixture seeded with EC. The model is in good agreement with the data for equivalence ratios of 1.2 and lower, and between ϕ = 2.0 and 2.5. The maximum flame speed at the peak is however over-estimated by about 15%, and the model seems to diverge from the data above ϕ = 2.5. Overall, given the uncertainty in the data due to the difficulties associated with the study of EC in gas phase, it can be concluded that the model can satisfactorily predict the data. For further validation and updates of the model, combustion and pyrolysis experiments of EC with a wide range of methods, conditions, and properties are required.

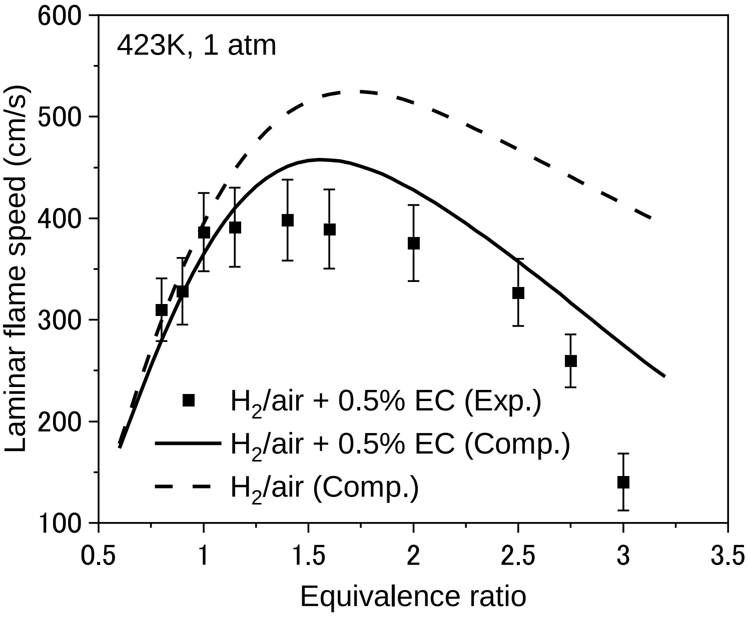

Figure 4.22 Laminar flame speed for H_2/air mixtures neat and seeded with 0.5 mol% EC at 423 K as initial conditions.

4.5 Conclusions

4.5.1 EC/DMC pyrolysis

The pyrolysis characteristics of EC was investigated by theoretical calculations and species measurements, and the detailed chemical kinetic model for linear carbonate esters constructed in Chapter 3 was extended by modeling EC pyrolysis (EC pyrolysis model, Section 4.3.2). The EC unimolecular decomposition calculated at the G4 level of theory indicate that EC = CH_3CHO + CO_2 (R4-1) is the energetically preferred decomposition channel. The calculated rate constant of R4-1 is 7.4 times higher as compared with that of the CO_2 elimination reaction of DMC (R4-4) from the literature at 1000 K. Species measurements for the EC/DMC pyrolysis diluted in 99.8% N_2 showed that the consumption of EC occurs at a lower temperature range (T_w = 1000–1050 K) than that of DMC (T_w = 1050–1100 K). The measured acetaldehyde rapidly increased at T_w = 1000–1050 K, being a good marker for the EC decomposition. The EC pyrolysis model reproduced the experimental results well. Based on reaction path analysis, R4-1 accounted for approximately 95% contribution to EC consumption analyzed at 1080 K (30% EC consumption).

4.5.2 EC oxidation

A LIB electrolyte surrogate model, consisting of a comprehensive detailed chemical kinetic model for the major LIB electrolyte components (dimethyl carbonate (DMC), diethyl carbonate (DEC), ethyl methyl carbonate (EMC), and ethylene carbonate (EC)), is proposed, with this study focusing on the EC sub-model. Ignition delay time (IDT) and CO laser absorption measurements for EC oxidation (ϕ = 0.5, 1.0 and 2.0) in diluents were conducted over the temperature range of 1228–1717 K and at near-atmospheric pressures behind reflected shock waves in a shock tube. The experimental IDTs showed a small effect of the equivalence ratio, and the present LIB electrolyte surrogate model reasonably reproduced the experimental results. The measured CO time-history profiles showed a strong temperature dependence, with a gradual and linear increase in the CO profile at low temperatures, a two-step increase at intermediate temperatures and a continuous and rapid increase at high temperatures. These trends were well-predicted using the present LIB electrolyte surrogate model although the computational results underpredicted the CO mole fractions at low-temperature and/or fuel-rich conditions. CO sensitivity analysis showed a high sensitivity for reactions related to C_2 oxygenates, e.g., acetaldehyde and ethylene oxide, suggesting the need for updates in the oxygenate chemistry. Laminar flame speeds of H_2/air mixtures seeded with 0.5% EC were measured at 423 K and 1 atm for $\phi = 0.8–3.0$ using a closed combustion vessel and were well-reproduced with the present model. Although additional experimental data with an extended range of combustion characteristics and experimental approaches are still required for validation and improvement of the model, the present LIB electrolyte surrogate model will be useful to predict combustion properties of the electrolyte components and assess the fire risks of LIBs.

Chapter 4 based on:

K. Kanayama, S. Takahashi, H. Nakamura, T. Tezuka and K. Maruta, Experimental and modeling study on pyrolysis of ethylene carbonate/dimethyl carbonate mixture, *Combust. Flame* 245 (2022) 112359.

K. Kanayama, C.M. Grégoire, S.P. Cooper, Y. Almarzooq, E.L. Petersen, O. Mathieu, K. Maruta and H. Nakamura, Experimental and chemical kinetic modeling study of ethylene carbonate oxidation: A lithium-ion battery electrolyte surrogate model, *Combust. Flame* 262 (2024) 113333.

Chapter 5

Global combustion properties of multi-component LIB electrolyte solvents

This chapter aims to obtain a general flammability trend of single- and multi-component LIB electrolyte solvents by simulating gas-phase global combustion properties (ignition delay times and laminar flame speeds) using the LIB electrolyte surrogate model. The newly constructed LIB electrolyte surrogate model is validated with laminar flame speeds and ignition delay times of single-component linear carbonate esters (DMC, DEC and EMC) available from the literature data. The gas-phase flammability is compared with the current liquid-based fire hazard classification.

5.1 Introduction

Inferring a possible fire incident that involves the production of flammable electrolyte gases through thermal runaway and venting events, their global combustion parameters, i.e., ignition delay time and laminar flame speed, are critical for the fire risks and damages. As both linear and cyclic carbonate esters are included in practical LIB electrolytes as shown in Table 1.1, e.g., EC/DMC (LP30, 50:50 wt% = 50:50 mol%), EC/DEC (LP40, 50:50 wt% = 57:43 mol%) and EC/EMC (LP50, 50:50 wt% = 54:46 mol%) [23,32], simulations of ignition delay times and laminar flame speeds for the mixtures of linear and cyclic carbonate esters are demonstrated herein, which benefited from the newly constructed LIB electrolyte surrogate model. This chapter comprises model predictions because there have been no such experiment for the multi-component carbonate esters so far. These predictions, however, could provide key combustion properties and relative suitability in terms of flammability for practical LIB electrolytes [36]. In addition, this chapter offers validation results of the LIB electrolyte surrogate model with ignition delay times and laminar flame speeds of DMC, DEC and EMC available from the literature.

5.2 Computational method

Computations for the ignition delay times were performed using a zero-dimensional adiabatic homogenous reactor model in the AURORA package implemented in ANSYS Chemkin-Pro v19 [145]. Computations for the laminar flame speeds were performed using a one-dimensional adiabatic freely propagating flame model PREMIX in ANSYS Chemkin-Pro v19 [145]. The newly constructed LIB electrolyte surrogate model was used as a chemical kinetic model. As representatives of the practical LIB electrolyte solvents, EC/DMC/air, EC/DEC/air and EC/EMC/air mixtures along with neat EC/air, DMC/air, DEC/air and EMC/air mixtures were targeted. The compositions of the multi-component carbonate esters were all set as 1:1 in liquid weight ratio according to the commercially used compositions (see Table 1.1). Initial conditions of ignition delay time computations were given as equivalence ratio of 1.0, pressure of 1.0 atm and temperature of 1200–1600 K (around $10^4/T$ = 6.3–8.3). Those of laminar flame speed computations were set to equivalence ratio of 0.6–2.0, pressure of 1.0 atm and temperature of 500 K, by considering the elevated temperature situations during thermal runaway and/or venting events.

5.3 Model validation with the literature data

Ignition delay times and laminar flame speeds of DMC are shown in Figure 5.1 and Figure 5.2, respectively. The present LIB electrolyte surrogate model reproduces the literature data well for both ignition delay times and flame speeds of DMC at various conditions. For instance, ignition delay times at $\phi = 1.0$ and near atmospheric pressure condition in air (Figure 5.1, top right), which would be similar to the LIB fire conditions, are predicted well. Similarly, the present model shows an excellent agreement with laminar flame speeds at 1 atm and elevated temperatures (Figure 5.2, left) over the equivalence ratio of around 0.7–1.5.

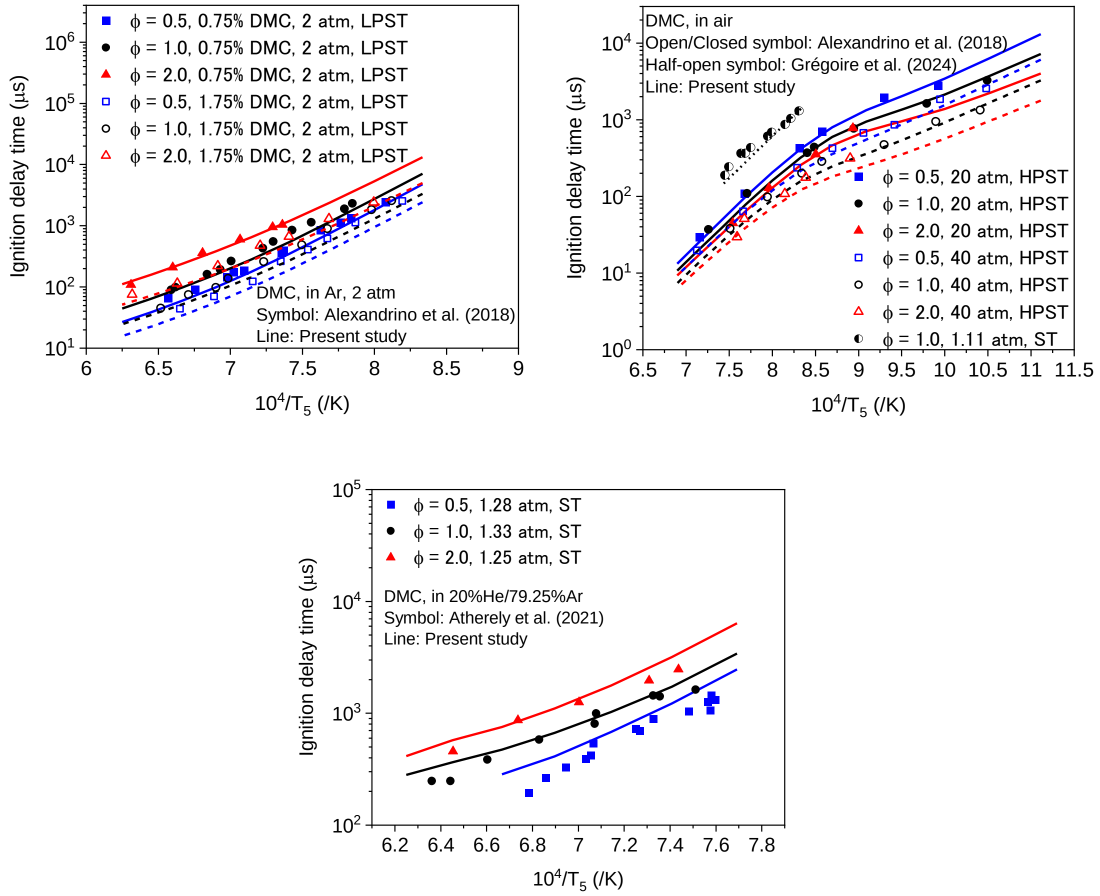

Figure 5.1 Ignition delay times of DMC at various conditions. Symbols are experimental data from the literature [126,127] and lines are computational results using the present LIB electrolyte surrogate model.

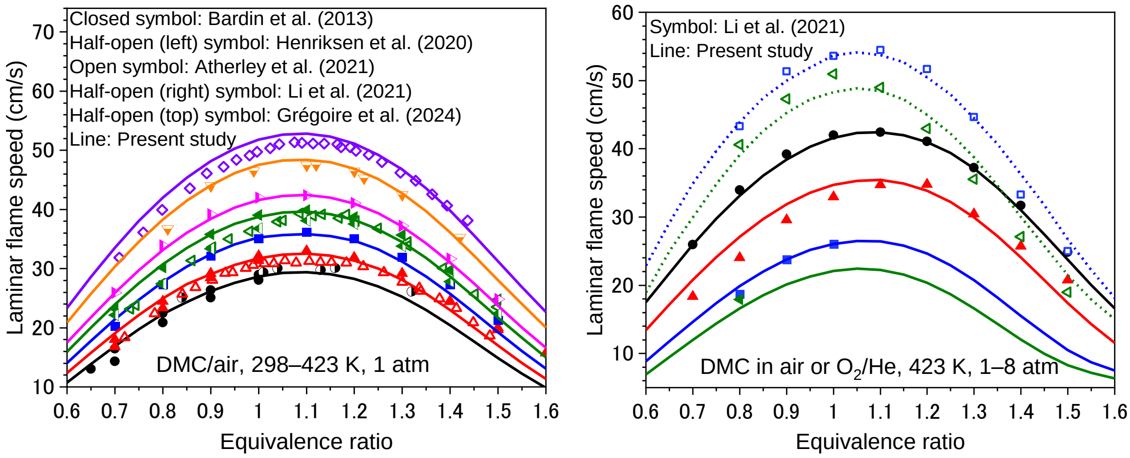

Figure 5.2 Laminar flame speeds of DMC/air at 298–423 K and 1–8 atm. Symbols are experimental data from the literature [124–126] and lines are computational results using the

present LIB electrolyte surrogate model.

Ignition delay times and laminar flame speeds of DEC are shown in Figure 5.3 and Figure 5.4, respectively. The present model agrees well with the literature data for both ignition delay times and flame speeds of DEC at various conditions as well. There is little equivalence ratio effect on the experimental ignition delay times near atmospheric pressure (Figure 5.3, right), which is captured by the model prediction although a slightly larger effect appears at higher temperatures (around 1350 K). Laminar flame speeds at elevated temperatures (around 400 K) at 1 atm are predicted well over the equivalence ratio of 0.8–1.4.

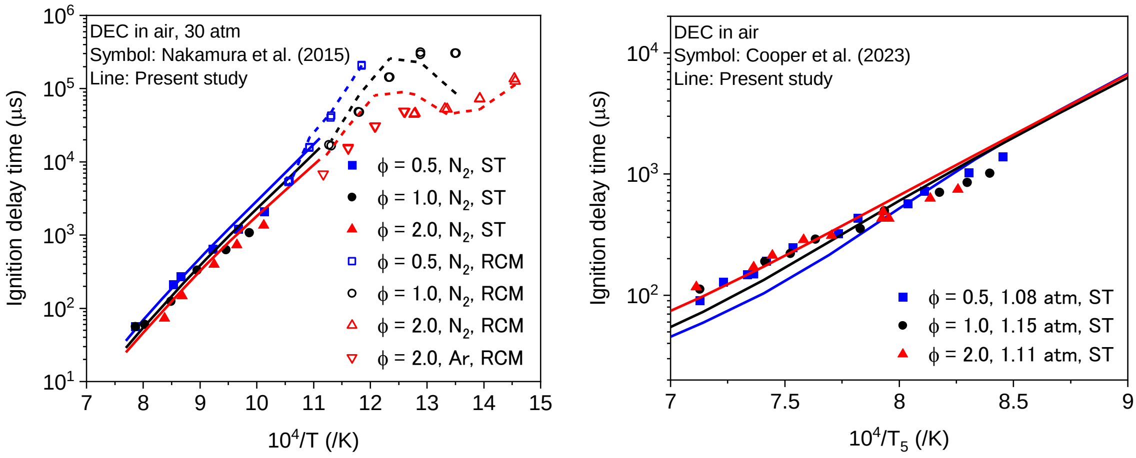

Figure 5.3 Ignition delay times of DEC at various conditions. Symbols are experimental data from the literature [45,131] and lines are computational results using the present LIB electrolyte surrogate model.

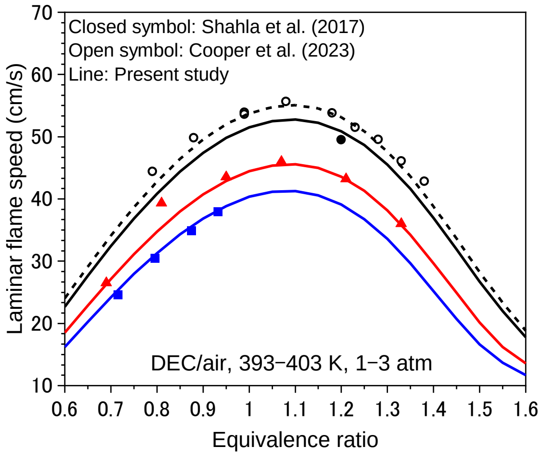

Figure 5.4 Laminar flame speeds of DEC/air at around 400 K and 1–3 atm. Symbols are experimental data from the literature [130,131] and lines are computational results using the

present LIB electrolyte surrogate model.

Ignition delay times and laminar flame speeds of EMC are shown in Figure 5.3 and Figure 5.4, respectively. Overall, the present model reproduces literature data for both ignition delay times and flame speeds of EMC well, especially at the near atmospheric pressure cases. From these validation results as well as by taking the results of ignition delay times and flame speeds of EC mixtures presented in Chapter 4 into account, the present model seems to be appliable for simulating these global combustion properties of carbonate esters, mimicking the LIB fire conditions (elevated temperatures and atmospheric pressure).

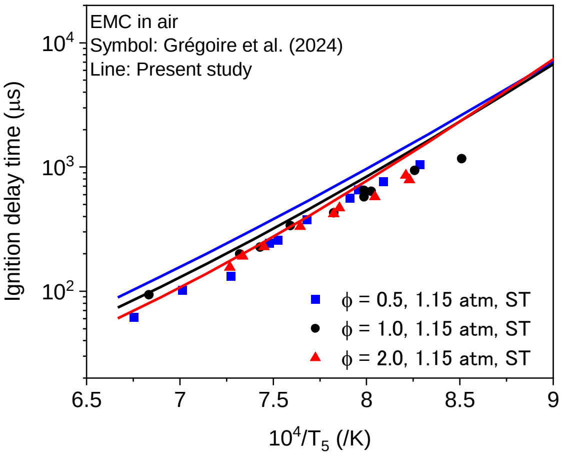

Figure 5.5 Ignition delay times of EMC at various conditions. Symbols are experimental data from the literature [129] and lines are computational results using the present LIB electrolyte surrogate model.

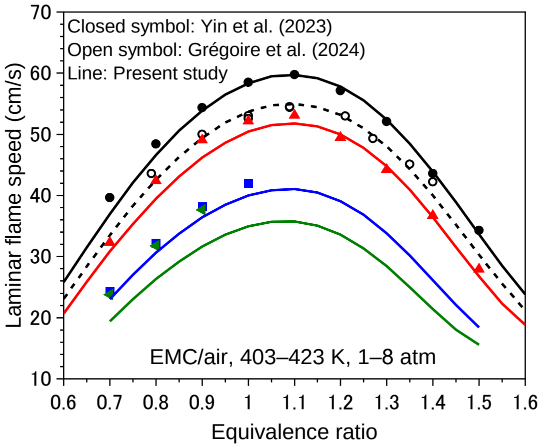

Figure 5.6 Laminar flame speeds of EMC/air at around 400 K and 1–8 atm. Symbols are experimental data from the literature [129,132] and lines are computational results using the

present LIB electrolyte surrogate model.

5.4 *Results and discussion*

5.4.1 *Ignition delay times of carbonate esters*

Ignition delay times of stoichiometric EC/DMC, EC/EMC, and EC/DEC mixtures as well as neat DMC, EMC, DEC and EC in air at 1 atm and above 1200 K are shown in Figure 5.7. When comparing the neat linear carbonate esters (dashed lines), DMC and DEC show almost identical ignition delay times over the temperatures, while EMC shows a longer ignition delay time, especially at a higher-temperature side. Meanwhile, among the multi-component electrolytes (solid lines), EC/DMC mixture shows a slightly shorter ignition delay time as compared to EC/DEC and EC/EMC mixtures above 1300 K, which possess almost the same ignition delay times over the temperature studied. The blending of EC with the linear carbonate esters shows small effect on ignition delay times of DMC and DEC, while shortens that of EMC at higher temperatures. Regardless of the mixtures, all the computational results converge to similar ignition delay times at around 1250 K (ca. 1 ms). Thus, the relationship of ignition delay times among the single-/multi-carbonate esters may differ at lower temperatures.

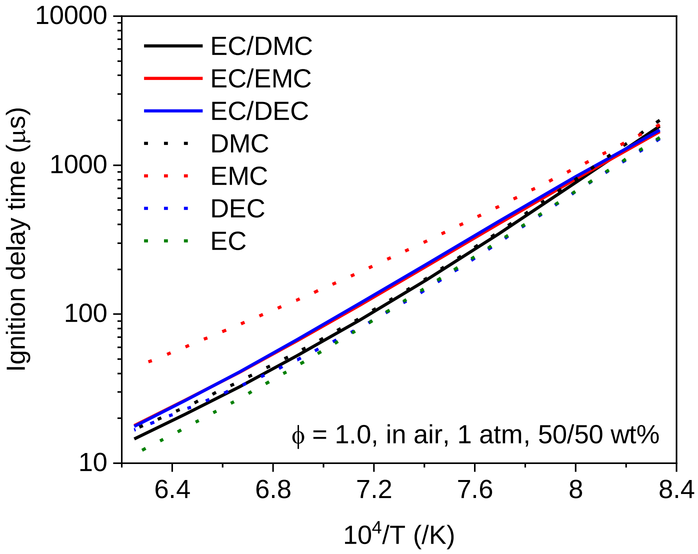

Figure 5.7 Ignition delay times of carbonate ester(s)/air mixtures at ϕ = 1.0 and 1 atm. 50/50 wt% EC/DMC, EC/EMC and EC/DEC mixtures and neat DMC, EMC, DEC and EC as

comparison were simulated using the LIB electrolyte surrogate model.

5.4.2 Laminar flame speeds of carbonate esters

Laminar flame speeds of EC/DMC, EC/EMC and EC/DEC mixtures as well as neat DMC, EMC, DEC and EC at 500 K and 1 atm are shown in Figure 5.8. EC/EMC and EC/DEC mixtures show almost identical results (both around 75 cm/s at $\phi = 1.1$), which are faster than an EC/DMC mixture (69 cm/s at $\phi = 1.1$). This tendency follows the neat DMC, EMC and DEC results, which show faster laminar flame speeds of the latter two carbonate esters that have an ethyl ester group, e.g., 72 cm/s for DMC and 81 cm/s for EMC and DEC at $\phi = 1.1$. Blending EC with the linear carbonate esters decreases the laminar flame speeds of DMC, EMC and DEC. The computed adiabatic flame temperatures at $\phi = 1.1$ were 2291, 2298, and 2307 K for EC/DMC, EC/EMC, and EC/DEC mixtures, respectively, and were 2284, 2299, 2314, and 2295 K for neat DMC, EMC, DEC, and EC, respectively. Thus, there is little difference in the adiabatic flame temperature. Although the amount of EC blended with the linear carbonate esters is larger as compared with H_2/air cases in Section 4.4.4, its effect on laminar flame speed is much smaller in the linear carbonate ester cases due to less influence on the diffusivity.

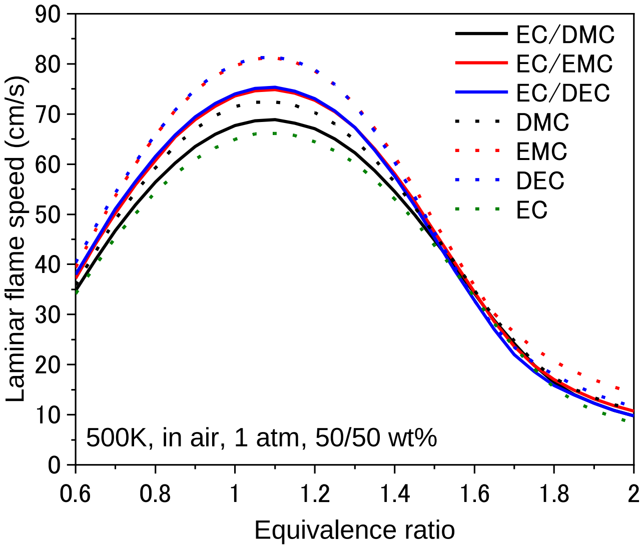

Figure 5.8 Laminar flame speeds of carbonate ester(s)/air mixtures at 500 K and 1 atm. 50/50 wt% EC/DMC, EC/EMC and EC/DEC mixtures and neat DMC, EMC, DEC and EC as

comparison were simulated using the LIB electrolyte surrogate model.

The NFPA fire hazard classification scheme [23,38] as well as the simulated laminar flame speeds of representative electrolyte solvents are compared in Table 5.1. According to the liquid-based fire hazard, EC/DMC is classified into higher flammability than EC/DEC and EC/EMC, whereas the opposite trend is given based on the simulated gas-phase flammability. Thus, gas-phase flammability should also need to be considered depending on the fire situation expected.

Table 5.1 Comparison of the gas-phase and liquid-based fire hazard of multi-component LIB electrolyte solvents.

Electrolyte solvents	Designation	Liquid-base (NFPA 30 [38])	Gas-phase (Laminar flame speed [a])
EC/DMC (1/1 wt/wt)	LP30	Higher (Class I-B)	Slower (69 cm/s)
EC/DEC (1/1 wt/wt)	LP40	Lower (Class I-C)	Faster (75 cm/s)
EC/EMC (1/1 wt/wt)	LP50	Lower (Class I-C)	Faster (75 cm/s)

[a] Simulated in this study with the initial conditions at $\phi = 1.1$, 500 K and 1 atm in air.

5.5 Conclusions

The simulated ignition delay time of a gas-phase EC/DMC mixture is slightly shorter than EC/EMC and EC/DEC mixtures above 1300 K, whereas the simulated laminar flame speed of the former is slower than the latter two. The liquid EC/DMC (50/50 wt%) is classified to be a higher fire hazard category than liquid EC/EMC and EC/DEC (50/50 wt%) according to the NFPA 30 classification scheme [23,38] as shown in Table 1.2, which is determined based on flash point and boiling point. As these properties largely rely on phase changes, LIB fire risk evaluation sorely based on the liquid flammability classification may cause serious misleading, especially when gas-phase carbonate esters are exhausted during the thermal runaway or venting events. Further experimental data on ignition and combustion properties of gas-phase electrolyte solvents not only single- but also multi-component is crucial to assess their fire hazard and to improve model capability.

Chapter 6

Photoelectron characterization of carbonic acid

This chapter aims to introduce the isomer-selective detection tool, i.e., PEPICO technique, by capturing the most fundamental CO_3-moiety, carbonic acid (H_2CO_3), produced from flash pyrolysis of di-*tert*-butyl carbonate. The gas-phase H_2CO_3 was detected conformer-selectively, and its first photoelectron spectrum was obtained using VUV synchrotron radiation and PEPICO spectroscopy. The PEPICO technique will be further applied to investigate the thermal decomposition reaction mechanism of trimethyl phosphate in the next chapter.

6.1 Introduction

Carbonic acid (H_2CO_3, **1**) plays a fundamental role in our daily lives [193] as constituent of the carbonate buffer stabilizing the pH of blood [194,195] and as a contributor to ocean acidification [196,197]. Laboratory experiments have been carried out on the production and spectroscopic characterization of **1** in the condensed phase to investigate its astrochemical role in water-rich ices when abundant CO_2 and CO are present [198–207]. Gaseous carbonic acid, **1**, a long predicted component in extraterrestrial environments [208–210], has only recently been detected towards the Galactic Center molecular cloud G+0.693–0.027 by Yebes and IRAM radio telescope measurements [211]. The chemistry of carbonic acid formation in the interstellar medium (ISM) is suggested to proceed at low temperatures along radical-driven routes on icy dust-grain surfaces yielding *cis* and *trans* HOCO radicals as intermediates, which form **1** upon reaction with a second hydroxyl radical [203]. An electron-driven route followed by radical association reactions to form **1** was also suggested [210]. These pathways may well be active in comets, such as Hale–Bopp, on the icy surfaces of the Galilean moons Europa and Callisto, as well as on Mars [212,213]. Based on computational and IR spectroscopic studies [195,214–216], **1** appears in three conformers with a relative stability of *cis-cis* (**1cc**) > *cis-trans* (**1ct**) ≫ *trans-trans* (**1tt**), as determined by intramolecular H-bonding and shown in Figure 6.1. The formation of **1cc** is further promoted by H atom tunneling in **1ct**, which makes **1cc** likely the most abundant conformer in the ISM, but only **1ct** could be detected by radio astronomy thanks to its higher dipole moment [211].

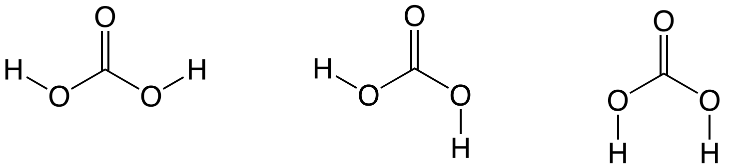

1cc
0 kJ mol^{-1}

1ct
6.7 kJ mol^{-1}

1tt
42.3 kJ mol^{-1}

Figure 6.1 Three conformers of carbonic acid (**1**). Relative energies taken from [195].

The spectroscopic characterization of gas-phase **1** is so far incomplete and limited to the infrared (IR) and microwave ranges. Figure 6.2 shows production and detection methods of gaseous **1**. **1** was first captured by Terlouw et al. [217] by heating up ammonium bicarbonate (NH_4HCO_3) and using electron ionization mass spectrometry for detection. Mori et al. [216,218] produced **1** using a pulsed discharge nozzle with a CO_2/Ar/H_2O and measured the microwave spectrum of both **1cc** and **1ct**. Bernard et al. [219] investigated the IR spectra of **1** in a low temperature Ar matrix produced through protonation of HCO_3^- with HCl in a methanolic solution or with HBr in an aqueous solution [199]. In a series of experiments two polymorphs of solid **1** were discussed (α- and β-polymorph, respectively) [199,212,219]. This assignment was later corrected by the matrix isolation IR spectrum of Reisenauer et al. [195], who produced **1** via twofold isobutene (C_4H_8) loss from di-*tert*-butyl carbonate (DTBC, **2**) during vacuum flash pyrolysis. They found that the methyl ester of carbonic acid caused the feature in the IR spectrum, incorrectly assigned to the a-polymorph [193].

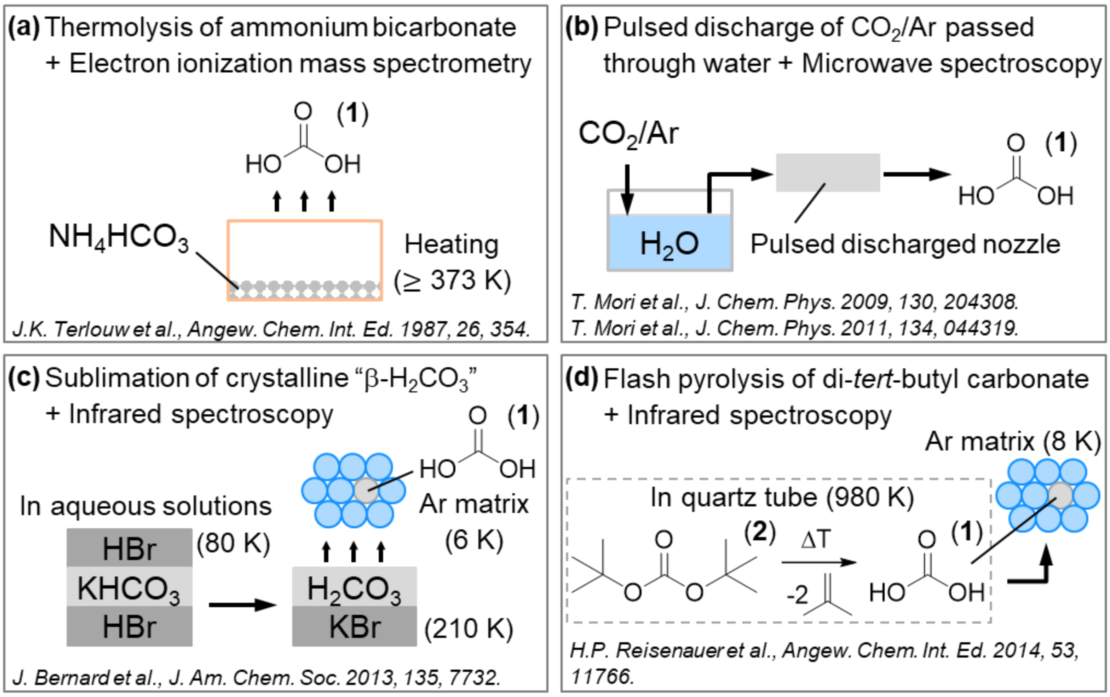

Figure 6.2 Schematics of production and detection methods of gaseous carbonic acid (H_2CO_3).

Multiplexed photoionization [220,221] and photoelectron spectroscopic [222–225] methods offer high sensitivity and selectivity because not only constitutional isomers, but also diastereomers often have different ionization energies (AIE) and vibronic structures. Thus, photoionization methods are utilized as a detection tool, among others, in terrestrial astrochemistry experiments to probe complex reactive environments and reveal gas-phase reaction pathways. Photoelectron photoion coincidence (PEPICO) spectroscopy [99,103] combines mass spectrometry and photoelectron spectroscopy to record photoion mass-selected threshold photoelectron spectra (ms-TPES). This allows for an isomer-selective assignment [99] of reactive intermediates in catalysis [103], combustion [226], and in reactions modeling the ISM [222]. This motivated us to investigate **1** using vacuum ultraviolet (VUV) synchrotron radiation to obtain the threshold photoelectron spectrum, to determine cation energetics and the geometry change upon ionization as driven by the electronic structure of **1**, similar to the approach employed for the picolyl radicals and *m*-xylylene or *m*-benzyne diradicals [227–229]. Our study will enable sensitive and multiplexed laboratory detection of **1** in complex reaction mixtures by means of photoionization and photoelectron spectroscopy. The ionization energies determined in this work are important properties to develop strategies to explore the excited states by resonance-enhanced multiphoton ionization (REMPI) and time-resolved photoelectron spectroscopy.

6.2 Experimental and theoretical approaches

The experiment was conducted utilizing the double imaging photoelectron photoion coincidence (i^2PEPICO) endstation at the vacuum ultraviolet (VUV) beamline of the Swiss Light Source (SLS) located at Paul Scherrer Institute, Switzerland [90,105–107]. Di-*tert*-butyl carbonate purchased from abcr GmbH (95% purity) was used as a precursor to produce carbonic acid (H_2CO_3, **1**) through flash vacuum pyrolysis. The precursor was placed in a container at a pressure of ca. 150 mbar at room temperature between a mass flow controller (MKS Instruments Inc.) and the high-vacuum molecular beam (MB) source chamber (10^{-5} mbar). The vaporized precursor was introduced into a resistively heated Chen-type SiC microtubular reactor [230] (ca. 40 mm length, 1 mm inner diameter, 2 mm outer diameter, and 15 mm heated length) installed in the MB source chamber at a flow rate of 20 sccm argon ($\geq$ 99.998%, PanGas) or helium ($\geq$ 99.996%, PanGas). The correlation between the reactor temperature and output wattage had been calibrated before. The gas temperature close to the reactor centerline is predicted to be approximately 10% lower than the reactor surface temperature [231,232]. Pressure and residence time in the reactor are estimated to be around 10–20 mbar and 10–50 μs, respectively [230–232]. The pyrolyzed gases leaving the reactor expand into high vacuum (10^{-5} mbar), forming a MB. The MB is skimmed using a Model 2 nickel skimmer (Beam Dynamics Inc., 2 mm aperture) and enters the ionization chamber (10^{-7} mbar) of the PEPICO spectrometer, where it is photoionized by VUV synchrotron radiation.

VUV light is provided by a bending magnet, collimated onto a plane blazed grating (150 grooves mm^{-1}) with an energy resolution of 1500, and focused on the exit slit (200 μm). A differentially pumped rare gas filter between the focusing mirror and the endstation, filled with a neon/argon mixture at 8.5 mbar over 10 cm suppresses higher order radiation from the grating [90]. Photoions and photoelectrons are accelerated in opposite directions under a constant electric field of 218 V cm^{-1} and detected by position-sensitive delay line anode detectors (DLD40, Roentdek) in delayed coincidence [108]. This enables time-of-flight (TOF) detection for cations and velocity map imaging (VMI) of both cations and electrons. Photoion mass-selected photoelectron spectrum (ms-TPES) as well as photoionization (PI) spectrum were recorded by scanning the photon energy in 10 meV steps from 11.10 eV to 11.87 eV. As for the ms-TPES, electrons with less than 10 meV kinetic energy were selected based on the photoelectron VMI. The threshold electrons in coincidence with cations in the room-temperature background signals arriving in the TOF range of interest were extracted based on the ion VMI to suppress hot band contributions [113]. Contributions of hot electrons that possess higher kinetic energy without off-axis momentum components were also subtracted [233].

Gaussian 16 [97] and Q-Chem 4.3 [234] were used for the computations. Geometry optimization and vibrational frequency calculations of the ground states were performed at the B3LYP/6-311++G(d,p), ωB97X-D/6-311++G(d,p), M06/6-311++G(d,p), G3, G4, CBS-QB3, CBS-APNO, W1BD, MP2/6-311++G(d,p), and CCSD/cc-pVTZ levels of theory. Cation excited states calculations were performed at the TD-B3LYP/6-311++G(d,p) level of theory. Adiabatic ionization energies were calculated with the aforementioned methods as well as at the (EOM-IP-)CCSD/cc-pVQZ level of theory, while the geometry optimization and vibrational frequencies were calculated utilizing (EOM-IP-)CCSD/cc-pVDZ. Franck–Condon (FC) simulations were performed at 300 K with the Franck–Condon–Herzberg–Teller method implemented in Gaussian 16 [97] and the stick spectra were convolved with a Gaussian function with a full width at half maximum of 33 meV.

6.3 *Results and discussion*

6.3.1 H_2CO_3 production

Carbonic acid (1) was produced by flash pyrolysis of the DTBC (2) precursor diluted in helium or argon following Reisenauer's strategy [195] as shown in Figure 6.3.

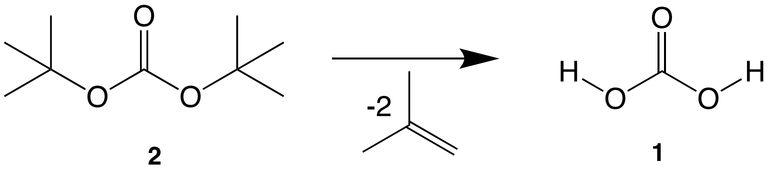

Figure 6.3 Schematics of production methods of gaseous carbonic acid (H_2CO_3) from DTBC pyrolysis.

We attempted to produce H_2CO_3 (**1**) by heating of NH_4HCO_3 (Figure 6.2a) and di-*tert*-butyl carbonate (**2**) (Figure 6.2b) as precursors. In addition to **2**, diethyl carbonate (DEC) was also used as a precursor to produce **1** via twofold ethylene (C_2H_4) loss as suggested by Bucher et al. [235] However, **1** was not sufficiently produced with the method using NH_4HCO_3, similarly reported by Reisenauer et al. [195], and the flash pyrolysis of DEC, being likely due to a competitive yet more preferable reaction channel producing CO_2 and ethanol (having a 20–25 kJ mol^{-1} lower energy barrier) [46,235]. The results shown in the present study are therefore only associated with flash pyrolysis of **2**.

The pyrolysis products expanded into high vacuum and formed a molecular beam. The sample was ionized by VUV synchrotron radiation and detected by PEPICO spectroscopy. Mass spectra at 11.5 eV (Figure 6.4) show that the parent ion of the precursor (*m/z* 174) is not stable and extensive dissociate ionization occurs at room temperature, giving rise to peaks at *m*/*z* 57, 59, 112, 115 and 119. At ca. 760 K a small peak is seen at *m/z* 62, which is assigned to carbonic acid **1**. Isobutene (C_4H_6, *m/z* 56) is formed as a byproduct of the reaction in Figure 6.3. Lower mass products, such as *m*/*z* 28 and 41, are likely produced via parallel decomposition channels of **2** or dissociative photoionization of e.g. isobutene. Increasing the pyrolysis temperature to above 900 K leads to full depletion of **1** producing mainly water and CO_2, emphasizing its elusive and reactive character. Mass spectrum for DTBC/He pyrolysis along with ion velocity map imaging (VMI) of *m/z* 62 are shown in Figure 6.5, providing further evidence that **1** is indeed formed via pyrolysis of **2**.

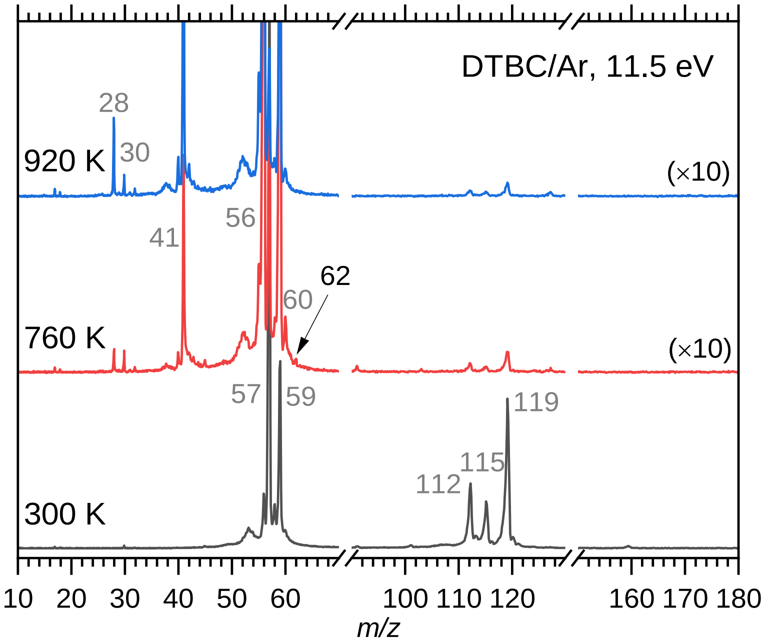

Figure 6.4 Mass spectra at 11.5 eV during the production of gaseous carbonic acid (H_2CO_3, **1**) from DTBC **2**. Extensive fragmentation at 300 K is responsible for the formation of *m/z* 119, 115, 112, 59 and 57. **1** (*m/z* 62) and isobutene (*m/z* 56) are produced in parallel according to Figure 6.3, while **1** rapidly decomposes above 760 K.

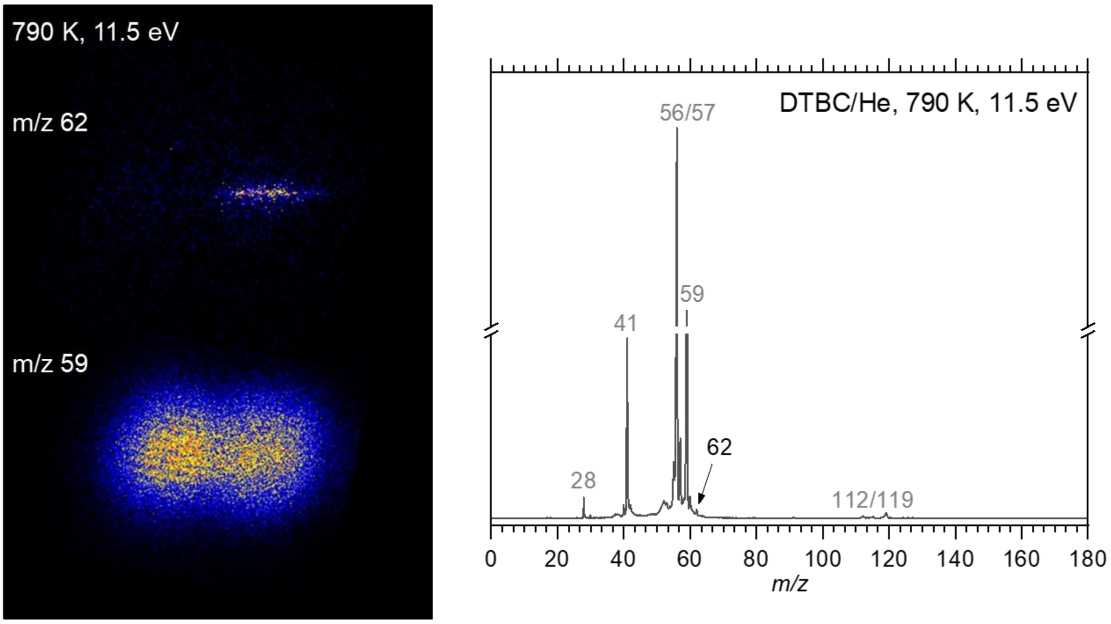

Figure 6.5 (left) Ion velocity map images (VMI) of *m/z* 62 and 59, which indicate that the *m/z* 62 signal results from direct photoionization of pyrolysis products and is not affected by dissociative photoionization (DPI) signal of the precursor **2** or any other pyrolysis intermediate. The VMI of *m/z* 59, on the other hand, shows broadening perpendicular to the MB axis, indicative of kinetic energy release in the dissociative ionization of the precursor **2**. (right) Mass spectrum of di-*tert*-butyl carbonate (**2**) pyrolysis at 790 K diluted with helium at photon energy of 11.5 eV.

6.3.2 Photoelectron characteristics of H_2CO_3

The ms-TPES as well as photoionization (PI) spectrum of room-temperature carbonic acid **1**, formed at a reactor temperature of 790 K are shown in Figure 6.6. The PI spectrum of *m/z* 62 starts to rise at around 11.18 eV and plateaus at 11.7 eV. On the one hand, the PI spectrum of carbonic acid is likely unique among *m*/*z* 62 species but, being broad and featureless, it lacks conformer-selectivity. The ms-TPES of *m/z* 62, on the other hand, clearly shows four intense peaks at 11.27, 11.45, 11.64, and 11.81 eV. Additional low-intensity bands are detected at 11.39, 11.50, 11.59, and 11.70 eV. We calculated adiabatic ionization energies (AIEs) of the three conformers, **1cc**, **1ct**, and **1tt**, using composite and EOM-CCSD methods as shown in Table 6.1, and found them to be 11.29 eV, 11.22 eV, and 11.08 eV, respectively, at the W1BD level of theory. According to the calculated potential energy surface of **1** [195,216], **1tt** is 42 kJ mol^{-1} less stable than **1cc** and **1ct** with a low-energy transition state in between. In thermal equilibrium at 790 K, the relative abundance of **1cc**:**1ct**:**1tt** is predicted to be 2.6:1:4.4×10^{-3} at the W1BD level of theory, meaning that **1tt** is unlikely to contribute to the signal above the detection limit. Thus, based on the ms-TPE and PI spectra, the first intense peak at 11.27 eV in the former and the onset of the latter at 11.18 eV correspond to the AIEs of **1cc** and **1ct**, respectively. These numbers are also in excellent agreement with the W1BD calculations with a difference of 20 and 40 meV for **1cc** and **1ct**, respectively.

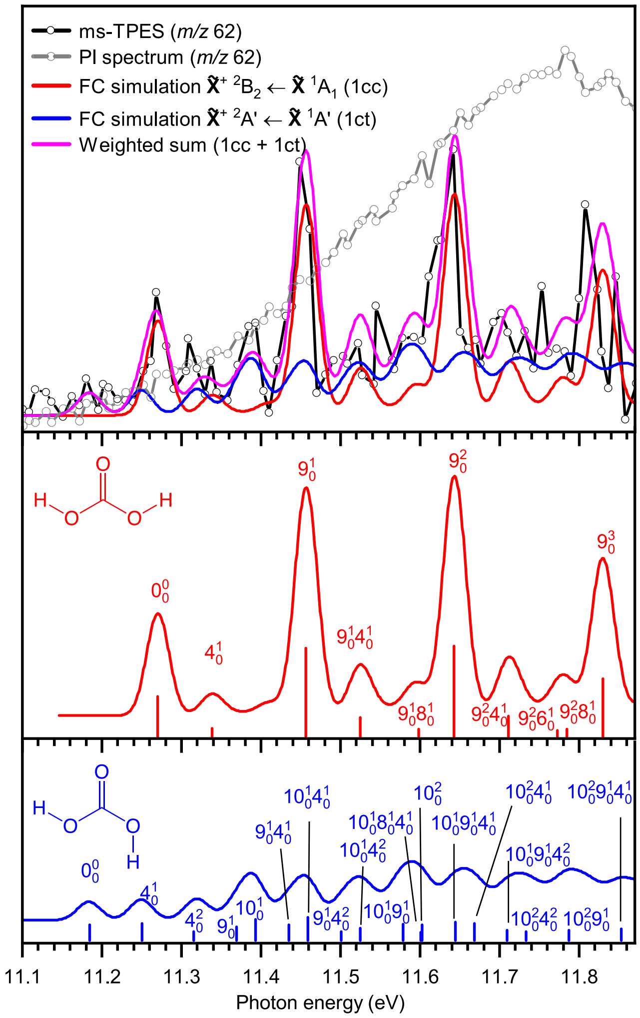

Figure 6.6 Photoion mass-selected threshold photoelectron (ms-TPE) and photoionization (PI) spectra of carbonic acid **1** (black and grey). Colored lines and sticks are Franck–Condon simulations for the transition from neutral to cation ground states of **1cc** (red) and **1ct** (blue) calculated at 300 K and the B3LYP/6-311++G(d,p) level of theory. The lines are convolved with Gaussian functions with a full width at half maximum of 33 meV to account for the rotational envelope. The linear combination of **1cc** and **1ct** (3:1 ratio) is shown in magenta and well represents the features in the experimental spectrum.

Table 6.1 Experimental and calculated ionization energies of the conformers of carbonic acid.

AIE (eV)	1cc	1ct	1tt
Experiment	11.27	11.18 [a]	-
G4	11.23	11.16	11.02
CBS- APNO	11.27	11.21	11.08
W1BD	11.29	11.22	11.08
EOM-IP-CCSD/cc-pVQZ	11.22	11.16	

[a] Determined based on the FC simulation fitted to the ms-TPES.

To assign the conformers of **1** and to obtain spectroscopic insights, Franck–Condon (FC) simulations were fitted to the bands of the ms-TPES (Figure 6.6). The simulation of **1cc** (red lines) is in good agreement with the intense peaks at 11.27, 11.45, 11.64, and 11.81 eV. Thus, the first peak at 11.27 ± 0.02 eV is assigned to the AIE of **1cc**, i.e., the transition into the cations' (**1cc**$^+$) vibrational ground state, in good agreement with the composite method results (Table 6.1). The following intense peaks (11.45, 11.64, and 11.81 eV) are assigned to a C=O/C–OH stretching mode of **1cc**$^+$ (ν_9^+) with a progression of ca. 186 meV (1500 cm^{-1}) (see Figure 6.6). Exciting an HO–C–OH bending mode, ν_4^+, and combination bands of ν_4^+ and ν_9^+ give rise to the low-intensity bands in the ms-TPES at 11.34, 11.52, and 11.71 eV, respectively. However, the FC spectrum of **1cc** does not explain the bands at 11.39, 11.50 and 11.59 eV. This could be remedied by adding the FC simulation of **1ct** (blue lines, Figure 6.6), which, unlike the FC simulation of **1cc**, shows a long progression with few well-resolved peaks. We relied on the most intense of the remaining bands at 11.39 and 11.59 eV to reproduce the missing bands in the ms-TPES using **1ct** FC simulation. This resulted in a good match to all observed features of the experimental spectrum (magenta lines, Figure 6.6). Based on the fitted **1ct** FC spectrum and the rising edge of the PI spectrum, the experimental AIE of **1ct** is determined to be 11.18 ± 0.03 eV, with a slightly larger uncertainty than for **1cc,** justified by varying the AIE by ± 1 one vibrational quantum number of ν_4^+ and in good agreement with the composite method results (Table 6.1). The relative contribution of both FC simulations to the experimental spectrum (Figure 6.6) are 3:1 for **1cc** and **1ct**, respectively, which agrees reasonably well with the expected relative abundance ratio at 790 K (2.6 : 1) if assuming that their photoionization cross sections are nearly equal. This gives further proof that **1cc** and **1ct** are the spectral carriers of the experimental ms-TPES. Major vibrational modes of **1ct**$^+$ are an HO–C–OH bending mode (ν_4^+) and two C=O/C–OH stretching vibrations (ν_9^+ and ν_{10}^+), shown in Figure 6.6. To test the sturdiness of the assignment, we also conducted FC simulations using different levels of theory and found that they were generally consistent with the B3LYP results, which also agreed best with the experimental ms-TPES (not shown here). Thanks to the good overlap of the simulation and the experimental spectra, two conformers of the carbonic acid **1**, **1cc** and **1ct**, can be identified as the spectral carriers of the ms-TPES. Beyond the sensitive detection of **1** in reactive mixtures, the spectra also allow for the assignment of two conformers out of the three possible. The much lower computed ionization energy of the high-energy **1tt** conformer implies that its photoionization signal could likely be assigned selectively, too. Thus, photoelectron spectroscopy is a well-suited tool for the conformer-selective identification of carbonic acid in photoionization-based experiments to unveil the chemistry of the ISM in terrestrial experiments. As the heat of formation of neutral **1** is listed in the Active Thermochemical Tables (ATcT) [236], the experimental ionization energies can be simply added to derive the enthalpies of formation of the cation conformers as $\Delta_f H^o{}_{0K}$ = 485 ± 2 and 482 ± 3 kJ mol^{-1} for **1cc**$^+$ and **1ct**$^+$, respectively. These thermochemical parameters can be utilized to calculate reaction enthalpies in ion–molecule reactions leading to or from **1**$^+$ in astrochemical models [237,238].

Besides acting as a fingerprint for the detection of **1** in reactive mixtures, the ms-TPES provides insights into the geometry change upon ionization, and, thus, into the electronic structure of **1cc** and **1ct**. The highest occupied molecular orbitals (HOMO) of **1cc** and **1ct** are shown in Figure 6.7. Both show nonbonding character at the oxygen atoms. The bare oxygen atom (O2) possesses the largest contribution, while the other two oxygen atoms (O1 and O3) have only smaller ones. Upon ionization of **1cc**, the O1–C–O3 and two H–O–C angles increase (Table 6.2) due to less repulsion from the lone pairs by reducing the electron density on the oxygen atom. Consequently, the C=O bond length elongates while two C–OH bonds shorten, resulting in three almost identical C–O bond distances upon ionization (Table 6.2). This change in the geometry is mirrored by two totally symmetric vibrational modes of **1cc**$^+$ observed in the ms-TPES, the HO–C–OH bending (ν_4^+) and the C=O/C–OH stretching (ν_9^+) vibration. A similar geometry change occurs also in **1ct**, but due to its lower, C_s symmetry, the latter mode splits into two, with asymmetric C–OH stretching contributions (ν_9^+ = 1492 cm^{-1} and ν_{10}^+= 1685 cm^{-1}). This leads to smaller FC factors as compared to **1cc**. The photoelectron spectra of **1cc** and **1ct**, in which the peaks for **1ct** are less intense than **1cc**, were successfully obtained using PEPICO spectroscopy. It is also worth mentioning that the **1ct**$^+$ and **1cc**$^+$ are quasi-isoenergetic at the W1BD level of theory. This, together with a low interconversion barrier (0.32 eV / 31 kJ mol^{-1}, W1BD) suggests close-to equal **1ct**$^+$ and **1cc**$^+$ abundance in equilibrium when the cation is formed by photoionization or ion–molecule reactions.

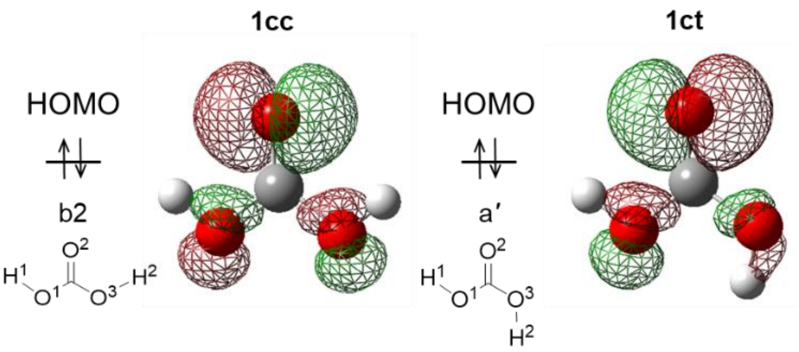

Figure 6.7 Highest occupied molecular orbitals (HOMO) of the two conformers of carbonic acid **1**, (left) **1cc** and (right) **1ct**. The numbering of each atom referred in the discussion is also presented.

Table 6.2 Bond lengths and angles of **1cc** and **1ct** calculated at the B3LYP/6-311++G(d,p) level of theory. See Figure 6.7 for the atom numbering.

Bond length (Å)	**1cc** ($\tilde{\mathbf{X}}\ ^1\mathrm{A}_1$)	**1cc**$^+$ ($\tilde{\mathbf{X}}^{+\,2}\mathrm{B}_2$)	**1ct** ($\tilde{\mathbf{X}}\ ^1\mathrm{A}'$)	**1ct**$^+$ ($\tilde{\mathbf{X}}^{+\,2}\mathrm{A}'$)
O1–H1	0.966	0.979	0.967	0.980
C–O1	1.340	1.279	1.360	1.287
C=O2	1.205	1.277	1.195	1.286
C–O3	1.340	1.279	1.339	1.268
O3–H2	0.966	0.979	0.966	0.979
Bond angle (°)	**1cc** ($\tilde{\mathbf{X}}\ ^1\mathrm{A}_1$)	**1cc**$^+$ ($\tilde{\mathbf{X}}^{+\,2}\mathrm{B}_2$)	**1ct** ($\tilde{\mathbf{X}}\ ^1\mathrm{A}'$)	**1ct**$^+$ ($\tilde{\mathbf{X}}^{+\,2}\mathrm{A}'$)
H1–O1–C	106.9	116.4	107.5	117.0
O1–C–O2	125.7	121.5	125.2	119.3
O1–C–O3	108.7	117.0	110.5	122.5
O2–C–O3	125.7	121.5	124.3	118.2
C–O3–H2	106.9	116.4	109.7	114.5

6.4 Conclusions

In conclusion, carbonic acid (H_2CO_3, **1**) was produced by flash pyrolysis of di-*tert*-butyl carbonate (**2**) [195] and detected utilizing photoelectron photoion coincidence (PEPICO) spectroscopy with vacuum ultraviolet (VUV) synchrotron radiation. Based on the recorded PI spectrum, ms-TPES and Franck–Condon simulations, the two most stable conformers of **1**, *cis-cis* (**1cc**) and *cis-trans* (**1ct**), could be identified. Together with the adiabatic ionization energies, these conformer-specific spectroscopic fingerprints are accessible in the PhotoElectron PhotoIon Spectral COmpendium (PEPISCO) database [94]. Our spectroscopic data lay the foundation for employing photoionization to identify **1cc** and **1ct** in terrestrial photoionization experiments to study astrochemically relevant reactions. In addition, PI and PE spectra enable to performing time-resolved pump–probe experiments. Furthermore, our ms-TPES and computational analyses provide thermochemical parameters, such as ionization energies and heats of formation as well as insights into the electronic structure of **1**, especially regarding molecular orbitals and geometries of both the neutral and cation.

Chapter 6 based on:

K. Kanayama, H. Nakamura, K. Maruta, A. Bodi and P. Hemberger, Conformer-Specific Photoelectron Spectroscopy of the Elusive Carbonic Acid: H_2CO_3, *The Journal of Physical Chemistry Letters*, submitted.

Chapter 7

Pyrolysis of trimethyl phosphate

This chapter investigates pyrolysis mechanisms of trimethyl phosphate (TMP) using PEPICO technique. Quantum chemical calculations are also conducted to confirm and identify the experimentally expected reaction pathways as well as towards a future chemical kinetic modeling of TMP aiming to be included in the LIB electrolyte surrogate model.

7.1 Introduction

Destruction mechanisms of organophosphorus compounds (OPCs) were intensively investigated in flames in the 1990s to early 2000s in a disarmament context, as their molecular structure is similar to that of nerve agents. Trimethyl phosphate (TMP) and dimethyl methylphosphonate (DMMP), shown in Figure 7.1, are typical OPCs. OPCs have also been studied as fire suppressants because phosphorus species can capture H and OH radicals catalytically in flames by reactions (R7-1–7-5) [239–241]:

$$H + PO_2 + M = HOPO + M \qquad \text{(R7-1)}$$

$$H + HOPO = H_2 + PO_2 \qquad \text{(R7-2)}$$

$$OH + HOPO = H_2O + PO_2 \qquad \text{(R7-3)}$$

$$OH + PO_2\ (+M) = HOPO_2\ (+M) \qquad \text{(R7-4)}$$

$$H + HOPO_2 = H_2O + PO_2 \qquad \text{(R7-5)}$$

The chemical inhibition effectivity of OPCs has, therefore, been assumed to be determined by how rapidly they reach this catalytic cycle by producing PO_2, HOPO and $HOPO_2$ species. Understanding the destruction mechanism of OPCs and the formation of these phosphorus-containing intermediates during pyrolysis, ignition, and combustion is thus important to rationalize their use as fire suppressants.

In light of the growing use of lithium-ion batteries (LIBs), LIB fire safety has become an urgent issue, especially for large-scale LIBs in the transportation and energy sectors. Owing to their good solubility in commercially used carbonate ester solvents, e.g., ethylene carbonate and dimethyl carbonate, TMP and DMMP are promising fire-retardant additive candidates for LIB electrolytes. In a LIB fire scenario where the electrolytes as well as OPC additives vaporize and are vented outside the cell, understanding and modeling their gas-phase chemistry is crucial to mitigate the LIB fire incident.

The consequences of TMP and DMMP addition to H_2 and C_1–C_3 hydrocarbon fuels on flame and ignition were investigated experimentally by several groups. Korobeinichev et al. studied the effect of adding TMP [240,242,243] and DMMP [244,245] to H_2, CH_4, and C_3H_8 flames. Knyazkov et al. and Jayaweera et al. followed up by studying TMP addition to a CH_4 flame [246] and DMMP addition to a C_3H_8 flame [49]. Mathieu et al. reported the effect of DMMP addition to H_2, CH_4, and C_2H_4 on their ignition delay times [241], while Sike et al. investigated its influence on flame speeds of H_2 and CH_4 [169]. Experimental studies on the chemistry of neat OPC molecules are, however, few and far between to understand the initial gas-phase chemistry of the flame-retardant action. Liang et al. investigated neat DMMP pyrolysis and oxidation [247,248]. Neupane et al. conducted CO laser absorption measurements during DMMP pyrolysis and oxidation [249]. More recently, Jing et al. performed DMMP pyrolysis experiment using a jet-stirred reactor [250]. Nevertheless, few experiments have been carried out on neat TMP to the best of our knowledge. The difference between TMP and DMMP is only a methyl group, which is swapped for a methoxy group in the former (Figure 7.1). In the case of DMMP, PO_2, one of the key phosphorus-containing intermediates in the OPC chemical inhibition mechanism (R7-1–7-5), was only produced under oxidative conditions, and the decomposition of neat DMMP gave rise to PO [247,248]. Thus, the question arises if adding another oxygen atom to DMMP, i.e., TMP, changes the decomposition mechanism to produce PO_2 in non-oxidative conditions at its early stage. To answer this question, a detailed understanding of the TMP unimolecular decomposition is important, especially for its kinetic modeling. For instance, a currently available chemical kinetic model of TMP [49] includes only bond-dissociation reactions accounting for the unimolecular decomposition of TMP.

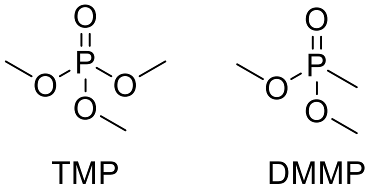

Figure 7.1 Molecular structures of trimethyl phosphate (TMP) and dimethyl methylphosphonate (DMMP).

This study aims to reveal the initial thermal decomposition mechanism of TMP as a first step towards the inclusion of TMP kinetics in our LIB electrolyte surrogate model [48]. We investigated the unimolecular thermal decomposition of TMP in a pyrolysis microreactor using vacuum ultraviolet (VUV) synchrotron radiation and photoelectron photoion coincidence (PEPICO) spectroscopy. Based on the experimental results supported by quantum chemical calculations, TMP thermal decomposition pathways are provided. In addition, the difference between TMP and DMMP unimolecular decomposition is discussed. Such results contribute to chemical kinetic modeling of TMP as well as DMMP.

7.2 Experimental method of PEPICO

To detect and identify phosphorus-containing, oxygenated, and hydrocarbon intermediates including radicals, isomer-selectively, double imaging photoelectron photoion coincidence (i^2PEPICO) spectroscopy with tunable VUV synchrotron radiation [106,107] was used. The photoionization cross sections of phosphorus-containing intermediates are generally not available. Although this makes quantification of the measured species elusive, the i^2PEPICO technique has a great multiplexing advantage, which allows us to explore the gas-phase chemistry of complex reactions ranging from pyrolysis and combustion to catalysis

[99,112,251], where fleeting reactive intermediates could be identified along with abundant reactants and product isomers.

TMP flash vacuum pyrolysis measurements were conducted at the *i*²PEPICO endstation at the VUV beamline of the Swiss Light Source, located at Paul Scherrer Institute [90,105]. TMP was purchased from Sigma-Aldrich (purity ≥ 99%). The liquid sample was vaporized at a temperature of 10 °C in ca. 0.1 bar helium (≥ 99.996%, PanGas), resulting in a mixture of 0.04% TMP. The gas was expanded at a flow rate of 14 sccm from a 0.2 mm nozzle into a SiC microtubular reactor [230] (1 mm inner diameter, 2 mm outer diameter, ca. 40 mm length) placed in a high-vacuum chamber (10^{-5} mbar). The reactor was resistively heated up to ca. 1400 K by applying a DC voltage over a 15 mm long heated zone. The correlation between the reactor temperature and output wattage had been calibrated previously. The gas temperature close to the reactor centerline along the flow direction is predicted to be approximately 10% lower than the reactor surface temperature [231,232]. Pressure and residence time in the reactor are estimated to be ca. 10–20 mbar and 10–50 μs, respectively [230–232]. The exhaust gases containing precursors, intermediates, and products expand into high vacuum, forming a molecular beam (MB), which is introduced into the ionization chamber (10^{-6} mbar) through a 2 mm skimmer.

The sample was photoionized by monochromatic VUV light. The resulting photoelectrons and photoions were detected in delayed coincidence [108]. This provides time-of-flight (TOF) mass spectra and velocity map images (VMIs) of both ions and electrons. By scanning the photon energy in 20 meV steps and selecting electrons with less than 7 meV kinetic energy based on the electron VMI for the cation TOF range of interest, photoion mass-selected threshold photoelectron spectra (ms-TPES) were recorded. The ion VMI enables us to distinguish ion signals due to ionization of the MB from the scattered, rethermalized room-temperature background (RT-BG) signal component [113]. In addition, the ion VMI can identify whether a signal possesses kinetic energy release in the MB component, which is indicative of dissociative photoionization (DPI, see Section 7.4.1 and Figure 7.3) [99].

7.3 Quantum chemical calculations

Franck–Condon (FC) simulations were performed to assign spectra for which reference ms-TPES are not available in the literature or in a database [94]. Geometry optimization and vibrational frequency calculations of neutral and cation ground states were conducted at the B3LYP/6-311++G(d,p) level of theory. FC simulations were performed utilizing the Franck–Condon–Herzberg–Teller method as implemented in Gaussian 16 [97]. FC stick spectra were convolved with a Gaussian function with a full width at half maximum of 33 meV to account for the rotational envelope and for comparison with the experimental data. Adiabatic ionization energies were calculated using the CBS-QB3 composite method.

Unimolecular decomposition channels of TMP were also theoretically investigated. Geometry optimizations and vibrational analyses of minima and transition states were initially carried out at the B3LYP/6-31G(2df,p) level of theory, and then recalculated at the G4 composite method as implemented in Gaussian 16 [97].

7.4 Results and discussion

Experimental results are presented in Section 7.4.1. Theoretical calculations of TMP unimolecular decomposition channels are described in Section 7.4.2. Based on these results, the reaction pathways of TMP unimolecular decomposition are discussed in Section 7.4.3. Finally, we compare the unimolecular decomposition of TMP and DMMP in Section 7.4.4.

7.4.1 Species measurements using i^{2}PEPICO spectroscopy

Temperature-dependent mass spectra for TMP pyrolysis recorded at a photon energy of 11.5 eV are depicted in Figure 7.2. To avoid a strong BG signal of *m/z* 140 due to the persistent signal of the low vapor-pressure TMP in the chamber, only MB signals are plotted.

The adiabatic ionization energy of TMP (*m/z* 140) was reported to be 10.0 eV [252] and was also calculated to be 10.0 eV at the CBS-QB3 level of theory herein. At 300 K, the signal at *m/z* 140 corresponds to the TMP molecular ion, whereas the peaks at *m/z* 80 and 110 represent daughter ions of *m/z* 140 formed by dissociative ionization. As the temperature increases to 750 K, the signal at *m/z* 140 decreases while the *m/z* 110 signal increases. Aside from a lateral broadening of the MB in the ion VMI (Figure 7.3a), the asymmetric peak shape at *m/z* 110 is further evidence for DPI of a metastable parent ion [253]. At 1030 K, peaks appear at *m/z* 30, 32, 78 and 95. Based on the ion VMI images, the *m/z* 95 signal showed a kinetic energy release distribution, while the *m/z* 78 as well as the *m/z* 30 and 32 signals showed a narrow MB component (see Figure 7.3b for *m/z* 30). The latter three peaks therefore correspond to direct ionization of the pyrolysis products formed in the reactor. At 1100 K, signals at *m/z* 15, 46, 47, 48 and 64 increase, while the signal at *m/z* 110 decreases. The signals at *m/z* 15, 46, 47, 48 and 64 are also decomposition products occurring in the reactor as shown in Figure 7.3c for the case of *m/z* 47. With further increase of the reactor temperature, the *m/z* 110 peak, most likely due to a TMP DPI fragment ion, disappears, while the signals of species below 64 amu increase. Thus, TMP is fully converted to intermediates and products at 1320 K. To identify the spectral carriers isomer-selectively, ms-TPES were recorded by scanning the photon energy at 1150 K, at which temperature pyrolysis intermediates were produced in abundance.

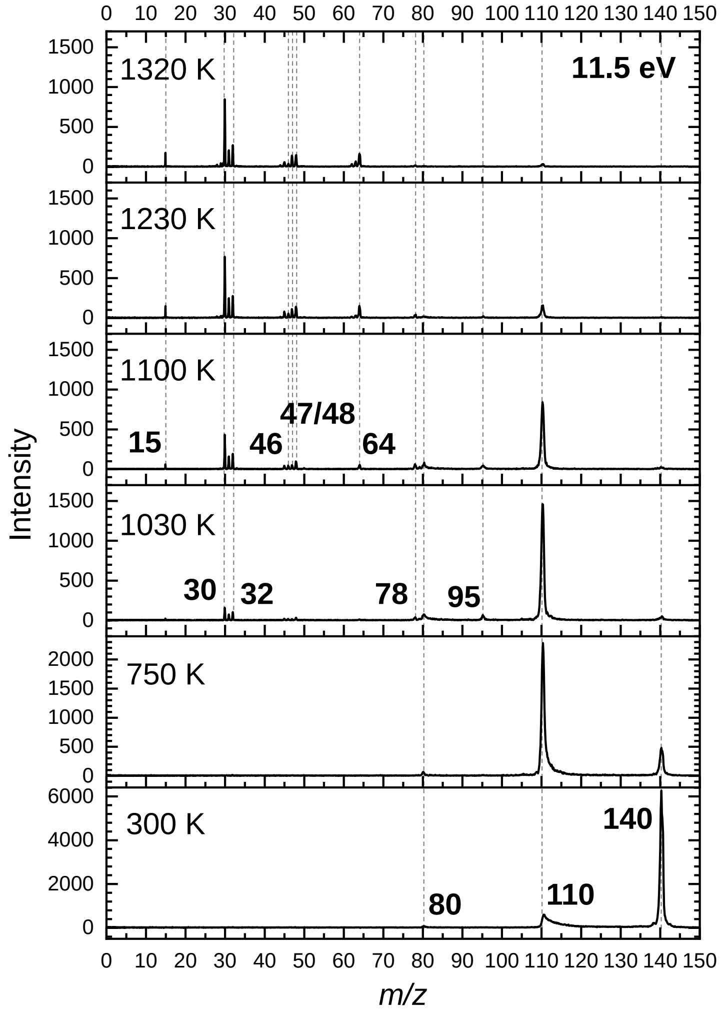

Figure 7.2 Temperature-dependent photoionization mass spectra of TMP/He mixtures recorded at 11.5 eV. TMP is 140 amu.

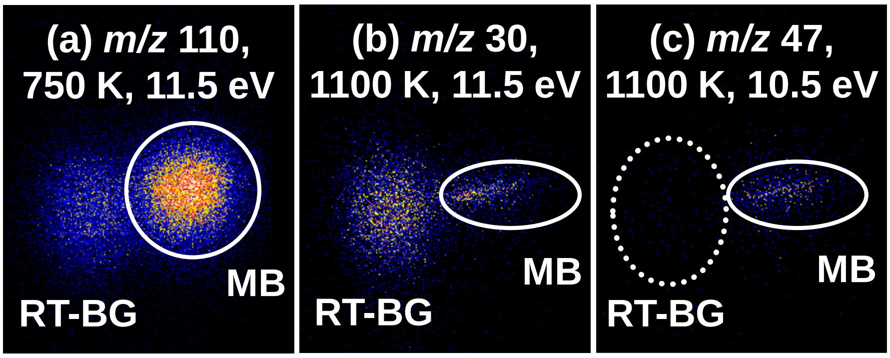

Figure 7.3 Representative ion velocity map images (VMIs) of (a) *m*/*z* 110, (b) *m*/*z* 30 and (c) *m*/*z* 47. (a) The lateral broadening of the molecular beam (MB) component is due to kinetic energy release, which is indicative of dissociative photoionization, (b and c) while the narrow distribution explains direct photoionization of sampled species. Restricting the ion signals to the MB component ensures indeed probing the exhaust of the reactor directly, but the MB spectra (MB ms-TPES) suffers from hot and sequence band transitions due to limited expansion cooling [28]. Thus, peak broadening and red shift affect the bands in the MB ms-TPES, while the room-temperature background (RT-BG) signal in the VMI gives rise to room-temperature spectra (BG ms-TPES) as recently shown [28]. However, wall collisions may lead the sampling effects. Certain TMP pyrolysis products, for instance, show only MB components, as an example shown in (c) (*m*/*z* 47).

By using ion VMI, we can distinguish the direct MB signal from that of the rethermerized room-temperature background (RT-BG) [112]. Thus, the ms-TPES can be plotted in coincidence with the RT-BG or with the MB. Recorded ms-TPES of *m/z* 15, 30, 32, 46, 47, 48, 64, 78, and 140 along with reference spectra are presented in Figure 7.4. Although there are slight differences between the BG and MB ms-TPES of *m/z* 15, 30, 32, and 46 (Figure 7.4a–d), most notably a slight red shift (i.e., a shift to lower photon energies) and broadening of peaks in the MB ms-TPES, due to the higher effective temperature in the MB [113], both BG and MB ms-TPES can be used to identify species. For the spectra in Figure 7.4a–d, methyl radicals (CH_3), formaldehyde (CH_2O), methanol (CH_3OH), and dimethyl ether (CH_3OCH_3, DME) can be assigned by comparison with reference ms-TPES [254–257]. Only MB ms-TPES could be obtained in the *m/z* 47, 48, and 64 channels, and the RT-BG signal was negligible (Figure 7.4e–g, see also Figure 7.3c for the ion VMI of *m/z* 47), indicating that the carriers of these peaks do not survive wall-collisions [112,113]. Based on calculated ionization energies and Franck–Condon (FC) simulations, 47 and 48 amu are assigned to be phosphorus monoxide (PO) and oxophosphane (HPO) with ionization energies of 8.4 eV [258] and 10.4 eV (CBS-QB3), respectively. As for 64 amu, the *trans*-/*cis*-HOPO conformers as well as HPO_2 contribute to the ms-TPES. Their calculated ionization energies are 10.9, 11.1, and 12.5 eV, respectively, confirming our assignment. Apart from these, excited cation states of HOPO may also contribute to the spectra at around 12.4 eV [248]. The ms-TPES of *m/z* 78 shows slight differences between the RT-BG and the MB. The RT-BG ms-TPES is well-reproduced by the FC simulation of $O{=}PHOCH_2$ and *cis*-$OPOCH_3$, of which calculated ionization energy is 10.4 and 10.5 eV, respectively. The MB ms-TPES, on the other hand, shows a red shift and additional bands, especially at 10.4 eV and 11.7 eV. The red shift may be caused by additional hot bands in the $O{=}PHOCH_2$ and *cis*-$OPOCH_3$ spectra, or isomerization may take place upon wall collisions during rethermalization. Regarding further PO_2CH_3 isomers in the MB ms-TPES, *trans*-$OPOCH_3$ and CH_3PO_2, with calculated ionization energies of 10.3 and 11.6 eV, respectively, can also be carriers of the spectrum. As the FC spectra of *trans*-$OPOCH_3$ and PO_2CH_3 match the additional bands well, they are tentatively assigned herein. Overall, the comparison of direct sampling MB and RT-BG ms-TPES indicate that $C_xH_yO_z$ species survive wall collisions and are rethermalized efficiently to be detected in the BG, whereas phosphorus-containing species hardly survive wall collisions and condense on the chamber wall, rearrange, or are destroyed (e.g., PO shown in Figure 7.3c), resulting in them only being detectable in the MB. The advantages of direct MB analysis to address sampling effects by ion VMI in double imaging technique i^2PEPICO are, thus, made evident in measuring involatile or unstable species in complex reactive mixtures. Nevertheless, it should be noted that PO_2 (63 amu) was not detected in the present TMP thermal decomposition experiment.

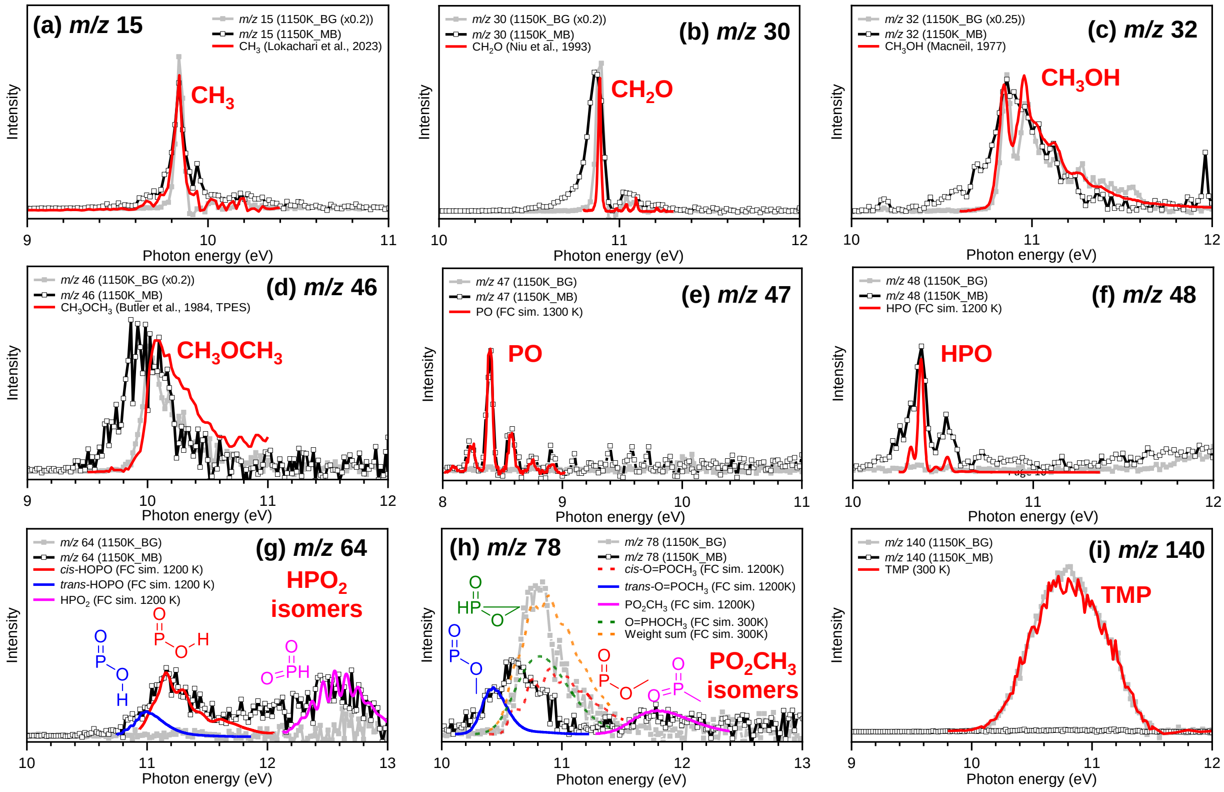

Figure 7.4 Photoion mass-selected threshold photoelectron spectra (ms-TPES) of TMP unimolecular thermal decomposition products. Gray and black lines with square plots are experimental spectra obtained at 1150 K. Colored lines are reference spectra obtained at room temperature (TMP), from literature (CH_4 [254], CH_2O [255], CH_3OH [256] and CH_3OCH_3 [257]) and by Franck–Condon (FC) simulations (PO, HPO, HPO_2 isomers and PO_2CH_3 isomers).

7.4.2 Theoretical calculations for TMP unimolecular decomposition

TMP unimolecular decomposition was explored by quantum chemical calculations. The calculated potential energy surface is illustrated in Figure 7.5. Molecular structures of the transition states are presented in Figure 7.6.

A hydrogen-transfer isomerization of TMP via TS1a possesses the lowest energy barrier at 65.9 kcal/mol:

$$\mathrm{TMP} = \mathrm{POH(OCH_3)_2(OCH_2)} \qquad \text{(R7-6a)}$$

This channel is followed by CH_3OH production via TS1b (72.9 kcal/mol) or PO–CH_3 bond dissociation (73.7 kcal/mol):

$$\mathrm{POH(OCH_3)_2(OCH_2)} = \mathrm{PO(OCH_3)(OCH_2)} + \mathrm{CH_3OH} \qquad \text{(R7-6b)}$$

$POH(OCH_3)_2(OCH_2) = PO(OH)(OCH_3)(OCH_2) + CH_3$ (R7-6c)

A direct CH_3OH loss channel from TMP producing the same products as R7-6b via TS3 shows a higher barrier at 90.3 kcal/mol:

$PO(OCH_3)_3 = PO(OCH_3)(OCH_2) + CH_3OH$ (R7-7)

The barrier heights of hydrogen-transfer channels leading to CH_2O from TMP are found to be 97.3 and 100.3 kcal/mol (TS4 and TS5), respectively, which are energetically even less preferable. The second energetically accessible dissociation channel proceeds via a methyl-transfer (TS2, 73.5 kcal/mol) leading to $PO_2(OCH_3)$ and DME:

$TMP = PO_2(OCH_3) + CH_3OCH_3$ (R7-8)

The barrier to the O–CH_3 bond-dissociation channel is found to be 89.0 kcal/mol:

$TMP = PO_2(OCH_3)_2 + CH_3$ (R7-9)

which is comparable to TS3, while the P–OCH_3 bond cleavage is much more endothermic (111.9 kcal/mol), making this reaction less accessible.

Additional quantum chemical calculations were carried out to investigate the fate of $PO(OCH_3)(OCH_2)$ and $PO_2(OCH_3)$, the OPC counter-products of CH_3OH and DME (R7-6b/R7-7 and R7-8), respectively, and will be discussed in the following part.

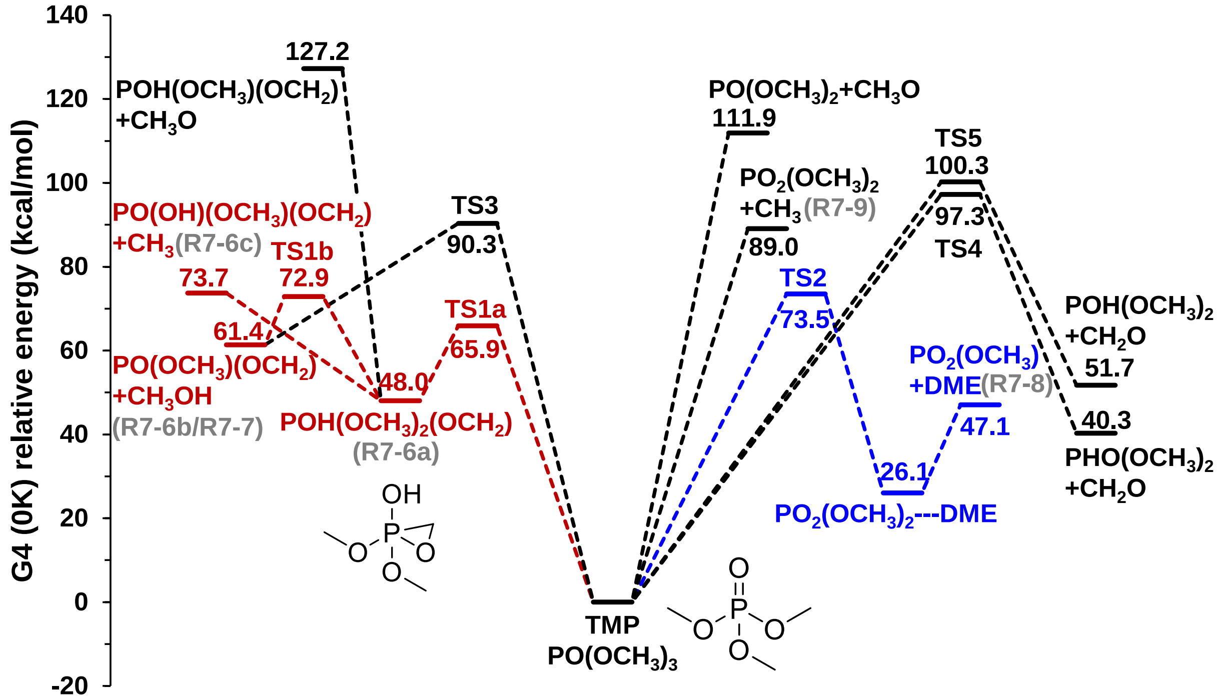

Figure 7.5 Potential energy surface of TMP unimolecular decomposition calculated at the G4 level of theory. The energies are relative to that of TMP (including zero-point energy correction). Reaction numbers referred in the text are also shown.

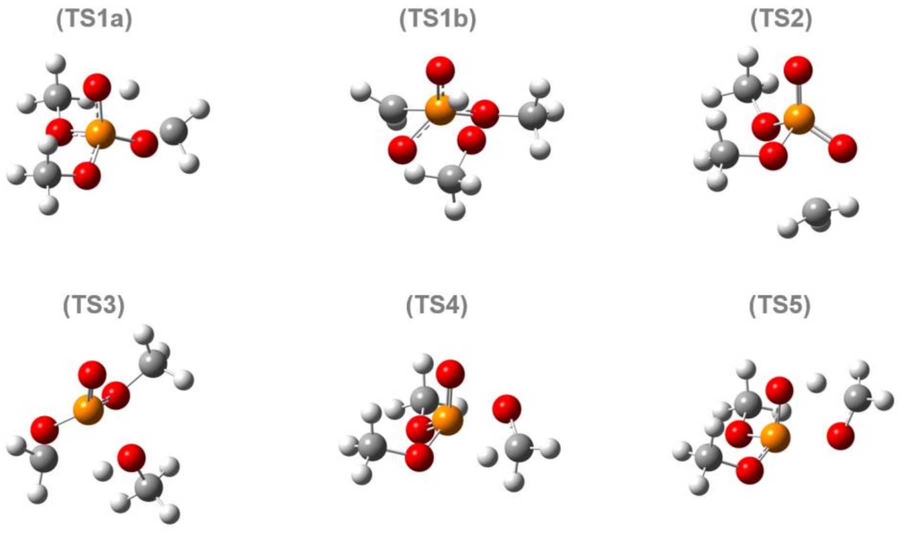

Figure 7.6 Transition state structures referred to in the text.

7.4.3 *TMP unimolecular thermal decomposition mechanism*

Based on the experiments and calculations, possible unimolecular decomposition pathways of TMP are summarized in Figure 7.7. The two isomerization channels are the major initiation pathways for the TMP decomposition, i.e., hydrogen- and methyl-transfer reactions (R7-6a and R7-8, respectively).

The former is followed by hydrogen transfer producing CH_3OH and $PO(OCH_3)(OCH_2)$ (108 amu) through R7-6b or by O–CH_3 bond dissociation producing CH_3 and $PO(OH)(OCH_3)(OCH_2)$ radicals (125 amu) through R7-6c. By performing additional calculations for $PO(OCH_3)(OCH_2)$ (108 amu) decomposition, we found a CH_2O-loss channel with a 36.6 kcal/mol barrier, leading to CH_3OPO (78 amu), as shown in Figure 7.8. CH_3OPO may isomerize and decompose into HPO and CH_2O or dissociate directly to CH_3 + PO_2/CH_3O + PO [259]. The absence of PO_2 in the present experiment may be due to the dominance of O=$PHOCH_2$, formed from CH_3OPO by hydrogen-transfer, thus suppressing the CH_3 + PO_2 channel. The formation of the $PO(OH)(OCH_3)(OCH_2)$ radical (125 amu) is followed by P–OCH_2 *b*-scission to afford *m/z* 95, which then decomposes to $HOPO_2$ + CH_3 or HOPO + CH_3O. However, $HOPO_2$ could not be identified in the experiment due to interference from TMP DPI, as discussed previously.

The intermediate from the methyl-transfer isomerization of TMP, $PO_2(OCH_3)$ (94 amu) is produced together with DME (R8). $PO_2(OCH_3)$ can isomerize via hydrogen transfer, followed by HOPO and CH_2O production over barriers of 66.3 and 52.2 kcal/mol, respectively (Figure 7.9). The larger intermediates, such as 94, 108 and 125 amu, were not observed in the experiment due to their rapid decomposition owing to the secondary reaction barriers being lower than the primary ones, as also observed in other OPCs [247,248]. However, thanks to their decomposition products and quantum chemical calculations, the likely TMP unimolecular decomposition pathways could still be established.

These pathways account for the formation of CH_3, CH_2O, CH_3OH, DME, PO, HPO, HOPO and CH_3PO_2 isomers observed in the experiment. PO_2 seems not to be a major product of the unimolecular thermal decomposition of TMP, similarly to DMMP. The TMP decomposition pathway producing DME (R7-8) was newly found in the experiment and confirmed by calculations.

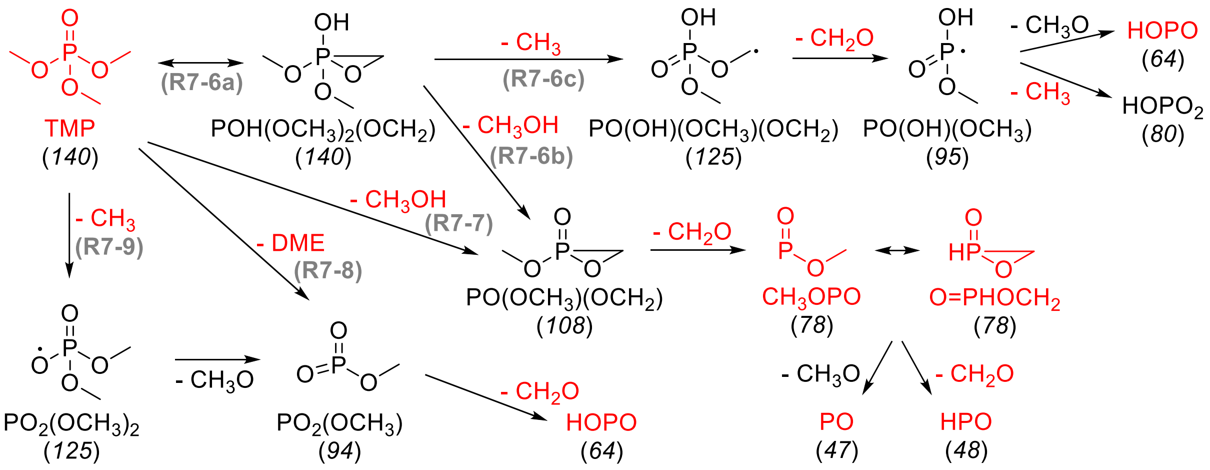

Figure 7.7 Unimolecular reaction pathways in TMP thermal decomposition. Detected species in this study are marked as red. Mass of each species is shown in *italic*.

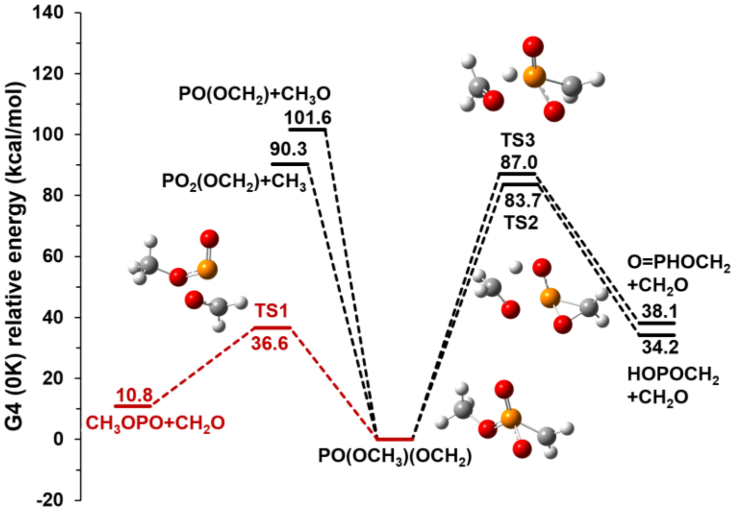

Figure 7.8 Decomposition channels of O=P(OCH$_3$)(OCH$_2$) (108 amu) producing 78 amu by losing CH$_2$O plotted together with the PO–CH$_3$ and P–OCH$_3$ bond-dissociation channels.

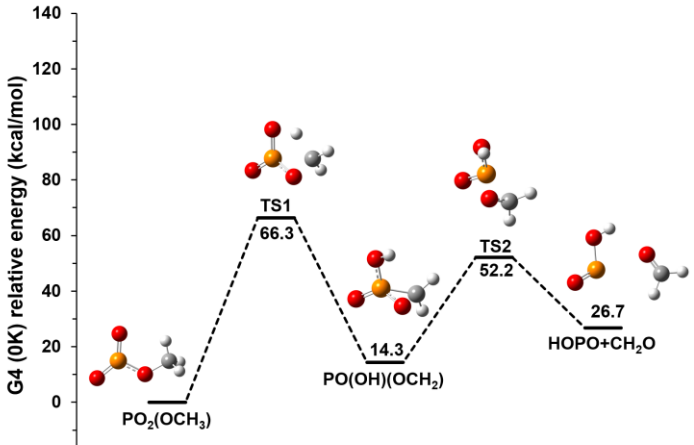

Figure 7.9 The decomposition channel of PO$_2$(OCH$_3$) (94 amu) producing HOPO and CH$_2$O.

7.4.4 Comparison with DMMP unimolecular decomposition

As shown in Figure 7.1, the structural difference in TMP and DMMP is just a single O atom, i.e., TMP contains three methoxy groups, whereas DMMP involves two methoxy groups and a methyl group. Jing et al. [250] calculated the potential energy surface of DMMP unimolecular decomposition at the CCSD(T)/CBS//MN15/6-311+G(2df,2p) level. Decomposition and isomerization channels involving the methyl group in DMMP are disregarded for the comparison with TMP herein. The lowest energy barriers were the hydrogen-transfer isomerization (60.8 kcal/mol), O–CH_3 bond-dissociation (86.5 kcal/mol) and direct CH_3OH production (87.7 kcal/mol) channels:

$$\text{DMMP} = \text{POH(OCH}_3\text{)(OCH}_2\text{)(CH}_3\text{)} \qquad \text{(R7-6a')}$$

$$\text{DMMP} = \text{PO}_2\text{(OCH}_3\text{)(CH}_3\text{)} + \text{CH}_3 \qquad \text{(R7-9')}$$

$$\text{DMMP} = \text{PO(OCH}_2\text{)(CH}_3\text{)} + \text{CH}_3\text{OH} \qquad \text{(R7-7')}$$

The major isomerization and decomposition channels are similar between TMP and DMMP except for channels involving the methyl group for DMMP. Note that the transition state of hydrogen-transfer isomerization of DMMP (R7-6a’) was calculated to be 62.5 kcal/mol at the G4 level in the present study. A major difference between the TMP unimolecular decomposition discussed here and the DMMP unimolecular decomposition from the literature is the DME production channel. In the present study, we found the barrier to DME production channel from TMP (R7-8) lying between R7-6a and R7-7/R7-9, while that in DMMP has not been reported so far. To identify whether this reaction channel is unique to TMP or also presents in DMMP, we explored this channel in DMMP. Indeed, we found a methyl-transfer transition state leading to DME in the DMMP unimolecular decomposition as well, at an energy barrier of 70.3 kcal/mol at the G4 level of theory:

$$\text{DMMP} = \text{PO(OCH}_2\text{)(CH}_3\text{)} + \text{DME} \qquad \text{(R7-8')}$$

Although DME was observed in the DMMP pyrolysis experiment by Jing et al. [250], they did not discuss its provenance. Our study sheds light on new reaction channels in the decomposition of not only TMP but also DMMP, giving rise to DME. Energetically favorable isomerization channels are sometimes overlooked in chemical kinetic models [260] as they may be pressure-dependent and overtaken by bond-dissociation reactions, especially in the high-pressure limit [261]. However, finding those isomerization channels and validating models are essential to determining their impacts on model predictions. As the currently available TMP chemical kinetic model [49] only includes bond-dissociation reactions (i.e., methyl, methoxy, and hydrogen loss) as unimolecular decomposition channels, those found in the present study may need to be included, and can also be applied to the DMMP model [250].

7.5 Conclusions

The formation of intermediates during thermal decomposition of trimethyl phosphate (TMP) was experimentally investigated utilizing vacuum ultraviolet (VUV) synchrotron radiation and double imaging photoelectron photoion coincidence (i^2PEPICO) spectroscopy. Phosphorous-containing species such as PO, HPO, HPO_2, and PO_2CH_3 isomers as well as CH_3, CH_2O, CH_3OH, and DME were isomer-selectively identified by their photoion mass-selected threshold photoelectron spectra (ms-TPES). Quantum chemical calculations performed for the TMP unimolecular decomposition indicate that hydrogen-transfer isomerization (R7-6a) followed by CH_3OH/CH_3 production (R7-6b/R7-6c) and methyl-transfer isomerization leading to the DME production (R7-8) are energetically preferable channels. The latter channel is also found in the unimolecular decomposition of dimethyl methylphosphonate (DMMP) and is newly reported. These reaction pathways need to be considered in chemical kinetic models as they potentially impact the model predictions. The proposed mechanism of unimolecular thermal decomposition of TMP can contribute to understanding and mitigating LIB fires, by integrating a TMP model with the LIB electrolyte surrogate model [48].

Chapter 7 based on:

K. Kanayama, H. Nakamura, K. Maruta, A. Bodi and P. Hemberger, Unimolecular Thermal Decomposition of Trimethyl Phosphate: A Combined Vacuum Ultraviolet Photoionization and Theoretical Investigation, *Proceedings of the Combustion Institute*, submitted.

Chapter 8

Conclusions

8.1 Summary of this thesis

This dissertation aimed to understand and model the pyrolysis and oxidation mechanisms of carbonate and phosphate esters through experimental, computational, and theoretical investigations. The goal of this project is to construct a comprehensive LIB surrogate chemical kinetic model that includes flammable carbonate ester solvents as well as fire-retardant additives such as phosphate esters. To this end, this dissertation worked on the principal electrolyte components, i.e., ethylene carbonate (EC), dimethyl carbonate (DMC), diethyl carbonate (DEC) and ethyl methyl carbonate (EMC), as well as a representative fire-retardant additive candidate, trimethyl phosphate (TMP). Pyrolysis and oxidation experiments were conducted using various tools, namely a micro flow reactor with a controlled temperature profile (MFR), shock tube, constant volume vessel for spherically propagating flame measurements and photoelectron photoion coincidence (PEPICO) setup. The first chemical kinetic model that covers the linear (DMC, DEC and EMC) and cyclic (EC) carbonate esters, the LIB electrolyte surrogate model, was constructed in this dissertation. With the LIB electrolyte surrogate model, combustion and ignition characteristics of multi-component electrolyte solvents were simulated. Apart from the LIB electrolytes, the most fundamental CO_3-moiety, carbonic acid (H_2CO_3), was also investigated regarding its photoelectron characteristics. Towards further extension of the LIB electrolyte surrogate model to the fire-retardant additives, TMP unimolecular thermal decomposition was investigated as a first step for its modeling.

Chapter 3 | Pyrolysis and oxidation of the linear carbonate esters (DMC, DEC and EMC) using MFR with gas chromatography (GC).

1. Pyrolysis and oxidation characteristics of DEC and EMC were similar to each other, while they were different from DMC. Based on their molecule structure, this can be classified by whether it involves an ethyl (ester) group or not.
2. Major consumption reactions of DMC were H-atom abstraction reactions and an unimolecular decomposition reaction, i.e., a four-centered CO_2 elimination reaction, at oxidation and pyrolysis conditions, respectively. Those of DEC and EMC were unimolecular decomposition reactions, i.e., six-centered C_2H_4 elimination reactions, at both oxidation and pyrolysis conditions.
3. Gas-phase reactivities were found to be DMC $<$ DEC $\approx$ EMC from the weak flame observations. The C_2H_4 elimination reactions took place at relatively low temperatures (around $T_w = 800$ K), leading to thermal decomposition driven multi-stage reactions of DEC and EMC, which were distinctive from low-temperature oxidation (LTO) driven multi-stage reactions observed in such as *n*-heptane and dimethyl ether (DME).
4. A chemical kinetic model that includes the three linear carbonate esters was constructed through the validation of literature models of DMC and DEC and the modeling of EMC.

Chapter 4 | Pyrolysis of the cyclic carbonate ester (EC) using MFR with GC and time-of-flight mass spectroscopy (TOF-MS), and oxidation with shock tube and flame speed measurements.

1. The most energetically favored EC unimolecular decomposition was found to be a CO_2 elimination reaction producing acetaldehyde (CH_3CHO) over an energy barrier of 67.4 kcal/mol calculated at the G4 level of theory.
2. The unimolecular decomposition reaction producing CO_2 and CH_3CHO was the

dominant EC consumption pathway during the pyrolysis as well as oxidation. This reaction led to EC decomposition at lower temperatures (around T_w = 1000–1050 K) as compared to DMC (around T_w = 1050–1100 K) in EC/DMC pyrolysis.

3. The first LIB electrolyte surrogate model that covers pyrolysis and oxidation of EC, DMC, DEC and EMC was constructed through EC modeling. The model reproduced ignition delay times and CO time-history profiles of EC at a wide range of conditions (equivalence ratios of 0.5, 1 and 2 and temperature range of 1200–1700 K at near atmospheric pressure) although some discrepancies appeared especially at lower-temperature and/or higher-equivalence ratio conditions studied.
4. Measured laminar flame speeds of H_2/air mixtures doped with 0.5% EC were well-predicted with the LIB electrolyte surrogate model, which showed a significant drop by the EC addition compared to neat H_2/air mixtures at equivalence ratios of 0.8–3.0.

Chapter 5 | Global combustion properties (laminar flame speeds and ignition delay times) of multi-component LIB electrolyte solvents.

1. The LIB electrolyte surrogate model was validated with laminar flame speeds and ignition delay times of DMC, DEC and EMC available from the literature, predicting the global combustion properties of the linear carbonate esters well especially at near atmospheric conditions.
2. Laminar flame speeds and ignition delay times of widely-used LIB electrolyte solvent mixtures, i.e., EC/DMC, EC/DEC and EC/EMC, as well as neat carbonate esters were simulated, showing the suppressing effects of the EC blending to the neat linear carbonate esters on flame speeds and the limited effects on ignition delay times in the case of DMC and DEC.
3. Simulated laminar flame speeds of EC/DEC and EC/EMC were faster than those of EC/DMC. This is the opposite trend to the current liquid-based fire hazard

classification, in which the former two are classified as lower and the latter as higher flammability, suggesting the importance of taking the gas-phase combustion properties into account.

Chapter 6 | Photoelectron characterization of the most fundamental CO_3-moiety, carbonic acid (H_2CO_3), using synchrotron vacuum ultraviolet (VUV) radiation and PEPICO spectroscopy.

1. Elusive gaseous H_2CO_3 was produced from pyrolysis of di-*tert*-butyl carbonate ester and detected conformer-selectively with PEPICO spectroscopy.
2. Photoionization (PI) and photoion mass-selected threshold photoelectron (ms-TPE) spectra of H_2CO_3 was reported for the first time, and its two of three conformers, namely *cis-cis* and *cis-trans* H_2CO_3, were assigned to the spectrum carriers with the help of Franck–Condon simulations.

Chapter 7 | Pyrolysis of a fire-retardant additive candidate, trimethyl phosphate (TMP), using synchrotron VUV radiation and PEPICO spectroscopy combined with a pyrolysis reactor.

1. Phosphorus-containing reactive intermediates including radicals, as well as those of hydrocarbon and oxygenated species, from TMP unimolecular thermal decomposition were detected and isomer-selectively identified by recording ms-TPE spectra.
2. Unimolecular decomposition of TMP was theoretically investigated, and H-transfer and CH_3-transfer isomerization were found to be the energetically favorable channels, which are followed by methanol/methyl loss and DME loss, respectively. These decomposition channels have been eluded discussion in the literature.
3. Based on the experimentally observed species and the quantum chemical calculations, reaction pathways of TMP thermal decomposition were proposed. The DME production channel was confirmed both with experiments and calculations, which is

not included in a currently available TMP chemical kinetic model.

4. Analogue DME production channel was also found in the unimolecular decomposition of dimethyl methylphosphonate (DMMP), which has a similar molecule structure to TMP, in this study. This reaction channel has not been reported in the literature nor included in a DMMP chemical kinetic model as well.

8.2 Future recommendations

The LIB electrolyte surrogate model constructed through this dissertation lays the foundation for further combustion experiments of carbonate esters and model developments of other LIB electrolyte-related compounds such as TMP. With the extension of the model, we can contribute to a mitigation strategy for LIB fires, especially in scenarios where vaporized electrolytes are present inside or vented outside a LIB cell.

Appendix A

Prediction of isomer-specific photoelectron characteristics of lutidyl radicals

This chapter aims to introduce the PEPICO technique as well as photoelectron characteristics that enable us to investigate reactive intermediates including radicals isomer-selectively. To this end, ms-TPES of lutidyl radical isomers, nitrogen- and methyl-substituted benzyl-type radicals, were obtained, and a correlation between their ionization energies and substitution patterns found was reported in this chapter.

A.1 Introduction

Fossil fuels, notably coal, and biofuels, often contain large amounts of nitrogen-containing organic compounds [262–264]. Their combustion and decomposition byproducts, such as soot, (nitrogen-substituted) polycyclic aromatic hydrocarbons [(N)PAHs], nitrogen oxides (NO_x), hydrogen cyanide (HCN), and ammonia are major concerns for the environment and human health. The gas-phase formation mechanism of these generally undesired PAHs and NO_x in combustion has been investigated extensively for the past decades [265,266]. Ammonia combustion is an emerging and attractive energy source. Blending ammonia with hydrogen or hydrocarbons addresses the low reactivity and burning velocity, and makes it more practical to utilize ammonia as a fuel [267]. The combustion of ammonia and hydrocarbon fuel mixes has been reported to reduce soot and PAH formation but the changes in combustion mechanism responsible for this effect, especially regarding the nitrogen–hydrocarbon interaction for larger than C_2 species, are not yet fully understood [268,269]. Even if PAH growth is inhibited by nitrogen intermediates, such as HCN [270], careful attention needs to be paid to NPAH formation, as these species are significantly more toxic than PAHs. NPAH formation and growth is also relevant in the astrochemical context, because their presence is inferred in circumstellar and interstellar environments, as well as in Titan’s nitrogen-rich and low-temperature atmosphere [271,272].

While nitrogen-substituted aromatic compounds play an important role in the chemistry of a wide variety of environments, their isomers are even more numerous than those of the analogous hydrocarbons. This makes their (isomer-)specific identification a challenge and provides motivation to further develop sensitive and isomer-selective detection techniques, for example synchrotron-based photoionization approaches [99]. Tian et al. [273,274] used molecular beam mass spectrometry and synchrotron radiation to investigate combustion intermediates from premixed pyrrole and pyridine flames. These heterocycles are considered to be mainly responsible for NO_x emissions in coal combustion [275]. Similarly, Lucassen et al. [276,277] investigated flames of morpholine, an oxygen- and nitrogen-containing model biofuel, by photoionization. However, the large number of potential nitrogen-substituted aromatic isomers and the limited beamtime mean that obtaining reference spectra for all isomers in exhaustive measurements is not feasible. As shown for the ionization potential of alkenes [278] or hydrocarbons in general [279], we can unveil systematic trends in the photoelectron spectroscopic features of substituted aromatics and relate these to the molecular structure to enable isomer identification in complex reactive mixtures. Benzyl derivatives include xylyl by methyl substitution and picolyl by the inclusion of a nitrogen heteroatom. Lutidyl radicals combine these two features and were chosen to fill the gap and connect the known ionization energies and the electronic structure of benzyl [280,281], picolyl [227,282], and xylyl [283,284] radicals. So far, Bray and Bernstein [285] have only reported the ionization energy of 3,6-lutidyl (in their nomenclature 2,5-lutidyl), one of ten lutidyl isomers, to be 7.33 eV by two color multiphoton ionization spectroscopy.

Here, we investigate three lutidyl radicals, namely 2,4-, 2,6-, and 3,5-lutidyl (Figure A.1), as further representatives of the ten possible isomers. Photoelectron photoion coincidence

(PEPICO) spectroscopy with vacuum ultraviolet (VUV) synchrotron radiation enables us to obtain spectroscopic insights into reactive intermediates [286] by recording photoion mass-selected threshold photoelectron (ms-TPE) spectra. 2,4-, 2,6-, and 3,5-lutidyl radicals are produced by flash vacuum pyrolysis [230] from 2-aminomethyl-4-methylpyridine (2AM4MP), 2-aminomethyl-6-methylpyridine (2AM6MP), and 3-aminomethyl-5-methylpyridine (3AM5MP) by deamination, respectively (Figure A.1), and sampled in a molecular beam.

The goal of this study is to reveal correlations between the position of the nitrogen atom as well as the methyl substitution and the photoelectron spectra, including the ionization energies. Quantum chemical calculations and Franck–Condon simulations provide further insights and help assign the ms-TPES. Based on calculated ionization energies of benzyl, picolyl, xylyl, and lutidyl radicals, a relationship is established between the ionization energy and molecular structure in the context of the charge distribution upon ionization. The substituent effects are found to be position-dependent and additive, which allows for a quantitative ionization energy prediction based on the substitution pattern in this class of benzyl derivatives.

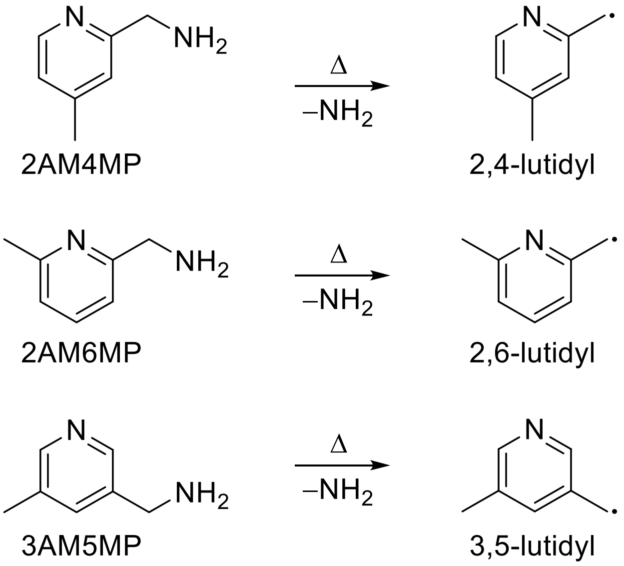

Figure A.1 Three isomers of lutidyl radicals produced by flash pyrolysis from aminomethyl methylpyridines. In the 2,4-lutidyl radical, the radical center is vicinal to the nitrogen heteroatom.

A.2 Experimental and theoretical approaches

The experiments were conducted with the double imaging photoelectron photoion coincidence (*i*²PEPICO) endstation at the vacuum ultraviolet (VUV) beamline of the Swiss Light Source (SLS) at Paul Scherrer Institute [90,105,107]. Flash vacuum pyrolysis of 2-aminomethyl-4-methylpyridine, 2-aminomethyl-6-methylpyridine and 3-aminomethyl-5-methylpyridine (95% purity, abcr GmbH) produced the lutidyl radicals. The precursor was placed in an in-vacuum stainless sample container, held in place with the help of glass wool and kept at 298–313 K. Argon (≥ 99.998%, PanGas) backing gas was supplied to the container at a flow rate of 20 or 30 sccm by a mass flow controller, which picked up the precursor vapors. The gas mixture expanded through a 100 or 200 μm pinhole at the tip of the container into a resistively heated SiC microtubular reactor (ca. 40 mm length, 1 mm inner diameter, 2 mm outer diameter, 15 mm heated length). The reactor temperature was controlled by varying the applied voltage/current with a DC power supply. The correlation between the reactor temperature and output wattage was measured previously. The gas temperature close to the reactor centerline is predicted to be ca. 10% lower than the reactor surface temperature [231,232]. Estimated pressure and residence time in the Chen-type reactor are 10–20 mbar and 10–50 μs, respectively [230–232]. The gaseous sample leaving the reactor expands into high vacuum (10^{-5} mbar), forming a molecular beam. The molecular beam is then skimmed using a Model 2 nickel skimmer from Beam Dynamics Inc. with 2 mm aperture as it enters the ionization chamber (10^{-6} mbar) of the PEPICO spectrometer. There, the molecular beam and the monochromatic VUV beam intersect perpendicularly. VUV light is provided by a bending magnet, collimated onto a plane blazed grating (150 grooves mm^{-1}) with an energy resolution of 1500 and focused on the exit slit. A differentially pumped rare gas filter (Ne/Ar/Kr mixture at 8.5 mbar over 10 cm) between the focusing mirror and the endstation suppresses higher order radiation from the grating [90]. Photoions and photoelectrons are accelerated in opposite directions under a constant electric field of 218 V cm^{-1} and detected in velocity map imaging (VMI) and, for the ions, space focusing conditions by position-sensitive delay-line anode detectors (DLD40, Roentdek) in a multiple-start multiple-stop scheme [108]. This enables us to obtain VMI of both ions and electrons as well as the time-of-flight (TOF) information for cations. Photoion mass-selected threshold photoelectron (ms-TPE) spectra were plotted by scanning the photon energy in 5 or 20 meV steps from 7.3 eV to 10.5 eV, selecting electrons with threshold kinetic energy of < 7 meV based on photoelectron VMI and extracting the threshold electrons in coincidence with cations arriving in the TOF range of interest. The contributions of hot electrons, i.e., higher kinetic energy electrons without off-axis momentum components, were subtracted [233]. As for the quantum chemical calculations, Gaussian 16 [97] and Q-Chem 4.3 [234] were used. Geometry optimizations and vibrational frequency calculations of neutral and cation ground states were performed at the B3LYP/6-311++G(d,p), B3LYP/6-311G(2d,d,p), G4, G3, CBS-QB3 and W1BD level of theories. Computation of the cation excited states were performed using the time-dependent density functional theory (TD-DFT), TD-B3LYP/6-311++G(d,p). Adiabatic ionization energies were calculated with the aforementioned DFT and composite methods. Adiabatic ionization and excitation energies of singlet and triplet cation states were calculated with the equation-of-motion (EOM) coupled-cluster theory, EOM-EE/EA-CCSD/cc-pVTZ at the (TD-)B3LYP/6-311++G(d,p) geometries, taking into account the (TD-)DFT zero-point corrections. Vertical excitation energies were computed utilizing the radicals' DFT-geometry at EOM-EE-CCSD/cc-pVTZ level of theory. Franck–Condon (FC) simulations were performed at 300 K with the Franck–Condon–Herzberg–Teller method implemented in Gaussian16 [97] and were convolved with a Gaussian function with a full width at half maximum of 33 meV.

A.3 Results and discussion

A.3.1 Temperature-dependent mass spectra of aminmetyl methylpyridine

Three lutidyl radical isomers, 2,4-, 2,6-, and 3,5-lutidyl, were produced from aminomethyl methylpyridine precursors by CH_2–NH_2 bond cleavage under pyrolysis conditions. The preference for NH_2 loss is attributed to the lower bond dissociation energy of the C–N bond compared with that of $>C–CH_2NH_2$ and $>C–CH_3$, calculated as 307, 379, and 408 kJ mol^{-1}, respectively, for 2AM6MP using the G4 composite method. Figure A.2a shows 2AM6MP mass spectra recorded at a photon energy of 10.5 eV as a function of the reactor temperature. At room temperature (298 K), an intense peak appears at *m/z* 122, which corresponds to the precursor's parent ion. The *m/z* 94 peak shows an asymmetric shape, which indicates dissociative photoionization (DPI) of a metastable parent ion [253]. This fragmentation step, likely CNH_2 loss from the parent ion, also appears in the electron ionization mass spectra of 2-, 3-, and 4-(aminomethyl)pyridine and benzylamine [287]. As the temperature increases to 990 K, a peak appears at *m/*z 106, assigned to the lutidyl radical. This is a symmetric peak, observed in an energy range where the parent ion of the precursor is metastable. Therefore, the lutidyl peak is unlikely to be a DPI product of the precursor. The cation velocity map image of *m/z* 106, shown in Figure A.2b for 3AM5MP pyrolysis, also confirms the lutidyl radical as a pyrolysis product. The strong molecular beam signal on the left exhibits no broadening of the lateral velocity distribution, which would be expected in dissociative ionization due to kinetic energy release [113]. Thus, the mass signal at *m/z* 106 stems exclusively from decomposition in the pyrolysis reactor and subsequent ionization. When further increasing the reactor temperature, the lutidyl peak intensity decreases again at 1260 K, while a peak appears at *m/z* 105, indicative of sequential H loss from lutidyl, or ammonia (NH_3) loss from the precursor in the pyrolysis source. The reactor temperature was optimized for each isomer to maximize the ion counts of the lutidyl radicals when recording their ms-TPE spectra.

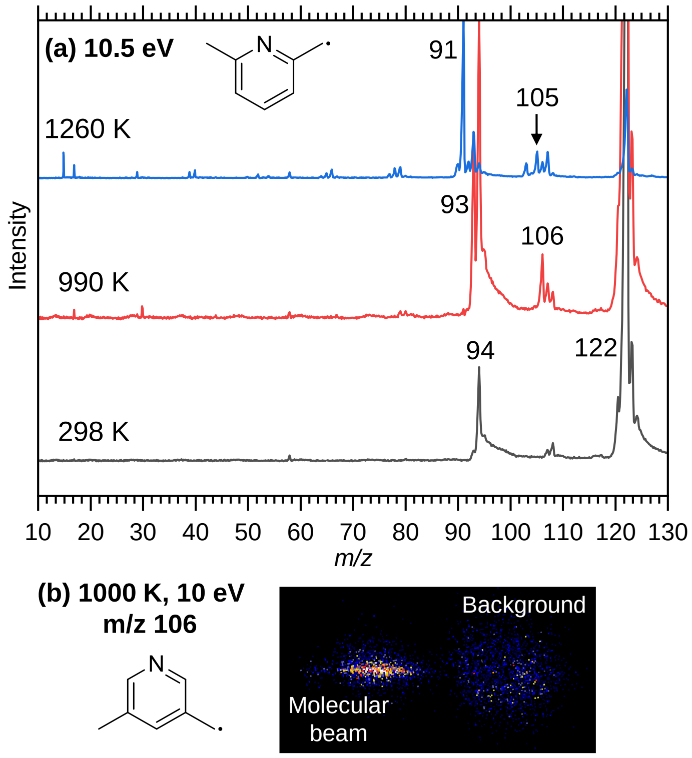

Figure A.2 (a) Mass spectra of 2-aminomethyl-6-methylpyridine (2AM6MP, *m/z* 122) at room, intermediate, and high temperatures measured at a photon energy of 10.5 eV. (b) Ion velocity map image of 3,5-lutidyl radical (*m/z* 106) produced from 3-aminomethyl-5-methylpyridine (3AM5MP, *m/z* 122) at a reactor temperature of 1000 K and photon energy of 10 eV. The molecular beam ion signal on the left side shows a narrow speed distribution perpendicular to the molecular beam axis, indicating that the observed *m/z* 106 signal in the mass spectra is due to direct ionization of a pyrolysis product.

A.3.2 ms-TPES of lutidyl radicals

The ms-TPE spectra of 2,4-, 2,6-, and 3,5-lutidyl radicals measured between the ionization onset and up to 10.5 eV at the optimized reactor temperature (1000–1175 K) are shown in Figure A.3. The spectra show similar features with intense and well-resolved peaks in the low-energy range (7.4–8.0 eV) and unstructured, broad bands between 8.5 and 10.5 eV. The ionization onsets are clearly offset but within 100 meV for these isomers.

The first dominant peak in the spectrum is located at 7.54, 7.50, and 7.45 eV and assigned to the adiabatic ionization energy (AIE) of the 2,4-, 2,6-, and 3,5-lutidyl radicals, respectively. 3,5-Lutidyl, in which the nitrogen heteroatom is in the *meta* position relative to the methylene group, has the lowest AIE, followed by 2,6- and 2,4-lutidyl radicals with nitrogen heteroatoms in the *ortho* position relative to the methylene group. With the help of Franck–Condon (FC) simulations presented as red traces and sticks in Figure A.3, the first peaks in the ms-TPE spectra are assigned to transitions from the ground state of the neutral into the singlet cation state ($\tilde{\mathbf{X}}^{+}\ {}^{1}\mathrm{A}' \leftarrow \tilde{\mathbf{X}}\ {}^{2}\mathrm{A}''$) of all three radicals. Initial FC simulations of the 2,6- and 3,5-isomers did not reproduce the experimental spectrum well (not shown here), which was found to be related to the internal rotation of the methyl group. The methyl internal rotational energy curves were calculated for the $\tilde{\mathbf{X}}\ {}^{2}\mathrm{A}''$ and $\tilde{\mathbf{X}}^{+}\ {}^{1}\mathrm{A}'$ states of the three isomers using the B3LYP functional and the 6-311++G(d,p) as well as the 6-311G(2d,d,p) basis sets, as shown in Figure A.4. In 2,6-lutidyl, B3LYP/6-311++G(d,p) yielded a 60° difference between the $\tilde{\mathbf{X}}\ {}^{2}\mathrm{A}''$ and $\tilde{\mathbf{X}}^{+}\ {}^{1}\mathrm{A}'$ methyl torsional angles at the optimized geometry, but no change in the torsional angle was found when using the 6-311G(2d,d,p) basis set. In 3,5-lutidyl, there was a 10–15° phase difference between the optimized methyl torsional angle in the $\tilde{\mathbf{X}}\ {}^{2}\mathrm{A}''$ and $\tilde{\mathbf{X}}^{+}\ {}^{1}\mathrm{A}'$ states with both basis sets, due to symmetry breaking in the pseudo-C_s symmetry neutral state. The methyl group is a virtually free rotor in the neutral with a rotational barrier of less than 3 meV [284]. FC simulations in the double harmonic approximation, *i.e.*, when the nuclear wave function is assumed to be harmonic both on the neutral and the cation surface, but with phase-shifted methyl dihedral angles in the minima lead to artifacts for the 2,6- and 3,5-lutidyl TPES. Thus, we used the methyl rotational "transition state" geometry of $\tilde{\mathbf{X}}\ {}^{2}\mathrm{A}''$, aligned with the minimum geometry of $\tilde{\mathbf{X}}^{+}\ {}^{1}\mathrm{A}'$, in the FC simulation, which reproduces the experiment well as shown in Figure A.3. We observe a progression with a ca. 70 meV (565 cm^{-1}) spacing, which is assigned to a ring deformation mode of the lutidyl cations (see below discussion on Figure A.5). The experimental AIEs as well as calculated ones at the B3LYP/6-311++G(d,p), G4, G3, CBS-QB3 and W1BD level of theories are summarized in Table A.1 and are in excellent agreement. TPES modeling by FC simulations in the double harmonic approximation is a routine task nowadays. Therefore, it is important to note that the inclusion of active large-amplitude motions upon ionization may not only lead to convergence issues but can also result in artifacts in the simulated spectrum.

An unstructured, broad band appears in the 8.5–10.5 eV energy range in each of the spectra, which may involve multiple singlet and triplet states. A similar band was also observed for the 4-picolyl radical with a maximum at 9.5 eV [227]. Xylyl radicals exhibit similarly broad but more resolved transitions, whereas benzyl radical displays sharp transitions in this energy range [281,284]. In all cases, singlet and triplet cation states were identified based on FC simulations, although hot bands, autoionization, and lifetime broadening were also suggested to contribute to the spectra [284]. We calculated vertical excitation energies of the lutidyl singlet and triplet cation states utilizing EOM-EE-CCSD/cc-pVTZ theory and found at least two singlet and three triplet states between 9.3 and 10.7 eV. We assigned the onset of the broad ms-TPES band to the triplet ground state ($\tilde{\mathbf{a}}^+\ {}^3\mathrm{A}''$) based on TD-DFT and EOM-EE/EA-CCSD calculations, which suggest that the AIE of the $\tilde{\mathbf{a}}^+\ {}^3\mathrm{A}''$ state is lower than that of the first cation singlet excited state ($\tilde{\mathbf{A}}^+\ {}^1\mathrm{A}''$) as listed in Table A.1. Thus, triplet-state FC simulations can be shifted to reproduce the broad band onsets below 9.1 eV, which yielded experimental adiabatic ionization energies at 8.82, 8.82, and 8.92 eV into the $\tilde{\mathbf{a}}^+\ {}^3\mathrm{A}''$ states of 2,4-, 2,6-, and 3,5-lutidyl, respectively. These are in good agreement with the composite method results with the largest discrepancy of 140 meV (Table A.1).

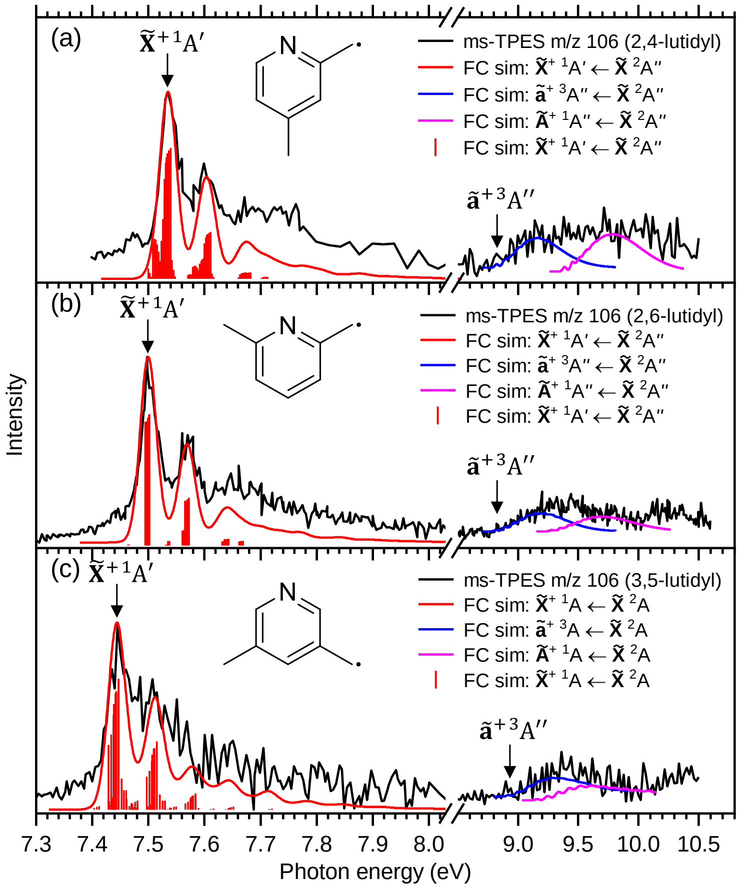

Figure A.3 ms-TPE spectra of (a) 2,4-lutidyl, (b) 2,6-lutidyl, and (c) 3,5-lutidyl (black lines). Note the difference in scale for the low-energy and high-energy sections. FC simulations for the transitions from the neutral ground state to the singlet ground state (red traces and sticks), triplet ground state (blue traces) and singlet excited state (magenta traces) cations were calculated at 300 K and the (TD-)B3LYP/6-311++G(d,p) level of theory and convolved with a 33 meV full width at half maximum Gaussian to account for the rotational envelope.

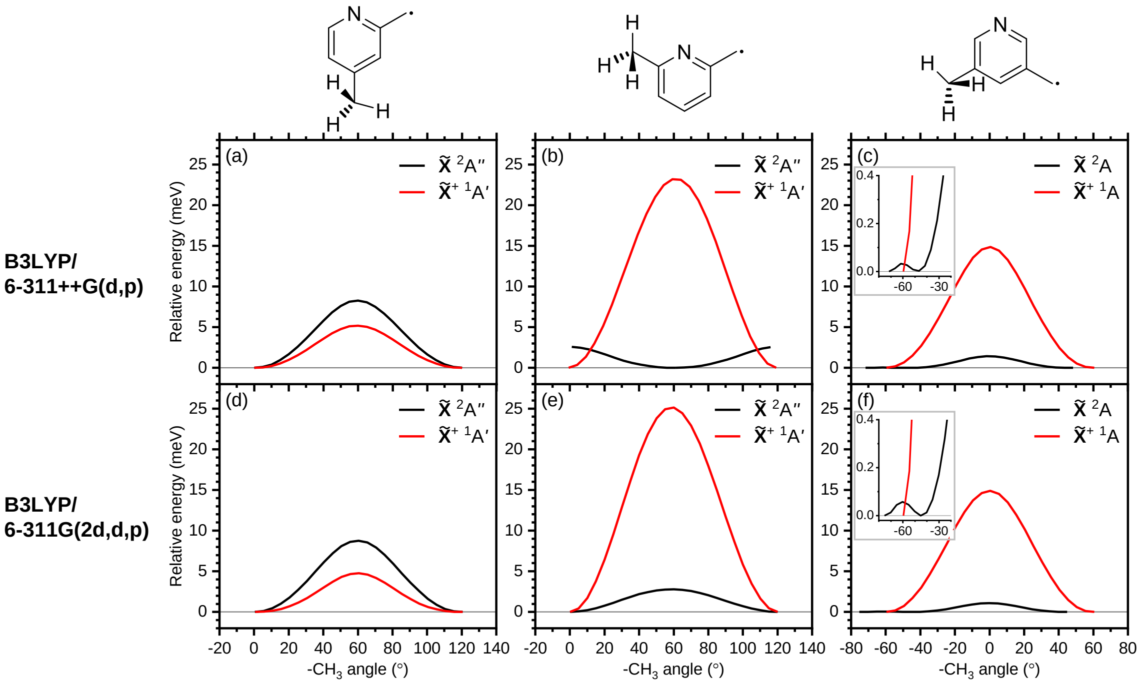

Figure A.4 Calculated potential energy surfaces for the rotation of the methyl group in the ground state neutral and singlet cation states of (a, d) 2,4-, (b, e) 2,6-, and (c, f) 3,5-lutidyl radicals using the B3LYP functional with the 6-311++G(d,p) (top) and 6-311G(2d,d,p) (bottom) basis sets. The molecular structures on the top represent 0° methyl group torsional angle.

Table A.1 Experimental and calculated ionization energies of the lutidyl radicals (eV).

	2,4-lutidyl			2,6-lutidyl			3,5-lutidyl		
Method	$\tilde{\mathbf{X}}^{+\,1}\mathrm{A}'$	$\tilde{\mathbf{a}}^{+\,3}\mathrm{A}''$	$\tilde{\mathbf{A}}^{+\,1}\mathrm{A}''$	$\tilde{\mathbf{X}}^{+\,1}\mathrm{A}'$	$\tilde{\mathbf{a}}^{+\,3}\mathrm{A}''$	$\tilde{\mathbf{A}}^{+\,1}\mathrm{A}''$	$\tilde{\mathbf{X}}^{+\,1}\mathrm{A}'$	$\tilde{\mathbf{a}}^{+\,3}\mathrm{A}''$	$\tilde{\mathbf{A}}^{+\,1}\mathrm{A}''$
Experiment	7.54	8.82[a]		7.50	8.82[a]		7.45	8.92[a]	
(TD-)B3LYP/ 6-311++G(d,p) [b]	7.51	8.70	8.93	7.48	8.62	8.81	7.42	8.77	8.85
G4	7.60	8.96		7.57	8.88		7.49	8.98	
G3	7.54	8.95		7.51	8.86		7.44	9.06	
CBS-QB3	7.59	8.92		7.56	8.84		7.49	8.98	
W1BD	7.56	8.92		7.52	8.84		7.45	8.98	
EOM-EE/EA-CCSD/ cc-pVTZ//(TD-)B3LYP [b]	7.37	8.95	9.34	7.32	8.86	9.22	7.25	9.06	9.21

[a] Determined by fitting the calculated, convolved Franck–Condon spectrum to the experimental ms-TPE spectrum. [b] The ground singlet and triplet cation states were calculated using DFT, while TD-DFT was applied to the excited singlet states. [c] pseudo.

The highest (singly) occupied molecular orbital (HOMO) and HOMO−1 of the 2,6-lutidyl radical is shown in Figure A.5 (only 2,6-lutidyl is shown here, but the following discussion also applies to the other isomers). Electron removal from these frontier orbitals dominates ionization to the first three ion states, *i.e.*, the ground-state singlet and triplet as well as the first singlet excited state [92]. The HOMO shows antibonding character along the C6–N and >C2–CH_2 bonds and bonding character at the diagonal position with respect to the methylene group, *i.e.*, along the C5–C6 bond. Consequently, the C5–C6 bond length increases while the C6–N and >C2–CH_2 bond lengths decrease upon ionization into the $\tilde{\mathbf{X}}^+\ {}^1A'$ state (See Table A.2). This change in geometry is in line with the active vibrational modes upon ionization of the three lutidyl radicals, associated with ring deformation (vide supra). Ionization from the HOMO−1 gives rise to the $\tilde{\mathbf{a}}^+\ {}^3A''$ and $\tilde{\mathbf{A}}^+\ {}^1A''$ states, associated with the removal of an electron from the nitrogen lone pair, meaning that this state is unique to the N-heteroatom containing benzyl derivatives. The decreased lone pair repulsion leads to an increase in the C6–N–C2 bond angle (Table A.2). FC simulations confirm the resulting large geometry change to be responsible for the unstructured, broad bands in the ms-TPE spectra (Figure A.3). In the absence of fine structure above 9 eV and because of the likely strong adiabatic coupling between the close-lying triplet states with an associated lifetime broadening [281,284,288], we refrain from further state assignments of the ms-TPES.

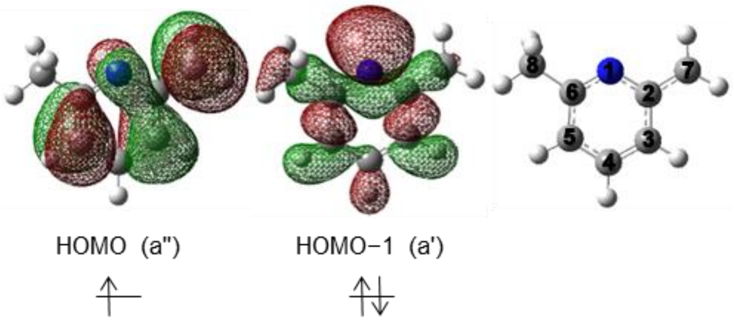

Figure A.5 Molecular orbitals of 2,6-lutidyl calculated at the B3LYP/6-311++G(d,p) level of theory. The numbering of the carbon atoms for 2,6-lutidyl is shown on the right.

Table A.2 Bond lengths and angles of 2,6-lutidyl calculated at the (TD-)B3LYP/6-311++G(d,p) level of theory. See Figure A.5 for the numbering of carbon atoms.

Bond length (Å)	$\tilde{\mathbf{X}}\,^{2}\mathrm{A}''$	$\tilde{\mathbf{X}}^{+\,1}\mathrm{A}'$	$\tilde{\mathbf{a}}^{+\,3}\mathrm{A}''$	$\tilde{\mathbf{A}}^{+\,1}\mathrm{A}''$
N–C2	1.367	1.377	1.350	1.357
C2–C3	1.422	1.428	1.437	1.418
C3–C4	1.382	1.386	1.381	1.399
C4–C5	1.396	1.388	1.398	1.376
C5–C6	1.408	1.441	1.417	1.440
C6–N	1.328	1.312	1.306	1.283
C2–C7	1.407	1.377	1.392	1.393
C6–C8	1.508	1.497	1.504	1.507
Bond angle (°)	$\tilde{\mathbf{X}}\,^{2}\mathrm{A}''$	$\tilde{\mathbf{X}}^{+\,1}\mathrm{A}'$	$\tilde{\mathbf{a}}^{+\,3}\mathrm{A}''$	$\tilde{\mathbf{A}}^{+\,1}\mathrm{A}''$
C6–N–C2	119.2	118.5	134.5	133.7
N–C2–C3	121.1	123.2	111.2	111.2
C2–C3–C4	119.1	118.3	120.2	121.0
C3–C4–C5	119.1	117.6	121.4	121.2
C4–C5–C6	119.0	121.6	119.4	118.2
C5–C6–N	122.5	120.8	113.3	114.8

A.3.3 Correlation of ionization energy and substituent patterns among benzyl derivatives

Together with the known ionization energies of picolyl [227], xylyl [284], and benzyl [281], as well as the measured 3,6-lutidyl AIE of 7.33 eV [285], the newly determined AIEs of 2,4-, 2,6-, and 3,5-lutidyl establish a sizeable dataset for N-heteroatom and methyl-substituted benzyl ionization energies. As shown in Table A.3, the G4 ionization energies are ca. 60 meV above the experimental values with a standard deviation of only 12 meV. The only exception is 3,6-lutidyl, for which the experimental value is 20 meV larger [285]. Thus, the differences between the ionization energies are expected to be superbly reproduced by the G4 composite method, which offers a consistent way to consider the substitution effects in all possible *ortho*, *meta*, and *para* combinations of none or one methyl and none or one N-heteroatom substitutions while eschewing the varying uncertainties of the experimental determinations. Hereafter, *ortho*, *meta*, and *para* refer to the positions relative to the methylene group. In this family of compounds, the singly occupied HOMO is dominated by the methylene radical center. Therefore, trends and patterns in the ionization energies are not only interesting to aid the assignment of ms-TPES but also provide insights into radical chemistry by reflecting the binding energy of the unpaired electron. Figure A.6 clearly shows that the presence of the nitrogen heteroatom increases, whereas the presence of a methyl substituent decreases the ionization energy consistently. Furthermore, the parallel changes in the ionization energy as a function of the substituent position suggest that this effect may be additive as it depends only on the substituent position with respect to the methylene group. The absence or the relative position of the other substituent plays a subordinate role. Finally, the neutral xylyl, picolyl, and lutidyl isomers are almost isoenergetic within the respective isomer group (the standard deviations are 5, 20, and 37 meV, respectively), and ionization energy trends are therefore primarily driven by the cation energetics.

Table A.3 Experimental and calculated adiabatic ionization energies of the benzyl, xylyl, picolyl, and lutidyl radicals. Asterisk (*) denotes this study.

Radical	Experiment (eV)	G4 calculation * (eV)	Difference (eV)
Benzyl	7.25 [281]	7.30	0.05
o-Xylyl	7.08 [284]	7.15	0.07
m-Xylyl	7.11 [284]	7.18	0.07
p-Xylyl	6.94 [284]	7.01	0.07
o-Picolyl	7.70 [227]	7.74	0.04
m-Picolyl	7.59 [227]	7.64	0.05
p-Picolyl	8.01 [227]	8.07	0.06
2,4-Lutidyl	7.54 *	7.60	0.06
2,6-Lutidyl	7.50 *	7.57	0.07
3,5-Lutidyl	7.45 *	7.49	0.04
3,6-Lutidyl	7.33 [285]	7.31	−0.02

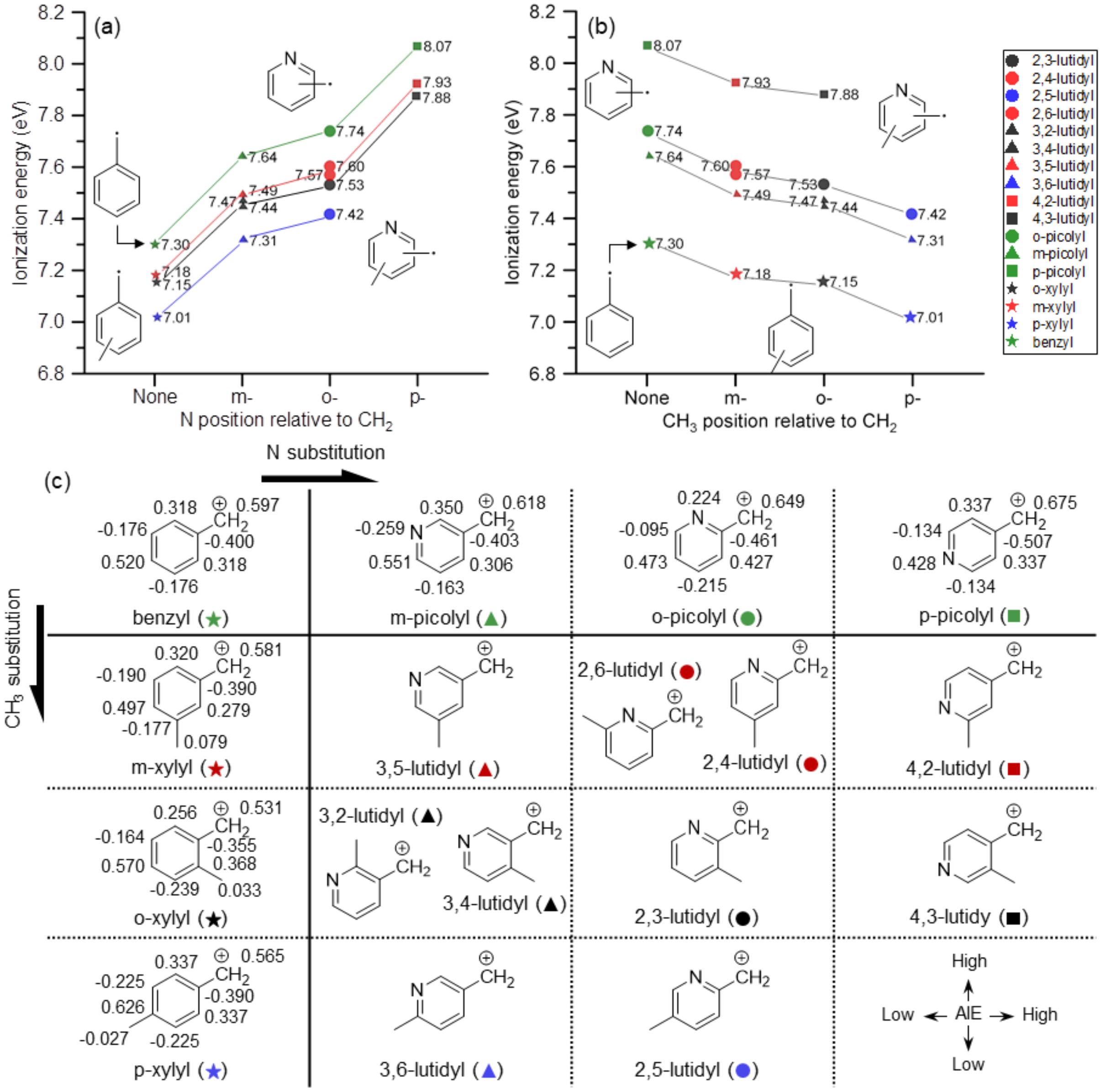

Figure A.6 Adiabatic ionization energies (AIEs) of lutidyl, picolyl, xylyl, and benzyl radicals as a function of (a) nitrogen atom and (b) methyl group position relative to the methylene group. AIEs were calculated with the G4 composite method. Plots are categorized based on the N position with respect of the CH_2 group: *ortho* (circle), *meta* (triangle), *para* (square) and no nitrogen atom (star); and CH_3 position with respect of the CH_2 group: *ortho* (black), *meta* (red), *para* (blue), and no methyl group (green). (c) Calculated APT charge differences in benzyl, picolyl, and xylyl isomers upon ionization at the B3LYP/6-311++G(d,p) level of theory.

Cursory observation suggests that the presence of a substituent in the *para* position has a larger effect than in the *meta* or even in the *ortho* position. This can be considered in the context of the resonance structures, which predict the charge to be delocalized between the methylene group as well as the *para* and *ortho* positions in the ring (Figure A.7). derivatives.

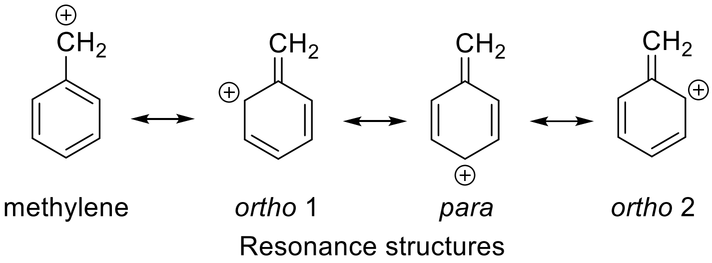

Figure A.7 Resonance structures for the benzyl cation. The charge is delocalized between the methylene group, the *para*, and *ortho* positions.

Based on these structures, increasing the electronegativity by substituting CH for a nitrogen heteroatom should raise the AIE in the *para* > *ortho* > *meta* order. Looking at Figure A.6, it does so in the *para* > *ortho* ≳ *meta* order instead. This raises the question whether substitution leads to changes in the weights of the resonance structures. Differences in the localization of the positive charge upon ionization approximate these changes in the weights of the resonance structures. Atomic polar tensor (APT) [289,290] charges are one of a multitude of charge localization schemes. We discuss APT charges herein, because they have been shown to be reliable to investigate the charge density localization and delocalization [291], *e.g.*, when studying substituent effects on electron-donating efficacy of pyridine [292]. The change in the APT charges upon ionization can be thought of as the weights of the resonance structures in the cation. As seen in Figure A.6c, the APT charges of the methylene (CH_2), the *ortho*, and *para* >CH groups increase by ca. 0.60, 0.32, and 0.52, respectively, in benzyl upon ionization. This suggests that the individual *ortho* resonance structures play a subordinate role, however their sum (*ortho* 1 + *ortho* 2) is comparable to the role of the methylene and the *para* positions. This is consistent with a ca. one-third weight for the methylene, *para*, and combined *ortho* resonance structures in Figure A.7. Curiously, the charges on the >C(–CH_2) ring carbon and the *meta* >CH group become more negative by ca. 0.40 and 0.18, respectively, upon ionization, suggesting enhanced electron localization there because these positions do not contribute significantly to the resonance structures.

In the presence of a nitrogen atom or after methyl substitution in the *meta* position, the total charge in both *meta* positions together decreases further by 0.07 (from –0.35 to –0.42) or increases by 0.06 (from –0.35 to –0.29), respectively, due to the electron withdrawing or donating character of the substituent. This leads to a minor change in the relative weights of the resonance structures, and consequently, the effect on the ionization potential (benzyl to *meta*-picolyl or *meta*-xylyl) is only a function of the inductive effect of the substituent.

Upon *ortho* substitution, the charge at the affected position decreases by 0.09 *vs.* increases by 0.08 for N and CH_3, respectively. However, this shift is compensated for by the 0.11 increase vs. 0.06 decrease in charge at the opposite *ortho* location. Furthermore, in *ortho*-picolyl, there is a large increase in the charge at the methylene and *meta* positions, while a decrease at the >C(–CH_2) carbon as well as in the *para* position. Similar changes with the opposite sign are observed for the *ortho*-xylyl charge distribution upon methyl substitution. Thus, *ortho* substitution perturbs the balance of the resonance structures, but its effect can be in part compensated by the other *ortho* >CH group. Consequently, a minor positional effect on the (de)stabilization of the cation is observed together with the inductive effect of the substituent. This leads to the slightly larger change in the AIE compared to the *meta* cases.

In contrast, *para* substitution affects the fundamentally more important *para* resonance structure, and the 0.09 decrease or 0.08 increase (for N or CH_3-substitution, respectively) of the *para* charge directly translates into a reduction or increase in the weight of the *para* resonance structure. Consequently, the electron donating methyl group can stabilize the cation the most, whereas the destabilization due to the nitrogen heteroatom is largest when they are in the *para* position, qualitatively explaining the observed trends of the AIE in Figure A.6.

To predict the shift in AIE upon N- or CH_3-substitution quantitatively, we attempt to establish position-dependent substituent effects. These were discussed by Crable and Kearns [293] regarding substituted benzene ionization energies. Efforts to quantify these effects on electrostatic potentials and local surface ionization energies [294], electron affinities and ionization energies [295], as well as conformational and ionization energies [296] are more recent and typically aim to establish relationships between an observable and a computational result, similar to the APT charge analysis presented above. DiLabio et al. [297] considered disubstituted benzenes and discussed the additivity of substituent effects on the ionization energy, particularly when an electron donating and an electron withdrawing substituent is combined, such as in our case. In our set of benzyl derivatives, the effect of the substituent on the ionization energy, *i.e.*, on the binding energy of the unpaired electron, seems to depend on only the position of the substituent relative to the methylene radical center and not on the relative position of the other substituent or its absence. This means that the substituent effects may be universal and additive in this compound family, which we aim to quantify for xylyl, picolyl, and lutidyl isomers.

We test this hypothesis by assuming a position-dependent effect of the methyl- and nitrogen-substitution on the ionization energy and propose that this effect is additive to the benzyl reference ionization energy if both substituents are present. The resulting six substituent effect values (Table A.4, bold numbers) were fitted to reproduce the G4-computed ionization energies. For example, the N heteroatom and the methyl group are both in the *meta* position with respect to the methylene group in 3,5-lutidyl. The predicted ionization energy is, therefore, 7.30 + 0.32 – 0.13 = 7.49 eV, which agrees exactly with the G4 result. Remarkably, this simple rule predicts the G4-computed ionization energies of methyl- and N-substituted benzyl radicals with an average absolute error of 10 meV and a maximum absolute error for *ortho*-xylyl at 23 meV. Thus, the effect of the substitution on the binding energy of the unpaired electron of the methylene group is indeed additive.

Table A.4 G4-computed benzyl, xylyl, picolyl, and lutidyl ionization energies. The position-dependent substituent effects are listed in bold. The difference of the predicted ionization energy based on the additivity rule and the G4-computed one is given in parentheses.

AIE (eV) (error)			N			
			None	*meta*	*ortho*	*para*
			0.00	0.32	0.42	0.76
CH_3	None	0.00	7.30	7.64 (−0.02)	7.74 (−0.02)	8.07 (−0.01)
	meta	−0.13	7.18 (−0.01)	7.49 (0.00)	7.59 [a] (0.00)	7.93 (0.00)
	ortho	−0.17	7.15 (−0.02)	7.46 [a] (0.00)	7.53 (0.02)	7.88 (0.01)
	para	−0.30	7.01 (−0.01)	7.31 (0.01)	7.42 (0.00)	–

[a] Two substituents in the *ortho* and *meta* positions, which may be vicinal or positioned across the ring. In these cases, the average ionization energy of the two isomers (differing by 30–40 meV) is given.

Furthermore, the effect of the electronegative N-heteroatom in the *meta* and *ortho* positions is 43% and 55% of that in the *para* one, and the AIE lowering effect of the electropositive methyl group is 43% and 57% in these two locations, respectively. Thus, even the relative magnitudes of the AIE shift is comparable as a function of the substituent location.

A prerequisite for the additive effect of substituents is that the HOMO character, which is dominated by the methylene lone pair in benzyl, does not change upon substitution. Although the HOMO−1 also has a nitrogen lone pair character in the N-containing derivatives, and electron removal from this orbital yields the $\tilde{\mathbf{a}}^{+}\ {}^{3}A''$ cation state (Figure A.5), this state is barely affected by the substitution pattern with an ionization energy scattering only slightly around 8.93 eV for lutidyl isomers. It remains to be seen how broadly additive substituent effects on radical ionization energies hold true for other systems, such as halogen-substituted benzyl radicals [298,299], phosphorus [300], and other pnictogens [301], or larger aromatic π systems [302]. If so, it would not only suggest that ionization energies and radical electron binding energies may be easily predicted with the help of additive rules but would also offer avenues to tune radical reactivities by targeted substitution in a predictable way.

A.4 Conclusions

Lutidyl radical isomers, nitrogen heteroatom containing and methyl-substituted benzyl derivatives belonging to the radical family of benzyl, xylyl, and picolyl isomers, were investigated using photoelectron photoion coincidence (PEPICO) spectroscopy utilizing vacuum ultraviolet (VUV) synchrotron radiation in the photon energy range of 7.3–10.5 eV. Three lutidyl isomers, 2,4-, 2,6-, and 3,5-lutidyl, were selectively produced by flash vacuum pyrolysis of aminomethyl methylpyridine precursors. Photoion mass-selected threshold photoelectron (ms-TPE) spectra of the lutidyl radicals showed similarities: a well-resolved band at lower energies (7.4–8.0 eV), followed by unstructured broad bands in the 8.5–10.5 eV energy range. This structure also resembles the TPES of the 4-picolyl radical [227]. Experimental adiabatic ionization energies (AIEs) into the singlet cation ground states correspond to the removal of the unpaired electron from the radical at 7.45, 7.50, and 7.54 eV for 3,5-, 2,6-, and 2,4-lutidyl radicals, respectively, accurately predicted by composite method calculations. With the additional help of EOM-EE-CCSD calculations and Franck–Condon (FC) spectral modeling, we can assign the onset of the broad, unstructured band in the higher energy range to the triplet ground state of the cation. Ionization from the nitrogen lone pair HOMO−1 is associated with a large increase in the C−N−C angle, because of the decreased lone pair repulsion and yields the $\tilde{\mathbf{a}}^{+}\ {}^{3}A''$ and the $\tilde{\mathbf{A}}^{+}\ {}^{1}A''$ states. The presence of up to five electronically excited cation states between 9.3 and 10.7 eV, supported by EOM-EE-CCSD calculations, likely leads to strong non-adiabatic interactions, which results in lifetime broadening and explains the broad and unstructured band system. The methyl group is essentially a free rotor in the neutral radical, and its orientation in the optimized geometry depends on the computational level of theory. Thus, it is sometimes predicted to be an active mode upon ionization. In such cases, its inclusion in the double harmonic FC simulation has led to artifacts.

The effect of nitrogen heteroatom and methyl substitution on the ionization energy, i.e., the bonding energy of the radical electron, has been found to be strongly position-dependent and additive. This is discussed in light of the changes in APT charges upon ionization, as a descriptor for the weight of the resonance structures. Based on G4 calculations, a nitrogen heteroatom raises the ionization energy by 0.32, 0.42, and 0.76 eV, while methyl substitution lowers it by 0.13, 0.17, and 0.30 eV in the *meta*, *ortho*, and *para* positions with respect to the methylene group, respectively. These additive substituent effects reproduced the computed ionization energies to within 20 meV. Revealing such additive substituent effects not only helps ms-TPES assignment of reactive mixtures representative in catalysis and combustion environments or modeling the chemistry of the interstellar medium, but also offers novel avenues to finetune the bonding energy of the unpaired electron and, thus, the reactivity and electronic structure in otherwise quasi-isoenergetic radicals. Furthermore, understanding additivity effects may be a route forward to using machine learning approaches to predict important thermochemical descriptors.

Appendix A based on:

K. Kanayama, C. Fernholz, H. Nakamura, K. Maruta, A. Bodi and P. Hemberger, Lutidyl Radical Photoelectron Spectra Reveal Additive Substituent Effects on Benzyl Derivatives' Ionization Energy, *ChemPhysChem* 24 (2023) e202300359.

Nomenclature

Symbol	Description	units
A	Cross-sectional area of the stream tube encompassing the flame	cm^2
c_p	Specific heat capacity at constant pressure of the gas mixture	ergs/(g· K)
c_{pk}	Specific heat capacity at constant pressure of the *k*th species	ergs/(g· K)
d	Inner diameter of the reactor	cm
h_k	Specific enthalpy of the *k*th species	ergs/g
K	Total number of species	-
$\dot{M}$	Mass flux	g/cm^3
Nu	Nusselt number	-
T	Gas phase temperature	K
T_w	Wall temperature of the micro flow reactor	K
V_k	Diffusion velocity of the *k*th species	cm/s
W_k	Molecular weight of the *k*th species	g/mole
Y_k	Mass fraction of the *k*th species	-
λ	Specific heat capacity at constant pressure of gas mixture	cm^2/s
ρ	Density of the mixture	kg/m^3
$\dot{\omega}$	Rate of production of the *k*th chemical species	mol/s
ϕ	Equivalence ratio	-

References

[1] W. Steffen, J. Crutzen, J.R. McNeill, The Anthropocene: are humans now overwhelming the great forces of Nature?, Ambio 36 (2007) 614–21.

[2] P.J. Crutzen, Geology of mankind, Nature 415 (2002) 23–23.

[3] J. Rockström, W. Steffen, K. Noone, Å. Persson, F.S. Chapin, E. F. Lambin, T. M. Lenton, M. Scheffer, C. Folke, H. J. Schellnhuber, B. Nykvist, C. A. de Wit, T. Hughes, S. van der Leeuw, H. Rodhe, S. Sörlin, P. K. Snyder, R. Costanza, U. Svedin, M. Falkenmark, L. Karlberg, R. W. Corell, V. J. Fabry, J. Hansen, B. Walker, D. Liverman, K. Richardson, P. Crutzen, J. A. Foley, A safe operation space for humanity, Nature 461 (2009) 472–475.

[4] J. Rockström, W. Steffen, K. Noone, Å. Persson, F.S. Chapin, E.F. Lambin, T.M. Lenton, M. Scheffer, C. Folke, H.J. Schellnhuber, B. Nykvist, C.A. De Wit, T. Hughes, S. Van Der Leeuw, H. Rodhe, S. Sörlin, P.K. Snyder, R. Costanza, U. Svedin, M. Falkenmark, L. Karlberg, R.W. Corell, V.J. Fabry, J. Hansen, B. Walker, D. Liverman, K. Richardson, P. Crutzen, J.A. Foley, Planetary Boundaries: Exploring the Safe Operating Space for Humanity, Ecol. Soc. 14 (2009) 32.

[5] W. Steffen, K. Richardson, J. Rockström, S.E. Cornell, I. Fetzer, E.M. Bennett, R. Biggs, S.R. Carpenter, W. de Vries, C.A. de Wit, C. Folke, D. Gerten, J. Heinke, G.M. Mace, L.M. Persson, V. Ramanathan, B. Reyers, S. Sörlin, Planetary boundaries: Guiding human development on a changing planet, Science 347 (2015) 1259855.

[6] K. Richardson, W. Steffen, W. Lucht, J. Bendtsen, S.E. Cornell, J.F. Donges, M. Drüke, I. Fetzer, G. Bala, W. von Bloh, G. Feulner, S. Fiedler, D. Gerten, T. Gleeson, M. Hofmann, W. Huiskamp, M. Kummu, C. Mohan, D. Nogués-Bravo, S. Petri, M. Porkka, S. Rahmstorf, S. Schaphoff, K. Thonicke, A. Tobian, V. Virkki, L. Wang-Erlandsson, L. Weber, J. Rockström, Earth beyond six of nine planetary boundaries, Sci. Adv. 9 (2023) 1–17.

[7] P.M. Forster, C.J. Smith, T. Walsh, W.F. Lamb, R. Lamboll, M. Hauser, A. Ribes, D. Rosen, N. Gillett, M.D. Palmer, J. Rogelj, K. von Schuckmann, S.I. Seneviratne, B. Trewin, X. Zhang, M. Allen, R. Andrew, A. Birt, A. Borger, T. Boyer, J.A. Broersma, L. Cheng, F. Dentener, P. Friedlingstein, J.M. Gutiérrez, J. Gütschow, B. Hall, M. Ishii, S. Jenkins, X. Lan, J.-Y. Lee, C. Morice, C. Kadow, J. Kennedy, R. Killick, J.C. Minx, V. Naik, G.P. Peters, A. Pirani, J. Pongratz, C.-F. Schleussner, S. Szopa, P. Thorne, R. Rohde, M. Rojas Corradi, D. Schumacher, R. Vose, K. Zickfeld, V. Masson-Delmotte, P. Zhai, Indicators of Global Climate Change 2022: annual update of large-scale indicators of the state of the climate system and human influence, Earth Syst. Sci. Data 15 (2023) 2295–2327.

[8] The Energy Institute, Statistical Review of World Energy 2023, 72nd edition (2023).

[9] International Energy Agency, Net Zero by 2050: A Roadmap for the Global Energy

Sector, (2021).

[10] UN General Assembly, Transforming our world: The 2030 agenda for sustainable development, Resolution adopted by the General Assembly on 25 September 2015 (2015), paper A/RES/70/1.

[11] J. Rockström, Planetary boundaries, Stockholm Resilience Centre, Stockholm University, available at <https://www.stockholmresilience.org/>.

[12] M. Crippa, D. Guizzardi, F. Pagani, M. Banja, M. Muntean, S. E., W. Becker, F. Monforti-Ferrario, R. Quadrelli, A. Risquez Martin, P. Taghavi-Moharamli, J. Köykkä, G. Grassi, S. Rossi, J. Brandao De Melo, D. Oom, A. Branco, J. San-Miguel, E. Vignati, GHG emissions of all world countries, Publications Office of the European Union, Publications Office of the European Union (2023), paper JRC134504.

[13] Ministry of Land Infrastructure Transport and Tourism, Green Growth Strategy Through Achieving Carbon Neutrality in 2050, (2021).

[14] S. Chu, A. Majumdar, Opportunities and challenges for a sustainable energy future, Nature 488 (2012) 294–303.

[15] J.A. Jeevarajan, T. Joshi, M. Parhizi, T. Rauhala, D. Juarez-Robles, Battery Hazards for Large Energy Storage Systems, Energy Lett. 7 (2022) 2725–2733.

[16] International Energy Agency, Global EV Outlook 2023, (2023).

[17] A.R. Baird, E.J. Archibald, K.C. Marr, O.A. Ezekoye, Explosion hazards from lithium-ion battery vent gas, J. Power Sources 446 (2020) 227257.

[18] A. Yoshino, Secondary Battery, US Patent 4668595, (1987).

[19] A. Yoshino, The Birth of the Lithium-Ion Battery, Angew. Chemie Int. Ed. 51 (2012) 5798–5800.

[20] H. Zhang, M.-Y. Zhou, C.-E. Lin, B.-K. Zhu, Progress in polymeric separators for lithium ion batteries, RSC Adv. 5 (2015) 89848–89860.

[21] A. Yoshino, Technology trend of separator for lithium ion battery, Kinoshi Kenkyu Kaishi/Annals High Perform. Pap. Soc. Japan 54 (2015) 9–13.

[22] Q. Wang, B. Mao, S.I. Stoliarov, J. Sun, A review of lithium ion battery failure mechanisms and fire prevention strategies, Prog. Energy Combust. Sci. 73 (2019) 95–131.

[23] G.G. Eshetu, S. Grugeon, S. Laruelle, S. Boyanov, A. Lecocq, J.-P. Bertrand, G. Marlair, In-depth safety-focused analysis of solvents used in electrolytes for large scale lithium ion batteries, Phys. Chem. Chem. Phys. 15 (2013) 9145–9155.

[24] Y. Nishi, The development of lithium ion secondary batteries, Chem. Rec. 1 (2001) 406–413.

[25] D. Ouyang, M. Chen, Q. Huang, J. Weng, Z. Wang, J. Wang, A Review on the thermal hazards of the lithium-ion battery and the corresponding countermeasures, Appl. Sci. 9 (2019) 2483.

[26] P. Sun, R. Bisschop, H. Niu, X. Huang, A Review of Battery Fires in Electric Vehicles,

Fire Technol. 56 (2020) 1361–1410.

[27] A. Blum, T. Bensen, P. Rogers, C. Grant, G. Hough, Victorian Big Battery Fire: July 30, 2021, Techinical report, Fisher Engineering, Inc. and Energy Safety Response Group, (2022).

[28] A. Jana, D.R. Ely, R.E. García, Dendrite-separator interactions in lithium-based batteries, J. Power Sources 275 (2015) 912–921.

[29] X. Feng, M. Ouyang, X. Liu, L. Lu, Y. Xia, X. He, Thermal runaway mechanism of lithium ion battery for electric vehicles: A review, Energy Storage Mater. 10 (2018) 246–267.

[30] D.R. Lide, CRC Handbook of Chemistry and Physics, Internet V, CRC Press, Boca Raton, FL, (2005).

[31] P. Ribière, S. Grugeon, M. Morcrette, S. Boyanov, S. Laruelle, G. Marlair, Investigation on the fire-induced hazards of Li-ion battery cells by fire calorimetry, Energy Environ. Sci. 5 (2012) 5271–5280.

[32] G.G. Eshetu, J.P. Bertrand, A. Lecocq, S. Grugeon, S. Laruelle, M. Armand, G. Marlair, Fire behavior of carbonates-based electrolytes used in Li-ion rechargeable batteries with a focus on the role of the LiPF6 and LiFSI salts, J. Power Sources 269 (2014) 804–811.

[33] L. Kong, C. Li, J. Jiang, M.G. Pecht, Li-ion battery fire hazards and safety strategies, Energies 11 (2018) 2191.

[34] O. Mathieu, T. Sikes, W.D. Kulatilaka, E.L. Petersen, Ignition delay time and laminar flame speed measurements of mixtures containing diisopropyl-methylphosphonate (DIMP), Combust. Flame 215 (2020) 66–77.

[35] E.P. Roth, Thermal response and flammability of Li-ion cells for HEV and PHEV applications, SAE Tech. Pap. (2008).

[36] S.J. Harris, A. Timmons, W.J. Pitz, A combustion chemistry analysis of carbonate solvents used in Li-ion batteries, J. Power Sources 193 (2009) 855–858.

[37] K. Kitoh, H. Nemoto, 100 Wh large size Li-ion batteries and safety tests, J. Power Sources 81–82 (1999) 887–890.

[38] National Fire Protection Association, NFPA 30, Flammable and Combustible Liquids Code, available at <https://www.nfpa.org/>.

[39] S. Hess, M. Wohlfahrt-Mehrens, M. Wachtler, Flammability of Li-Ion Battery Electrolytes: Flash Point and Self-Extinguishing Time Measurements, J. Electrochem. Soc. 162 (2015) A3084–A3097.

[40] T. Tsujikawa, K. Yabuta, T. Matsushita, T. Matsushima, K. Hayashi, M. Arakawa, Characteristics of lithium-ion battery with non-flammable electrolyte, J. Power Sources 189 (2009) 429–434.

[41] J.K. Feng, X.P. Ai, Y.L. Cao, H.X. Yang, Possible use of non-flammable phosphonate ethers as pure electrolyte solvent for lithium batteries, J. Power Sources 177 (2008)

194–198.

[42] P.A. Glaude, W.J. Pitz, M.J. Thomson, Chemical kinetic modeling of dimethyl carbonate in an opposed-flow diffusion flame, Proc. Combust. Inst. 30 (2005) 1111–1118.

[43] E. Hu, Y. Chen, Z. Zhang, L. Pan, Q. Li, Y. Cheng, Z. Huang, Experimental and kinetic study on ignition delay times of dimethyl carbonate at high temperature, Fuel 140 (2015) 626–632.

[44] W. Sun, B. Yang, N. Hansen, C.K. Westbrook, F. Zhang, G. Wang, K. Moshammer, C.K. Law, An experimental and kinetic modeling study on dimethyl carbonate (DMC) pyrolysis and combustion, Combust. Flame 164 (2016) 224–238.

[45] H. Nakamura, H.J. Curran, A. Polo Córdoba, W.J. Pitz, P. Dagaut, C. Togbé, S.M. Sarathy, M. Mehl, J.R. Agudelo, F. Bustamante, An experimental and modeling study of diethyl carbonate oxidation, Combust. Flame 162 (2015) 1395–1405.

[46] W. Sun, C. Huang, T. Tao, F. Zhang, W. Li, N. Hansen, B. Yang, Exploring the high-temperature kinetics of diethyl carbonate (DEC) under pyrolysis and flame conditions, Combust. Flame 181 (2017) 71–81.

[47] S. Takahashi, K. Kanayama, S. Morikura, H. Nakamura, T. Tezuka, K. Maruta, Study on oxidation and pyrolysis of carbonate esters using a micro flow reactor with a controlled temperature profile. Part II: Chemical kinetic modeling of ethyl methyl carbonate, Combust. Flame 238 (2022) 111878.

[48] K. Kanayama, C.M. Grégoire, S.P. Cooper, Y. Almarzooq, E.L. Petersen, O. Mathieu, K. Maruta, H. Nakamura, Experimental and Chemical Kinetic Modeling Study of Ethylene Carbonate Oxidation: A Lithium-Ion Battery Electrolyte Surrogate Model, Combust. Flame 262 (2024) 113333.

[49] T.M. Jayaweera, C.F. Melius, W.J. Pitz, C.K. Westbrook, O.P. Korobeinichev, V.M. Shvartsberg, A.G. Shmakov, I.V. Rybitskaya, H.J. Curran, Flame inhibition by phosphorus-containing compounds over a range of equivalence ratios, Combust. Flame 140 (2005) 103–115.

[50] H.J. Curran, Developing detailed chemical kinetic mechanisms for fuel combustion, Proc. Combust. Inst. 37 (2019) 57–81.

[51] K. Maruta, T. Kataoka, N. Il Kim, S. Minaev, R. Fursenko, Characteristics of combustion in a narrow channel with a temperature gradient, Proc. Combust. Inst. 30 (2005) 2429–2436.

[52] K. Maruta, Micro and mesoscale combustion, Proc. Combust. Inst. 33 (2011) 125–150.

[53] F.L. Dryer, F.M. Haas, J. Santner, I. Farouk, M. Chaos, Interpreting chemical kinetics from complex reactioneadvectione diffusion systems: Modeling of flow reactors and related experiments, Prog. Energy Combust. Sci. 44 (2014) 19–39.

[54] Y. Ju, K. Maruta, Microscale combustion: Technology development and fundamental research, Prog. Energy Combust. Sci. 37 (2011) 669–715.

[55] K. Maruta, Micro and mesoscale combustion, Procee[1] K. Maruta, Micro Mesoscale Combust. Proc. Combust. Inst. 33 125–150.Dings Combust. Inst. 33 (2011) 125–150.

[56] Y. Tsuboi, T. Yokomori, K. Maruta, Lower limit of weak flame in a heated channel, Proc. Combust. Inst. 32 (2009) 3075–3081.

[57] S. Minaev, K. Maruta, R. Fursenko, Nonlinear dynamics of flame in a narrow channel with a temperature gradient, Combust. Theory Model. 11 (2007) 187–203.

[58] H. Nakamura, K. Maruta, New Application of Microcombustion: Fuel Reactivity Measurement and Research Tool for Combustion Chemical Kinetics, J. Combust. Soc. Japan 55 (2013) 264–271.

[59] T. Kamada, H. Nakamura, T. Tezuka, S. Hasegawa, K. Maruta, Study on combustion and ignition characteristics of natural gas components in a micro flow reactor with a controlled temperature profile, Combust. Flame 161 (2014) 37–48.

[60] H. Nakamura, R. Tanimoto, T. Tezuka, S. Hasegawa, K. Maruta, Soot formation characteristics and PAH formation process in a micro flow reactor with a controlled temperature profile, Combust. Flame 161 (2014) 582–591.

[61] H. Nakamura, S. Suzuki, T. Tezuka, S. Hasegawa, K. Maruta, Sooting limits and PAH formation of n-hexadecane and 2,2,4,4,6,8,8-heptamethylnonane in a micro flow reactor with a controlled temperature profile, Proc. Combust. Inst. 35 (2015) 3397–3404.

[62] A.K. Dubey, T. Tezuka, S. Hasegawa, H. Nakamura, K. Maruta, Study on sooting behavior of premixed C1–C4 n-alkanes/air flames using a micro flow reactor with a controlled temperature profile, Combust. Flame 174 (2016) 100–110.

[63] T. Okuno, H. Nakamura, T. Tezuka, S. Hasegawa, K. Maruta, Ultra-lean combustion characteristics of premixed methane flames in a micro flow reactor with a controlled temperature profile, Proc. Combust. Inst. 36 (2017) 4227–4233.

[64] A.K. Dubey, T. Tezuka, S. Hasegawa, H. Nakamura, K. Maruta, Analysis of kinetic models for rich to ultra-rich premixed CH4/air weak flames using a micro flow reactor with a controlled temperature profile, Combust. Flame 206 (2019) 68–82.

[65] P. Grajetzki, H. Nakamura, T. Tezuka, S. Hasegawa, K. Maruta, A novel reactivity index for SI engine fuels by separated weak flames in a micro flow reactor with a controlled temperature profile, Fuel 245 (2019) 429–437.

[66] K. Maruta, Micro flow reactor with prescribed temperature profile, First Int. Work. Flame Chem., Warsaw, Poland, 2012.

[67] A. Yamamoto, H. Oshibe, H. Nakamura, T. Tezuka, S. Hasegawa, K. Maruta, Stabilized three-stage oxidation of gaseous n-heptane/air mixture in a micro flow reactor with a controlled temperature profile, Proc. Combust. Inst. 33 (2011) 3259–3266.

[68] H. Oshibe, H. Nakamura, T. Tezuka, S. Hasegawa, K. Maruta, Stabilized three-stage oxidation of DME/air mixture in a micro flow reactor with a controlled temperature

profile, Combust. Flame 157 (2010) 1572–1580.

[69] S. Kikui, H. Nakamura, T. Tezuka, S. Hasegawa, K. Maruta, Study on combustion and ignition characteristics of ethylene, propylene, 1-butene and 1-pentene in a micro flow reactor with a controlled temperature profile, Combust. Flame 163 (2016) 209–219.

[70] H. Nakamura, A. Yamamoto, M. Hori, T. Tezuka, S. Hasegawa, K. Maruta, Study on pressure dependences of ethanol oxidation by separated weak flames in a micro flow reactor with a controlled temperature profile, Proc. Combust. Inst. 34 (2013) 3435–3443.

[71] S. Suzuki, M. Hori, H. Nakamura, T. Tezuka, S. Hasegawa, K. Maruta, Study on cetane number dependence of diesel surrogates/air weak flames in a micro flow reactor with a controlled temperature profile, Proc. Combust. Inst. 34 (2013) 3411–3417.

[72] Y. Murakami, H. Nakamura, T. Tezuka, G. Asai, K. Maruta, Reactivity of CO/H2/CH4/Air Mixtures Derived from In-Cylinder Fuel Reformation Examined by a Micro Flow Reactor with a Controlled Temperature Profile, Combust. Sci. Technol. 193 (2021) 266–279.

[73] H. Nakamura, H. Takahashi, T. Tezuka, S. Hasegawa, K. Maruta, K. Abe, Effects of CO-to-H2 ratio and diluents on ignition properties of syngas examined by weak flames in a micro flow reactor with a controlled temperature profile, Combust. Flame 172 (2016) 94–104.

[74] S. Takahashi, H. Nakamura, T. Tezuka, K. Maruta, Effects of blending ratios on the reactivities of CH2F2/C2HF5 refrigerant blends, Proc. Combust. Inst. 38 (2021) 2487–2495.

[75] Y. Murakami, H. Nakamura, T. Tezuka, K. Hiraoka, K. Maruta, Effects of mixture composition on oxidation and reactivity of DME/NH3/air mixtures examined by a micro flow reactor with a controlled temperature profile, Combust. Flame 238 (2022) 111911.

[76] M. Hori, A. Yamamoto, H. Nakamura, T. Tezuka, S. Hasegawa, K. Maruta, Study on octane number dependence of PRF/air weak flames at 1–5 atm in a micro flow reactor with a controlled temperature profile, Combust. Flame 159 (2012) 959–967.

[77] M. Hori, H. Nakamura, T. Tezuka, S. Hasegawa, K. Maruta, Characteristics of n-heptane and toluene weak flames in a micro flow reactor with a controlled temperature profile, Proc. Combust. Inst. 34 (2013) 3419–3426.

[78] S. Kikui, T. Kamada, H. Nakamura, T. Tezuka, S. Hasegawa, K. Maruta, Characteristics of n-butane weak flames at elevated pressures in a micro flow reactor with a controlled temperature profile, Proc. Combust. Inst. 35 (2015) 3405–3412.

[79] T. Shimizu, H. Nakamura, T. Tezuka, S. Hasegawa, K. Maruta, OH and CH2O Laser-Induced Fluorescence Measurements for Hydrogen Flames and Methane, n-Butane, and Dimethyl Ether Weak Flames in a Micro Flow Reactor with a Controlled Temperature Profile, Energy and Fuels 31 (2017) 2298–2307.

[80] H. Nakamura, T. Sugita, T. Tezuka, K. Maruta, Study on methane oxidation affected by dimethyl ether oxidation at low temperatures using a micro flow reactor with a controlled temperature profile, Combust. Flame 223 (2021) 320–329.

[81] Y. Sakai, H. Nakamura, T. Sugita, T. Tezuka, Y. Uygun, Chemical Interpretation on the Multi-Stage Oxidation of Diethyl Ether, J. Therm. Sci. 32 (2023) 513–520.

[82] S. Takahashi, H. Nakamura, T. Tezuka, S. Hasegawa, K. Maruta, Multi-stage oxidation of a CH2F2/air mixture examined by weak flames in a micro flow reactor with a controlled temperature profile, Combust. Flame 201 (2019) 140–147.

[83] H. Nakamura, S. Hasegawa, Combustion and ignition characteristics of ammonia/air mixtures in a micro flow reactor with a controlled temperature profile, Proc. Combust. Inst. 36 (2017) 4217–4226.

[84] S. Takahashi, H. Nakamura, T. Tezuka, K. Maruta, Oxidation of a C2HF5/air mixture examined by weak flames in a micro flow reactor with a controlled temperature profile, Combust. Flame 217 (2020) 12–20.

[85] K. Tamaoki, Y. Murakami, K. Kanayama, T. Tezuka, M. Izumi, H. Nakamura, Roles of NH2 reactions in ammonia oxidation at intermediate temperatures: Experiments and chemical kinetic modeling, Combust. Flame 259 (2024) 113177.

[86] K. Kanayama, A.K. Dubey, T. Tezuka, S. Hasegawa, H. Nakamura, K. Maruta, Study on Products from Fuel-rich Methane Combustion near Sooting Limit Temperature Region and Importance of Methyl Radicals for the Formation of First Aromatic Rings, Combust. Sci. Technol. 194 (2022) 832–849.

[87] T. Harada, Y. Murakami, K. Tamaoki, K. Kanayama, T. Tezuka, M. Izumi, H. Nakamura, N2O Consumption by Thermal Decomposition and Reduction with CH4, C2H6 and NH3, Combust. Sci. Technol., accepted.

[88] H. Nakamura, S. Hasegawa, T. Tezuka, Kinetic modeling of ammonia/air weak flames in a micro flow reactor with a controlled temperature profile, Combust. Flame 185 (2017) 16–27.

[89] P.S. Institut, Swiss Light Source - SLS, available at <https://www.psi.ch/en/sls/about-sls>.

[90] M. Johnson, A. Bodi, L. Schulz, T. Gerber, Vacuum ultraviolet beamline at the Swiss Light Source for chemical dynamics studies, Nucl. Instruments Methods Phys. Res. Sect. A Accel. Spectrometers, Detect. Assoc. Equip. 610 (2009) 597–603.

[91] J.H.D. Eland, Photoelectron Spectroscopy, 2nd editio, Elsevier Butterworth-Heinemann, UK, (1984).

[92] T. Koopmans, Über die Zuordnung von Wellenfunktionen und Eigenwerten zu den Einzelnen Elektronen Eines Atoms, Physica 1 (1934) 104–113.

[93] J.H.D. Eland, Photoelectron Spectroscopy, 2nd editio, Elsevier Butterworth-Heinemann, UK, (1984).

[94] P. Hemberger, Z. Pan, X. Wu, Z. Zhang, K. Kanayama, A. Bodi, Photoion Mass-

Selected Threshold Photoelectron Spectroscopy to Detect Reactive Intermediates in Catalysis: From Instrumentation and Examples to Peculiarities and a Database, J. Phys. Chem. C 127 (2023) 16751–16763.

[95] K. Tsukiyama, S. Hoshino, Ultraviole-Visible and Fluorescence Spectroscopy, The Spectroscopical Society of Japan, JP, (2021).

[96] R. Tuckett, J. Harvey, P. Hemberger, A. Bodi, The vacuum-ultraviolet photoelectron spectra of CH2F2 and CH2Cl2 revisited, J. Mol. Spectrosc. 315 (2015) 172–183.

[97] M.J. Frisch, G.W. Trucks, H.B. Schlegel, G.E. Scuseria, M.A. Robb, J.R. Cheeseman, G. Scalmani, V. Barone, G.A. Petersson, H. Nakatsuji, X. Li, M. Caricato, A. V. Marenich, J. Bloino, B.G. Janesko, R. Gomperts, B. Mennucci, H.P. Hratchian, J. V. Ortiz, A.F. Izmaylov, J.L. Sonnenberg, D. Williams-Young, F. Ding, F. Lipparini, F. Egidi, J. Goings, B. Peng, A. Petrone, T. Henderson, D. Ranasinghe, V.G. Zakrzewski, J. Gao, N. Rega, G. Zheng, W. Liang, M. Hada, M. Ehara, K. Toyota, R. Fukuda, J. Hasegawa, M. Ishida, T. Nakajima, Y. Honda, O. Kitao, H. Nakai, T. Vreven, K. Throssell, J.A. Montgomery, J.E. Peralta, F. Ogliaro, M.J. Bearpark, J.J. Heyd, E.N. Brothers, K.N. Kudin, V.N. Staroverov, T.A. Keith, R. Kobayashi, J. Normand, K. Raghavachari, A.P. Rendell, J.C. Burant, S.S. Iyengar, J. Tomasi, M. Cossi, J.M. Millam, M. Klene, C. Adamo, R. Cammi, J.W. Ochterski, R.L. Martin, K. Morokuma, O. Farkas, J.B. Foresman, D.J. Fox, Gaussian 16, Revision C.01, available at <https://gaussian.com/gaussian16/>.

[98] S. Gozem, A.I. Krylov, The ezSpectra suite: An easy-to-use toolkit for spectroscopy modeling, WIREs Comput. Mol. Sci. 12 (2022) 1–22.

[99] P. Hemberger, A. Bodi, T. Bierkandt, M. Köhler, D. Kaczmarek, T. Kasper, Photoelectron Photoion Coincidence Spectroscopy Provides Mechanistic Insights in Fuel Synthesis and Conversion, Energy and Fuels 35 (2021) 16265–16302.

[100] F. Qi, Combustion chemistry probed by synchrotron VUV photoionization mass spectrometry, Proc. Combust. Inst. 34 (2013) 33–63.

[101] C.A. Taatjes, N. Hansen, A. McIlroy, J.A. Miller, J.P. Senosiain, S.J. Klippenstein, F. Qi, L. Sheng, Y. Zhang, T.A. Cool, J. Wang, P.R. Westmoreland, M.E. Law, T. Kasper, K. Kohse-Höinghaus, Enols Are Common Intermediates in Hydrocarbon Oxidation, Science 308 (2005) 1887–1889.

[102] N. Hansen, T.A. Cool, P.R. Westmoreland, K. Kohse-Höinghaus, Recent contributions of flame-sampling molecular-beam mass spectrometry to a fundamental understanding of combustion chemistry, Prog. Energy Combust. Sci. 35 (2009) 168–191.

[103] P. Hemberger, J.A. van Bokhoven, J. Pérez-Ramírez, A. Bodi, New analytical tools for advanced mechanistic studies in catalysis: Photoionization and photoelectron photoion coincidence spectroscopy, Catal. Sci. Technol. 10 (2020) 1975–1990.

[104] A. Bodi, P. Hemberger, J. Pérez-ramírez, Photoionization reveals catalytic mechanisms, Nat. Catal. 5 (2022) 850-851.

[105] A. Bodi, M. Johnson, T. Gerber, Z. Gengeliczki, B. Sztáray, T. Baer, Imaging photoelectron photoion coincidence spectroscopy with velocity focusing electron optics, Rev. Sci. Instrum. 80 (2009) 034101.

[106] A. Bodi, P. Hemberger, T. Gerber, B. Sztáray, A new double imaging velocity focusing coincidence experiment: I2PEPICO, Rev. Sci. Instrum. 83 (2012) 083105.

[107] B. Sztáray, K. Voronova, K.G. Torma, K.J. Covert, A. Bodi, P. Hemberger, T. Gerber, D.L. Osborn, CRF-PEPICO: Double velocity map imaging photoelectron photoion coincidence spectroscopy for reaction kinetics studies, J. Chem. Phys. 147 (2017) 013944.

[108] A. Bodi, B. Sztáray, T. Baer, M. Johnson, T. Gerber, Data acquisition schemes for continuous two-particle time-of-flight coincidence experiments, Rev. Sci. Instrum. 78 (2007) 084102.

[109] C. for N. photoIonization M. Spectrometry, Photoionization Cross Section database, available at <https://flame.nsrl.ustc.edu.cn/database/?version=en>.

[110] N.I. of S. and T. Technology, NIST Chemistry WebBook, available at <https://webbook.nist.gov/chemistry/>.

[111] T. Bierkandt, P. Hemberger, P. Oßwald, M. Köhler, T. Kasper, Insights in m-xylene decomposition under fuel-rich conditions by imaging photoelectron photoion coincidence spectroscopy, Proc. Combust. Inst. 36 (2017) 1223–1232.

[112] D. Krüger, P. Oßwald, M. Köhler, P. Hemberger, T. Bierkandt, T. Kasper, The fate of the OH radical in molecular beam sampling experiments, Proc. Combust. Inst. 37 (2019) 1563–1570.

[113] P. Hemberger, X. Wu, Z. Pan, A. Bodi, Continuous Pyrolysis Microreactors: Hot Sources with Little Cooling? New Insights Utilizing Cation Velocity Map Imaging and Threshold Photoelectron Spectroscopy, J. Phys. Chem. A 126 (2022) 2196–2210.

[114] A. Arteconi, A. Mazzarini, G. Di Nicola, Emissions from ethers and organic carbonate fuel additives: A review, Water. Air. Soil Pollut. 221 (2011) 405–423.

[115] A.O.G. Abdalla, D. Liu, Dimethyl carbonate as a promising oxygenated fuel for combustion: A review, Energies 11 (2018) 1552.

[116] M. Kozak, J. Merkisz, P. Bielaczyc, A. Szczotka, The Influence of Oxygenated Diesel Fuels on a Diesel Vehicle PM/NOx Emission Trade-Off, SAE Technical Paper (2009), paper 2009-01–2696.

[117] P. Rounce, A. Tsolakis, P. Leung, A.P.E. York, A Comparison of Diesel and Biodiesel Emissions Using Dimethyl Carbonate as an Oxygenated Additive, Energy and Fuels 24 (2010) 4812–4819.

[118] L. Xiaolu, C. Hongyan, Z. Zhiyong, H. Zhen, Study of combustion and emission characteristics of a diesel engine operated with dimethyl carbonate, Energy Convers. Manag. 47 (2006) 1438–1448.

[119] J.H. Chan, A. Tsolakis, J.M. Herreros, K.X. Kallis, C. Hergueta, S. Sittichompoo, M.

Bogarra, Combustion, gaseous emissions and PM characteristics of Di-Methyl Carbonate (DMC)-gasoline blend on gasoline Direct Injection (GDI) engine, Fuel 263 (2020) 116742.

[120] A.H. Tamboli, A.A. Chaugule, H. Kim, Catalytic developments in the direct dimethyl carbonate synthesis from carbon dioxide and methanol, Chem. Eng. J. 323 (2017) 530–544.

[121] M. Honda, S. Kuno, N. Begum, K.I. Fujimoto, K. Suzuki, Y. Nakagawa, K. Tomishige, Catalytic synthesis of dialkyl carbonate from low pressure CO2 and alcohols combined with acetonitrile hydration catalyzed by CeO2, Appl. Catal. A Gen. 384 (2010) 165–170.

[122] T.R. Jow, K. Xu, O. Borodin, M. Ue, Electrolytes for Lithium and Lithium-Ion Batteries, Springer, New York, (2014).

[123] F. Guo, Y. Ozaki, K. Nishimura, N. Hashimoto, O. Fujita, Influence of lithium salts on the combustion characteristics of dimethyl carbonate-based electrolytes using a wick combustion method, Combust. Flame 213 (2020) 314–321.

[124] M.E. Bardin, E. V. Ivanov, E.J.K.K. Nilsson, V.A. Vinokurov, A.A. Konnov, Laminar burning velocities of dimethyl carbonate with air, Energy and Fuels 27 (2013) 5513–5517.

[125] M. Henriksen, K. Vaagseather, A. V. Gaathaug, J. Lundberg, S. Forseth, D. Bjerketvedt, Laminar Burning Velocity of the Dimethyl Carbonate–Air Mixture Formed by the Li-Ion Electrolyte Solvent, Combust. Explos. Shock Waves 56 (2020) 383–393.

[126] T. Atherley, S. de Persis, N. Chaumeix, Y. Fernandes, A. Bry, A. Comandini, O. Mathieu, S. Alturaifi, C.R. Mulvihill, E.L. Petersen, Laminar flame speed and shock-tube multi-species laser absorption measurements of Dimethyl Carbonate oxidation and pyrolysis near 1 atm, Proc. Combust. Inst. 38 (2021) 977–985.

[127] K. Alexandrino, M.U. Alzueta, H.J. Curran, An experimental and modeling study of the ignition of dimethyl carbonate in shock tubes and rapid compression machine, Combust. Flame 188 (2018) 212–226.

[128] X. Li, W. Xu, Y. Li, Y. Jiang, Investigation of Laminar Burning Velocities and Cellular Instability for Dimethyl Carbonate at Elevated Pressures, Energy & Fuels 35 (2021) 6210–6218.

[129] C.M. Grégoire, Y.M. Almarzooq, E.L. Petersen, O. Mathieu, Experimental and modeling study of the combustion of ethyl methyl carbonate, a battery electrolyte, Combust. Flame 260 (2024) 113225.

[130] R. Shahla, C. Togbé, S. Thion, R. Timothée, M. Lailliau, F. Halter, C. Chauveau, G. Dayma, P. Dagaut, Burning velocities and jet-stirred reactor oxidation of diethyl carbonate, Proc. Combust. Inst. 36 (2017) 553–560.

[131] S.P. Cooper, C.M. Grégoire, Y.M. Almarzooq, E.L. Petersen, O. Mathieu,

Experimental Kinetics Study on Diethyl Carbonate Oxidation, Fuels 4 (2023) 243–260.

[132] L. Yin, W. Xu, Y. Hu, Y. Jiang, Experimental and theoretical investigation of ethyl methyl carbonate/air flames: Laminar burning velocity and cellular instability at elevated pressures, Fuel 346 (2023) 128206.

[133] A. Sinha, M.J. Thomson, The chemical structures of opposed flow diffusion flames of C3 oxygenated hydrocarbons (isopropanol, dimethoxy methane, and dimethyl carbonate) and their mixtures, Combust. Flame 136 (2004) 548–556.

[134] K. Kanayama, S. Takahashi, S. Morikura, H. Nakamura, T. Tezuka, K. Maruta, Study on oxidation and pyrolysis of carbonate esters using a micro flow reactor with a controlled temperature profile. Part I: Reactivities of dimethyl carbonate, ethyl methyl carbonate and diethyl carbonate, Combust. Flame 237 (2022) 111810.

[135] C.M. Grégoire, S.P. Cooper, M. Khan-Ghauri, S.A. Alturaifi, E.L. Petersen, O. Mathieu, Pyrolysis study of dimethyl carbonate, diethyl carbonate, and ethyl methyl carbonate using shock-tube spectroscopic CO measurements and chemical kinetics investigation, Combust. Flame 249 (2023) 112594.

[136] P. Sela, Y. Zhang, J. Herzler, M. Fikri, C. Schulz, S. Peukert, Pyrolysis of diethyl carbonate: Shock-tube and flow-reactor measurements and modeling, Proc. Combust. Inst. 38 (2021) 987–996.

[137] W.K. Metcalfe, S.M. Burke, S.S. Ahmed, H.J. Curran, A hierarchical and comparative kinetic modeling study of C1-C2 hydrocarbon and oxygenated fuels, Int. J. Chem. Kinet. 45 (2013) 638–675.

[138] S.L. Fischer, F.L. Dryer, H.J. Curran, The reaction kinetics of dimethyl ether. I: High-temperature pyrolysis and oxidation in flow reactors, Int. J. Chem. Kinet. 32 (2000) 713–740.

[139] C.-W. Zhou, Y. Li, E. O'Connor, K.P. Somers, S. Thion, C. Keesee, O. Mathieu, E.L. Petersen, T.A. DeVerter, M.A. Oehlschlaeger, G. Kukkadapu, C.-J. Sung, M. Alrefae, F. Khaled, A. Farooq, P. Dirrenberger, P.-A. Glaude, F. Battin-Leclerc, J. Santner, Y. Ju, T. Held, F.M. Haas, F.L. Dryer, H.J. Curran, A comprehensive experimental and modeling study of isobutene oxidation, Combust. Flame 167 (2016) 353–379.

[140] S. Dooley, H.J. Curran, J.M. Simmie, Autoignition measurements and a validated kinetic model for the biodiesel surrogate, methyl butanoate, Combust. Flame 153 (2008) 2–32.

[141] S. Dooley, M.P. Burke, M. Chaos, Y. Stein, F.L. Dryer, V.P. Zhukov, O. Finch, J.M. Simmie, H.J. Curran, Methyl formate oxidation: Speciation data, laminar burning velocities, ignition delay times, and a validated chemical kinetic model, Int. J. Chem. Kinet. 42 (2010) 527–549.

[142] S.L. Peukert, R. Sivaramakrishnan, J. V Michael, High Temperature Shock Tube Studies on the Thermal Decomposition of O3 and the Reaction of Dimethyl Carbonate with O-Atoms, J. Phys. Chem. A 117 (2013) 3729–3738.

[143] S.L. Peukert, R. Sivaramakrishnan, J. V Michael, High Temperature Shock Tube and Theoretical Studies on the Thermal Decomposition of Dimethyl Carbonate and Its Bimolecular Reactions with H and D-Atoms, J. Phys. Chem. A 117 (2013) 3718–3728.

[144] D.G. Goodwin, H.K. Moffat, I. Schoegl, R.L. Speth, B.W. Weber, Cantera: An object-oriented software toolkit for chemical kinetics, thermodynamics, and transport processes, available at <https://www.cantera.org/>.

[145] Chemkin-Pro V19.0, ANSYS Inc., San Diego.

[146] Y. Kizaki, H. Nakamura, T. Tezuka, S. Hasegawa, K. Maruta, Effect of radical quenching on CH4/air flames in a micro flow reactor with a controlled temperature profile, Proc. Combust. Inst. 35 (2015) 3389–3396.

[147] Y. Saiki, Y. Suzuki, Effect of wall surface reaction on a methane-air premixed flame in narrow channels with different wall materials, Proc. Combust. Inst. 34 (2013) 3395–3402.

[148] R. Notario, J. Quijano, C. Sánchez, E. Vélez, Theoretical study of the mechanism of thermal decomposition of carbonate esters in the gas phase, J. Phys. Org. Chem. 18 (2005) 134–141.

[149] E.R. Ritter, J.W. Bozzelli, THERM: Thermodynamic property estimation for gas phase radicals and molecules, Int. J. Chem. Kinet. 23 (1991) 767–778.

[150] S.W. Benson, Thermochemical Kinetics, 2nd ed., Wiley, New York, (1976).

[151] A. Miyoshi, KUCRS software library, revision 2021.12.26, available at <http://akrmys.com/KUCRS/>.

[152] J. Herzler, J.A. Manion, W. Tsang, Single-Pulse Shock Tube Studies of the Decomposition of Ethoxy Compounds, J. Phys. Chem. A 101 (1997) 5494–5499.

[153] M. AlAbbad, B.R. Giri, M. Szőri, B. Viskolcz, A. Farooq, A high temperature kinetic study for the thermal unimolecular decomposition of diethyl carbonate, Chem. Phys. Lett. 684 (2017) 390–396.

[154] A. Farooq, D.F. Davidson, R.K. Hanson, C.K. Westbrook, A comparative study of the chemical kinetics of methyl and ethyl propanoate, Fuel 134 (2014) 26–38.

[155] W.K. Metcalfe, S. Dooley, H.J. Curran, J.M. Simmie, A.M. El-Nahas, M. V. Navarro, Experimental and modeling study of C5H10O2 ethyl and methyl esters, J. Phys. Chem. A 111 (2007) 4001–4014.

[156] L. Zhang, P. Zhao, M. Xu, X. Wang, Computational identification of the safety regime of Li-ion battery thermal runaway, Appl. Energy 261 (2020) 114440.

[157] A. Cellier, F. Duchaine, T. Poinsot, G. Okyay, M. Leyko, M. Pallud, An analytically reduced chemistry scheme for large eddy simulation of lithium-ion battery fires, Combust. Flame 250 (2023) 112648.

[158] S. Kinoshita, M. Kotato, Y. Sakata, M. Ue, Y. Watanabe, H. Morimoto, S. Tobishima, Effects of cyclic carbonates as additives to γ-butyrolactone electrolytes for rechargeable lithium cells, J. Power Sources 183 (2008) 755–760.

[159] K. Xu, Nonaqueous Liquid Electrolytes for Lithium-Based Rechargeable Batteries, Chem. Rev. 104 (2004) 4303–4417.

[160] L. Xing, W. Li, C. Wang, F. Gu, M. Xu, C. Tan, J. Yi, Theoretical investigations on oxidative stability of solvents and oxidative decomposition mechanism of ethylene carbonate for lithium ion battery use, J. Phys. Chem. B 113 (2009) 16596–16602.

[161] C.M. Grégoire, E.L. Petersen, O. Mathieu, Shock-tube CO measurements during the pyrolysis of ethylene carbonate, Combust. Flame 257 (2023) 113019.

[162] V. Pokorný, V. Štejfa, M. Fulem, C. Červinka, K. Růžička, Vapor Pressures and Thermophysical Properties of Ethylene Carbonate, Propylene Carbonate, γ-Valerolactone, and γ-Butyrolactone, J. Chem. Eng. Data 62 (2017) 4174–4186.

[163] E.L. Petersen, Interpreting Endwall and Sidewall Measurements in Shock-Tube Ignition Studies, Combust. Sci. Technol. 181 (2009) 1123–1144.

[164] E.L. Petersen, M.J.A. Rickard, M.W. Crofton, E.D. Abbey, M.J. Traum, D.M. Kalitan, A facility for gas- and condensed-phase measurements behind shock waves, Meas. Sci. Technol. 16 (2005) 1716–1729.

[165] O. Mathieu, C. Mulvihill, E.L. Petersen, Shock-tube water time-histories and ignition delay time measurements for H2S near atmospheric pressure, Proc. Combust. Inst. 36 (2017) 4019–4027.

[166] S.A. Alturaifi, C.R. Mulvihill, O. Mathieu, E.L. Petersen, Speciation measurements in shock tubes for validation of complex chemical kinetics mechanisms: Application to 2-Methyl-2-Butene oxidation, Combust. Flame 225 (2021) 196–213.

[167] R.M. Spearrin, C.S. Goldenstein, J.B. Jeffries, R.K. Hanson, Quantum cascade laser absorption sensor for carbon monoxide in high-pressure gases using wavelength modulation spectroscopy, Appl. Opt. 53 (2014) 1938–1946.

[168] C.R. Mulvihill, H2O Laser Absorption and OH* Chemiluminescence Measurements of H2-NO2 Oxidation in a Shock Tube, Doctoral dissertation, Texas A&M University, (2019).

[169] T. Sikes, O. Mathieu, W.D. Kulatilaka, M.S. Mannan, E.L. Petersen, Laminar flame speeds of DEMP, DMMP, and TEP added to H2- and CH4-air mixtures, Proc. Combust. Inst. 37 (2019) 3775–3781.

[170] M.C. Krejci, O. Mathieu, A.J. Vissotski, S. Ravi, T.G. Sikes, E.L. Petersen, A. Kérmonès, W. Metcalfe, H.J. Curran, Laminar Flame Speed and Ignition Delay Time Data for the Kinetic Modeling of Hydrogen and Syngas Fuel Blends, J. Eng. Gas Turbines Power 135 (2013).

[171] C.L. Keesee, B. Guo, E.L. Petersen, Proper interpretation and overall accuracy of laminar flame speed measurements of single- and multi-component liquid fuels, Proc. Combust. Inst. 38 (2021) 2225–2234.

[172] C.L. Keesee, B. Guo, E.L. Petersen, Laminar Flame Speed Measurements of Kerosene-Based Fuels Accounting for Uncertainties in Mixture Average Molecular Weight, J.

Eng. Gas Turbines Power 143 (2021).

[173] Z. Chen, On the extraction of laminar flame speed and Markstein length from outwardly propagating spherical flames, Combust. Flame 158 (2011) 291–300.

[174] T. Sikes, M.S. Mannan, E.L. Petersen, An experimental study: laminar flame speed sensitivity from spherical flames in stoichiometric CH4-air mixtures, Combust. Sci. Technol. 190 (2018) 1594–1613.

[175] S. Maeda, Y. Harabuchi, Y. Sumiya, M. Takagi, K. Suzuki, K. Sugiyama, Y. Ono, M. Hatanaka, Y. Osada, T. Taketsugu, K. Morokuma, K. Ohno, Global Reaction Route Mapping (GRRM) Program, available at <https://iqce.jp/GRRM/index_e.shtml>.

[176] S. Maeda, T. Taketsugu, K. Morokuma, K. Ohno, Anharmonic Downward Distortion Following for Automated Exploration of Quantum Chemical Potential Energy Surfaces, Bull. Chem. Soc. Jpn. 87 (2014) 1315–1334.

[177] A. Wildenberg, Y. Fenard, M. Carbonnier, A. Kéromnès, B. Lefort, Z. Serinyel, G. Dayma, L. Le Moyne, P. Dagaut, K.A. Heufer, An experimental and kinetic modeling study on the oxidation of 1,3-dioxolane, Proc. Combust. Inst. 38 (2021) 543–553.

[178] P. Zhang, S. Li, Y. Wang, W. Ji, W. Sun, B. Yang, X. He, Z. Wang, C.K. Law, F. Zhang, Measurement of reaction rate constants using RCM: A case study of decomposition of dimethyl carbonate to dimethyl ether, Combust. Flame 183 (2017) 30–38.

[179] R. Añez, A. Herize, A. Sierraalta, T. Cordova, G. Chuchani, DFT study of substituent effects of 2-substituted alkyl ethyl methylcarbonates in homogeneous, unimolecular gas phase elimination kinetics, Int. J. Chem. Kinet. 38 (2006) 184–193.

[180] K. Kanayama, S. Takahashi, H. Nakamura, T. Tezuka, K. Maruta, Experimental and modeling study on pyrolysis of ethylene carbonate/dimethyl carbonate mixture, Combust. Flame 245 (2022) 112359.

[181] A. Miyoshi, GPOP software, rev. 2013.07.15m10, available at <http://akrmys.com/gpop/>.

[182] A. Miyoshi, SSUMES software, rev. 2018.06.14m5, available at <http://akrmys.com/ssumes/>.

[183] A. Wildenberg, M. Döntgen, I.S. Roy, C. Huang, B. Lefort, L. Le Moyne, A. Kéromnès, K. Leonhard, K.A. Heufer, Solving the riddle of the high-temperature chemistry of 1,3-dioxolane, Proc. Combust. Inst. 39 (2023) 705–713.

[184] Y. Wu, S. Panigrahy, A.B. Sahu, C. Bariki, J. Beeckmann, J. Liang, A.A.E. Mohamed, S. Dong, C. Tang, H. Pitsch, Z. Huang, H.J. Curran, Understanding the antagonistic effect of methanol as a component in surrogate fuel models: A case study of methanol/n-heptane mixtures, Combust. Flame 226 (2021) 229–242.

[185] M. Baigmohammadi, V. Patel, S. Nagaraja, A. Ramalingam, S. Martinez, S. Panigrahy, A.A.E.-S. Mohamed, K.P. Somers, U. Burke, K.A. Heufer, A. Pekalski, H.J. Curran, Comprehensive Experimental and Simulation Study of the Ignition Delay Time

Characteristics of Binary Blended Methane, Ethane, and Ethylene over a Wide Range of Temperature, Pressure, Equivalence Ratio, and Dilution, Energy & Fuels 34 (2020) 8808–8823.

[186] O. Mathieu, C.M. Grégoire, M.A. Turner, D.J. Mohr, S.A. Alturaifi, J.C. Thomas, E.L. Petersen, Experimental Investigation of the Combustion Properties of an Average Thermal Runaway Gas Mixture from Li-Ion Batteries, Energy and Fuels 36 (2022) 3247–3258.

[187] A. Joshi, X. You, T.A. Barckholtz, H. Wang, Thermal Decomposition of Ethylene Oxide: Potential Energy Surface, Master Equation Analysis, and Detailed Kinetic Modeling, J. Phys. Chem. A 109 (2005) 8016–8027.

[188] Y. Fenard, A. Gil, G. Vanhove, H.H. Carstensen, K.M. Van Geem, P.R. Westmoreland, O. Herbinet, F. Battin-Leclerc, A model of tetrahydrofuran low-temperature oxidation based on theoretically calculated rate constants, Combust. Flame 191 (2018) 252–269.

[189] B.R. Giri, F. Khaled, M. Szori, B. Viskolcz, A. Farooq, An experimental and theoretical kinetic study of the reaction of OH radicals with tetrahydrofuran, Proc. Combust. Inst. 36 (2017) 143–150.

[190] L.-S. Tran, M. Verdicchio, F. Monge, R.C. Martin, R. Bounaceeur, B. Sirjean, P.-A. Glaude, M.U. Alzueta, F. Battin-Leclerc, An experimental and modeling study of the combustion of tetrahydrofuran, Combust. Flame 162 (2015) 1899–1918.

[191] D.L. Allara, R. Shaw, A compilation of kinetic parameters for the thermal degradation of n-alkane molecules, J. Phys. Chem. Ref. Data 9 (1980) 523–560.

[192] O. Mathieu, C.M. Grégoire, M. Khan-Ghauri, S.P. Cooper, E.L. Petersen, Experimental study of the formation of CO during ethanol pyrolysis and dry reforming with CO2, Appl. Energy Combust. Sci. 11 (2022) 100076.

[193] G. Bucher, W. Sander, Clarifying the structure of carbonic acid, Science (80-.). 346 (2014) 544–545.

[194] K. Adamczyk, M. Prémont-Schwarz, D. Pines, E. Pines, E.T.J. Nibbering, Real-Time Observation of Carbonic Acid Formation in Aqueous Solution, Science (80-.). 326 (2009) 1690–1694.

[195] H.P. Reisenauer, J.P. Wagner, P.R. Schreiner, Gas-Phase Preparation of Carbonic Acid and Its Monomethyl Ester, Angew. Chemie Int. Ed. 53 (2014) 11766–11771.

[196] K. Caldeira, M.E. Wickett, Anthropogenic carbon and ocean pH, Nature 425 (2003) 365–365.

[197] S.K. Reddy, S. Balasubramanian, Carbonic acid: Molecule, crystal and aqueous solution, Chem. Commun. 50 (2014) 503–514.

[198] M.H. Moore, R.K. Khanna, Infrared and mass spectral studies of proton irradiated H2O + CO2 ice: Evidence for carbonic acid, Spectrochim. Acta Part A Mol. Spectrosc. 47 (1991) 255–262.

[199] W. Hage, A. Hallbrucker, E. Mayer, Metastable intermediates from glassy solutions

part 5: FTIR spectroscopic characterization of isolated α- and β-carbonic acid, J. Mol. Struct. 408–409 (1997) 527–531.

[200] J. Brucato, M. Palumbo, G. Strazzulla, Carbonic Acid by Ion Implantation in Water/Carbon Dioxide Ice Mixtures, Icarus 125 (1997) 135–144.

[201] P.A. Gerakines, M.H. Moore, R.L. Hudson, Carbonic acid production in H2O:CO2 ices - UV photolysis vs. proton bombardment, Astron. Astrophys. 357 (2000) 793–800.

[202] M. Garozzo, D. Fulvio, O. Gomis, M.E. Palumbo, G. Strazzulla, H-implantation in SO2 and CO2 ices, Planet. Space Sci. 56 (2008) 1300–1308.

[203] Y. Oba, N. Watanabe, A. Kouchi, T. Hama, V. Pirronello, Formation of Carbonic Acid (H2CO3) by Surface Reactions of Non-Energetic OH Radicals with CO Molecules at Low Temperatures, Astrophys. J. 722 (2010) 1598–1606.

[204] B.M. Jones, R.I. Kaiser, G. Strazzulla, UV-Vis, Infrared, and Mass Spectroscopy of Electron Irradiated Frozen Oxygen and Carbon Dioxide Mixtures with Water, Astrophys. J. 781 (2014) 85.

[205] S. Pavithraa, J.I. Lo, B.M. Cheng, B.N.R. Sekhar, N.J. Mason, B. Sivaraman, Identification of a unique VUV photoabsorption band of carbonic acid for its identification in radiation and thermally processed water-carbon dioxide ices, Spectrochim. Acta - Part A Mol. Biomol. Spectrosc. 215 (2019) 130–132.

[206] X. Wang, T. Bürgi, Observation of Carbonic Acid Formation from Interaction between Carbon Dioxide and Ice by Using In Situ Modulation Excitation IR Spectroscopy, Angew. Chemie Int. Ed. 60 (2021) 7860–7865.

[207] S. Ioppolo, Z. Kaňuchová, R.L. James, A. Dawes, A. Ryabov, J. Dezalay, N.C. Jones, S. V. Hoffmann, N.J. Mason, G. Strazzulla, Vacuum ultraviolet photoabsorption spectroscopy of space-related ices: Formation and destruction of solid carbonic acid upon 1 keV electron irradiation, Astron. Astrophys. 646 (2021) 1–15.

[208] G. Strazzulla, J.R. Brucato, G. Cimino, M.E. Palumbo, Carbonic acid on Mars?, Planet. Space Sci. 44 (1996) 1447–1450.

[209] M.L. Delitsky, A.L. Lane, Ice chemistry on the Galilean satellites, J. Geophys. Res. Planets 103 (1998) 31391–31403.

[210] W. Zheng, R.I. Kaiser, On the formation of carbonic acid (H2CO3) in solar system ices, Chem. Phys. Lett. 450 (2007) 55–60.

[211] M. Sanz-Novo, V.M. Rivilla, I. Jiménez-Serra, J. Martín-Pintado, L. Colzi, S. Zeng, A. Megías, Á. López-Gallifa, A. Martínez-Henares, S. Massalkhi, B. Tercero, P. de Vicente, S. Martín, D.S. Andrés, M.A. Requena-Torres, Discovery of the Elusive Carbonic Acid (HOCOOH) in Space, Astrophys. J. 954 (2023) 3.

[212] W. Hage, K.R. Liedl, A. Hallbrucker, E. Mayer, Carbonic acid in the gas phase and its astrophysical relevance, Science 279 (1998) 1332–1335.

[213] Z. Peeters, R.L. Hudson, M.H. Moore, A. Lewis, The formation and stability of carbonic acid on outer Solar System bodies, Icarus 210 (2010) 480–487.

[214] M.T. Nguyen, T.K. Ha, A Theoretical Study of the Formation of Carbonic Acid from the Hydration of Carbon Dioxide: A Case of Active Solvent Catalysis, J. Am. Chem. Soc. 106 (1984) 599–602.

[215] C.A. Wight, A.I. Boldyrev, Potential energy surface and vibrational frequencies of carbonic acid, J. Phys. Chem. 99 (1995) 12125–12130.

[216] T. Mori, K. Suma, Y. Sumiyoshi, Y. Endo, Spectroscopic detection of isolated carbonic acid, J. Chem. Phys. 130 (2009) 204308.

[217] J.K. Terlouw, C.B. Lebrilla, H. Schwarz, Thermolysis of NH4HCO3—A Simple Route to the Formation of Free Carbonic Acid(H2CO3) in the Gas Phase, Angew. Chemie Int. Ed. 26 (1987) 354–355.

[218] T. Mori, K. Suma, Y. Sumiyoshi, Y. Endo, Spectroscopic detection of the most stable carbonic acid, cis-cis H2CO3, J. Chem. Phys. 134 (2011) 044319.

[219] J. Bernard, R.G. Huber, K.R. Liedl, H. Grothe, T. Loerting, Matrix Isolation Studies of Carbonic Acid—The Vapor Phase above the β-Polymorph, J. Am. Chem. Soc. 135 (2013) 7732–7737.

[220] D.S.N. Parker, R.I. Kaiser, T.P. Troy, M. Ahmed, Hydrogen Abstraction/Acetylene Addition Revealed, Angew. Chemie Int. Ed. 53 (2014) 7740–7744.

[221] T. Yang, R.I. Kaiser, T.P. Troy, B. Xu, O. Kostko, M. Ahmed, A.M. Mebel, M. V. Zagidullin, V.N. Azyazov, HACA's Heritage: A Free-Radical Pathway to Phenanthrene in Circumstellar Envelopes of Asymptotic Giant Branch Stars, Angew. Chemie Int. Ed. 56 (2017) 4515–4519.

[222] J. Bouwman, M.N. McCabe, C.N. Shingledecker, J. Wandishin, V. Jarvis, E. Reusch, P. Hemberger, A. Bodi, Five-membered ring compounds from the ortho-benzyne + methyl radical reaction under interstellar conditions, Nat. Astron. 7 (2023) 423–430.

[223] M.N. McCabe, P. Hemberger, E. Reusch, A. Bodi, J. Bouwman, Off the Beaten Path: Almost Clean Formation of Indene from the ortho -Benzyne + Allyl Reaction, J. Phys. Chem. Lett. 11 (2020) 2859–2863.

[224] L.B. Tuli, S.J. Goettl, A.M. Turner, A.H. Howlader, P. Hemberger, S.F. Wnuk, T. Guo, A.M. Mebel, R.I. Kaiser, Gas phase synthesis of the C40 nano bowl C40H10, Nat. Commun. 14 (2023) 1527.

[225] S.J. Goettl, L.B. Tuli, A.M. Turner, Y. Reyes, A.H. Howlader, S.F. Wnuk, P. Hemberger, A.M. Mebel, R.I. Kaiser, Gas-Phase Synthesis of Coronene through Stepwise Directed Ring Annulation, J. Am. Chem. Soc. (2023).

[226] J. Krüger, G.A. Garcia, D. Felsmann, K. Moshammer, A. Lackner, A. Brockhinke, L. Nahon, K. Kohse-Höinghaus, Photoelectron–photoion coincidence spectroscopy for multiplexed detection of intermediate species in a flame, Phys. Chem. Chem. Phys. 16 (2014) 22791–22804.

[227] E. Reusch, F. Holzmeier, P. Constantinidis, P. Hemberger, I. Fischer, Isomer-Selective Generation and Spectroscopic Characterization of Picolyl Radicals, Angew. Chemie Int.

Ed. 56 (2017) 8000–8003.

[228] M. Steglich, V.B.F. Custodis, A.J. Trevitt, G. DaSilva, A. Bodi, P. Hemberger, Photoelectron Spectrum and Energetics of the meta-Xylylene Diradical, J. Am. Chem. Soc. 139 (2017) 14348–14351.

[229] M. Gerlach, E. Karaev, D. Schaffner, P. Hemberger, I. Fischer, Threshold Photoelectron Spectrum of m -Benzyne, J. Phys. Chem. Lett. 13 (2022) 11295–11299.

[230] D.W. Kohn, H. Clauberg, P. Chen, Flash pyrolysis nozzle for generation of radicals in a supersonic jet expansion, Rev. Sci. Instrum. 63 (1992) 4003–4005.

[231] Q. Guan, K.N. Urness, T.K. Ormond, D.E. David, G. Barney Ellison, J.W. Daily, The properties of a micro-reactor for the study of the unimolecular decomposition of large molecules, Int. Rev. Phys. Chem. 33 (2014) 447–487.

[232] S. Grimm, S.-J. Baik, P. Hemberger, A. Bodi, A.M. Kempf, T. Kasper, B. Atakan, Gas-phase aluminium acetylacetonate decomposition: revision of the current mechanism by VUV synchrotron radiation, Phys. Chem. Chem. Phys. 23 (2021) 15059–15075.

[233] B. Sztáray, T. Baer, Suppression of hot electrons in threshold photoelectron photoion coincidence spectroscopy using velocity focusing optics, Rev. Sci. Instrum. 74 (2003) 3763–3768.

[234] Y. Shao, Z. Gan, E. Epifanovsky, A.T.B. Gilbert, M. Wormit, J. Kussmann, A.W. Lange, A. Behn, J. Deng, X. Feng, D. Ghosh, M. Goldey, P.R. Horn, L.D. Jacobson, I. Kaliman, R.Z. Khaliullin, T. Kuš, A. Landau, J. Liu, E.I. Proynov, Y.M. Rhee, R.M. Richard, M.A. Rohrdanz, R.P. Steele, E.J. Sundstrom, H.L. Woodcock, P.M. Zimmerman, D. Zuev, B. Albrecht, E. Alguire, B. Austin, G.J.O. Beran, Y.A. Bernard, E. Berquist, K. Brandhorst, K.B. Bravaya, S.T. Brown, D. Casanova, C.M. Chang, Y. Chen, S.H. Chien, K.D. Closser, D.L. Crittenden, M. Diedenhofen, R.A. Distasio, H. Do, A.D. Dutoi, R.G. Edgar, S. Fatehi, L. Fusti-Molnar, A. Ghysels, A. Golubeva-Zadorozhnaya, J. Gomes, M.W.D. Hanson-Heine, P.H.P. Harbach, A.W. Hauser, E.G. Hohenstein, Z.C. Holden, T.C. Jagau, H. Ji, B. Kaduk, K. Khistyaev, J. Kim, J. Kim, R.A. King, P. Klunzinger, D. Kosenkov, T. Kowalczyk, C.M. Krauter, K.U. Lao, A.D. Laurent, K. V. Lawler, S. V. Levchenko, C.Y. Lin, F. Liu, E. Livshits, R.C. Lochan, A. Luenser, P. Manohar, S.F. Manzer, S.P. Mao, N. Mardirossian, A. V. Marenich, S.A. Maurer, N.J. Mayhall, E. Neuscamman, C.M. Oana, R. Olivares-Amaya, D.P. Oneill, J.A. Parkhill, T.M. Perrine, R. Peverati, A. Prociuk, D.R. Rehn, E. Rosta, N.J. Russ, S.M. Sharada, S. Sharma, D.W. Small, A. Sodt, T. Stein, D. Stück, Y.C. Su, A.J.W. Thom, T. Tsuchimochi, V. Vanovschi, L. Vogt, O. Vydrov, T. Wang, M.A. Watson, J. Wenzel, A. White, C.F. Williams, J. Yang, S. Yeganeh, S.R. Yost, Z.Q. You, I.Y. Zhang, X. Zhang, Y. Zhao, B.R. Brooks, G.K.L. Chan, D.M. Chipman, C.J. Cramer, W.A. Goddard, M.S. Gordon, W.J. Hehre, A. Klamt, H.F. Schaefer, M.W. Schmidt, C.D. Sherrill, D.G. Truhlar, A. Warshel, X. Xu, A. Aspuru-Guzik, R. Baer, A.T. Bell, N.A. Besley, J. Da Chai, A. Dreuw, B.D. Dunietz, T.R. Furlani, S.R. Gwaltney, C.P.

Hsu, Y. Jung, J. Kong, D.S. Lambrecht, W. Liang, C. Ochsenfeld, V.A. Rassolov, L. V. Slipchenko, J.E. Subotnik, T. Van Voorhis, J.M. Herbert, A.I. Krylov, P.M.W. Gill, M. Head-Gordon, Advances in molecular quantum chemistry contained in the Q-Chem 4 program package, Mol. Phys. 113 (2015) 184–215.

[235] G. Bucher, Ester Pyrolysis of Carbonates: Bis(benzene hydrate) Carbonate as Potential Precursor for Monomeric Carbonic Acid, European J. Org. Chem. 2010 (2010) 1070–1075.

[236] B. Ruscic, Active Thermochemical Tables (ATcT) ver. 1.124, available at <https://atct.anl.gov/>.

[237] P. Thaddeus, M. Guelin, R.A. Linke, Three new “nonterrestrial” molecules, Astrophys. J. 246 (1981) L41–L45.

[238] L. Majumdar, P. Gratier, V. Wakelam, E. Caux, K. Willacy, M.E. Ressler, Detection of HOCO+ in the protostar IRAS 16293−2422, Mon. Not. R. Astron. Soc. 477 (2018) 525–530.

[239] A. Twarowski, Reduction of a phosphorus oxide and acid reaction set, Combust. Flame 102 (1995) 41–54.

[240] O.P. Korobeinichev, V.M. Shvartsberg, A.G. Shmakov, T.A. Bolshova, T.M. Jayaweera, C.F. Melius, W.J. Pitz, C.K. Westbrook, H. Curran, Flame inhibition by phosphorus-containing compounds in lean and rich propane flames, Proc. Combust. Inst. 30 (2005) 2353–2360.

[241] O. Mathieu, W.D. Kulatilaka, E.L. Petersen, Experimental and modeling study on the effects of dimethyl methylphosphonate (DMMP) addition on H2, CH4, and C2H4 ignition, Combust. Flame 191 (2018) 320–334.

[242] O.P. Korobeinichev, V.M. Shvartsberg, A.A. Chernov, The Destruction Chemistry of Organophosphorus Compounds in Flames - II: Structure of a Hydrogen–OxygenFlame Doped with Trimethyl Phosphate.pdf, Combust. Flame 118 (1999) 727–732.

[243] O.P. Korobeinichev, T.A. Bolshova, V.M. Shvartsberg, A.A. Chernov, Inhibition and promotion of combustion by organophosphorus compounds added to flames of CH4 or H2 in O2 and Ar, Combust. Flame 125 (2001) 744–751.

[244] O.P. Korobeinichev, S.B. Ilyin, V. V. Mokruchin, A.G. Shmakov, Destruction Chemistry of Dimethyl Methylphosphonate in H2/O2/Ar Flame Studied by Molecular Beam Mass Spectrometry, Combust. Sci. Technol. 116–117 (1996) 51–67.

[245] O.P. Korobeinichev, S.B. Ilyin, V.M. Shvartsberg, A.A. Chernov, The destruction chemistry of organophosphorus compounds in flames - I: Quantitative determination of final phosphorus-containing species in hydrogen-oxygen flames, Combust. Flame 118 (1999) 718–726.

[246] D.A. Knyazkov, V.M. Shvartsberg, A.G. Shmakov, O.P. Korobeinichev, Influence of organophosphorus inhibitors on the structure of atmospheric lean and rich methane-oxygen flames, Combust. Explos. Shock Waves 43 (2007) 143–151.

[247] S. Liang, P. Hemberger, N.M. Neisius, A. Bodi, H. Grützmacher, J. Levalois-Grützmacher, S. Gaan, Elucidating the Thermal Decomposition of Dimethyl Methylphosphonate by Vacuum Ultraviolet (VUV) Photoionization: Pathways to the PO Radical, a Key Species in Flame-Retardant Mechanisms, Chem. - A Eur. J. 21 (2015) 1073–1080.

[248] S. Liang, P. Hemberger, M. Steglich, P. Simonetti, J. Levalois-Grützmacher, H. Grützmacher, S. Gaan, The Underlying Chemistry to the Formation of PO2 Radicals from Organophosphorus Compounds: A Missing Puzzle Piece in Flame Chemistry, Chem. – A Eur. J. 26 (2020) 10795–10800.

[249] S. Neupane, F. Barnes, S. Barak, E. Ninnemann, Z. Loparo, A.E. Masunov, S.S. Vasu, Shock Tube/Laser Absorption and Kinetic Modeling Study of Triethyl Phosphate Combustion, J. Phys. Chem. A 122 (2018) 3829–3836.

[250] Y. Jing, J. Cui, B. Liu, Q. Zhu, Q. Xu, Z. Hu, F. Fu, L. Xing, Z. Wang, Pyrolysis and kinetic study of dimethyl methylphosphonate (DMMP) by synchrotron photoionization mass spectrometry, Combust. Flame 255 (2023) 112919.

[251] N. Gaiser, T. Bierkandt, P. Oßwald, J. Zinsmeister, P. Hemberger, S. Shaqiri, M. Aigner, T. Kasper, M. Köhler, Oxidation of linear and branched ethers: A comparative flow reactor study of OME2 and trimethoxymethane, Proc. Combust. Inst. 39 (2023) 685–693.

[252] S. Chattopadhyay, G.L. Findley, S.P. McGlynn, Photoelectron spectroscopy of phosphites and phosphates, J. Electron Spectros. Relat. Phenomena 24 (1981) 27–36.

[253] B. Sztáray, A. Bodi, T. Baer, Modeling unimolecular reactions in photoelectron photoion coincidence experiments, J. Mass Spectrom. 45 (2010) 1233–1245.

[254] N. Lokachari, G. Kukkadapu, B.D. Etz, G.M. Fioroni, S. Kim, M. Steglich, A. Bodi, P. Hemberger, S.S. Matveev, A. Thomas, H. Song, G. Vanhove, K. Zhang, G. Dayma, M. Lailliau, Z. Serinyel, A.A. Konnov, P. Dagaut, W.J. Pitz, H.J. Curran, A comprehensive experimental and kinetic modeling study of di-isobutylene isomers: Part 2, Combust. Flame 251 (2023) 112547.

[255] B. Niu, D.A. Shirley, Y. Bai, High resolution photoelectron spectroscopy and femtosecond intramolecular dynamics of H2CO+ and D2CO+, J. Chem. Phys. 98 (1993) 4377–4390.

[256] K.A.G. Macneil, R.N. Dixon, High-resolution photoelectron spectroscopy of methanol and its deuterated derivatives: Internal rotation in the ground ionic state, J. Electron Spectros. Relat. Phenomena 11 (1977) 315–331.

[257] J.J. Butler, D.M.P. Holland, A.C. Parr, R. Stockbauer, A threshold photoelectron-photoion coincidence spectrometric study of dimethyl ether (CH3OCH3), Int. J. Mass Spectrom. Ion Process. 58 (1984) 1–14.

[258] J.M. Dyke, A. Morris, A. Ridha, Study of the ground state of PO+ using photoelectron spectroscopy, J. Chem. Soc. Faraday Trans. 2 78 (1982) 2077.

[259] X. Zhao, X. Chu, G. Rauhut, C. Chen, C. Song, B. Lu, X. Zeng, Phosphorus Analogues of Methyl Nitrite and Nitromethane: CH3OPO and CH3PO2, Angew. Chemie Int. Ed. 58 (2019) 12164–12169.

[260] T. Yu, X. Wu, X. Zhou, A. Bodi, P. Hemberger, Hydrogen migration as a potential driving force in the thermal decomposition of dimethoxymethane: New insights from pyrolysis imaging photoelectron photoion coincidence spectroscopy and computations, Combust. Flame 222 (2020) 123–132.

[261] T.M. Pazdera, J. Wenz, M. Olzmann, The unimolecular decomposition of dimethoxymethane: channel switching as a function of temperature and pressure, Faraday Discuss. 238 (2022) 665–681.

[262] P. Glarborg, A.D. Jensen, J.E. Johnsson, Fuel nitrogen conversion in solid fuel fired systems, Prog. Energy Combust. Sci. 29 (2003) 89–113.

[263] K. Kohse-Höinghaus, P. Oßwald, T.A. Cool, T. Kasper, N. Hansen, F. Qi, C.K. Westbrook, P.R. Westmoreland, Biofuel Combustion Chemistry: From Ethanol to Biodiesel, Angew. Chemie Int. Ed. 49 (2010) 3572–3597.

[264] M. Pelucchi, S. Arunthanayothin, Y. Song, O. Herbinet, A. Stagni, H.-H. Carstensen, T. Faravelli, F. Battin-Leclerc, Pyrolysis and Combustion Chemistry of Pyrrole, a Reference Component for Bio-oil Surrogates: Jet-Stirred Reactor Experiments and Kinetic Modeling, Energy & Fuels 35 (2021) 7265–7284.

[265] P. Glarborg, J.A. Miller, B. Ruscic, S.J. Klippenstein, Modeling nitrogen chemistry in combustion, Prog. Energy Combust. Sci. 67 (2018) 31–68.

[266] I. Glassman, Soot formation in combustion processes, Symp. Int. Combust. 22 (1988) 295–311.

[267] H. Kobayashi, A. Hayakawa, K.D.K.A. Somarathne, E.C. Okafor, Science and technology of ammonia combustion, Proc. Combust. Inst. 37 (2019) 109–133.

[268] M.J. Montgomery, H. Kwon, J.A.H. Dreyer, Y. Xuan, C.S. McEnally, L.D. Pfefferle, Effect of ammonia addition on suppressing soot formation in methane co-flow diffusion flames, Proc. Combust. Inst. 38 (2021) 2497–2505.

[269] A.M. Bennett, P. Liu, Z. Li, N.M. Kharbatia, W. Boyette, A.R. Masri, W.L. Roberts, Soot formation in laminar flames of ethylene/ammonia, Combust. Flame 220 (2020) 210–218.

[270] P. Liu, B. Chen, A. Bennett, H. Pitsch, W.L. Roberts, Probing the influence of hydrogen cyanide on PAH chemistry, Proc. Combust. Inst. 39 (2023) 1139-1146.

[271] A. Landera, A.M. Mebel, Mechanisms of formation of nitrogen-containing polycyclic aromatic compounds in low-temperature environments of planetary atmospheres: A theoretical study, Faraday Discuss. 147 (2010) 479–494.

[272] D.S.N. Parker, R.I. Kaiser, On the formation of nitrogen-substituted polycyclic aromatic hydrocarbons (NPAHs) in circumstellar and interstellar environments, Chem. Soc. Rev. 46 (2017) 452–463.

[273] Z. Tian, Y. Li, T. Zhang, A. Zhu, Z. Cui, F. Qi, An experimental study of low-pressure premixed pyrrole/oxygen/argon flames with tunable synchrotron photoionization, Combust. Flame 151 (2007) 347–365.

[274] Z. Tian, Y. Li, T. Zhang, A. Zhu, F. Qi, Identification of combustion intermediates in low-pressure premixed pyridine/oxygen/argon flames, J. Phys. Chem. A 112 (2008) 13549–13555.

[275] J.A. Miller, C.T. Bowman, Mechanism and modeling of nitrogen chemistry in combustion, Prog. Energy Combust. Sci. 15 (1989) 287–338.

[276] A. Lucassen, P. Oßwald, U. Struckmeier, K. Kohse-Höinghaus, T. Kasper, N. Hansen, T.A. Cool, P.R. Westmoreland, Species identification in a laminar premixed low-pressure flame of morpholine as a model substance for oxygenated nitrogen-containing fuels, Proc. Combust. Inst. 32 (2009) 1269–1276.

[277] A. Lucassen, N. Labbe, P.R. Westmoreland, K. Kohse-Höinghaus, Combustion chemistry and fuel-nitrogen conversion in a laminar premixed flame of morpholine as a model biofuel, Combust. Flame 158 (2011) 1647–1666.

[278] P. Masclet, D. Grosjean, G. Mouvier, J. Dubois, Alkene ionization potentials: Part I: Quantitative determination of alkyl group structural effects, J. Electron Spectros. Relat. Phenomena 2 (1973) 225–237.

[279] G. Bieri, F. Burger, E. Heilbronner, J.P. Maier, Valence Ionization Energies of Hydrocarbons, Helv. Chim. Acta 60 (1977) 2213–2233.

[280] G.C. Eiden, K.T. Lu, J. Badenhoop, F. Weinhold, J.C. Weisshaar, Threshold photoionization spectra of benzyl radical: Cation vibrational states and ab initio calculations, J. Chem. Phys. 104 (1996) 8886–8895.

[281] J.D. Savee, J. Zádor, P. Hemberger, B. Sztáray, A. Bodi, D.L. Osborn, Threshold photoelectron spectrum of the benzyl radical, Mol. Phys. 113 (2015) 2217–2227.

[282] T.F. Palmer, F.P. Lossing, Free Radicals by Mass Spectrometry. XXX. Ionization Potentials of Anilino and 2-, 3- and 4-Pyridylmethyl Radicals, J. Am. Chem. Soc. 85 (1963) 1733–1735.

[283] K. Hayashibara, G.H. Kruppa, J.L. Beauchamp, Photoelectron spectroscopy of the o-, m-, and p-methylbenzyl radicals. Implications for the thermochemistry of the radicals and ions, J. Am. Chem. Soc. 108 (1986) 5441–5443.

[284] M. Steglich, A. Bodi, J.P. Maier, P. Hemberger, Probing different spin states in xylyl radicals and ions, Phys. Chem. Chem. Phys. 20 (2018) 7180–7189.

[285] J.A. Bray, E.R. Bernstein, 3-Picolyl and 2,5-Lutidyl Radicals: Generation, Optical Spectroscopy, and ab Initio Calculations, J. Phys. Chem. A 103 (1999) 2208–2213.

[286] I. Fischer, P. Hemberger, Photoelectron Photoion Coincidence Spectroscopy of Biradicals, ChemPhysChem (2023) e202300334.

[287] W.E. Wallace, “Mass Spectra” in NIST Chemistry WebBook, available at <https://doi.org/10.18434/T4D303>.

[288] C. Fernholz, A. Bodi, P. Hemberger, Threshold Photoelectron Spectrum of the Phenoxy Radical, J. Phys. Chem. A 126 (2022) 9022–9030.

[289] J. Cioslowski, General and unique partitioning of molecular electronic properties into atomic contributions, Phys. Rev. Lett. 62 (1989) 1469–1471.

[290] J. Cioslowski, A new population analysis based on atomic polar tensors, J. Am. Chem. Soc. 111 (1989) 8333–8336.

[291] K.C. Gross, P.G. Seybold, C.M. Hadad, Comparison of different atomic charge schemes for predicting pKa variations in substituted anilines and phenols, Int. J. Quantum Chem. 90 (2002) 445–458.

[292] A.A.G. Al Abdel Hamid, S. Kanan, Z.A. Tahat, DFT analysis of substituent effects on electron-donating efficacy of pyridine, Res. Chem. Intermed. 41 (2015) 6859–6875.

[293] G.F. Crable, G.L. Kearns, Effect of Substituent Groups on the Ionization Potentials of Benzenes, J. Phys. Chem. 66 (1962) 436–439.

[294] M. Haeberlein, J.S. Murray, T. Brinck, P. Politzer, Calculated electrostatic potentials and local surface ionization energies of para -substituted anilines as measures of substituent effects, Can. J. Chem. 70 (1992) 2209–2214.

[295] C. Dahlstrand, K. Yamazaki, K. Kilså, H. Ottosson, Substituent Effects on the Electron Affinities and Ionization Energies of Tria-, Penta-, and Heptafulvenes: A Computational Investigation, J. Org. Chem. 75 (2010) 8060–8068.

[296] C. Cauletti, G. Di Maio, W. Li, E. Vecchi, T. Vondrák, Substituent effects on ionization energies in some 4r-substituted cyclohexanones, Tetrahedron 42 (1986) 3677–3682.

[297] G.A. DiLabio, D.A. Pratt, J.S. Wright, Theoretical Calculation of Ionization Potentials for Disubstituted Benzenes: Additivity vs Non-Additivity of Substituent Effects, J. Org. Chem. 65 (2000) 2195–2203.

[298] M. Fukushima, K. Obi, Laser-induced fluorescence spectra of jet cooled p-chlorobenzyl radical, Chem. Phys. Lett. 248 (1996) 269–276.

[299] S.Y. Chae, S.K. Lee, S.H. Kim, Observation of Vibronic Emission Spectra of Jet-Cooled o-Chlorobenzyl Radical, Bull. Korean Chem. Soc. 23 (2002) 795–797.

[300] D.P. Mukhopadhyay, M. Gerlach, S. Hartweg, I. Fischer, J.-C. Loison, Photoelectron spectroscopy of low valent organophosphorus compounds, P–CH3, H–P=CH2 and P=CH2, Phys. Chem. Chem. Phys. 24 (2022) 10993–10999.

[301] E. Karaev, M. Gerlach, L. Faschingbauer, J. Ramler, I. Krummenacher, C. Lichtenberg, P. Hemberger, I. Fischer, Bonding in Low-Coordinated Organoarsenic and Organoantimony Compounds: A Threshold Photoelectron Spectroscopic Investigation, Chem. – A Eur. J. 29 (2023) e202300637.

[302] A.G. Harrison, F.P. Lossing, Free Radicals by Mass Spectrometry. XVIII. The Ionization Potentials of Conjugated Hydrocarbon Radicals and the Resonance Energies of Radicals and Carbonium Ions, J. Am. Chem. Soc. 82 (1960) 1052–1054.

Acknowledgements

First of all, I would like to thank from the bottom of my heart all those who have been involved with me during my PhD journey. Without any single one of them, I could not have accomplished this dissertation.

I would like to express my sincere gratitude to my supervisor at Tohoku University, Professor Hisashi Nakamura, for his guidance and support for my whole master’s and PhD research over seven years. Everything I learned about research, not only scientific topics but also how to work on research, comes from him. I would also like to express my sincere gratitude to Professor Kaoru Maruta for motivating and stimulating me to pursue a PhD degree. He taught me that research is both enjoyable and challenging, unlike merely taking credits, ever since I joined his laboratory in 2017. I am immensely grateful for all the kind guidance from my supervisor at Paul Scherrer Institut, Dr. Patrick Hemberger. His warm acceptance of having me at PSI has enriched my experience and broadened my scientific, global and life perspectives. I would also like to acknowledge Professor Koji Amezawa and Professor Akihiro Hayakawa for dedicating their time and effort to my defense and dissertation. Professor Youhi Morii and Professor Yuji Saito always provided me with interesting topics through not only research discussions but also daily communication in the lab. Professor Ajit K. Dubey taught me about soot topics during my bachelor’s and master’s degrees as well as various scientific subjects when we met at a conference. All my experiments at Tohoku University would not have been possible without the assistance of Mr. Takuya Tezuka and Mr. Masahiko Izumi. I deeply appreciate their tremendous help. I would also like to extend my thanks to Ms. Hiromi Ito and Ms. Reiko Chiba for handling all my administrative tasks.

To my colleagues in the Energy Dynamics Laboratory at Tohoku University, thank you for making my lab life enjoyable. Great thanks to Dr. Yuki Murakami and Dr. Shintaro Takahashi for their encouragement and assistance in accomplishing the work as well as for taking me out beyond the lab on holidays. Mr. Takaki Akiba and Mr. Keisuke Akita, who ran through the seven-year course with me, although our main research interest were different, we discussed and talked a lot every day. Without them, I might not be able to complete this long run. And also, I would like to thank Mr. Shota Morikura who previously worked on the carbonate ester project and continued to care about me even after he graduated from the university. I greatly appreciate all the other lab members and visiting scholars as well whose names are not given here.

To all my colleagues in the Reaction Dynamics Group at Paul Scherrer Institut, namely Dr. Andras Bodi, Dr. Zeyou Pan, Dr. Xiangkun Wu and Dr. Zihao Zhang, thank you so much for welcoming and helping me during my stay at PSI. Even though I came from a different field from them, they always kindly taught me their knowledge as well as supported

my beamtimes at SLS. My friends within and outside PSI made my days and gave me wonderful memories over my stay in Switzerland.

I would also like to thank our research corroborators from Professor Eric L. Petersen’s group, the Turbo Machinery Laboratory at Texas A&M University. A special thanks to Professor Olivier Mathieu and Ms. Claire M. Grégoire who worked enthusiastically on the project with us. Not only the experiments but also fruitful discussions each time we saw each other at a conference everywhere significantly propelled our project forward.

Last but not least, I would like to express my gratitude to my family for always standing by me. My parents, Takahiko and Yukari, let me do what I wanted and offered warm support whenever I needed it. My brother, Shota, and sister, Mayu, both abroad, gave me advice and encouraged my decision to study abroad. Finally, to our dog, Michelle, who may not speak, but is always waiting for me at home and makes me relaxed.

This work had been mainly carried out at the Institute of Fluid Science, Tohoku University, Japan and at Paul Scherrer Institut, Switzerland. I acknowledge the financial support from the Research Fellowship Program for Young Scientists provided by the Japan Society for the Promotion of Science, Grants in Aid for JSPS Fellows Grant Number 22J13787; the Support for Pioneering Research Initiated by the Next Generation provided by the Japan Science and Technology Agency, JST SPRING Grant Number JPMJSP2114; Graduate Program for Integration of Mechanical Systems (GP-Mech); and IFS-GCORE Overseas Dispatch Program.

January 9, 2024
Keisuke Kanayama